Electronic Structure of Open-shell Transition Metal Complexes

Tobias Krämer

Linacre College

A thesis submitted for the degree of
Doctor of Philosophy

Department of Chemistry
University of Oxford

Michaelmas Term 2011

Electronic Structure of Open-shell Transition Metal Complexes

Tobias Krämer, Linacre College

A Thesis submitted for the degree of Doctor of Philosophy
Department of Chemistry, University of Oxford

Michaelmas 2011

Abstract

This thesis presents electronic structure calculations on problems related to the bonding in inorganic coordination compounds and clusters. A wide range of molecules with the ability to exist in different structural forms or electronic states has been selected and density functional theory is systematically applied in order to gain detailed insight into their characteristics and reactivity at the electronic level. First, we address the question of redox non-innocent behaviour of bipyridine in a series of 1st row transition metal complexes. Complexes of the type $[M(2,2'\text{-bipyridine})(mes)_2]^0$ (M = Cr, Mn, Fe, Co, Ni; mes = 2,4,6-$Me_3C_6H_2$) and their one-electron reduced forms have been explored. The results clearly show that the anions are best described as complexes of the monoanionic bipyridine radical ($S_{bpy} = 1/2$), giving a rationale for the observed structural changes within the ligand. Likewise, we have identified dianionic bipyridine in both the complexes $[Zn_2(4,4'\text{-bpy})(mes)_4]^{2-}$ and $[Fe(2,2'\text{-bpy})_2]^{2-}$. In no case have we found evidence for significant metal-to-ligand backbonding. The subject of redox-noninnocence is further revisited in a comparative study of the two complexes [M(*o*-Clpap)$_3$] (M = Cr, Mo; *o*-Clpap = 2-[(2-chlorophenyl)azo]-pyridine), and their associated electron transfer series. The results indicate that all electron transfer processes are primarily ligand-based, although in the case of the Mo analogue these are coupled to substantial electron density changes at the metal. The ability of pap to form radical anions finds a contrasting case in the dinuclear Rh complex $[Rh_2(\mu\text{-}p\text{-Clpap})_2(cod)Cl_2]$, where the two ligand bridges act as acceptors of strong dπ^* backbonding from a formally Rh^{-I} centre. We then direct our attention to the endohedral Zintl clusters $[Fe@Ge_{10}]^{3-}$ and $[Mn@Pb_{12}]^{3-}$, which reveal peculiar topologies. We have probed the electronic factors that influence their geometric preferences, and propose a model based on the shift of electron density from the endohedral metal to the cage to account for the observed geometries. Subsequently, we reassess the electronic structure of the xenophilic clusters $Mn_2(thf)_4(Fe(CO)_4)_2$ and $[Mn(Mn(thf)_2)_3(Mn(CO)_4)_3]^-$. We conclude that these are best viewed as exchange coupled Mn^{II} centres bridged by closed-shell carbonylate fragments. In the closing chapter the reduction of NO_2^- to NO by the complex $[Cu(tct)(NO_2)]^+$ (tct = *cis*,*cis*-1,3,5-tris(cinnamylideneamino)cyclohexane) is studied, a process that mimics the enzyme-catalysed reaction. Two viable pathways for the reaction have been traced and key intermediates identified. Both direct release of NO or via decomposition of a Cu-NO complex are kinetically and thermodynamically feasible.

“Die Quanten sind doch eine hoffnungslose Schweinerei.”

Max Born in a letter to Albert Einstein.

For my parents

Author's declaration

This thesis is an account of work carried out by the author in the Department of Chemistry, University of Oxford, under supervision of Prof. John E. McGrady. No part of this work has previously been submitted for a degree in this University or elsewhere. The work of other authors has been freely drawn and is duly acknowledged in the text. A list of references is given at the end of the thesis.

Tobias Krämer

Oxford, 11^{th} October 2011

Acknowledgements

I owe my deepest gratitude to my supervisor and 'Doktorvater' Prof. John E. McGrady for his constant guidance and support over the past several years. John has been an excellent mentor and teacher, always being helpful and encouraging.

I would like to thank Dr. Hans M. Senn who took on the role as a second supervisor in the initial years of my doctoral studies. Hans has generously provided his time to introduce me to the secrets of the projector-augmented wave method and the CP-PAW code. The results of this project have unfortunately not made it into this thesis. I would also like to thank Prof. Peter E. Blöchl who has answered lots of my questions regarding his CP-PAW program, either on the phone or via email.

During my time in the McGrady group I have been fortunate to work with a number of interesting people (Dr. Muhsen Al-Ibadi, Dr. Thomas Davin, Prof. Michel Etienne, Dr. Vihar P. Georgiev, Mohan Janakiraman), here in Oxford and in Glasgow. I would like to thank them for their thoughtful input, many stimulating discussions, scientific or otherwise, and last but not least, for creating a friendly atmosphere in the 'lab'. I am particularly indebted to Dr. Ekaterina Zueva and Dr. Chamil Sameera for their scientific guidance on the broken-symmetry methodology, and to Dr. Dimitrios Pantazis for his support with the ORCA package.

Collaborations with several groups here and elsewhere have been central to this work, and I want to thank everybody involved for the smooth teamwork.

A big thanks goes to the members of IT support, especially Tom Bradshaw, Keith Waters and also Pete Biggs, for swiftly dealing with all kinds of computer issues and problems related to the group's clusters.

I want to thank everybody at Linacre College for their kind support, especially Dr. Asel Sartbaeva for the many pieces of good advice on academic questions.

Certainly, the many friends that I have met at the stages of my way so far deserve a thank you, especially friends from Bonn (Jenny, Rainer and Janna for the funny times we shared during our studies at the Uni Bonn and beyond) and Hamburg (Jörg and Ingo "den GR20 machen wir auf jeden Fall noch", Nadine, Jan 'der Doc', Lena, Michael, Hinni, Caro, Jana, Dana, Kat). Of course a big thank you goes to all the people I met up in Glasgow, especially to Frank, Mona, Daniela, Johannes, Filip, Raphaëlle and Flo, for the many unforgotten times while hiking in the Scottish Highlands or elsewise. Thanks also to Dan 'Tremé' McAteer for many interesting conversations regarding various aspects of chemistry and life.

A very special thank you goes to Kay for her understanding, support and patience (especially during the months when this thesis was written), and for her endurance as a 'PhD widow'.

Above all, I am deeply grateful to my parents who have made available their support in many ways. This thesis would not have been possible without their tireless encouragement.

Contents

List of Figures

List of Schemes

List of Tables

Preface

In this thesis we discuss computational investigations of a variety of chemical systems that contain open-shell transition metals and that are characterised by bonding-situations which do not fall into traditional classifications. The projects span a broad spectrum of inorganic chemistry, from bioinorganic and metal cluster chemistry to the study of redox non-innocent ligands. More specifically, we have used quantum chemical methods in order to explore the potential energy surfaces of these intriguing molecular systems, with the aim of gaining detailed insight into the electronic structure of the particular compound, and relating this information to its observed properties. The defining feature of this work has been the close interaction with experimentalists, both in Oxford and elsewhere.

Over the last decade the rapid advances in hardware architecture and algorithm design have been paralleled by an impressive progress in quantum chemical software. Calculations can be performed with high efficiency, and this has allowed for the modelling of chemical systems that were considered computationally intractable until some years ago, owing to their size and complexity. Density functional theory has emerged as one of the most popular methods, and proves to be a good compromise between high accuracy and low computational cost. Modern implementations of density functional theory form the basis for all studies presented herein.

A general overview of quantum chemical methods will be given in Chapter 1,

setting off with the fundamental concepts and approximations and then introducing the basic *ab initio* approaches to treat electron correlation. Density functional theory and the Kohn-Sham formalism are then discussed and a brief overview of different functionals is given. We close this chapter with a concise summary of the broken-symmetry method, which has been extensively used throughout this thesis. After this overview of theoretical methods the specific topics covered in this thesis are dealt with in subsequent chapters, organised as follows:

In Chapter 2 and 3 we present computational studies on the electronic structure of transition metal complexes containing redox non-innocent ligands. These are defined as ligands which participate in intra- or intermolecular electron transfer processes, and have attracted considerable attention in recent years. Attributing definitive oxidation states to metal centres and ligands in these systems is challenging, and generally requires extensive magnetic and spectroscopic data. We have considered two distinct but closely related ligand types, bipyridine (Chapter 2) and arylazopyridine (Chapter 3), which form complexes with various transition metals (Cr, Mo, Mn, Fe, Co, Ni, Zn). Although both ligands can act as 'electron reservoirs' to some extent, the electronic structure maps a continuum between true radical character and strong metal-to-ligand backdonation, depending on the precise combination of metal and ligand and the coordination environment.

The chemistry of endohedral Zintl clusters has been studied in Chapter 4. In particular, we have studied two open-shell Zintl anions, $[Mn@Pb_{12}]^{3-}$ and $[Fe@Ge_{10}]^{3-}$, both of which reveal unprecedented distortions from perfect deltahedral symmetry. The Mn cluster has a D_{2h}-symmetric structure, while the Fe cluster adopts an Archimedean pentagonal prismatic topology. Our detailed analysis of their electronic structures suggests that the remarkable pentagonal prismatic structure of the latter is the consequence of a drift of electron density from the metal

centre into the formally vacant orbitals of the cluster cage. The precise nature of the distortion is driven not by the amount of electron density transferred to the cluster (as is the case in the Wade-Mingos rules) but rather by the number of occupied orthogonal d orbitals over which electron density is shared. In $[Mn@Pb_{12}]^{3-}$ the presence of three spin-β 3d electrons (formally d^8 Mn^{-I}) drives the prolate D_{2h}-symmetric distortion that stabilises precisely three orbitals on the cluster.

Intermetallic interactions such as those discussed in the context of Zintl ions also play an important role in metallic clusters such as $Mn_2(thf)_4(Fe(CO)_4)_2$, which is discussed in Chapter 5. This is a classic case of a 'xenophilic' cluster, containing both paramagnetic (Werner-type) and closed-shell organometallic compounds. The nature of the bonding in these species remains controversial, and has, in our opinion, been misrepresented in the literature. Some discuss the electronic structure of these compounds from a molecular orbital perspective, and argue in favour of strong overlap of the metal-based orbitals, while others argue that metal-metal bonding is entirely electrostatic, with only very minor contribution from direct overlap of the d orbitals on adjacent metals. This controversy tempted us to re-investigate the bonding situation in the exemplary cluster mentioned above. The DFT calculations show that this cluster is best described as an exchange-coupled Mn_2^{II} dimer, the closed-shell $[Fe(CO)_4]^{2-}$ fragments acting as bridging ligands. The high-spin configuration of the Mn^{II} ions leads to single occupation of the Mn-Fe π^* orbitals and therefore substantially weaker metal-metal bonding than in conventional low-valent organometallic clusters. The results obtained for the dimer case can to a first approximation be extrapolated to a larger but related system, the disc-like species $[Mn_7(thf)_6(CO)_{12}]^-$.

Chapter 6 addresses a problem related to the mechanism for the reduction of nitrite, NO_2^-, in a system that models the key features of the enzyme Copper Nitrite Reductase (CuNiR). The ligand system of the complex is based on *cis*,*cis*-triaminocyclohexane (tach) and provides the κ^3N-motif, widely found in active sites of metalloproteins. Biomimetic copper complexes of this ligand catalyse the reduction of nitrite at high reaction rates. The ability of the substrate to undergo facile linkage isomerism has been a matter of debate with relevance to the mechanism of the enzyme. We have performed a detailed survey of the reaction coordinate for this reaction, and established viable pathways for the overall cycle. Importantly, we have found strong evidence that the coordinated nitrite undergoes linkage isomerisation during which the initially O-bound nitrite changes to the N-nitrito isomer. The latter then forms a NO complex upon protonation and releases a molecule of water. However, a second ('shunt') pathway where protonation of O-bound nitrous acid releases NO directly has also evolved as an option. We are not able to differentiate between these two based on energetics and suggest that both would be operative during catalysis.

Each chapter of this thesis is self-contained. A detailed introduction to the particular topic is given at the beginning, embedding the problem under study into a wider context and providing general background information as well as problem-specific details. Chapters 2 and 3 both address issues of 'redox non-innocent ligands' and a comprehensive introduction to the topic is given at the beginning of Chapter 2. A methodology section follows the introduction part, giving details on the chosen level of theory for the particular system. A complete account of the research carried out together with the results is given in subsequent sections and subsections.

1

Theory

Computational chemistry is a discipline that uses quantum mechanics to solve chemical problems, thereby making use of a range of methods for the mathematical description of chemical systems. Methodologies exist in a large variety, and encompass empirical, semi-empirical and *ab initio* approaches. Methods that bypass solving the Schrödinger equation are collectively known as empirical methods, resting on the laws of classical physics. These methods, which include molecular mechanics and classical molecular dynamics, require experimental data for parametrisation, but are less useful for modelling chemical reactivity.

Semi-empirical methods also take advantage from using adjustable parameters obtained from experimental data, but nevertheless acknowledge the quantum aspects of the electronic structure by using a simplified Hamiltonian. On the other hand, *ab initio* methods are based solely on quantum mechanics, and rely exclusively on the fundamental constants contained in its equations. They intend to solve the electronic structure problem from first principles without recourse to experimental data, and therefore represent the purest theoretical approach. Methods that fall into this class include molecular orbital theory and Hartree-Fock theory. Density functional theory is often considered as an *ab initio* method, even though many of the most common functionals use parameters derived from empirical data.

In this chapter I give a general overview of quantum chemical methods, as presented

in standard text books of quantum chemistry.[1–8] I will begin with an introduction to the basic concepts and approximations of quantum mechanics. The next section will then review *ab initio* methods, primarily Hartree-Fock theory and electron correlation methods based thereon. In the main section the method central to the computational work in this thesis will be presented: density functional theory. The first chapter will then be closed with a description of some important concepts of basis sets as well as the broken-symmetry approach.

1.1 Elementary concepts of quantum mechanics

The primary objective of quantum chemistry is to gain detailed insight into the electronic structure of atoms and molecules, and relate this information to their observed physical and chemical properties. For this purpose approximate solutions to the time-independent and non-relativistic Schrödinger equation are sought,[9–12] which is commonly expressed in the form

$$\hat{\mathcal{H}}\Psi = E\Psi \tag{1.1}$$

The Hamiltonian $\hat{\mathcal{H}}$ is the operator related to the total energy of the system and Ψ represents the wave function. The wave function, synonymous with quantum state, is, in principle, the most complete description that can be given to a physical system. Within the Born interpretation the square modulus of the wave function $|\Psi|^2$ is understood as a probability density, and the probability of finding a particle in a volume element $d\tau$ is proportional to the product $|\Psi|^2 d\tau$. The form of the Schrödinger equation is characteristic of an eigenvalue equation, with Ψ being an eigenfunction of $\hat{\mathcal{H}}$ and the corresponding eigenvalue E. The eigenfunction corresponding to the lowest energy yields the ground state of the system and all possible

information about its properties can be derived from it. For a system of electrons and nuclei described by position vectors $\mathbf{r}_i$ and $\mathbf{R}_A$ the Hamiltonian operator can be written as the sum of kinetic and potential energy operators for each particle. In atomic units,* the Hamiltonian for N electrons and M nuclei in its mathematical notation is written as

$$\hat{\mathcal{H}} = -\sum_{i=1}^{N} \frac{1}{2}\nabla_i^2 - \sum_{A=1}^{M} \frac{1}{2M_A}\nabla_A^2 - \sum_{i=1}^{N}\sum_{A=1}^{M} \frac{Z_A}{r_{iA}} + \sum_{i=1}^{N}\sum_{j>i}^{N} \frac{1}{r_{ij}} + \sum_{A=1}^{M}\sum_{B>A}^{M} \frac{Z_A Z_B}{R_{AB}} \quad (1.2)$$

where $r_{iA} = |\mathbf{r}_i - \mathbf{R}_A|$ is the distance between the ith electron and the Ath nucleus, $r_{ij} = |\mathbf{r}_i - \mathbf{r}_j|$ the distance between the ith and the jth electron, and the distance between the Ath and Bth nucleus is $R_{AB} = |\mathbf{R}_A - \mathbf{R}_B|$. M_A and Z_A are the mass and atomic number of nucleus A, respectively. The following terms can be identified in the above expression: the operators for the kinetic energy of the electrons and the kinetic energy of the nuclei, the operators for the attractive Coulomb interaction between the nuclei and electrons, and the repulsive interactions for the electrons as well as the nuclei. Thus, the Hamiltonian operator can be cast into a more compact form

$$\hat{\mathcal{H}} = \hat{T}_\mathrm{e} + \hat{T}_\mathrm{n} + \hat{V}_\mathrm{ne} + \hat{V}_\mathrm{ee} + \hat{V}_\mathrm{nn} \quad (1.3)$$

The connection between theory and experimental observation is made by a fundamental postulate in quantum mechanics, which states that the mean value of an observable in a series of measurements is equal to the expectation value of the corresponding operator. As an example, the total energy of a wave function can be calculated as an expectation value of the Hamiltonian, given by

$$E = \langle\hat{\mathcal{H}}\rangle = \frac{\int \Psi^* \hat{\mathcal{H}} \Psi d\tau}{\int \Psi^* \Psi d\tau} = \frac{\langle\Psi|\hat{\mathcal{H}}|\Psi\rangle}{\langle\Psi|\Psi\rangle} \quad (1.4)$$

*$\hbar = m_\mathrm{e} = e = 4\pi\epsilon_0 = 1$. See also the section 'Units' in the Appendix.

where the Dirac notation has been introduced for the last term. Exact analytical solutions to the Schrödinger equation only exist for facile systems (e.g. the hydrogen atom). This is due to the existence of the pairwise interactions between the particles in the Hamiltonian, resulting in the inseparability of the variables of motion. In other words, the motion of each particle is dependent on that of all the others. For many-particle systems one must resort to approximate solutions. In this context it is useful to state another fundamental theorem of quantum mechanics, the so called variation principle. According to this theorem, the expectation value for the energy that is calculated with a trial wave function Ψ' cannot be lower than the true energy of the system

$$E' = \frac{\langle \Psi' | \hat{\mathcal{H}} | \Psi' \rangle}{\langle \Psi' | \Psi' \rangle} \geq E_0 = \frac{\langle \Psi_0 | \hat{\mathcal{H}} | \Psi_0 \rangle}{\langle \Psi_0 | \Psi_0 \rangle} \tag{1.5}$$

The equality holds only when Ψ' is identical to Ψ_0. The variation principle provides a criterion for the optimisation of trial wave functions: since the expectation value of the Hamiltonian is always an upper bound to the exact ground state energy, if an approximate wave function is used, the procedure to obtain an improved wave function is to vary the parameters in terms of which Ψ' is expressed until the expectation value for the energy reaches its minimal value. Usually the complete Hamiltonian operator is not employed in practice, and the Born-Oppenheimer (BO) approximation is introduced in order to simplify the full Hamiltonian. The fundamental idea of this approximation rests on the fact that, due to their higher mass,[†] the nuclei in a molecule move much more slowly than the electrons. Hence, the electrons are considered to be moving in the constant field of the nuclei, thereby rapidly adjusting their distribution to the changing nuclear geometry. As a result, the motion of the nuclei and electrons can be considered separately. Since the

[†] $m_\mathrm{p} = 1.67262 \cdot 10^{-27}\,\mathrm{kg}, m_\mathrm{n} = 1.67493 \cdot 10^{-27}\,\mathrm{kg}, m_\mathrm{e} = 9.10938 \cdot 10^{-31}\,\mathrm{kg}$.

nuclei are held fixed, $\hat{T}_{\mathrm{n}}$ is zero and $\hat{V}_{\mathrm{nn}}$ becomes a constant. The remaining terms are collected into the electronic Hamiltonian,

$$\hat{H}_{\mathrm{e}} = \hat{T}_{\mathrm{e}} + \hat{V}_{\mathrm{ne}} + \hat{V}_{\mathrm{ee}} = -\sum_{i=1}^{N} \frac{1}{2}\nabla_i^2 - \sum_{i=1}^{N}\sum_{A=1}^{M} \frac{Z_A}{r_{iA}} + \sum_{i=1}^{N}\sum_{j>i}^{N} \frac{1}{r_{ij}} \tag{1.6}$$

The electronic Hamiltonian $\hat{H}_{\mathrm{e}}$ then contains only those kinetic and potential energy terms that act upon the electrons. Within this framework, we have to solve the electronic Schrödinger equation, which describes the motion of N electrons in the potential field of M stationary point charges

$$\hat{H}_{\mathrm{e}}\Psi_{\mathrm{e}}(\mathbf{r};\mathbf{R}) = E_{\mathrm{e}}\Psi_{\mathrm{e}}(\mathbf{r};\mathbf{R}) \tag{1.7}$$

Here, Ψ_{e} is the electronic wave function, which describes the motion of the electrons and explicitly depends on the electronic coordinates $\mathbf{r}$, but has a parametric dependence on the nuclear coordinates $\mathbf{R}$. That is, for different arrangements of the nuclei, Ψ_{e} is a different function of the electronic coordinates. In electronic structure calculations the nuclear repulsion energy connected to V_{nn} is calculated at the final stage and added to $E_{\mathrm{e}}(\mathbf{R})$ to yield the total energy $E_{\mathrm{tot}}(\mathbf{R})$ of the system. The energy $E_{\mathrm{tot}}(\mathbf{R})$ provides the potential for nuclear motion, or in other words, the nuclei move on a potential energy surface obtained by solving the electronic problem. This is an important point and it reveals an important conceptual implication of the BO approximation. For a diatomic molecule $E_{\mathrm{tot}}(\mathbf{R})$ will have the form of a potential curve, while for a polyatomic system $E_{\mathrm{tot}}(\mathbf{R})$ will in general be a potential energy (hyper)surface (PES) of dimensionality $3M$, where M is the number of nuclei. Many problems in computational chemistry involve the exploration of potential energy surfaces and localisation of stationary points: minima on the PES correspond to equilibrium structures, which are the possible geometries a

molecule would have if the nuclei were in fact stationary; first order saddle points correspond to transition states for chemical reactions; moreover, the overall topology of the PES is frequently interpreted in terms of reaction paths and reaction energy profiles. Before we proceed to the next section, in which we discuss methods for solving the electronic Schrödinger equation, we have to establish a reasonable formulation of the wave function. The antisymmetry principle states that a wave function describing a system of fermions must be antisymmetric with respect to the interchange of the coordinates of any two fermions, requiring the wave function to change sign

$$\Psi(\mathbf{x}_1, \ldots, \mathbf{x}_i, \mathbf{x}_j, \ldots, \mathbf{x}_N) = -\Psi(\mathbf{x}_1, \ldots, \mathbf{x}_j, \mathbf{x}_i, \ldots, \mathbf{x}_N) \tag{1.8}$$

By using Slater determinants in the construction of wave functions the antisymmetry requirement is enforced.

$$\Psi_{\mathrm{SD}} = \frac{1}{\sqrt{N!}} \begin{vmatrix} \psi_1(1) & \psi_2(1) & \ldots & \psi_N(1) \\ \psi_1(2) & \psi_2(2) & \ldots & \psi_N(2) \\ \vdots & \vdots & \ddots & \vdots \\ \psi_1(N) & \psi_2(N) & \ldots & \psi_N(N) \end{vmatrix} \tag{1.9}$$

In this notation the columns in a Slater determinant are labeled by single electron wave functions (spin orbitals), while the rows are labeled by the electron indices. The spin orbitals ψ_i represent products of a spatial and spin function, $\psi_i = \phi(\mathbf{r})\alpha(\omega)$ or $\phi(\mathbf{r})\beta(\omega)$. Each of these is called a molecular orbital (MO) when molecules are considered in the calculation.

1.2 Hartree-Fock method

Recall that the fundamental problem behind solving the Schrödinger equation is the presence of pairwise Coulomb interactions. Within the BO approximation these reduce to the electron-electron potential energy, depending on the interelectron separations r_{ij}. The underlying idea of the Hartree-Fock (HF) method is to treat theses electron-electron repulsions in an average way. Each electron is considered to be moving independently in a potential which is the spherical average of the potential due to all remaining electrons. In the HF method a Slater determinant is selected in order to span the wave function, and the variation principle is subsequently applied to search for the best set of spin orbitals ψ_i that minimises the electronic energy. The minimisation procedure reduces the N-particle problem to a set of one-particle eigenvalue problems, known as the Hartree-Fock equations

$$\hat{f}_i \psi_i = \varepsilon_i \psi_i \tag{1.10}$$

An orbital ψ_i is an eigenfunction of the effective one-particle Hamiltonian $\hat{f}_i$, known as Fock operator, with corresponding energy ε_i. The Fock operator for each electron is the sum of the core Hamiltonian operator $\hat{h}_i$ and an effective one-electron potential operator termed the Hartree-Fock potential

$$\begin{aligned} \hat{f}_i &= \hat{h}_i + \hat{V}_i^{\mathrm{HF}} = -\frac{1}{2}\nabla_i^2 - \sum_{A=1}^{M} \frac{Z_A}{r_{iA}} + \sum_j \big(\hat{J}_j(1) - \hat{K}_j(1)\big) \\ \hat{h}_i &= -\frac{1}{2}\nabla_i^2 - \sum_{A=1}^{M} \frac{Z_A}{r_{iA}} \qquad\qquad \hat{V}_i^{\mathrm{HF}} = \sum_j \big(J_j(1) - K_j(1)\big) \end{aligned} \tag{1.11}$$

where the Coulomb operator, $\hat{J}_j$, and exchange operator, $\hat{K}_j$, are defined as

$$\begin{aligned}\hat{J}_j(1)|\psi_i(1)\rangle &= \left\langle \psi_j(2)\middle|\frac{1}{r_{12}}\middle|\psi_j(2)\right\rangle|\psi_i(1)\rangle \\ \hat{K}_j(1)|\psi_i(1)\rangle &= \left\langle \psi_j(2)\middle|\frac{1}{r_{12}}\middle|\psi_i(2)\right\rangle|\psi_j(1)\rangle\end{aligned} \tag{1.12}$$

The Coulomb operator accounts for the Coulomb repulsion between electrons, while the exchange operator represents a modification of this energy that can be ascribed to the effects of spin correlation. Each orbital ψ_i is obtained as a solution to the eigenvalue equation with the corresponding operator $\hat{f}_i$. Since $\hat{f}_i$ depends on the orbitals of all other electrons, an iterative approach is required in order to solve the HF equations. This procedure is known as the self-consistent field (SCF) method and works in the following way: by initially guessing a set of orbitals, the average potential can be calculated; using this value for the field a new set of orbitals is obtained by solving the HF equations and the cycle is repeated until self-consistency is reached. In practice, the differential equations are converted to a set of matrix equations by introducing a finite set of K known basis functions $\{\phi_\mu(\mathbf{r})\}$, forming the basis set. Each molecular orbital is expanded in terms of these basis functions, which are commonly referred to as atomic orbitals

$$\psi_i = \sum_{\mu=1}^{K} c_{\mu i}\phi_\mu(\mathbf{r}) \tag{1.13}$$

Therefore this method is known as LCAO-MO (linear combination of atomic orbitals to give molecular orbitals). Adopting the above substitution for ψ_i, the Hartree-Fock equations can be rewritten as

$$\hat{f}_i \sum_{\mu=1}^{K} c_{\mu i}\phi_\mu(\mathbf{r}) = \varepsilon_i \sum_{\mu=1}^{K} c_{\mu i}\phi_\mu(\mathbf{r}) \tag{1.14}$$

Collecting all the K equations into a single matrix equation for the expansion coefficients yields the Roothaan-Hall equations

$$\mathbf{FC} = \mathbf{SC}\boldsymbol{\varepsilon} \tag{1.15}$$

where the Fock matrix $\mathbf{F}$ has the elements $F_{\mu\nu} = \langle\phi_\mu|\hat{f}|\phi_\nu\rangle$, $\mathbf{S}$ contains the overlap elements between basis functions, $S_{\mu\nu} = \langle\phi_\mu|\phi_\nu\rangle$, $\mathbf{C}$ is a $K \times K$ matrix composed of the expansion coefficients $c_{\mu i}$, and $\boldsymbol{\varepsilon}$ is a $K \times K$ diagonal matrix of orbital energies ε_i. Thus, the essence of the Roothaan ansatz is that, by introducing a set of distinct basis functions, the coupled Hartree-Fock integro-differential equations are converted into a matrix eigenvalue problem, which is then solved by standard matrix techniques. Using a set of K basis functions to solve the Roothaan-Hall equations for a system of N electrons, generates $2K$ spin orbitals in total, N of which will be occupied (hole spin orbitals) and $2K-N$ unoccupied (virtual spin orbitals). The Slater determinant formed from the occupied spin orbitals corresponds to the Hartree-Fock wave function and is the best variational approximation to the ground state of the system. However, limitations to the accuracy are introduced by both the single determinantal nature of the Slater determinant and through the use of finite basis sets. The larger and more complete the basis set is, the greater will be the flexibility in the expansion of the orbitals and the lower the expectation value for the energy. If the expansion of the spin orbitals was complete, i.e. using an infinite basis set, the obtained energies would reach the so called Hartree-Fock limit.

1.3 Post Hartree-Fock methods

In the preceding section it has been shown that HF theory is based on averaged electron-electron repulsions, neglecting instantaneous interactions between the electrons. As a result they are allowed to move closer to each other than if the individual electron-electron interactions were taken into account explicitly, leading to computed energies that lie above the exact values. This primary deficiency of the HF methodology is often stated as the neglect of electron correlation effects. The correlation energy is defined as the difference between the exact nonrelativistic energy of the system and the HF energy at the basis set limit

$$E_{\text{corr}} = E_{\text{exact}} - E_{\text{HF}} < 0 \tag{1.16}$$

Although HF wave functions account for ∼99% of the total energy, given a sufficiently large basis set, the remaining ∼1% due to electron correlation cannot be ignored in the description of chemical phenomena. Frequently a distinction is made between dynamic and static correlation. The former is somewhat intuitively associated with the instant correlation between electrons, such as those occupying the same orbital trying to avoid each other (e.g. in the He atom). The static (non-dynamical) contribution is attributed to situations where electrons avoid each other more permanently, for example those residing in different orbitals. Static correlation becomes important for systems where a single determinant is insufficient to represent nearly degenerate configurations (e.g. H_2 at the dissociation limit).
Improving the accuracy of calculated energies and molecular geometries is highly desired and ways are sought to include correlation effects. An adequate treatment of correlation is even more critical in cases such as transition metal systems, where

the neglect of correlation effects often leads to intolerable errors. In order to reach this aim one has to go beyond HF theory. The majority of electron correlation (post-HF) methods use the HF wave function as a starting point and then try to make improvements by increasing its flexibility. This is achieved by promoting electrons from the occupied into the virtual orbitals of the HF reference determinant, generating new Slater determinants. These are classified as singly, doubly, triply, quadruply, etc., excited (S, D, T, Q,...), according to the number of electrons that have been promoted into virtual orbitals of the HF reference (Scheme 1.1).

Scheme 1.1: Reference state and various possible excited determinants.

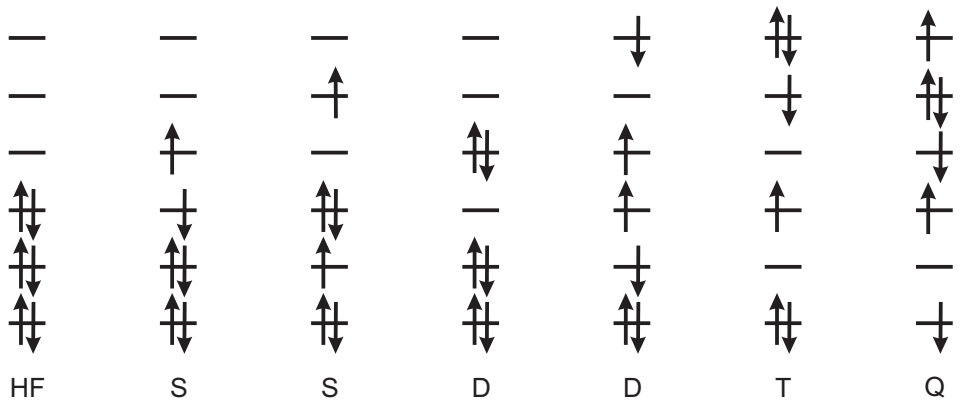

In Configuration Interaction (CI) methods linear combinations of these Slater determinants are taken to construct a wave function

$$\Psi_{\mathrm{CI}} = c_0\Psi_{\mathrm{HF}} + \sum_{\mathrm{S}} c_{\mathrm{S}}\Psi_{\mathrm{S}} + \sum_{\mathrm{D}} c_{\mathrm{D}}\Psi_{\mathrm{D}} + \sum_{\mathrm{T}} c_{\mathrm{T}}\Psi_{\mathrm{T}} + \sum_{\mathrm{Q}} c_{\mathrm{Q}}\Psi_{\mathrm{Q}} + \ldots \qquad (1.17)$$

The expansion coefficients c_i are then determined by using the linear variational method, yielding the final CI wave function. As the basis set approaches completeness, a full configuration interaction calculation (FCI), i.e. one that comprises all possible excitations, would yield the exact ground state energy. In practice, within the finite basis set limit, FCI yields the lowest energy value possible and the

difference between the HF and FCI energies corresponds to the correlation energy within the given basis set. Unfortunately, FCI calculations are unattainable for all but the smallest systems, and the number of excited determinants in the CI expansion has to be truncated in order to arrive at computationally feasible models. Usually one includes determinants up to double and triple excitations, giving rise to the CISD and CISDT method (configuration interaction including singles and doubles or singles, doubles and triplets, respectively). For medium-sized molecules, CISD typically recovers ∼90% of the correlation energy. The computational cost is further reduced by utilising the frozen core approximation, in which excitations from inner shell (core) orbitals are omitted. An unwelcome effect of restricting the excitations is that the truncated CI methods, in contrast to FCI, are neither size-consistent nor size-extensive. However, both of the above methods are variational in character.

The main principle of the multiconfigurational SCF (MCSCF) method is very similar to that of the CI method, although the configurations in the multideterminantal wave function are limited to a smaller number. However, while in CI the orbitals entering the excited determinants are left unaltered, both the expansion coefficients and the orbitals contained in the excited determinants are optimised iteratively within MCSCF. The most frequently used kind of MCSCF method is the complete active space self-consistent field (CASSCF) method, in which the configurations to be included into the wave function expansion are selected by partitioning the orbitals into active and inactive spaces. The active space typically ranges over some of the highest occupied to some of the lowest unoccupied valence orbitals of the HF reference, whereas the inactive space includes all orbitals that are considered unimportant for the particular chemical problem, and are thus not included in the calculation. The CAS(n,m) notation has been introduced, where n is the number

of active electrons and m is the total number of orbitals assigned to the active space. Within the active space a full CI is performed, followed by the MCSCF optimisation. The choice of appropriate configurations is critical in CASSCF, with up to 16 orbitals being the current limit that can be handled. Because a full valence wave function becomes unmanageable for systems of real size, usually much less than the complete number of valence electrons and orbitals is incorporated into the active space. However, choosing the important contributions is not trivial and largely depends on the chemical problem at hand. This is a problem particularly in transition metal chemistry, where the situation is complicated due to the presence of a large number of critically important orbitals. Careful inspection of the intricate bonding situation between metal and ligands is required. Often a poorly selected active space leads to inaccurate results by introducing a bias towards a particular bonding description.

A different systematic procedure, which is not variational but size-consistent, for recovering the electron correlation energy is perturbation theory (PT). Perturbation theory rests on the basic idea that a small term (or perturbation) is added to the mathematical description of a solvable problem (exactly or approximately). In other words, it is assumed that the solution to the already known system is not far from the correct answer of the actual problem at hand. Within this framework, electron correlation is applied as a perturbation to the ground state wave function. In Møller-Plesset Perturbation Theory (MPPT) the wave function that is being used is the HF determinant. The unperturbed Hamiltonian operator is taken as a sum of Fock operators. Due to the definition of the unperturbed system, the perturbative treatment yields the following energies (using the notation MPn to indicate the total energy up to order n): MP0 (zeroth-order energy) is simply the sum of the HF one-electron MO energies and MP1 (first-order correction to energy)

gives the correct HF energy (MP1 = E_{HF}). The second order correction to the energy (MP2) only involves interactions of doubly excited configurations with the HF reference determinant, bringing in the first contribution to the correlation energy. The practical limit is normally reached with the introduction of fourth-order corrections (MP4). A downside of this method is the non-convergent behaviour of the MPn perturbation series which is often observed, and only few chemical systems show smooth monotonic convergence towards a limiting value. The method by far most often used is MP2, which typically accounts for ∼80-90% of the correlation energy and also has the advantage of being economical in terms of computational costs. Another factor which makes MP2 attractive is the availability of analytical gradients and second derivatives, which are routinely implemented in standard software packages. For transition metal systems MP2 has posed a feasible correlated *ab initio* method for a long time. However, due to the rapid advances in computer technology and improvements in algorithmic design, more sophisticated *ab initio* methods like Coupled Cluster (see below) and CASSCF have become accessible for systems of realistic size, and will likely become the norm in the near future.

Coupled Cluster (CC) theory offers yet another approach for the treatment of electron correlation effects. While perturbation methods add all types of corrections to the reference wave function to a given order, the idea of CC is to include all corrections of a given type to infinite order. An exponential operator is defined that operates on the HF determinant with the effect to express Ψ_{CC} as linear combination of Slater determinants that includes Ψ_{HF} and all possible excitations of electrons from occupied to virtual orbitals

$$\Psi_{\mathrm{CC}} = e^{\hat{T}}\Psi_{\mathrm{HF}} \qquad \hat{T} = \hat{T}_1 + \hat{T}_2 + \hat{T}_3 + \ldots + \hat{T}_n \tag{1.18}$$

In the above expression $\hat{T}$ is the cluster operator and the $\hat{T}_i$ are excitation operators,

which create all possible excitations up to ith order. The resulting wave function is equivalent to the exact FCI solution. In CC theory it is customary to truncate the expansion after the second or third term, in order to reduce the computational cost. With the single, double or up to triple excitations included in $e^{\hat{T}}$, one obtains the the CCSD and CCSDT methods, respectively. A widely used method is CCSD(T), coupled cluster with singles and doubles and perturbative approximation of triple excitations. Coupled cluster methods are currently among the most popular high-level *ab initio* methods, owing to both the fact that they recover a large percentage of the correlation energy and their size-consistent behaviour.

1.4 Density functional theory

1.4.1 Foundations

The development of density functional theory (DFT) has introduced a different methodical philosophy into the quest for a solution to the electronic structure problem. DFT begins with the concept of electron density instead of the conventional wave function. Taking advantage of the electron density as the central entity brings along some significant advantages. First, the electron density depends on many fewer variables than the wave function: a wave function for a N-electron system depends on a total of $4N$ coordinates (three spatial and one spin variable for each of the N electrons). The complexity of such an object increases rapidly with the number of electrons in the system. In contrast, electron density is an object in three-dimensional space, and is therefore only dependent on three spatial coordinates, irrespective of the number of electrons in the system. Secondly, electron correlation is intrinsically incorporated into the electron density, and thus accounted for. Central to DFT is the idea that the energy of an electronic system

can be expressed in terms of the electron density $\rho(\mathbf{r})$. The electronic energy is said to be a functional of the electron density and denoted $E[\rho]$, in the sense that for a given function $\rho(\mathbf{r})$ there is a single corresponding energy, or in other words, the density is directly mapped onto the energy. For a system of N electrons, $\rho(\mathbf{r})$ denotes the total electron density at a particular point $\mathbf{r}$ in space. The concept of using a density functional for the energy dates back to the early days of quantum mechanics, and prominent examples of such approaches include the Thomas-Fermi model[13,14] as well as the Xα or Hartree-Fock-Slater method, initially developed by Slater as an approximation to the Hartree-Fock scheme.[15] The foundation of modern density functional theory was laid in 1964, when Hohenberg and Kohn formally proved with their first theorem that the use of the electron density $\rho(\mathbf{r})$ as the basic variable is legitimate. It states, that '$v(\mathbf{r})$ is (to within a constant) a unique functional of $n(\mathbf{r})$; since, in turn, $v(\mathbf{r})$ fixes H we see that the full many-particle ground state is a unique functional of $n(\mathbf{r})$'.[16] It is worth commenting on the notation used within the original paper, and put it into context with contemporary notation to prevent confusion. The authors use the variable $n(\mathbf{r})$ for the electron density, instead of the now usual Greek $\rho(\mathbf{r})$. Further, within density functional theory $v(\mathbf{r})$ specifies the so called external potential, which is often also written as V_{ext}. Note that in the case of a molecular system V_{ext} is specified by the attraction due to the nuclei and is synonymous with the V_{ne} term appearing in the expression for the molecular Hamiltonian. Hence the ground state electron density uniquely determines the molecular electronic Hamiltonian, and so determines the ground-state wave function. Consequently, the energy and essentially all other observables of a stationary quantum state can be deduced, in principle exactly, from the ground state density alone

$$\rho_0 \Rightarrow \{N, Z_A, R_A\} \Rightarrow \hat{H} \Rightarrow \Psi_0 \Rightarrow E_0 \quad \text{and all other properties} \tag{1.19}$$

Since the energy is a functional of the function $\rho(\mathbf{r})$, it can be separated into three parts, each of which is a functional of $\rho(\mathbf{r})$ itself

$$\begin{aligned} E[\rho] &= T[\rho] + E_{\text{ee}}[\rho] + E_{\text{ne}}[\rho] = F_{\text{HK}}[\rho] + \int \rho(\mathbf{r}) V_{\text{ext}} d\mathbf{r} \\ \text{where} \quad F_{\text{HK}}[\rho] &= T[\rho] + E_{\text{ee}}[\rho] \end{aligned} \tag{1.20}$$

In this expression only the $E_{\text{ne}}[\rho]$ term, i.e. the potential energy due to nuclei-electron attraction,[‡] is dependent on the actual system, while the other two, the kinetic energy $T[\rho]$ and the electron-electron interaction $E_{\text{ee}}[\rho]$, are universally valid. This means that their form is independent of the particular system, and the system-independent parts have been collected into the universal functional $F_{\text{HK}}[\rho]$.[§] If this functional was known exactly, the problem of finding an exact solution to the Schrödinger equation would have been cracked. Unfortunately, the explicit form of the universal functional is completely unknown. At least, from the $E_{\text{ee}}[\rho]$ term one can recover the classical Coulomb part $J[\rho]$ (the only term that *is* known) and recast the universal functional into

$$\begin{aligned} F_{\text{HK}}[\rho] &= T[\rho] + J[\rho] + E_{\text{ncl}}[\rho] \\ J[\rho] &= \frac{1}{2} \iint \frac{\rho(\mathbf{r})\rho(\mathbf{r}')}{|\mathbf{r} - \mathbf{r}'|} d\mathbf{r} d\mathbf{r}' \end{aligned} \tag{1.21}$$

All effects of the self-interaction correction as well as exchange and Coulomb correlation are absorbed into $E_{\text{ncl}}[\rho]$, which represents the non-classical contribution to the electron-electron interaction. Having established that all properties of interest can be derived from the ground state density, the question is how to verify that

[‡]Remember that $V_{\text{ext}} = V_{\text{ne}}$ in the limit of a system of fully interacting electrons.

[§]$F_{\text{HK}}[\rho]$ is defined independently of the external potential; this makes it an universal functional.

a certain density corresponds to the ground state density. The answer lies in the second theorem by Hohenberg and Kohn,[16] providing the energy variational principle. It asserts that no eligible trial electron density, $\tilde{\rho}$, can give a lower ground state energy than the true ground state electron density. In other words, when $E[\rho]$ is evaluated (by using the exact $F[\rho]$), the $E_0[\rho_0] \leq E[\tilde{\rho}]$ inequality holds. Importantly, the applicability of the variational principle is limited to the ground state energy only.

1.4.2 Kohn-Sham approach

The next major step in the development of DFT came when Kohn and Sham derived a set of equations, from which the electron density could be obtained.[17] Alternative implementations of DFT have been explored, that directly depend on the electron density, as opposed to the orbital-based variant proposed by Kohn and Sham. Yet at present these methods lack the accuracy that is desired, making modern DFT tantamount to the Kohn-Sham (KS) DFT method.

To begin with, Kohn and Sham invoked the idea of setting up a fictitious reference system of non-interacting electrons. Clearly the Hamiltonian of this reference system does not contain any electron-electron interaction

$$\hat{H}_{\mathrm{S}} = \sum_{i=1}^{N} \Big[-\frac{1}{2}\nabla_i^2 + \hat{V}_{\mathrm{S}}(\mathbf{r}) \Big] = \sum_{i=1}^{N} \hat{h}_i^{\mathrm{KS}} \quad \text{where} \quad \hat{h}_i^{\mathrm{KS}} = -\frac{1}{2}\nabla_i^2 + \hat{V}_{\mathrm{S}}(\mathbf{r}) \tag{1.22}$$

where $\hat{h}_i^{\mathrm{KS}}$ is the one-electron Kohn-Sham operator and $\hat{V}_{\mathrm{S}}(\mathbf{r})$ describes the effective potential of the non-interacting reference system. After reintroducing one-electron functions in the form of Kohn-Sham orbitals φ_i, the ground state wave function of the non-interacting reference system can be constructed as a Slater determinant[¶]

[¶]This is where the subscript S occurring in the equations of the reference system comes from.

of these Kohn-Sham orbitals. Each φ_i is an eigenfunction of $\hat{h}_i^{\mathrm{KS}}$

$$\Big[-\frac{1}{2}\nabla_i^2 + \hat{V}_{\mathrm{S}}(\mathbf{r}) \Big] \varphi_i(\mathbf{r}) = \epsilon_i \varphi_i(\mathbf{r}) \tag{1.23}$$

Once the KS orbitals have been determined, the total density can be calculated from the usual sum over the square-moduli of the orbitals φ_i

$$\rho(\mathbf{r}) = \sum_{i=1}^{N} |\varphi_i(\mathbf{r})|^2 \tag{1.24}$$

The connection between the artificial reference system and the real system is made by adjusting $\hat{V}_{\mathrm{S}}(\mathbf{r}_i)$ such that the ground state electron density $\rho_{\mathrm{S}}(\mathbf{r})$ of the reference system equals the exact ground state density $\rho_0(\mathbf{r})$ of the real system. Although the kinetic energy of the non-interacting reference system is not known exactly as a functional of ρ, it can be expressed exactly in terms of the Kohn-Sham orbitals

$$T_{\mathrm{S}}[\rho] = -\frac{1}{2} \sum_{i=1}^{N} \left\langle \varphi_i \left| \nabla_i^2 \right| \varphi_i \right\rangle \tag{1.25}$$

It is self-evident that $T_{\mathrm{S}}[\rho]$ is not equal to the true kinetic energy of the interacting system, even though it has been ensured that both share the same density. However, the advantage of the non-interacting reference system becomes clear in the fact that by use of this concept the major part of the true kinetic energy can be recovered, while the remainder is dealt with in an approximate way. To produce the desired separation of $T_{\mathrm{S}}[\rho(\mathbf{r})]$ as the kinetic energy component, it is convenient to rewrite the original functional as

$$F[\rho(\mathbf{r})] = T_{\mathrm{S}}[\rho(\mathbf{r})] + J[\rho(\mathbf{r})] + E_{\mathrm{XC}}[\rho(\mathbf{r})] \tag{1.26}$$

where the residual part of the kinetic energy has been absorbed into an exchange-correlation functional E_{XC}. More explicitly, the exchange-correlation functional is given by the expression

$$E_{\mathrm{XC}}[\rho] = (T[\rho] - T_{\mathrm{S}}[\rho]) + (E_{\mathrm{ee}}[\rho] - J[\rho]) = T_{\mathrm{C}}[\rho] + E_{\mathrm{ncl}}[\rho] \tag{1.27}$$

where $T[\rho]$ and $T_{\mathrm{C}}[\rho]$ denote the true kinetic energy and the kinetic correlation energy, respectively. Thus, $E_{\mathrm{XC}}[\rho]$ incorporates all the contributions to the energy that cannot be accounted for exactly. It therefore includes not only the electron exchange and correlation energies, but also the correction for self-interaction that is incorporated into the Coulomb term, and the portion of the kinetic energy that corresponds to the difference between the non-interacting and the real system. It is now possible to repartition the total energy functional into the following parts

$$\begin{aligned} E[\rho] =& T_{\mathrm{S}}[\rho] + E_{\mathrm{ne}}[\rho] + J[\rho] + E_{\mathrm{XC}}[\rho] = \\ & T_{\mathrm{S}}[\rho] + \int [\hat{V}_{\mathrm{ext}}(\mathbf{r}) + \hat{J}(\mathbf{r})]\, \rho(\mathbf{r})\, d\mathbf{r} + E_{\mathrm{XC}}[\rho] \end{aligned} \tag{1.28}$$

with the usual meanings for the classical Coulomb interaction $\hat{J}(\mathbf{r})$ between the electrons and the potential $\hat{V}_{\mathrm{ext}}$ arising from the nuclei

$$\hat{J}(\mathbf{r}) = \int \frac{\rho(\mathbf{r}')}{|\mathbf{r}' - \mathbf{r}|} d\mathbf{r}' \qquad \hat{V}_{\mathrm{ext}} = \sum_A \frac{Z_A}{|\mathbf{R_A} - \mathbf{r}|} \tag{1.29}$$

The variational theorem ensures that the ground state energy can be found by varying ρ, so as to minimise the functional $E[\rho]$. Equivalently, instead of varying ρ, one can vary the KS orbitals φ_i, which determine ρ. The KS orbitals that minimise the expression for $E[\rho]$ for the molecular ground state energy satisfy the

following expression (known as canonical KS orbital equations)

$$\begin{aligned}[-\frac{1}{2}\nabla_i^2+\hat{V}_{\text{eff}}(\mathbf{r})]\varphi_i &= \epsilon_i\varphi_i \\ \hat{V}_{\text{S}}(\mathbf{r}) \equiv \hat{V}_{\text{eff}}(\mathbf{r}) &= \hat{V}_{\text{ext}}(\mathbf{r}) + \hat{J}(\mathbf{r}) + V_{\text{XC}}(\mathbf{r})\end{aligned} \tag{1.30}$$

The exchange-correlation potential is found as the functional derivative of the exchange correlation energy

$$V_{\text{XC}} = \frac{\delta E_{\text{XC}}}{\delta \rho} \tag{1.31}$$

In the same way as the HF-equations, the Kohn-Sham one-electron equations have to be solved in an iterative fashion. The exact form of $\hat{V}_{\text{eff}}(\mathbf{r})$ is dependent on the exchange-correlation functional E_{XC}. Importantly, if E_{XC} and V_{XC} were known, then the KS strategy would yield the exact energy, because no approximations have been introduced *a priori*, despite the reformulations of the Hohenberg-Kohn theorems. Unfortunately, an exact expression for E_{XC} is completely unknown, and the major challenge in modern density functional theory is the development of improved approximations to this exchange-correlation functional. The approximate nature of E_{XC} really is the only source of error in KS-DFT. For practical reasons, approximations to E_{XC} are given as sum of exchange and correlation functionals. It should be noted, however, that the separation E_{XC} into exchange (E_{X}) and correlation (E_{C}) is somewhat arbitrary and not well defined in principle. Only if the KS orbitals were identical to HF orbitals, would this interpretation be justified. Various schemes have been worked out to find approximate exchange-correlation functionals of high quality, and the most important approaches will be pointed out in the following section.

1.4.3 Functionals

Local density methods

The simplest approximation makes use only of the density ρ at a particular point to evaluate the exchange-correlation energy at this point, and is called the local density approximation (LDA). Extending the LDA to the unrestricted case, where α and β densities are not equal, one arrives at the local spin density approximation (LSDA). The derivation of the exchange-correlation functional is based on the homogeneous electron gas. The exchange-correlation energy can be very accurately expressed as the integral

$$E_{\mathrm{XC}}^{\mathrm{LDA}}[\rho] = \int \rho(\mathbf{r})\varepsilon_{\mathrm{XC}}(\rho(\mathbf{r}))d\mathbf{r} \tag{1.32}$$

where $\varepsilon_{\mathrm{XC}}(\rho(\mathbf{r}))$, the exchange-correlation energy per particle, is further decomposed into separate exchange and correlation contributions

$$\varepsilon_{\mathrm{XC}}(\rho(\mathbf{r}))d\mathbf{r} = \varepsilon_{\mathrm{X}}(\rho(\mathbf{r})) + \varepsilon_{\mathrm{C}}(\rho(\mathbf{r})) \tag{1.33}$$

The exchange term has an analytical solution in the form of the Slater-Dirac exchange energy functional

$$\varepsilon_{\mathrm{X}}(\rho(\mathbf{r})) = \frac{3}{4}\left(\frac{3}{\pi}\right)^{1/3}(\rho(\mathbf{r}))^{1/3} \tag{1.34}$$

Since no explicit expression for the correlation part is known, the correlation energy has been determined to a high precision by quantum Monte Carlo methods.[18] Analytic interpolations of these results have been developed by Vosko, Wilk and Nusair (VWN),[19] and more recently by Perdew and Wang (PW),[20] both of which

are widely used. Similar expressions for the exchange and correlation energy exist for the spin polarised case. The combination of the Slater local exchange functional and the VWN local correlation functional is commonly referred to as SVWN. Although being based on a rather crude model, the L(S)DA in general delivers good results for equilibrium geometries, vibrational frequencies and dipole moments, with an accuracy comparable to HF methods. However, in molecular systems the exchange energy is commonly largely underestimated, while the electron correlation is often overestimated by a factor of 2, leading to large errors in energies. As a result, this method is notoriously overbinding, i.e. bonds are described as too strong. Nonetheless, L(S)DA is regularly applied to extended systems such as solids, where the approximation of a uniformly distributed electron density is much more justified.

Gradient corrected methods

In order to advance beyond the local density approximation, one has to account for the inhomogeneity of the electron density. For this reason, the information about the local density ρ has been supplemented by the information about the gradient of the density, $\nabla\rho$. Thus, in the so called generalised gradient approximation (GGA), the exchange and correlation energy depend on both of these quantities

$$E_{\mathrm{XC}}^{\mathrm{GGA}}[\rho_\sigma] = \int f(\rho_\sigma(\mathbf{r}), \nabla\rho_\sigma(\mathbf{r}))d\mathbf{r} \quad \text{with} \quad \sigma = \alpha, \beta \tag{1.35}$$

where the spin dependence is implied by the variable σ which runs over α and β spins. The function f depends on the densities and their gradients and is the entity to be determined. At this time, an extensive number of exchange and correlation functionals exist, which are usually named after the authors' initials and sometimes augmented by the publication year. A stringent nomenclature, however, has not

been introduced yet. One of the earliest and most popular GGA exchange functionals (known as B or B88) was proposed by Becke in 1988 as a correction to the LSDA exchange energy.[21] The explicit form of the B88 exchange functional is

$$E_{\mathrm{X}}^{\mathrm{B88}} = E_{\mathrm{X}}^{\mathrm{LSDA}} - \beta \sum_{\sigma=\alpha,\beta} \int \frac{\rho_\sigma^{4/3} x_\sigma^2}{(1 + 6\beta x_\sigma \sinh^{-1} x_\sigma)} d\mathbf{r} \quad \text{where} \quad x_\sigma = \frac{|\nabla \rho_\sigma|}{\rho_\sigma^{4/3}} \tag{1.36}$$

The variable x_σ is the reduced density gradient for spin σ, which is to be understood as a local inhomogeneity parameter. The single empirical parameter β has been optimised by fitting to the exchange energies of the six noble gases. This exchange functional shows the correct long-range asymptotic behaviour for the energy density. On the side of correlation functionals, the Perdew 1986 (P86) gradient correction to the LSDA experiences much popularity.[22] It employs one empirical parameter fitted to the correlation energy of the neon atom. A refinement of their correlation functional was later introduced by Perdew and Wang, leading to the parameter free PW91.[23–25] Probably the most extensively used GGA correlation functional is due to Lee, Yang and Parr (LYP).[26,27] The empirical parameters contained in it have been fitted to data for the helium atom and its overall good performance seems to originate from an efficient handling of the self-interaction error in many-electron systems. The Perdew-Burke-Ernzerhof (PBE) exchange and correlation functional also belongs to the class of parameter-free functionals.[28] In principle, any exchange functional from one source can be combined with any correlation functional from another, but certain pairs have become established as reliable and accurate for a range of systems. A complete specification of the exchange and correlation functional is achieved by concatenating their acronyms in that order. For example, BLYP and BP86 are among the widely used functionals. GGA methods outperform L(S)DA methods, yielding geometries and vibrational frequencies that are usually superior to MP2 results. Occasionally problems with

predicting accurate reaction barriers and relative energies for different electronic states are observed.

Kinetic-energy density methods

Further corrections based on higher derivatives have only recently gained attention and have been termed meta-GGAs. These depend on the kinetic-energy density and can also include the second derivative of ρ. The spin-dependent form can be formulated in a general way as

$$E_{\mathrm{XC}}^{\mathrm{MGGA}}[\rho_\sigma] = \int f(\rho_\sigma(\mathbf{r}), \nabla\rho_\sigma(\mathbf{r}), \nabla^2\rho_\sigma(\mathbf{r}), \tau_\sigma)d\mathbf{r} \tag{1.37}$$

where the kinetic energy density for the occupied Kohn-Sham orbitals, $\varphi_{i\sigma}^{\mathrm{KS}}$, is defined as

$$\tau_\sigma = \frac{1}{2}\sum_i \left|\nabla\varphi_{i\sigma}^{\mathrm{KS}}\right|^2 \tag{1.38}$$

The meta-GGA correlation functional (B95) designed by Becke has the advantage over previous functionals that the correlation vanishes for one-electron systems and thus is free of the self-interaction problem.[29] Perhaps the most frequently used out of this class is the non-empirical TPSS functional introduced by Tao, Perdew, Staroverov and Scuseria.[30] The somewhat improved performance of meta-GGAs over GGAs is outbalanced by a higher computational cost due to their additional complexity.

Hybrid methods

The HF exchange energy of a Slater determinant can be computed exactly, while DFT only provides an approximate solution to the exchange energy. At first sight, the appropriate strategy to follow for arriving at a more accurate exchange-

correlation energy seems to be to replace the approximate exchange functional with the exact HF term and merge the latter with an approximate correlation functional. Unfortunately, this approach provides no improvement over the GGA method for atoms. Worse still, it completely fails if applied to molecules. The reason is that the cancellation of errors resulting from the use of approximated expressions for both E_{X} and E_{C} breaks down when the exact HF exchange is applied. Nonetheless, admixing a certain percentage of exact exchange into density functionals, by expressing the exchange energy as combination of LSDA, HF and GGA terms, enhances the performance dramatically. The first successful hybrid functional is the three-parameter B3PW91 functional[31] proposed by Becke in 1993

$$E_{\mathrm{XC}}^{\mathrm{B3PW91}} = (1-a)E_{\mathrm{X}}^{\mathrm{LSDA}} + aE_{\mathrm{X}}^{\mathrm{HF}} + b\Delta E_{\mathrm{X}}^{\mathrm{B88}} + E_{\mathrm{C}}^{\mathrm{LSDA}} + c\Delta E_{\mathrm{C}}^{\mathrm{PW91}} \tag{1.39}$$

The three empirical parameters were chosen to optimally reproduce atomisation and ionisation energies as well as proton affinities included in the G2 database, and also some total energies. This led to the values 0.20, 0.72 and 0.81 for a, b and c, respectively. The amount of exact exchange (20%) is determined through the parameter a. A modification of this functional by Stephens et al., where the PW91 correlation part is replaced by the LYP functional, led to the famous B3LYP functional.[32] This functional perhaps is currently the most popular hybrid functional. The PBE functional has also been improved by the addition of exact exchange (25%) to give the PBE0 (or PBE1PBE1) functional.[33–35] Similarly, the TPSS functional has been augmented with ∼10% exact exchange to give the TPSSh method,[36] an example of a hybrid meta-GGA functional. A comprehensive suite of meta-hybrid functionals coming from the group of Truhlar, including M06, M06-HF, M06-2X, M05-2X, has been tested on various systems and the functionals show excellent accuracy.[37–42] The half-and-half functionals BHandH and BHandHLYP

incorporate 50% of exact exchange. Very recent developments in the field include a new class of functionals coined double hybrid density functionals, since they admix not only exact exchange but also some correlation calculated by the MP2 method. Within this group two examples are P2PLYP and mPW2PLYP.[43–46] Inclusion of HF exchange is often found to improve results, and hybrid DFT methods outperform GGA in most respects. For a long time now, they have been extensively and successfully applied to transition metal systems, especially of the first row, and are usually considered to perform better than many *ab initio* methods.[7,47] Importantly, the optimal amount of exact exchange to be included in a hybrid functional is normally system-dependent and careful adjustment of the optimum fraction to the specific property of interest is required.

1.5 Basis sets

In the context of wave function-based methods such as HF theory, orbitals are naturally used to construct the approximate wave function. On the other hand, within the Kohn-Sham formulation of DFT, orbitals play an indirect role and are introduced as a tool to construct the charge density. While basis set-free DFT implementations do exist, most quantum chemical program packages employ basis functions to expand the KS orbitals. This section will give a concise overview of the main concepts and issues regarding the construction and use of basis sets.

A set of functions that is used to describe the orbitals in an atom or molecule is designated by the term basis set. Thus, the wave function, unknown at the start of the calculation, is expanded in a finite set of known mathematical functions. Commonly, basis functions are centred on atoms, and are thus often referred to as Atomic Orbitals (AOs), although they are strictly speaking not solutions to the Schrödinger equation. There are two types of basis functions that are commonly

used in electronic structure calculations, Slater-type orbitals (STOs) and Gaussian-type Orbitals (GTOs). Explicitly, Slater-type orbitals are of the functional form

$$\chi_{\zeta,n,l,m}(r,\theta,\varphi) = NY_{l,m}(\theta,\phi)r^{n-1}e^{-\zeta r} \tag{1.40}$$

where N is a normalisation constant, and $Y_{l,m}$ are spherical harmonic functions, describing the shape of the orbital. The quantum numbers n, l and m have their usual meaning. The radial part is given by the exponential term and r^{n-1}, with ζ being the Slater orbital exponent. On the other hand, Gaussian-type orbitals can be written in the following form, where the cartesian notation has been used

$$\chi_{\zeta,l_x,l_y,l_z}(x,y,z) = Nx^{l_x}y^{l_y}z^{l_z}e^{-\alpha r^2} \tag{1.41}$$

where N again is a normalisation constant, α is the Gaussian orbital exponent and l_x, l_y and l_z are non-negative integers. The exponent α controls the contraction of the resulting function, where the function gets more diffuse the smaller its value. The orbital type is classified with help of the exponents l_i, somewhat resembling the quantum number of angular momentum l (for example $l_x + l_y + l_z = 1$ is a p-orbital). The dependence on r^2 in the exponential makes the GTOs inferior to the STOs in two respects. At the nucleus ($r = 0$) a GTO has a zero slope, in contrast to a STO, which reveals a 'cusp' (discontinuous derivative), and GTOs therefore are problematic in describing the proper behaviour near the nucleus. The second problem is that GTOs in the long range ($r \to \infty$) decay too rapidly compared to STOs, and the 'tail' of the wave function is consequently poorly represented. Despite these shortcomings, GTOs have the advantage that they can be handled very efficiently computationally. The product of two GTOs centred on different atoms is a third GTO located in between, an important feature for solving two-

electron integrals occurring within SCF calculations. This property is absent in STOs. In order to find a compromise between the accuracy of STOs and the numerical convenience of GTOs, several GTOs are routinely grouped together to form so called contracted Gaussian functions (CGF). Each contracted Gaussian is a linear combination of the original (or primitive) GTOs, centred on the same atomic nucleus, aiming to reproduce a STO as precisely as possible.

$$\chi^{\mathrm{CGF}} = \sum_i a_i \chi_i^{\mathrm{GTO}} \tag{1.42}$$

Each CGF is defined by the contraction coefficients of the component GTO and their individual exponents. The basis set is then formed from these contracted functions. Gaussian-type basis sets are default in most standard quantum chemical programs, although there are some exceptions, such as the Amsterdam Density Functional package, which implements basis sets of Slater-type. The basis set is classified by the number of functions it includes. Using only the smallest possible number of functions, i.e. one for each atomic orbital, results in a minimal basis set. For example, the first row would be described by two single s-functions (1s and 2s) and one set of p-functions ($2p_x$, $2p_y$ and $2p_z$). One example is the STO-nG basis set, designating the expansion of an STO in terms of n primitive GTOs (in particular, STO-3G has been a common choice, giving a set of contracted Gaussians including three GTOs). Minimal basis sets are often referred to as being of single-ζ (SZ) quality.[‖] However, a higher grade of sophistication is needed to achieve results beyond a purely qualitative level. For this reason current basis sets use two or more functions for each type of orbitals, giving rise to double-ζ (DZ), triple-ζ (TZ) etc. basis sets. Using the above example, a double-ζ basis set utilises four s-functions (1s, 1s′, 2s and 2s′) and two sets of p-functions (2p and 2p′) for first row elements.

[‖]The term zeta is a reference to the exponent of the STO basis function.

Chemical bonding is a physical phenomenon that is governed by the valence shell of atoms. Thus, it has been a plausible step in basis set design to allow higher flexibility in the valence region, while treating the core region in a more minimal way. This approach led to the development of so called split-valence (SV) basis sets, which can be viewed as a compromise between the inaccuracy of minimal basis sets and the computational demand of DZ and TZ basis sets. A prominent example is the series of SV basis sets developed by Pople and co-workers, which are expressed by the *n*-*ij*G or *n*-*ijk*G nomenclature. Here, n indicates the number of primitives used for representing the core region, while ij and ijk indicate both how many functions the valence orbitals are split into (two and three, corresponding to a DZ and TZ split valence), and how many primitives are used for their representation. Taking 6-31G as an example, the notation implies that a core orbital is described by a single CGF constructed from six primitive GTOs, while a valence orbital is described by two functions, one of which consists of three primitive and the other one is uncontracted. Contraction schemes are often used to summarise the contractions applied for the construction of a specific basis set. Commonly, a given basis set is extended by addition of polarisation functions, which are essential for a more realistic description of chemical bonds. These auxiliary functions are always of higher angular momentum l than the maximum value of the orbitals occupied in the atomic ground state configuration (for example, a set of d functions is added to a carbon atom). Polarisation functions allow the orbitals to distort from their original symmetry as a response to the influence of adjacent atoms. Basis sets of polarised double- and triple-ζ quality are routinely used in modern quantum chemistry, largely replacing the use of minimal basis sets. Some problems necessitate augmentation of the basis set with diffuse functions. These functions, having small exponents, are spatially more shallow than the standard functions,

and can be important when considering anions, large and 'soft' molecular systems and excited electronic states. For systems involving heavier elements at the lower end of the periodic table, such as transition metal complexes of the second and third row, the situation is complicated because of the large number of electrons in the core region. In order to arrive at a proper description of the valence orbitals, a large number of basis functions is needed to expand the corresponding orbitals of the core region, and in this way account for the effects of electron-electron repulsion on the valence electrons. Unfortunately, this often leads to intractable problems, simply because of the unmanageably large number of basis functions. Moreover, relativistic effects start to become important for atoms with large charges Z, further complicating matters. A solution to the above problems is at hand in form of effective core potentials (ECP), also called pseudopotentials. The trick is to neglect an explicit treatment of the inner-shell electrons but instead replace them by a parameterised analytical function that models the combined effect of the nuclear-electronic core on the valence region. Once derived from relativistic calculations, effective core potentials can be used to model relativistic effects. Usually effective core potentials are expanded as a finite sum of Gaussians multiplied by powers of the electron-core distance r

$$U(r) = \sum_k A_k r^{n_k} e^{-\zeta_k r^2} \tag{1.43}$$

where the contraction coefficients A_k and Gaussian exponents ζ_k have to be determined by a suitable fitting procedure, and n_k is the exponent to the r term.

An alternative to the basis sets discussed above are plane wave basis sets. These are primarily used when three-dimensional extended (infinite) systems with periodic boundary conditions are considered, being superior to GTO basis sets in such cases. The electrons are described by orbitals which are expanded in terms of complex

exponential functions which depend on a wave vector **k**. The wave vector can be thought of as a frequency factor, with high **k** values indicating rapid oscillations, corresponding to high energies.

1.6 Unrestricted Kohn-Sham formalism and broken-symmetry approach

It is convenient at this point to introduce the topic of unrestricted determinants, because their computation and interpretation forms a recurring part of this thesis. The wave function for an electron that describes both the electron's spatial distribution and its spin is represented by a spin orbital, usually constructed by multiplying each spatial orbital by either the α or β spin function. A given spatial orbital can be occupied by a single electron (α or β) or by two electrons with paired spins. Such spin orbitals and the determinants formed from them are called restricted. In contrast, within the unrestricted formalism, a determinant is composed of unrestricted spin orbitals. In this case, two individual sets of spatial orbitals are used for each spin manifold. Consequently, the resulting spin orbitals are not constrained to be identical for α and β spins, but have different spatial parts for different spins, and are thus given the freedom to localise in separate compartments of a molecule. For simplicity, we consider a two-spin system (e.g. a dinuclear transition metal system) with two unpaired electrons in two nonorthogonal orbitals on sites a and b. The two possibilities for the spin quantum number m_s on each site gives rise to the four micro spinstates $|\alpha\alpha\rangle$, $|\alpha\beta\rangle$, $|\beta\alpha\rangle$ and $|\beta\beta\rangle$. Both $|\alpha\alpha\rangle$ and $|\beta\beta\rangle$ correspond to the $M_S = 1$ and $M_S = -1$ component of the overall triplet state for the system (i.e. $|1,1\rangle$ and $|1,-1\rangle$), resulting from parallel alignment of the two site spins S_a and S_b to produce the maximum total spin S. On the contrary, linear combinations of the

remaining two micro spinstates give rise to the $M_S = 0$ components of the triplet ($|1,0\rangle$) and singlet state ($|0,0\rangle$), the second of which results from a minimisation of the total spin S. Explicitly, the singlet state is given by

$$|\Psi_{\mathrm{S}}\rangle = \frac{1}{\sqrt{2}}(|\varphi_a\bar{\varphi}_b| - |\bar{\varphi}_a\varphi_b|) \tag{1.44}$$

This expression emphasises the multireference nature of such a wave function, which is unsuitable for a KS-DFT treatment due to the restriction of being a single-determinant method. In this context the broken-symmetry (BS) approach first proposed by Ginsberg[48] and Noodleman[49–52] has emerged as a powerful tool to describe interactions between multiple spin sites, where antiferromagnetic coupling between magnetic orbitals is a frequently met case. One advantage of the BS technique is that it provides an accurate treatment of systems with multiradical character without having to resort to CI methods. One starts from a single determinant wave function that reflects the antiferromagnetic state, which is then subjected to the variational principle in order to achieve orbital relaxation

$$|\Phi_{\mathrm{BS}}^{\mathrm{guess}}\rangle = |\varphi_a\bar{\varphi}_b| \xrightarrow{relaxation} |\Phi_{\mathrm{BS}}\rangle = |\tau_a\bar{\tau}_b| \tag{1.45}$$

It can be shown that the final BS wave function is a weighted linear combination of neutral and ionic configurations. While φ_a and φ_b are orthogonal in their space parts, this is no longer true for the optimised orbitals τ_a and τ_b. While the BS method yields physically correct charge densities, the same is not true for spin densities. The occurrence of net spin density in certain regions in space is an artifact of the method. Most importantly, having obtained solutions for the determinants of maximum spin and broken spin symmetry, it is now possible to extrapolate the energies of the pure spin states by using well-developed projection techniques. We

refrain from going into detail here, but will return to this subject at a later point. Importantly, restricted and unrestricted determinants differ in their behaviour with respect to spin operators. In particular, while restricted determinants are eigenfunctions of both $\hat{S}^2$ and $\hat{S}_z$, unrestricted determinants are not eigenfunctions of $\hat{S}^2$. In this case the expectation value of $\hat{S}^2$ diverges from the exact value, $S(S+1)$, and it can be shown that the expectation value in this case is given by the relation

$$\langle \hat{S}^2 \rangle = S(S+1) + N_\beta - \sum_{ij}^{N_{\mathrm{MO}}} \langle \varphi_i^\alpha | \varphi_j^\beta \rangle^2 \tag{1.46}$$

where N_β is the number of β electrons (assuming $N_\alpha \geq N_\beta$) and the last term corresponds to the sum of overlap integrals between all occupied α and β spin orbitals.

It needs to be emphasised that an unrestricted wave function does not correspond to a pure spin state, but it can be expanded in terms of pure spin states of higher multiplicities. Thus, it is contaminated by higher multiplicity components. The expectation value of $\hat{S}^2$ will frequently be used as a probe for the extent of spin contamination in a computed determinant, and will be employed particularly in the context of broken-symmetry DFT in order to extrapolate the energies of pure spin states.

However, it should be noted that the expectation value of $\hat{S}^2$ within the KS formalism has less significance than in the unrestricted HF formalism, because the employed determinants of each scheme do not parallel each other. In fact, it has been argued that spin contamination is not well defined within DFT.[53] In all cases where unrestricted calculations are performed, we will also discuss the computed spin densities, which arise as a result of the localisation of the unrestricted spin orbitals on different spatial parts of a molecule.

1.7 Computational methods

All calculations described in this thesis have been performed with the Gaussian09,[54] Gaussian03,[55] Amsterdam Density Functional (ADF 2008.01-2010.02),[56–58] Jaguar 7.6,[59] and ORCA 2.6[60] program suites. Throughout this work density functional theory has been the method of choice. The calculations typically utilised the B3LYP hybrid functional[19,26,31,32] or the BP86 functional[21,22] from the GGA family. Commonly, basis sets of triple-ζ quality (TZ) have been used on transition metal centres and all coordinated atoms, in conjunction with double-ζ basis sets (DZ) on the remaining atoms in the molecule. For metal centres, the Stuttgart-Dresden basis set (SDD) and effective core potential has alternatively been employed.[61] Initial atomic coordinates were taken from single-crystal X-ray diffraction experiments, where available. Unless stated otherwise, geometries were fully optimised without imposing any symmetry constraints (C_1 symmetry). Stationary points were characterised by analysis of their vibrational frequencies, with minima having no imaginary frequencies and transition states having exactly one. Complete details of the methodology used are presented separately in each chapter. The topological properties of the electron density have been characterised by using the Atoms In Molecules (AIM) theory by Bader.[62] For the visualisation of the electron density the AIM2000 program has been applied.[63] Percentage compositions of canonical and corresponding molecular orbitals were calculated using the AOMix program.[64,65] Mulliken spin densities were used for analysis of spin populations on ligand and metal centres.[66–69] All results of the quantum chemical calculations have been visualised using the Chemcraft 1.6 software[70] or ADF-GUI.[71]

2

Non-innocent complexes of the bipyridine ligand

In this chapter we discuss examples of non-innocent behaviour of two isomers of the bipyridine (bpy) ligand family, which are ubiquitous in coordination chemistry. This work has been done in collaboration with Dr. Goicoechea and his group here in Oxford, and parts of the results have been jointly published in Ref. [255] and [256]. In the first part of this chapter we analyse the electronic structures of complexes M(2,2′-bpy)$(mes)_2$, where M is a first-row transition metal and mes = 2,4,6-$Me_3C_6H_2$, and their one-electron reduced forms of general formula [M(2,2′-bpy)$(mes)_2]^-$. The combined structural, spectroscopic and computational data unequivocally show that the reduction is a ligand-based event in all cases, and the extra electron is located in a π^* orbital of mainly bpy LUMO character. In the second part of this chapter, we look at cases where bipyridine is even further reduced to its dianionic form. The two complexes $[Fe^{II}(2,2'\text{-bpy})_2]^{2-}$ and $[Zn_2(4,4'\text{-bpy})(mes)_4]^{2-}$ serve as examples.

2.1 Introduction

The concept of non-innocence has received wide recognition in the last decade. New reports on complexes showing non-innocent behaviour are weekly added to the current literature, underlining the increasing popularity of this field of inorganic chemistry. The potential applications of redox-active ligands in organometallic catalysis and their relevance in biological catalytic systems are the driving force of this fast development. Understanding the bonding and physical properties of these complexes is of fundamental importance for gaining insight into their reactivity.[72–74] Several reviews have been devoted to the various classes of non-innocent ligand metal complexes, summarising the developments in this research area.[75–89]

For a long time the doctrine persisted in coordination chemistry that the central metal ion is responsible for the redox behaviour of a complex while the surrounding ligands are mere spectators. Indeed, this is true for the majority of inorganic compounds. The assignment of oxidation states is straightforward for classical Werner-type compounds such as *cis*-$[Co(NH_3)_4(Cl_2)]$ or organometallic species such as ferrocene. However, the above view experienced a dramatic change with the appearance of complexes for which the convention of metal-centred electron transfer processes seemed to be not valid any longer. The term 'innocent ligand' was coined in the 1960's by Jørgensen and refers to situations in which the charge on the ligand is well-defined, allowing for an unambiguous determination of the oxidation state of the metal centre. The original statement from his paper reads, "ligands are innocent, when they allow oxidation states of the central atoms to be defined".[90] Examples that fall into this class are H_2O and NH_3. In the contrasting case of 'non-innocent' behaviour, the ligand itself can undergo intra- and intermolecular electron transfer, thereby changing its own oxidation state and making a definitive

assignment of the metal oxidation state difficult. Indeed the concept of oxidation state itself is poorly defined in such circumstances. Unsurprisingly, the detailed electronic structure of this type of complex is often complicated, and can only be formulated in terms of limiting resonance structures.

Interestingly, even the simplest of ligands such as NO and O_2 can give rise to an oxidation state ambiguity (again quoting from Jørgensen's paper, "The simplest case of a suspect ligand is NO"). Indeed, the ambivalence of the Fe-NO moiety, for example, is reflected in the ion $[Fe(NO)(H_2O)_5]^{2+}$, which may be formulated as one of the electromeric forms $Fe^{I}-NO^{+}$, $Fe^{II}-NO^{\cdot}$ or $Fe^{III}-NO^{2-}$.* It has been shown that the latter formulation is most suitable.[92]

Examples of non-innocent behaviour in transition metal complexes have been known since the 1960s, when a series of square-planar dithiolene complexes $[M(dithiolene)_2]$ of the group 10 triad (M = Ni, Pd, Pt) were isolated.[93] 1,2-disubstituted chelating ligands like dithiolenes are prototypical for non-innocent behaviour, and transition metal dithiolenes arguably belong to the most studied group within the family of non-innocent complexes. The interpretation of their exact electronic structure and the confusion about the related redox and electronic spectroscopic properties has caused much debate over decades.[94] In terms of a formal valence bond picture these complexes have been described in the limits of delocalised covalent and localised diradical formulations, depicted in Scheme 2.1. As a consequence, precise oxidation states and charges on the metal centre as well as the ligand could not unambiguously be determined for a long time. From an experimental perspective, a combination of spectroscopic and magnetic data is generally necessary to unravel the complexities of the bonding. Indeed, the development of modern electron paramagnetic resonance (ESR) spectrometers, supercon-

*By using the Enemark-Feltham notation,[91] in this case $\{FeNO\}^7$, one intentionally tries to avoid an exact assignment of formal oxidation states within the Fe-NO unit.

Scheme 2.1: Possible resonance forms for planar bis(dithiolene) complexes of nickel, palladium and platinum.

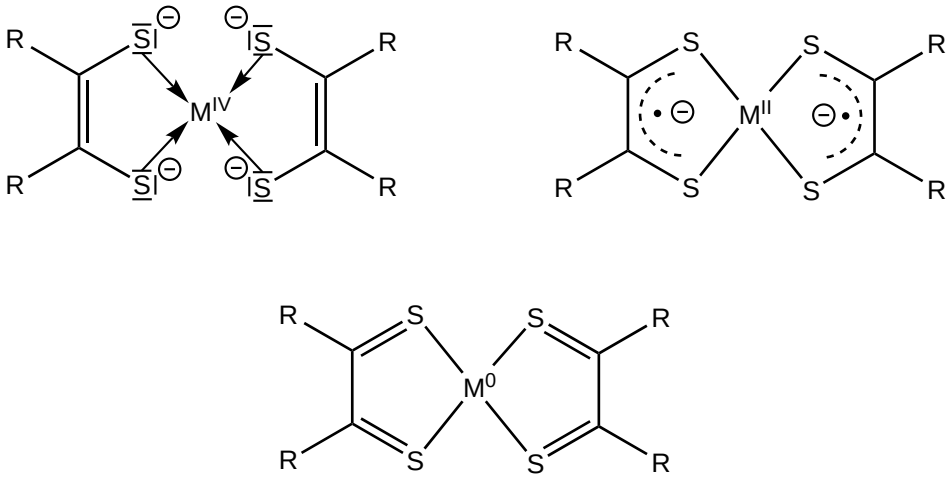

ducting quantum interference device (SQUID) magnetometers and high-resolution X-ray diffractometers has been integral to the development of the field, and many previously unsuspected cases of non-innocent behaviour have been exposed in biological and non-biological systems. The roles of ligands previously supposed to be mere spectators have had to be re-evaluated, and it now appears that transition metal complexes of radical organic ligands are key intermediates in many enzyme-catalysed transformations. First indication of non-innocence often comes from single crystal X-ray crystallography, as the ligand's bond lengths are different at different oxidation levels. There are, however, cases of 'hidden non-innocence' where bond lengths change rather little and thus a structure-oxidation state correlation does not exist.[95] Other spectroscopic methods that are frequently used to determine the electron density distribution in complexes with non-innocent behaviour include UV-vis, IR and Mössbauer spectroscopy, as well as (spectro)electrochemical techniques. More recently, various flavors of K-edge X-ray absorption spectroscopy (XAS) have also been applied to directly probe the bonding and covalency in non-innocent complexes. These methods have especially proven to be useful in determining the oxidation states in a large range of dithiolene complexes.[94,96] The

information content of the experimental data is often enhanced by density functional theory or *ab initio* calculations. The interpretation of these data is often controversial, and careful cross referencing to experiment is essential if a consistent model of electron structure is to be reached.

It has been suggested that the formal oxidation state (FOS)[97] of a metal in a mononuclear coordination compound should be distinguished from the physical oxidation state (POS).[98,99] The former is determined as the charge remaining on the metal after removal of all ligands in their normal closed-shell electronic configurations, and as such is a non-measurable integer number. On the other hand, the physical oxidation state is derived from the d^n electronic configuration of the metal, which is a measurable quantity that can be determined spectroscopically. For that reason the physical oxidation state is sometimes also referred to as the spectroscopic oxidation state.[100] In a large number of cases the FOS and POS are identical, exemplified by the complex $[Cu^{II}(NH_3)_4]^{2+}$ where the d^9 copper centre possesses a physical and formal +II oxidation state. The problem arises in cases where paramagnetic organic radicals are coordinated to the transition metal ion. The O-coordinated phenoxyl radical complex of an iron ion with a d^5 configuration, $Fe^{III}-O^{\cdot}-Ph$, serves as an illustrative example. Apparently, the formal oxidation state of +IV differs from the physical oxidation state of +III, which corresponds to a high-spin d^5 configuration unequivocally justified by Mössbauer and resonance Raman spectroscopy.

The term 'non-innocent' has become frequent in the last few years, and the sense in which it is regularly used is synonymous with 'non-innocent ligand' (NIL). However, an important aspect to be considered is the fact that the same redox-active ligand can behave both in an innocent and in a non-innocent manner. Thus, it has been emphasised by Ward and McCleverty that non-innocence should not be

understood as a function of the ligand alone, but that it is necessary to consider a particular coordination situation as a whole and refer to it as 'non-innocent behaviour'.[81] Therefore, in this view the participation of the metal centre is naturally integrated, and the term 'non-innocent' is used for the combination of metal and the ligand. (In this chapter we will nonetheless use the expression 'non-innocent ligand' (NIL), but it should be kept in mind that this expression in principle always refers to a property of the full complex).

The possibility of non-innocent behaviour in a complex requires strong mixing between metal- and ligand-centred frontier orbitals. The ligand orbitals need to be energetically raised above the metal d manifold in order to activate them for ligand-based redox processes. The pictorial MO diagram in Scheme 2.2, originally derived to describe the bonding in dithiolene complexes, summarises the important features that contribute to the non-innocent behaviour.

Scheme 2.2: Schematic MO diagrams of normal and inverted bonding scenarios.

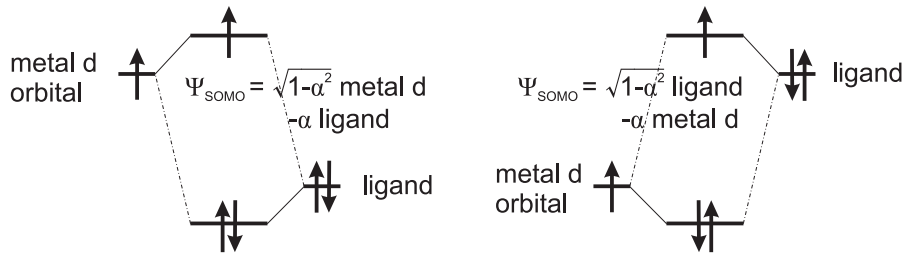

Innocent coordination compounds can be described with the normal bonding scheme, in which the redox active orbitals are based on the metal and the metal-ligand interaction is mainly ionic, with low covalency. On the other hand, non-innocent complexes have an inverted bonding scheme, with the donor orbitals largely destabilised relative to the acceptor metal orbitals, resulting in activation of the ligand for redox chemistry. Multi-dentate ligands with conjugated π-systems are ideal candidates to fulfill the energetic constraints, this being the reason why chelating ligands of the 'catecholate-type' containing the vicinal 1,2-

disubstitution motif ('binding pocket') are so prevalent among non-innocent complexes (Scheme 2.3).

Scheme 2.3: The dioxolene redox series: quinone, semiquinone, catecholate.

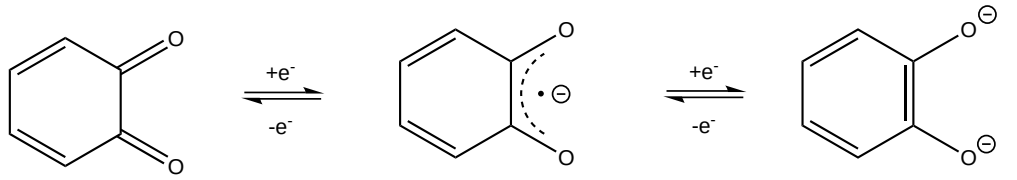

o-quinone, (q) *o*-semiquinone, $(sq)^{-}$ catecholate, $(cat)^{2-}$

The extended π-delocalisation is well suited to stabilise radicals through conjugation. At the same time, the rigid arrangement of the σ-donor orbitals facilitates ligand-ligand repulsion between the lone pairs, and thus destabilisation with respect to the metal frontier orbitals.

The alternative coordination situations between a redox-active ligand and a transition metal can give rise to either a resonance scenario with delocalised valences describing one species in a single-well minimum, or an equilibrium situation between two (or more) redox isomeric (valence tautomeric) species in a double (multi) minimum array (Scheme 2.4).[84] This latter case is associated with activation barriers separating the different minima, whereas the electron delocalised case certainly is barrierless. The main contribution to the resonance forms may be established experimentally or computationally. These two cases of single- and double-well curves also form limiting formulations within the Robin-Day classification scheme,[101] used to categorise mixed-valence systems.

Scheme 2.4: Resonance form and valence tautomeric scenarios in redox non-innocent complexes.

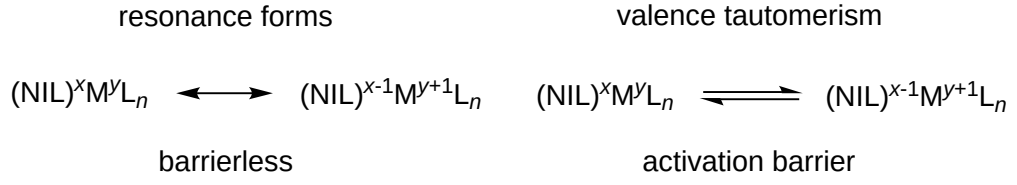

Valence tautomeric complexes form an interesting subclass within the framework of non-innocent behaviour.[84,102] Each individual electronic isomer present in the equilibrium reveals characteristic optical, electric and magnetic properties. Thus, the possibility of inducing reversible changes in the electronic distribution makes them ideal candidates for use in information storage and integrated molecular devices.[103] Moreover, they are good models for studying electron transfer processes. The cobalt bis(quinone) complex shown in Figure 2.1 serves as a good example for valence tautomerism,[104] where the proximity of ligand- and metal-centred redox orbitals leads to a finely balanced equilibrium in solution. Changes can be induced by variations of temperature, and monitored by magnetic and spectroscopic methods. An increase in temperature promotes an intra-molecular electron transfer such that the Co^{III} tautomer converts into the Co^{II} isomer as one of the ligands is oxidised from its catecholate to the semiquinonato form. Interestingly, the optical changes are accompanied by a spin-crossover on the metal centre, which changes from low-spin Co^{III} ($S = 0$) to a high-spin Co^{II} configuration ($S = 2$). The interconversion is driven by a large entropy gain due to population of the higher spin state.

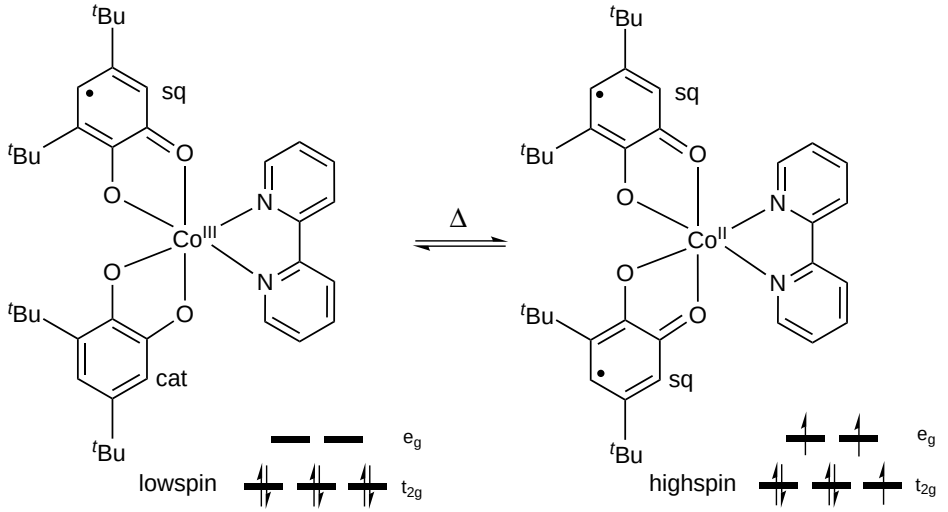

Figure 2.1: Thermal equilibrium of the tautomeric catecholate-semiquinone interconversion in Co(bpy)(3,5-DBQ)$_2$ (3,5-DBQ = 3,5-di-*tert*-butylquinone).

Survey of non-innocent ligands

Many transition metal complexes of radical organic ligands are key intermediates in catalysis or important biological processes. Before discussing some examples from bioinorganic and chemical catalysis, a brief survey of ligands with potential for non-innocent behaviour will be given. It goes without saying that in addition to the simplest of cases such as NO (**I**, Figure 2.2) and O_2, a large number of other ligands has been identified as redox-ambivalent. The most extensively studied are the complexes of the α-diketo compounds, especially *o*-quinones[83,84,103,105–112] (**IIa**, E = O) and α-dithiolenes (**IIa**, E = S),[96,113–124] and phenoxyl radicals.[125] Other early recognised candidates which exhibit non-innocent behaviour include α-diimines such as 1,4-diazabutadiene (**IIb**, E = NR),[126–130] azo compounds (**III**),[131] and polycyano ligands such as tetracyanoethylene (TCNE; **IV**) and TCNQ.[132] 1,2,4,5-Tetrazines (**V**),[133] tetrazenes,[134] 2,2′-bipyridines (**VI**),[135–138] α-iminopyridines,[139,140] α-imino- ketones,[141] imino- and thio-phenolates[98,142–148] can also serve as NILs. Many of these ligands feature the 'bay region' motif, which enables them to form five-membered chelate rings when bound to a metal. In addition to the above NILs, which can be considered as classical examples, more recently pincer-type chelating ligand frameworks have gained considerable attention owing to their ability to act as cooperative ligands in homogeneous catalysis.[149,150] As an example, the phosphine ligand PPP-H (**VII**), used in its deprotonated form, falls into this group of 'non-classical' NILs. The first family of aminyl radical complexes was also reported in the chemical literature, of which $trop_2N$ (**VIII**, trop = 5-H-dibenzo[a,d]cycloheptene5-yl) is an interesting representative.[151–153] Besides the quinones and phenoxyl radicals already mentioned, flavins,[154,155] tetrapyrrole macrocycles,[156–158] and pterins[155] were also shown to qualify as redox NILs within a biological context.

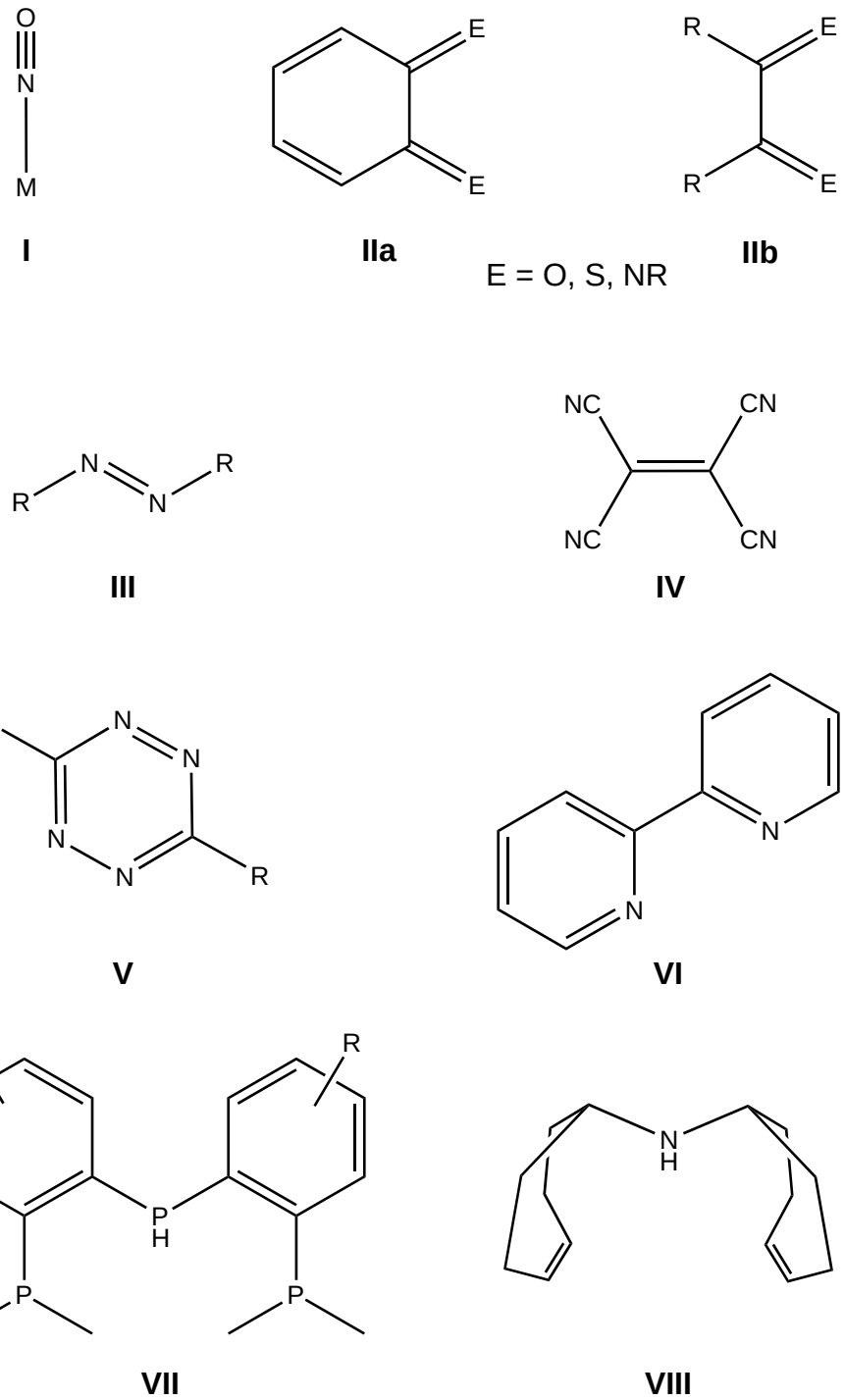

Figure 2.2: Representative examples of potentially non-innocent ligands (NIL).

Relevance for bioinorganic chemistry

As mentioned in the previous paragraph, non-innocent behaviour was not only found within synthetic complexes, but frequently recognised in a biochemical context. Soon it became obvious that non-innocent ligands are not just a spectroscopic curiosity, but that they also play an important part in enzymatic catalysis, either as substrates (e.g. O_2, NO, quinones) or as supporting ligands, modifying the properties of cofactors (e.g. porphyrins, quinones, dithiolates). Many metalloenzymes have evolved to incorporate abundant metal ions (e.g. iron and copper), which preferentially react as one-electron redox couples.[159] On the other hand, many biological transformations are multielectron processes. Thus, utilising redox-active supporting ligands is an elegant way used by Nature to resolve this paradox and perform the desired multielectron chemistry, while at the same time preventing unwanted radical side reactions.

The most extensively researched transition metal complexes of radical anions are those of semiquinone and phenoxyl radicals, and both of these can also be viewed as prototypes of non-innocent behaviour. Their biological relevance is exemplified by their role in photosynthesis, respiration and many other bio-catalytic processes mediated by several metalloenzymes (e.g. catechol oxidase). One of the best understood examples is galactose oxidase (GAO), where the oxidation of primary alcohols to aldehydes is achieved by the combined action of a Cu^{II}/tyrosinyl pair.[160,161] The phenoxyl radical forms an integral part, allowing a copper-based active site, which intrinsically is limited to a one-electron (Cu^{I}/Cu^{II}) couple, to catalyse two-electron chemistry. The important and rate-determining step within the mechanistic cycle (Figure 2.3), following initial substrate binding and deprotonation, is the homolytic cleavage of the alcoholic C-H bond and abstraction of a hydrogen atom, which is transferred to the tyrosinyl oxygen atom.

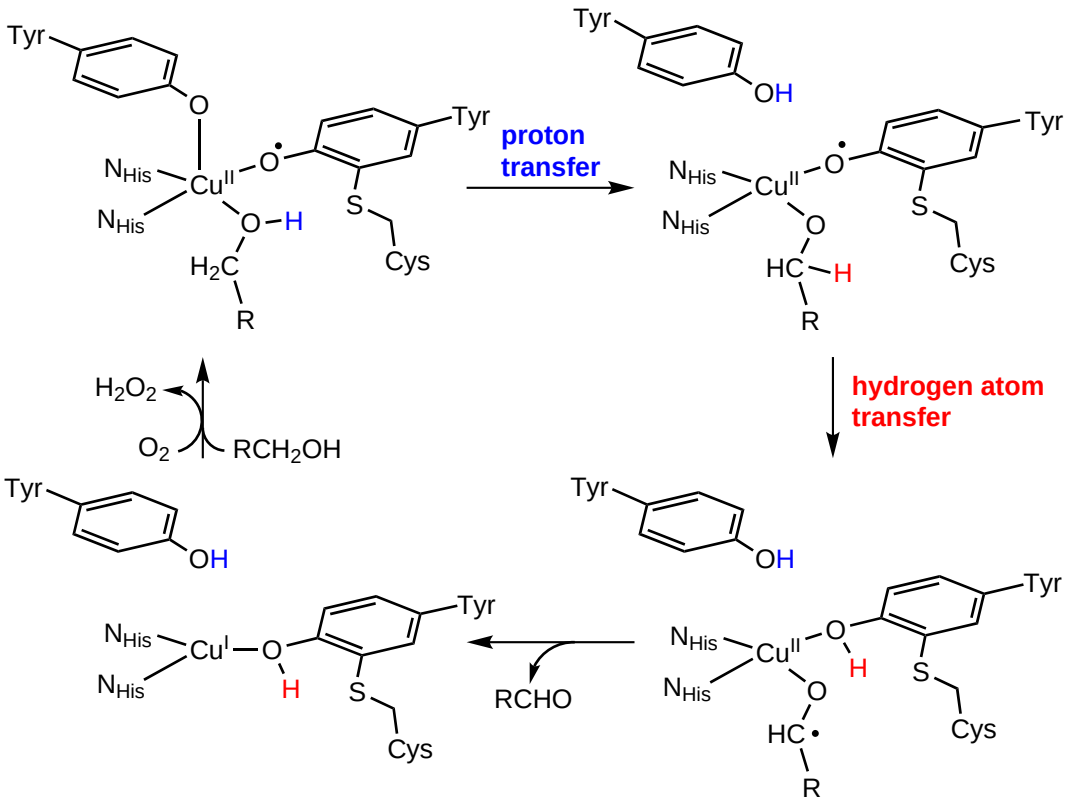

Figure 2.3: Schematic representation of the catalytic cycle of galactose oxidase.

The oxidative phase is completed by intramolecular electron transfer from the putative ketyl radical to Cu^{II} followed by the loss of aldehyde, generating the reduced form of the enzyme. The second phase of the mechanism involves oxidation of the reduced form by O_2, which is converted to H_2O_2 using the protons available from substrate. The redox event takes place at the tyrosinato ligand, and not at the copper centre. Presumably, a Cu^{II}-hydroperoxide is involved as an intermediate in this process, although no such species has been observed during this last phase.

Some further examples of NILs in bioinorganic systems are shown in Figure 2.4, including topa-quinone amineoxidase (**I**), molybdopterin (**II**), the molybdenum cofactor of oxotransferases, and the haem moiety (**III**). The latter plays an important role as a prosthetic group in the active site of cytochrome P450 enzymes, which affect a vast range of oxidation reactions in nature. The putative P450 oxidant is usually thought to be a Fe^{IV}=O porphyrin radical cation species ("Compound I").

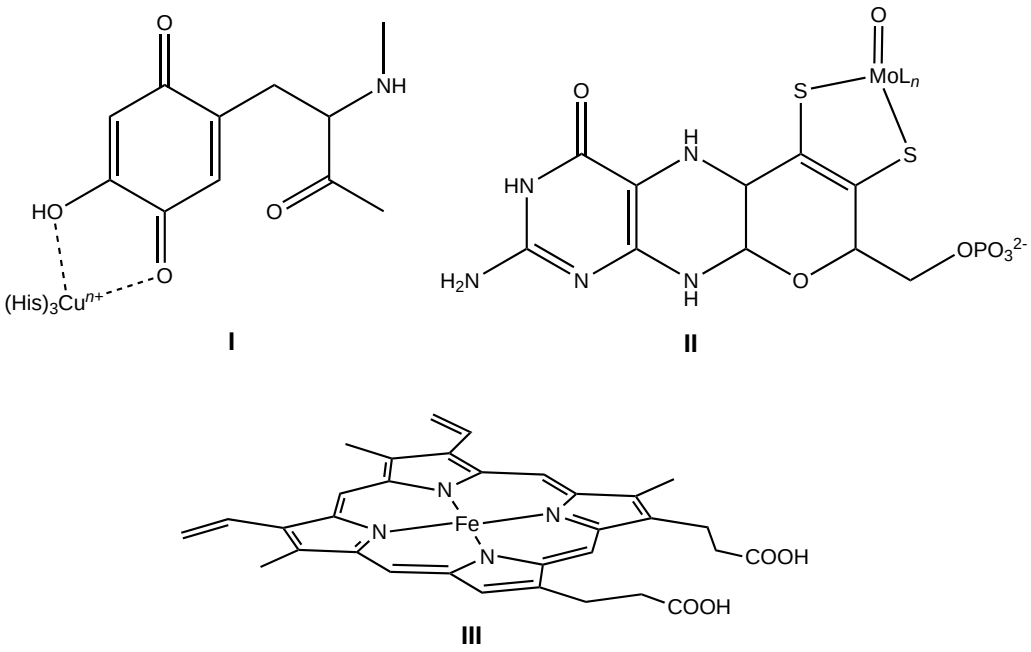

Figure 2.4: Functional transition metal / NIL combinations appearing in biological systems.

Relevance for chemical catalysis

The design of new non-innocent ligands and their metal complexes, followed by detailed characterisation of their electronic structure is a very active field of chemical research. One aim is the development of functional model compounds of metalloenzymes. More recently, researchers have also started to systematically investigate the (catalytic) reactivity of metal complexes with radicals on the supporting ligands in organometallic reactions,[72,149,162] drawing inspiration from biological systems that exploit non-innocent behaviour. In this respect, redox non-innocence offers a great potential for reaction control, but research in this direction is still in its infancy. Current research interest into NILs in catalysis is twofold (Scheme 2.5). Many transition-metal catalysed transformations involve elementary steps wherein electrons are transferred from and to the metal centre. Redox-active ligands may assist in these processes and thus offer opportunities for unexpected reactivity, owing to their capacity to serve as electron buffers, which reversibly accept and donate electrons. This concept is nicely illustrated in an example reported by Chirik

Scheme 2.5: Approaches to exploit non-innocent behaviour in catalysis. Adapted from a review by de Bruin and co-workers.[162]

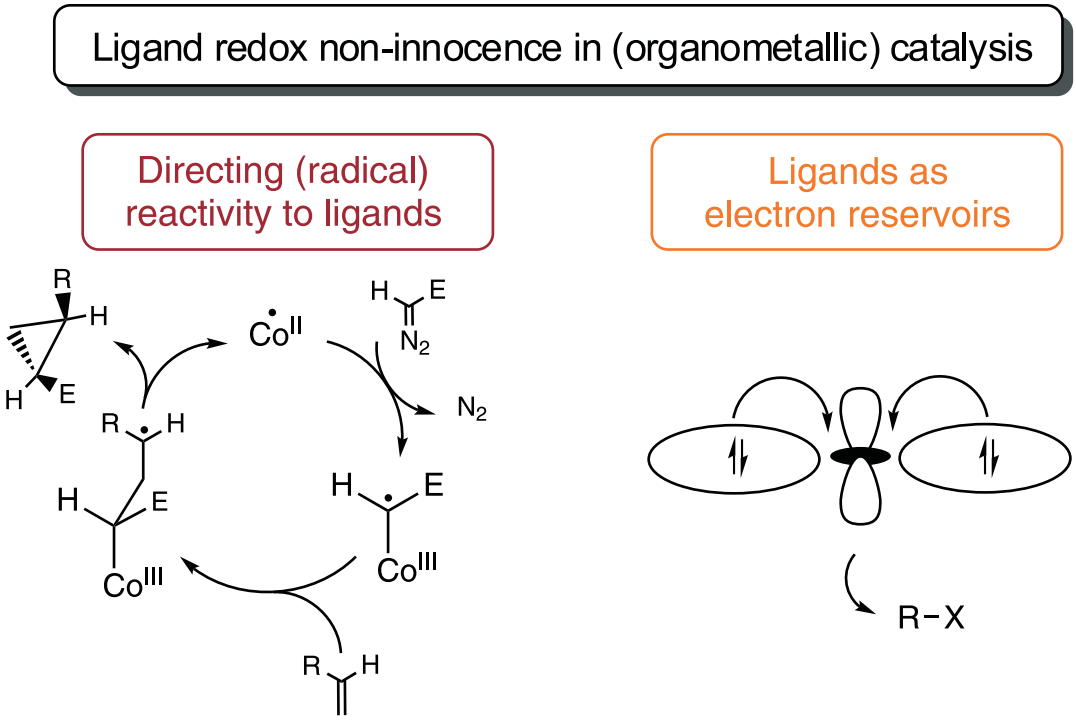

and co-workers, in which a redox non-innocent derivative of pyridine-2,6-diimine (PDI)[163] is used for selective C-C coupling in $[2\pi+2\pi]$ cycloisomerisation reactions of α,ω-dienes with iron (Figure 2.5).[164] The electrons for the oxidative addition and reductive elimination processes related to the C-C bond formation are provided by the ligand, whereas the oxidation state of the metal is maintained throughout the reaction ('pseudo-oxidative addition / reductive elimination').[165] Thus, the ligand preserves the ferrous oxidation state of the iron centre, preventing formation of unstable redox states. In terms of a more general concept it has been noted that the PDI ligand confers some degree of noble character on the iron, implying that it may be possible to substitute noble metals currently used in organometallic catalysis with cheaper and more abundant transition metals.[166]

A second approach, albeit less common, uses redox non-innocence to generate reactive ligand radicals and thus force ligand-centred reactivity during catalysis.[167]

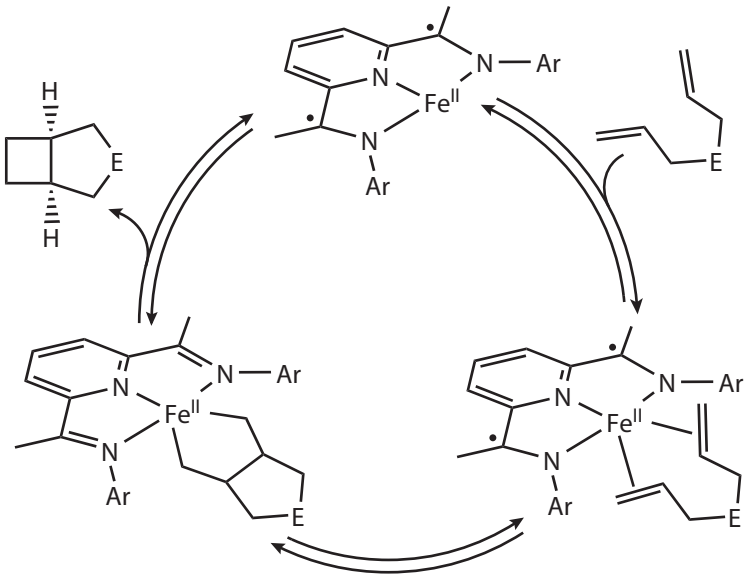

Figure 2.5: Catalytic cycle of the [2π+2π] ring-formation reaction catalysed by ($^{i\mathrm{Pr}}$PDI)Fe without changing the Fe oxidation state. Electrons shuttle between the iron centre and the $^{i\mathrm{Pr}}$PDI ligand during the cycle. The group E can be an alkyl or nitrogen-substituted alkyl group.

An example for this type of reaction is the Co$^{\mathrm{II}}$(porphyrin)-mediated cyclopropanation of olefins with diazoesters from the group of de Bruin.[168] During the reaction a 'non-innocent' carbene radical is formed, which subsequently reacts in a radical addition reaction to the olefinic double bond. The resulting γ-alkyl radical finally collapses to the cyclopropane product.

In addition to their importance for catalytic processes, non-innocent complexes have potential applications in materials science, where one wishes to exploit their properties for information processing and optical materials. The spin information associated with the ligand radical character can be utilised in metal-ligand spin arrays of varying complexity or in spin-crossover effects discussed above in the context of valence tautomerism.[169] Complexes with low and high molecular weights that possess low-lying absorptions in the visible and near-infrared region are interesting candidates for optical materials. Such complexes include polynuclear complexes with bridging ligands such as poly-dioxolene.[81]

The studies presented in this and the following chapter encompass two distinct but closely related non-innocent ligands of the π-system type, bipyridine (bpy) and 2-(phenylazo)pyridine (pap), which form complexes with various transition metals (Fe, Rh, Cr, Mo, Zn). Arguably, 2,2′-bipyridine and its derivatives is one of the most versatile bidentate ligands used in coordination chemistry,[170] compatible with many main-group, lanthanoid, actinoid and transition metal ions. The chemical and electrochemical reduction of free 2,2′-bipyridine (2,2′-bpy^{0}) to the π-radical monoanionic form (2,2′-bpy$^{\cdot -}$) and even dianionic forms (2,2′-bpy^{2-}) has long been established,[171–185] and all of these forms have been structurally characterised by X-ray crystallography.[135,186,187]

A number of well-defined coordination compounds of the 2,2′-bpy ligand in its different oxidation states have been reported in the field of main-group[188,189] coordination chemistry (e.g. $[Al^{III}Cl_2(bpy)_2]Cl$), as well as lanthanide[190–193] (e.g. $[(Cp^*)_2Yb^{III}(bpy^{\cdot -})]^0$, Cp^* = pentamethylcyclopentadienyl), and actinide[194] (e.g. $[(Tp^*)_2U^{III}(bpy^{\cdot -})]^0$, Tp^* = hydrotris(3,5-dimethylpyrazolyl)borate) coordination chemistry. Transition metal complexes with neutral bpy as coligand are well known, represented for example by the octahedral complexes $[M^{II}(bpy^0)_3]^{2+}$ (M = Fe, Ru, Os).[195–197] Research on homoleptic first-row transition metal complexes of 2,2′-bpy highlighted the possibility of bipyridyl radical coordination to transition metal ions and several examples have now been spectroscopically characterised via EPR, IR, electronic and/or resonance Raman measurements. Bond metric parameters of a series of crystallographically characterised transition metal complexes containing 2,2′-bpy as co-ligand support the possibility of radical (or even dianionic) character,[135,198–203] of which $[La^{III}(Tp^*)_2(bpy^{\cdot -})]^0$ serves as one example.[204] However, we believe that the interpretation of the structural data is ambiguous, simply because a one electron reduction of the ligand has the same qualitative ef-

fect as enhanced π-backbonding from a reduced metal centre (Scheme 2.6). Both result in population of the lowest unoccupied molecular orbital (LUMO) of 2,2′-bpy and hence result in the same structural changes within the ligand skeleton, especially contraction of the C-C bond linking the two rings. Examples of N,N′-coordinated (bpy^{2-}) are by far less common, and the few existing complexes where the characterisation is unequivocal encompass $[Al^{III}(bpy^{2-})_2]^-$, $[Zr^{IV}(bpy^{2-})_3]^{2-}$ and $[La^{III}(Tp^*)(bpy^{2-})(thf)_2]^0$.[189,201,204]

Scheme 2.6: Ligand radical (left) and enhanced π-backbonding (right).

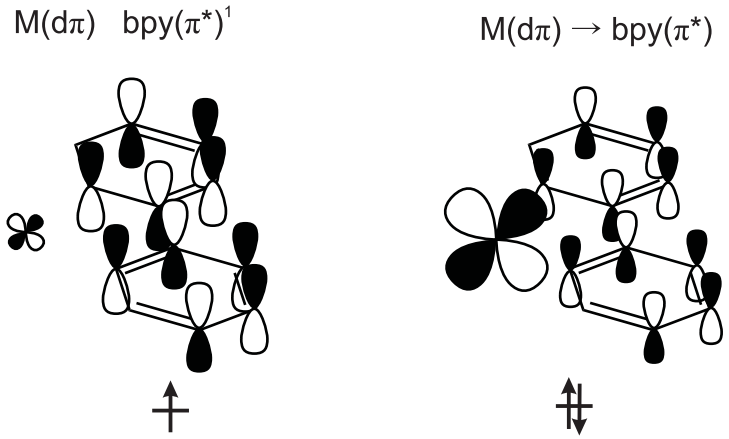

Combined experimental and theoretical studies have become common practice in order to understand the intricate electronic structures of non-innocent complexes. It is interesting to note that computational evidence for the monoanionic radical form of 2,2′-bpy has existed for a long time. For example, in a report from 1979, Stucky et al.[198] concluded from Fenske-Hall MO calculations on the complex $[Cp_2Ti^{III}(bpy^{\cdot-})]^0$ that, "the electronic structure of the triplet state of the complex is approximately described as a titanium(III) centre bound to a bipyridyl radical anion."

Very recently, Scarborough and Wieghardt reported an in depth DFT survey of the electronic structures of 20 organometallic complexes containing η^5- and η^3-coordinated cyclopentadienyl anions and 2,2′-bipyridine ligands at varying oxida-

tion levels.[205] These authors conclude that the assignment of the oxidation level of bpy in a given coordination compound can be done on basis of the bpy bond parameters alone, while backbonding effects are negligible. They argue that bpy^0 acts as a very weak π- acceptor, ($bpy^{\cdot -}$) is well suited for antiferromagnetic coupling with open-shell transition metal-complexes and (bpy^{2-}) may be a strong π-donor.

The 2,2′-bpy (and also one example of 4,4′-bpy) chemistry discussed in this chapter was studied in collaboration with the Goicoechea group here in Oxford, and involves the isolation and electronic characterisation of a series of anionic first row transition metal complexes $[M(2,2'\text{-bpy})(mes)_2]^-$ (Scheme 2.7, mes = 2,4,6,-$(Me)_3C_6H_2$); M = Cr, Mn, Fe, Co, Ni), obtained from their neutral parent compounds $M(2,2'\text{-bpy})(mes)_2$ by chemical reduction using potassium.

Scheme 2.7: Structural formulas and numbering of $[M(2,2'\text{-bpy})(mes)_2]^{0/-}$ complexes explored in this study.

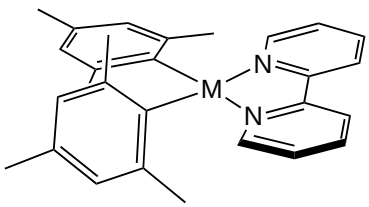

square-planar

$[Cr^{II}(2,2'\text{-bpy})(mes)_2]^{0/-}$ (**1**$^{\mathbf{0}}$,**1**$^{-}$)
$[Co^{II}(2,2'\text{-bpy})(mes)_2]^{0/-}$ (**4**$^{\mathbf{0}}$, **4**$^{-}$)
$[Ni^{II}(2,2'\text{-bpy})(mes)_2]^{0/-}$ (**5**$^{\mathbf{0}}$, **5**$^{-}$)

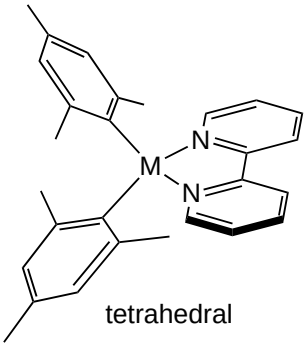

tetrahedral

$[Mn^{II}(2,2'\text{-bpy})(mes)_2]^{0/-}$ (**2**$^{\mathbf{0}}$, **2**$^{-}$)
$[Fe^{II}(2,2'\text{-bpy})(mes)_2]^{0/-}$ (**3**$^{\mathbf{0}}$, **3**$^{-}$)

Single-crystal X-ray diffraction, Mössbauer (for M = Fe) and EPR spectroscopy as well as SQUID magnetometry have been applied to identify their electronic structures. We have used density functional theory to obtain detailed insight into their properties on the electronic level. The combined physicochemical measurements and calculated electronic structures are consistent with the presence of a 2,2′-bipyridyl radical anion in $[M(2,2'\text{-bpy})(mes)_2]^-$, and suggest antiferromagnetic

coupling between the unpaired electron of the ligand radical ($S_{\text{bpy}} = 1/2$) and the electrons on the M^{II} centres.

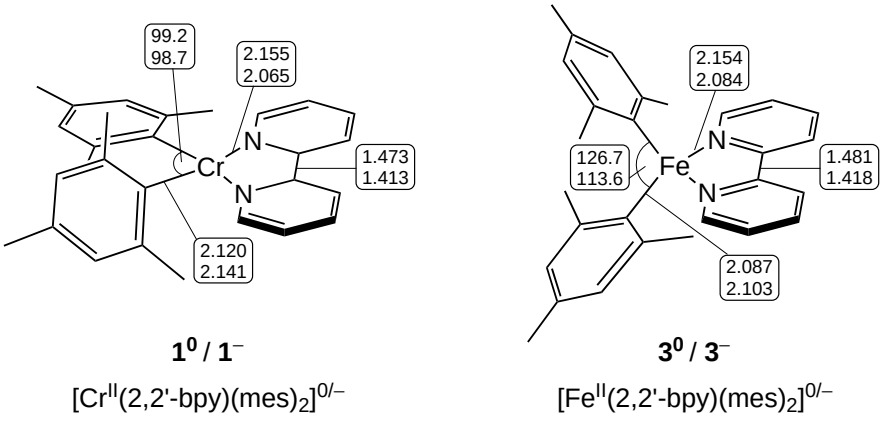

Figure 2.6: Structures of complexes $[Cr(2,2'\text{-bpy})(mes)_2]^{0/-}$ ($\mathbf{1^0}$, $\mathbf{1^-}$) and $[Fe(2,2'\text{-bpy})(mes)_2]^{0/-}$ ($\mathbf{3^0}$, $\mathbf{3^-}$), including key bond lengths (Å). The upper and lower value in each box refers to the neutral and anionic species, respectively.

Further work has also focused on two cases where the coordinated bpy ligand has been further reduced to its dianionic form. Two candidates have been synthesised, $[Zn_2(4,4'\text{-bpy})(mes)_4]^{2-}$ ($\mathbf{7^{2-}}$),[†] where the assignment is unambiguous, and $[Fe(2,2'\text{-bpy})_2]^{2-}$ ($\mathbf{6^{2-}}$) where it is not. In this case Fe^0 and Fe^{II} formulations are conceivable. Our calculations favour the latter - the occupation of the π^* antibonding bpy-based orbital by two electrons.

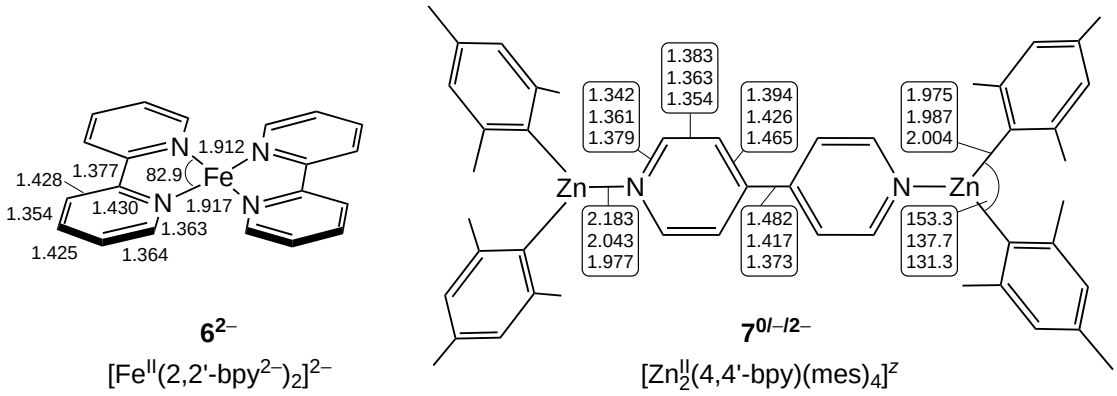

Figure 2.7: Structures of complexes $\mathbf{6^{2-}}$ and $\mathbf{7^{0/-/2-}}$, including key bond lengths (Å). The upper, middle and lower value in each box refers to the neutral, mono- and dianionic complex, respectively.

[†]Part of the electron transfer series $[Zn_2(4,4'\text{-bpy})(mes)_4]^z$ ($z = 0, 1-, 2-$).

2.2 Methodology

2,2′-*bipyridine complexes*: All calculations on the mononuclear transition metal complexes (**1**-**6**) containing the 2,2′-isomer of bipyridine were performed with the ORCA program package.[60] Unrestricted geometry optimisations were carried out using the B3LYP functional[19,26,31,32] in combination with the TZVP[206] basis set of Ahlrichs and co-workers on metal atoms (Cr, Mn, Fe, Co, Ni) and all coordinating atoms (N(1), N(2), N(3), N(4), C(11), C(21)), and the SVP[207] basis set elsewhere. In the case of complex **6** solvation effects were included using the conductor-like screening model (COSMO),[208] where the solvent water was modelled with a dielectric constant of 80.4 and a refraction index of 1.330. For the computation of Mössbauer parameters of the iron complexes $\mathbf{3^0}$ and $\mathbf{3^-}$, non-relativistic single point calculations were carried out on the single-crystal X-ray structures using the B3LYP functional in combination with the CP(PPP) basis set[209] for Fe and TZVP for nitrogen, carbon and hydrogen atoms.

4,4′-*bipyridine complexes*: Calculations on a series of dinuclear Zn complexes ($\mathbf{7^0}$, $\mathbf{7^-}$, $\mathbf{7^{2-}}$) having the 4,4′-isomer of bipyridine as the coligand were carried out with the Gaussian09 program package,[54] employing the M05-2X hybrid meta exchange correlation-functional developed by Truhlar and co-workers.[42] This functional has been recommended for use with Zn compounds and in this study afforded slightly better geometries compared to B3LYP. Again, the TZVP basis set was used on Zn and all coordinating atoms (N and C(1) of mesityl groups), while the SVP basis set was used on the remainder. The topological properties of electron densities, obtained at the same level of theory, were characterised using the Atoms in Molecules theory (AIM) of Bader with the AIM2000 program package.[62,63]

^{1}H NMR chemical shifts were calculated with the Gauge-Independent Atomic Orbital (GIAO) method,[210,211] using geometries obtained at the M05-2X/TZVP/SVP level, as described above. These calculations were done with the B3LYP functional, with a basis set optimised for shielding constants, aug-pcS-2[212] (triple-ζ quality) on the hydrogen atoms of the bipyridine moiety and one mesityl group, which was used as internal standard. For the remaining atom the same basis set as defined above was used (TZVP on Zn and coordinating atoms, SVP for all other atoms). Relative chemical shifts (δ) were obtained by referencing the nuclear magnetic shielding constants of the probe atoms against the arithmetic mean of the isotropic magnetic shielding constants of the *ortho*-methyl protons. These appear as an intense singlet in the experimental NMR spectrum with $\delta = 2.42$ and 2.32 ppm for complexes $\mathbf{7^0}$ and $\mathbf{7^{2-}}$, respectively. Nucleus-Independent Chemical Shifts (NICS) values were calculated at the same level using the GIAO method as recommended by Schleyer et al.[213,214] The NICS probes (ghost atoms) were placed 1 Å above the centres of the rings (defined as the average of the Cartesian coordinates of the ring atoms).

2.3 Complexes of monoanionic bipyridine

2.3.1 Preliminary calculations

The bipyridine ligand plays an important role for the electronic structure of the complexes presented in this chapter. It is therefore reasonable the begin the analysis by modelling the free ligand in order to gain some insight into the basic bonding features of this prevalent ligand system. Figure 2.8 shows the highest energy orbitals of the *s-cis* isomer of 2,2′-bipyridine (C_2 symmetry) in the frontier molecular orbital region, optimised at the B3LYP/TZVP level. The non-planarity of the pyridyl rings is a result of hydrogen-hydrogen and nitrogen lone-pair repulsions. The HOMO (3a) represents part of the π manifold centred at the pyridyl rings, composed of p orbitals on the carbon atoms. The LUMO (4b) of 2,2′-bipyridine is a π^* antibonding orbital with an in-phase relationship between the p orbitals on the carbon atoms linking the two rings. The UV-vis $\pi \rightarrow \pi^*$ feature observed at 282 nm in the experimental absorption spectrum[215] of 2,2′-bipyridine has been assigned to a HOMO/LUMO transition.[216,217] This LUMO becomes the SOMO in the 2,2′-bipyridyl radical ($bpy^{\cdot -}$) and the HOMO in the 2,2′-bipyridyl dianion (bpy^{2-}). The occupation of the vacant LUMO in the neutral ligand causes large changes in the bonding parameters within the ring scaffold (Scheme 2.8). The in-phase π interactions lead to a higher degree of double bond character, manifested in shorter bond lengths, while the out-of-phase interactions become more antibonding, resulting in longer bond lengths. Consequently, in the numbering scheme introduced in Scheme 2.8, bonds 1 and 6 experience a contraction, while bonds 2, 5 and 7 become elongated.[186,218,219] The higher degree of π overlap in the central bond also enforces coplanarity of the two pyridyl moieties.

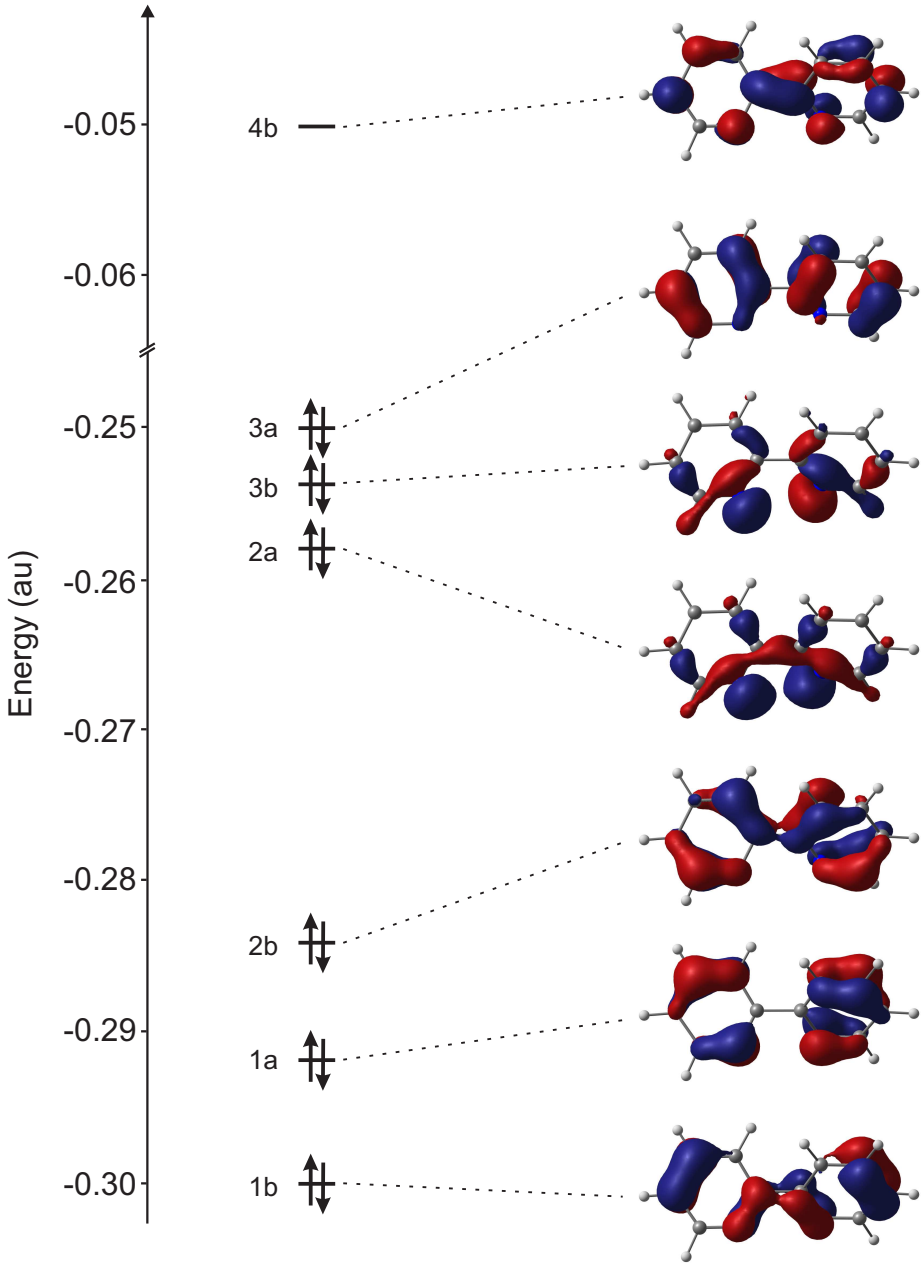

Figure 2.8: Selected molecular orbitals of the *s-cis* 2,2′-bipyridine ligand. [Original in colour]

The most important orbitals for metal bonding are the in-plane HOMO-1 (3b) and HOMO-2 (2a) with out-of-phase and in-phase combinations of p-orbitals localised on the nitrogen atoms. These two orbitals will interact most strongly with a metal centre in a σ-type interaction. Lower down in energy are further orbitals belonging to different π-type combinations within the pyridyl manifold.

Scheme 2.8: Different redox states of 2,2′-bipyridine with characteristic bond distances. Blue labels correspond to the bond numbering scheme employed for discussion of bond metric data.

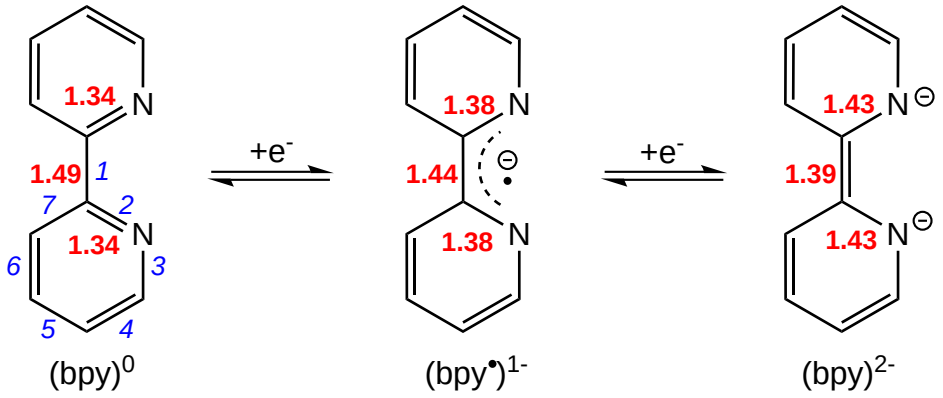

2.3.2 Fe^{II}(2,2′-bpy)$(mes)_2$ and its anion

In contrast to the free ligand, where reduction places the extra electron unambiguously onto the ligand, the situation becomes less clear cut when the same ligand is involved in metal coordination. Thus, the population of the LUMO of 2,2′-bipyridine, that is apparent from the contraction of the central C-C bond in the crystal structure of $\mathbf{3}^-$ could, in principle, be rationalised by either of two limiting formulations of the reduced species: a one-electron reduction of the ligand, leading to a radical species, $[Fe^{II}(2,2'\text{-bpy}^{\bullet -})(mes)_2]^-$, or alternatively, metal-based reduction giving an iron(I) species, $[Fe^{I}(2,2'\text{-bpy})(mes)_2]^-$, with strong metal-to-ligand backbonding.[135,199] To distinguish these possibilities, the electronic structures of both the neutral and the reduced species were analysed.

Optimised geometries

Geometry optimisations afforded the structures shown in Figure 2.9, and important bond metric data are summarised in Table 2.1. The neutral complex ($\mathbf{3^0}$) has a quintet ($S = 2$) ground state and a highly distorted pseudo-tetrahedral coordination

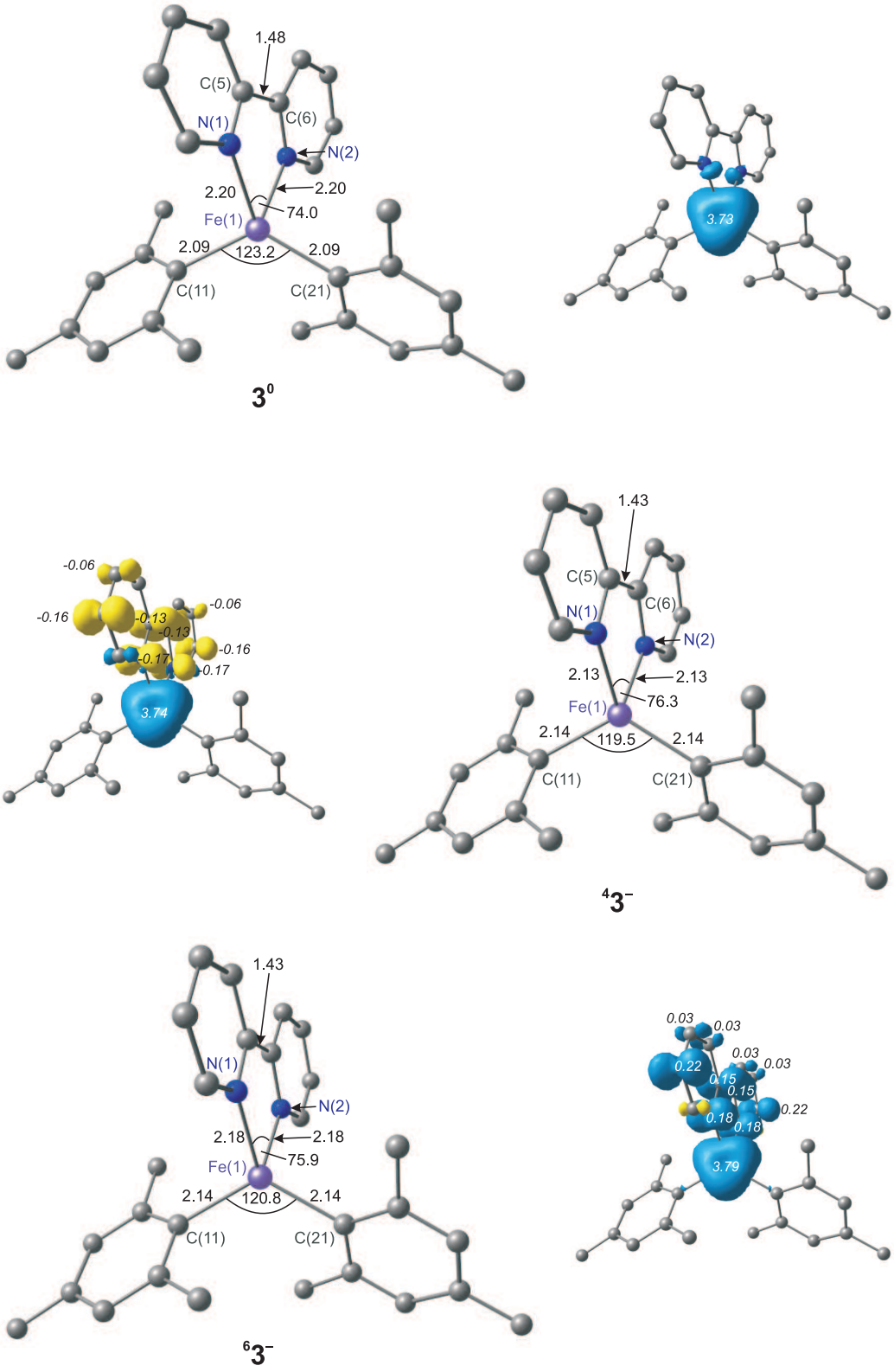

Figure 2.9: Optimised molecular structures (Å, °) of complex $\mathbf{3^0}$, $^4\mathbf{3}^-$ and $^6\mathbf{3}^-$, along with plots of the total spin density (contour value 0.005). [Original in colour]

geometry around the iron(II) ion. The important structural features of the coordination sphere around the metal centre are well reproduced by the calculations, with C-C, C-N, and Fe-C bond distances within ±0.01 Å of their crystallographic counterparts. The Fe-N distances (2.20 Å) are overestimated by ∼0.04 Å compared to their crystallographic counterparts, errors that are typical of calculations with

Table 2.1: Selected optimised bond lengths (Å) and angles (°) for $\mathbf{3^0}$ and $\mathbf{3^-}$. Experimental data are given for comparison. For the computed structures the expectation value of the square of the total spin angular momentum operator ($\langle S^2 \rangle$) and Mulliken spin populations (ρ) on the iron centre and the 2,2′-bpy ligand are also given.

Parameter	**3** (exp.)	$\mathbf{3^0}$	$\mathbf{3^-}$ (exp.)	$^4\mathbf{3^-}$	$^6\mathbf{3^-}$
Fe(1)-N(1)	2.156(2)	2.20	2.090(15)	2.13	2.18
Fe(1)-N(2)	2.154(2)	2.20	2.084(15)	2.13	2.18
Fe(1)-C(11)	2.087(2)	2.09	2.103(17)	2.14	2.14
Fe(1)-C(21)	2.083(2)	2.09	2.095(16)	2.14	2.14
C(5)-C(6)	1.481(3)	1.48	1.418(3)	1.43	1.43
N(1)-Fe(1)-N(2)	75.14(16)	74.0	77.00(6)	76.3	75.9
N(1)-Fe(1)-C(11)	95.54(7)	100.5	109.53(6)	104.7	104.0
N(1)-Fe(1)-C(21)	122.34(7)	125.8	119.99(6)	123.0	123.1
N(2)-Fe(1)-C(11)	122.31(8)	125.5	124.32(6)	123.0	123.1
N(2)-Fe(1)-C(21)	104.04(7)	99.9	108.35(6)	103.8	103.0
C(11)-Fe(1)-C(22)	126.74(8)	123.2	113.56(6)	119.5	120.8
ϕ^a	70.2	67.5	78.6	73.8	73.0
ρ Fe/2,2′-bpy		3.73		3.74/-0.86	3.79/1.07
$\langle S^2 \rangle$		6.05		4.62	8.78

[a]Defined as angle between the C(11)-Fe-C(21) and N(1)-Fe-N(2) planes.

the B3LYP functional. The calculated angle of 67.5° between the planes defined by atoms Fe(1), N(1), and N(2) and Fe(1), C(11), and C(21) is in excellent agreement with the experimental value (70.2°).

Detailed bond lengths of the 2,2′-bipyridine moiety in free as well as coordinated form in the neutral and anionic complexes discussed here are summarised in Table 2.2. The oxidation state of the metal in $\mathbf{3^0}$ renders the bipyridine neutral, and its bond lengths serve to validate that this is indeed the case, most notably the long bond length of 1.48 Å between the carbon bridge atoms.

Table 2.2: Bond lengths (Å) of the 2,2′-bipyridine moieties in 2,2′-bipyridine, the 2,2′-bipyridyl radical anion, and the optimised structures of $\mathbf{3^0}$, $^{\mathbf{4}}\mathbf{3}^-$ and $^{\mathbf{6}}\mathbf{3}^-$ as well as their experimental counterparts.

bond	2,2′-bpy	2,2′-bpy$^{\cdot-}$	**3** (exp.)	$\mathbf{3^0}$	$\mathbf{3}^-$ (exp.)	$^{\mathbf{4}}\mathbf{3}^-$	$^{\mathbf{6}}\mathbf{3}^-$
1	1.490(3)	1.430(av)	1.481(3)	1.48	1.418(3)	1.43	1.43
2	1.346(2)	1.389(av)	1.356(3)	1.35	1.385(2)	1.39	1.39
			1.347(3)		1.386(2)		
3	1.341(2)	1.337(av)	1.345(3)	1.34	1.354(3)	1.35	1.34
			1.342(3)		1.357(2)		
4	1.384(2)	1.376(av)	1.378(4)	1.39	1.371(3)	1.39	1.39
			1.385(4)		1.372(3)		
5	1.383(3)	1.404(av)	1.377(4)	1.40	1.400(4)	1.42	1.42
			1.383(5)		1.400(3)		
6	1.385(2)	1.364(av)	1.382(4)	1.39	1.352(4)	1.38	1.38
			1.384(4)		1.365(3)		
7	1.394(2)	1.428(av)	1.389(4)	1.40	1.420(3)	1.43	1.43
			1.395(4)		1.417(3)		

For the anionic complex $\mathbf{3}^-$, we have identified two distinct electronic states with tetrahedral geometry, a broken-symmetry quartet (M_S = 3/2), $^{\mathbf{4}}\mathbf{3}^-$, and the corresponding high-spin sextet, $^{\mathbf{6}}\mathbf{3}^-$, both of which contain localised electron distributions characteristic of iron(II) and 2,2′-bpy$^{\cdot-}$ groups (*vide infra*). The adiabatically excited sextet state was found to be 3.9 kcal mol^{-1} higher in energy than the corresponding broken-symmetry solution. Both $^{\mathbf{4}}\mathbf{3}^-$ and $^{\mathbf{6}}\mathbf{3}^-$ exhibit a distorted pseudo-tetrahedral coordination geometry around the iron(II) centre, similar to the neutral complex, with angles of 73.8° and 73.0° between the ligand planes for $^{\mathbf{4}}\mathbf{3}^-$ and $^{\mathbf{6}}\mathbf{3}^-$, respectively.

Occupation of the LUMO of 2,2′-bipyridyl upon reduction leads to a notable change in the C(5)-C(6) bond distance, which contracts from 1.48 Å in $\mathbf{3^0}$ to 1.43 Å in the anionic complex, irrespective of the chosen state (Table 2.2). The degree of contraction of this C-C bond is very similar to that observed in recent studies on the reduction of bipyridine to the corresponding anion and dianion.[186,218] Although the reduction event can primarily be viewed as being ligand-based, it still has a

significant impact on the iron coordination sphere. The most significant differences between the anionic structures and the neutral complex are apparent in the Fe-N distances, which are 0.02 Å and 0.07 Å more contracted in $^{6}\mathbf{3}^{-}$ and $^{4}\mathbf{3}^{-}$, respectively, and in the Fe-C bonds, which are somewhat longer in $\mathbf{3}^{-}$ (2.14 Å for both states) than $\mathbf{3^0}$ (2.09 Å). The latter structural changes is a consequence of the Fe-C σ antibonding character of the d_{xz} orbital which accepts electron density from the 2,2′-bpy π^* orbital in $\mathbf{3}^{-}$.

Finally, despite extensive efforts using various starting geometries and initial guess densities with different degrees of spin polarisation, we have been unable to locate an alternative stable minimum for $\mathbf{3}^{-}$ corresponding to the $[Fe^{I}$(2,2′-bipyridine)$(mes)_2]^{-}$ form. In addition to the two tetrahedral structures described above we have also modeled the iron centre in a square-planar ligand environment, in either the high-spin ($S_{Fe} = 3/2$) or low-spin ($S_{Fe} = 1/2$) state. However, in each case the optimisation afforded a square-planar geometry with an electronic structure featuring a ligand radical. Thus, the low-spin doublet state converged to a broken-symmetry state ($\langle S^2 \rangle = 1.71$) with antiferromagnetically coupled metal ($\rho_{Fe} = 2.13$) and ligand ($\rho_{bpy} = -0.97$) radical centres. Likewise, the high-spin state yielded the isoenergetic complementary state with ferromagnetically coupled centres ($S_{Fe} = 2.37$, $\rho_{bpy} = 0.84$). Both states, however, are destabilised by $\sim$6 kcal mol^{-1} compared to the local minimum $^{4}\mathbf{3}^{-}$. In order to test the robustness of the broken-symmetry solution of the latter complex, we have also performed complementary calculations on the tetrahedral geometry, employing a conventional unrestricted $S = 3/2$ spin state. The result was the same as above: the pure Kohn-Sham quartet state collapsed to the broken-symmetry solution, due to spontaneous symmetry-breaking during the optimisation, unambiguously recovering $^{4}\mathbf{3}^{-}$.

Electronic structure

Analysis of the electronic structure of $\mathbf{3^0}$ reveals an electronic distribution typical of a high-spin iron(II) ion, with a Mulliken spin density of 3.73 electrons on the metal and negligible elsewhere. In the anionic quartet state, $^{\mathbf{4}}\mathbf{3}^{-}$, the Mulliken spin density on the metal centre ($\rho_{\mathrm{Fe}} = 3.74$) is essentially unchanged from that in $\mathbf{3^0}$, diagnostic of a divalent iron, while an unpaired electron of opposite spin is now located on the bipyridyl ligand ($\rho_{\mathrm{bpy}} = -0.86$). Strong spin contamination is apparent from an $\langle S^2 \rangle$ value of 4.62 that greatly exceeds that of a pure quartet ($\langle S^2 \rangle = S(S+1) = 3.75$) and approaches the limit anticipated for completely localised antiferromagnetically coupled $S_{\mathrm{Fe}} = 2$ and $S_{\mathrm{bpy}} = 1/2$ radicals ($\langle S^2 \rangle = S(S+1)+1 = 4.75$). In the related sextet $S = 5/2$ state ($^{\mathbf{6}}\mathbf{3}^{-}$), the basic features of the structure and Mulliken spin populations are very similar to those in $^{\mathbf{4}}\mathbf{3}^{-}$, the major difference being that the unpaired electrons on the iron(II) centre and the 2,2′-bpy ligand are aligned parallel to each other. The isodensity surfaces obtained from the Mulliken spin populations shown in Figure 2.9 for all three complexes provide a nice visualisation of the constant spin density on the iron centre and the ligand-centred radical.[220]

Corresponding orbital analysis

Identifying the magnetic orbitals of unpaired spins within the set of canonical KS orbitals can be difficult sometimes, due to spin polarisation effects and strong mixing with other orbitals. A more unequivocal picture is obtained from the corresponding orbital transformation (COT) of Amos and Hall.[221–223] This procedure performs a unitary transformation of the spin-orbitals within each spin manifold such that the overlap between an individual orbital from the α-set with an orbital from the β-set is maximised, while leaving the BS determinant invariant. Thus, the

individual spin-orbitals are matched up into pairs of maximum similarity. However, the resulting schemes are purely qualitative, because information about orbital energies is lost. The MOs are reorganised into three groups: first, those with a spatial overlap of essentially unity ($S_{\mathrm{ab}} = 1$) correspond to doubly occupied closed-shell MOs. Secondly, those with overlaps substantially different from zero or unity ($0 < S_{\mathrm{ab}} < 1$), representing the valence orbitals of overlapping nonorthogonal magnetic orbitals of the BS determinant. Thirdly, those singly-occupied α-spin orbitals that are unmatched by β-spin orbitals ($S_{\mathrm{ab}} = 0$), corresponding to the SOMOs of the system. Qualitative MO diagrams derived from the corresponding orbitals of the three complexes discussed above are summarised in Figures 2.10-2.12. The corresponding orbital diagram for neutral complex $\mathbf{3^0}$ (Figure 2.10) clearly highlights the high-spin quintet configuration at the iron(II) centre ($S_{\mathrm{Fe}} = 2$). The spin-α components of all five metal-based d orbitals are occupied, as is the spin-β component of one ($\mathrm{d}_{x^2-y^2}$ in the coordinate system defined in Figure 2.10), fully consistent with the Mulliken spin density ($\rho_{\mathrm{Fe}} = 3.73$). For the doubly occupied $\mathrm{d}_{x^2-y^2}$ orbital the overlap $S_{\mathrm{ab}} = 1$, while for the four SOMOs the overlap $S_{\mathrm{ab}} = 0$. Turning to the anion, corresponding orbitals for $^{\mathbf{4}}\mathbf{3}^-$ are summarised in Figure 2.11. The occupation of the spin-α and spin-β components of the five metal-based d orbitals is similar to the one in $\mathbf{3^0}$, indicating that the local high-spin d^6 configuration on iron(II) has been conserved. In contrast, only the spin-β component of the 2,2′-bpy LUMO is occupied, having 91% ligand character. The spatial overlaps between corresponding spin-α and spin-β orbitals are zero (SOMOs) and unity ($\mathrm{d}_{x^2-y^2}$), except for the d_{xz} / bpy LUMO pair where $S_{\mathrm{ab}} = 0.39$. The deviation from zero is characteristic of antiferromagnetic coupling, and arises from the tails on the ligand and metal in the spin-α and spin-β components shown in Figure 2.11, respectively. The spatial overlap for the nonorthogonal magnetic orbitals in $^{\mathbf{4}}\mathbf{3}^-$ can be compared

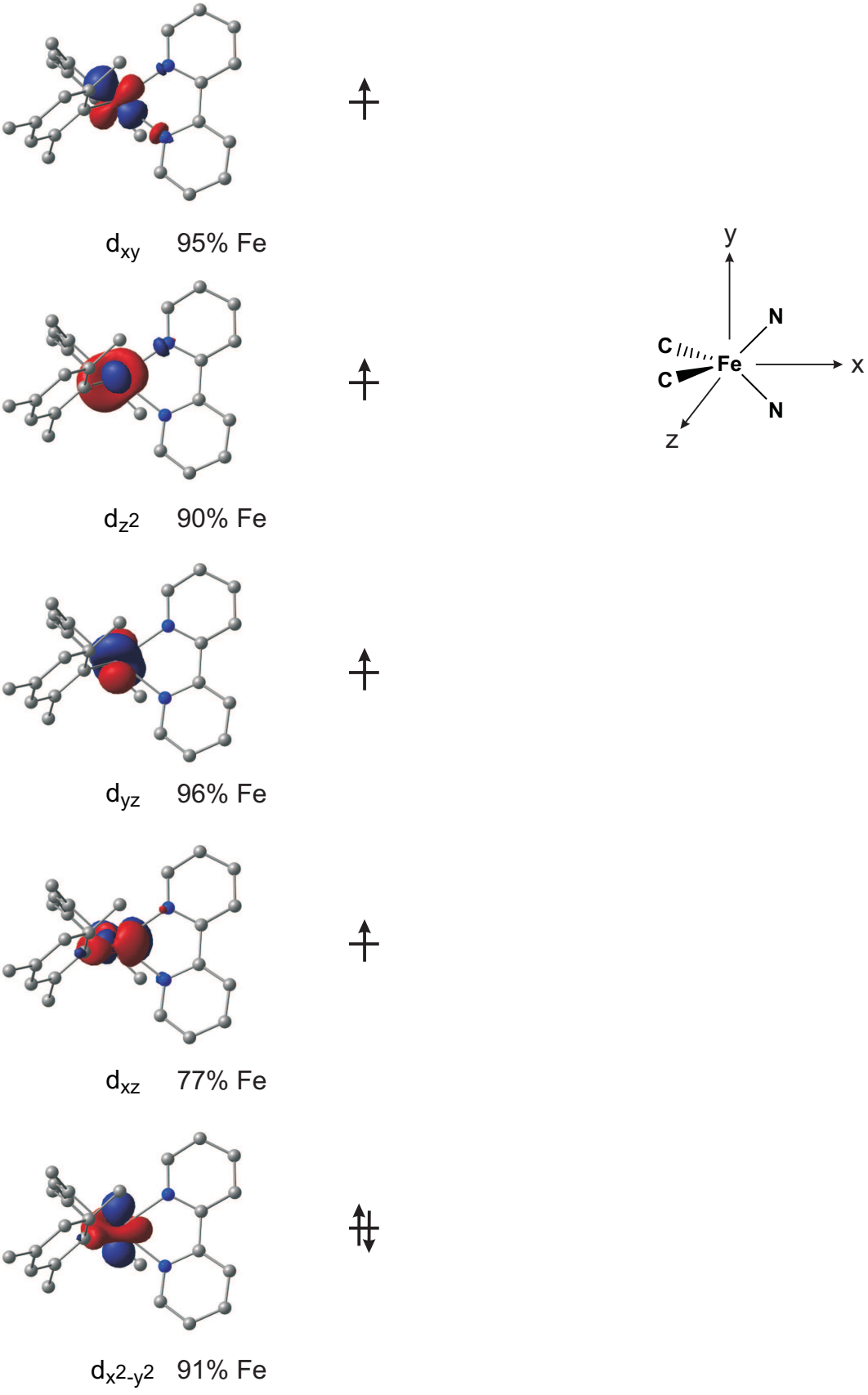

Figure 2.10: Qualitative MO diagram for complex $\mathbf{3^0}$. [Original in colour]

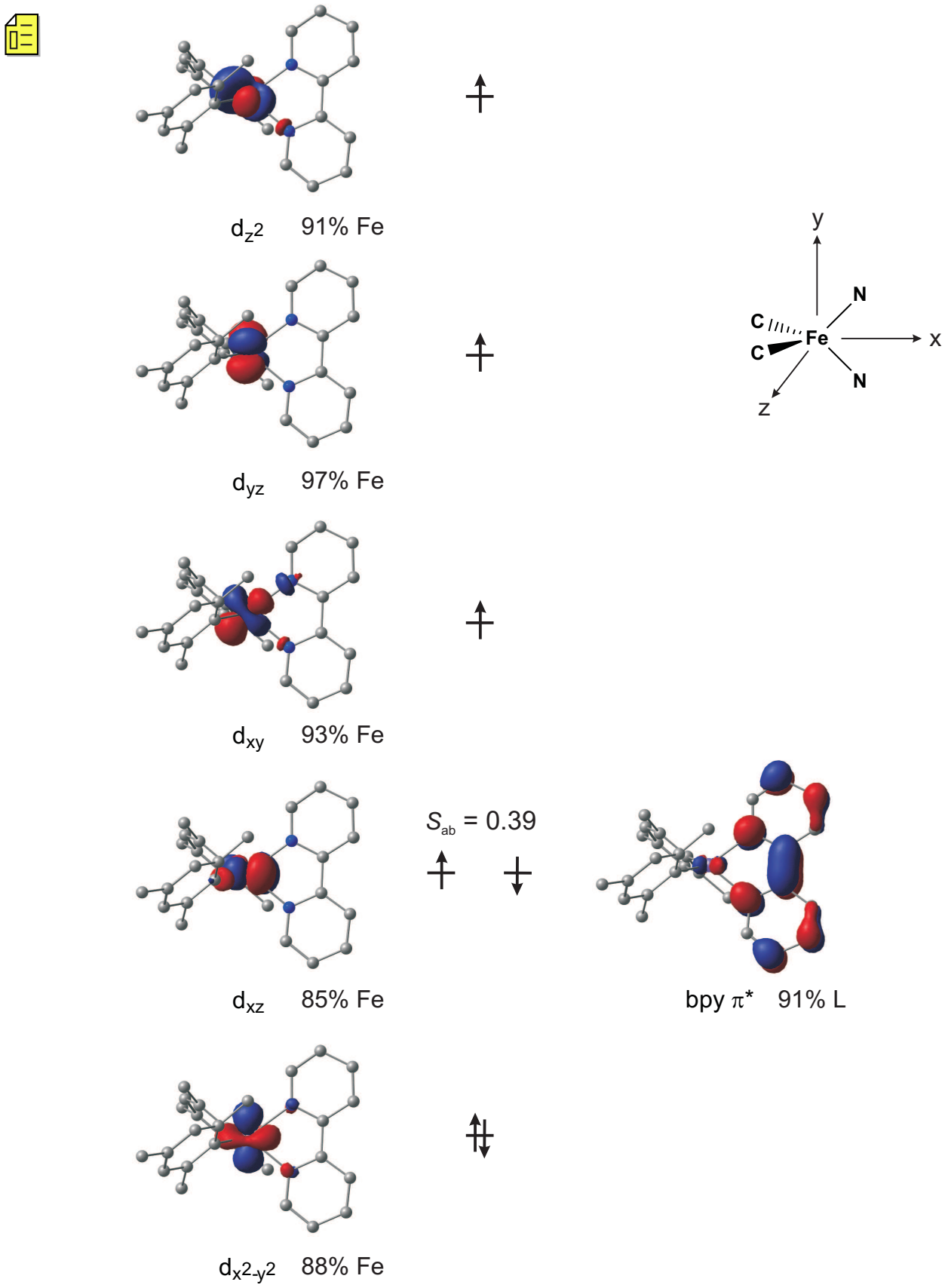

Figure 2.11: Qualitative MO diagram for complex $^{4}\mathbf{3}^{-}$. [Original in colour]

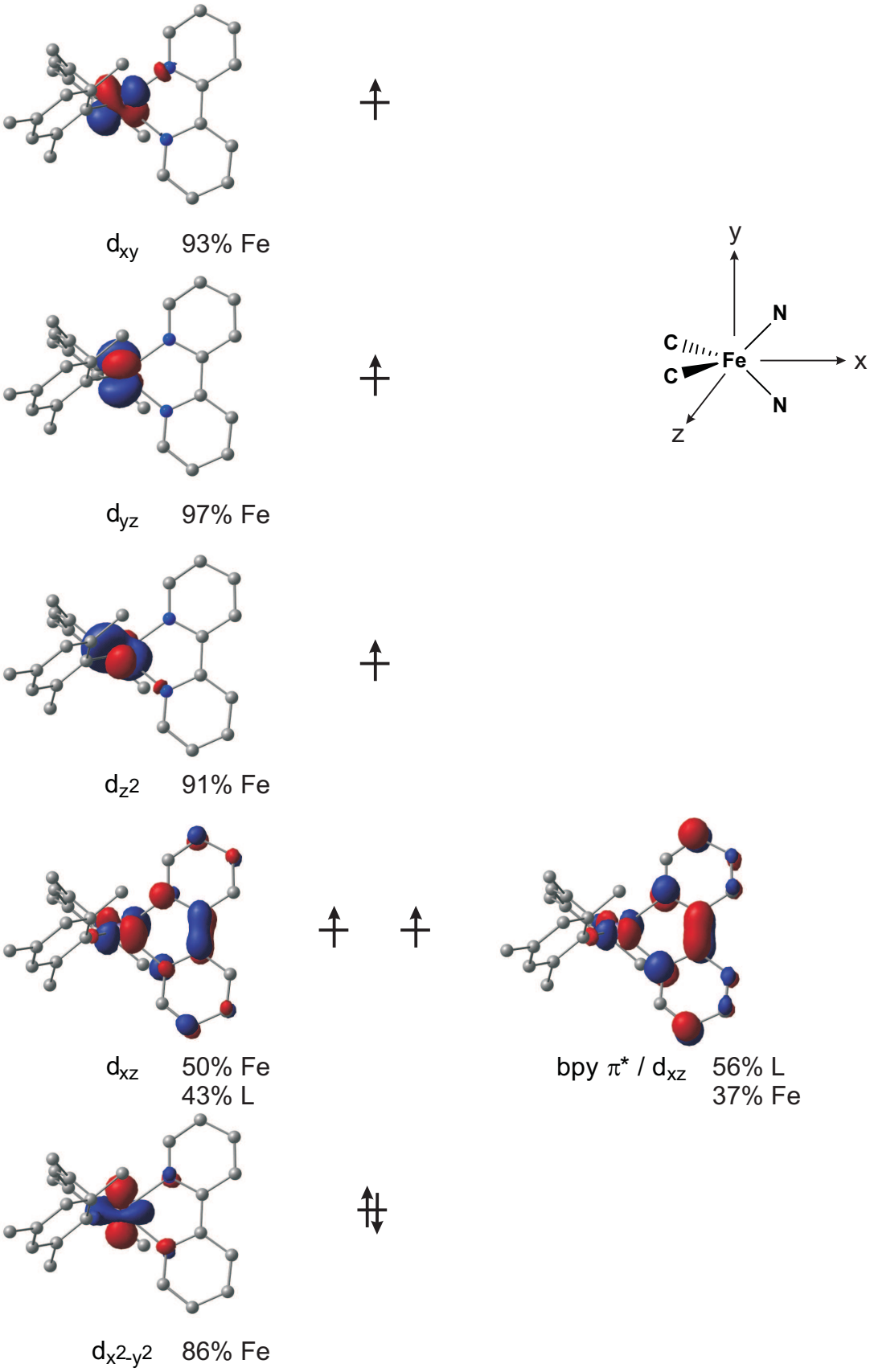

Figure 2.12: Qualitative MO diagram for complex $^{6}\mathbf{3}^{-}$. [Original in colour]

to the ones found for two related iron(II) complexes with $M_S = 3/2$ electronic ground states, ($^{\mathrm{Me}}$PDI)FeCl with $S_{\mathrm{ab}} = 0.41$,[224] and ($^{i\mathrm{Pr}}$PDI)Fe(CH_2CMe_3) with $S_{\mathrm{ab}} = 0.47$.[225] The 'diradical' character of the BS solution can be related to the overlap integral between the two magnetic orbitals through $R_{\mathrm{BS}} = 100(1 + |S_{\mathrm{ab}}|)(1 - |S_{\mathrm{ab}}|)$,[223] thus a value of 0.39 maps onto 85% diradical character.

The situation in $^{\mathbf{6}}\mathbf{3}^-$ is reminiscent of the quartet state, with the difference that the π^* orbital of bpy is now occupied by an electron of α-spin, mixing more strongly with the d_{xz} orbital, a situation typical for a high-spin state. Both electronic structures are characteristic of a non-innocent bipyridine ligand (in line with the observed spin densities), and account for the structural changes induced into the ligand upon reduction. The bonding nature of the orbital interaction between the bpy LUMO and the d_{xz} on Fe in $^{\mathbf{4}}\mathbf{3}^-$ results in a more contracted Fe-N bond length, compared to $^{\mathbf{6}}\mathbf{3}^-$, where this interaction is antibonding.

The $\langle S^2 \rangle$ value (4.62) for $^{\mathbf{4}}\mathbf{3}^-$ is very close to the theoretical value of 4.75, obtained with Equation 1.46 (Chapter 1). According to Dai and Whangbo,[226] the BS state for a spin dimer with 4 unpaired spins ($M = 4$) at one centre and 1 unpaired spin ($N = 1$) on the other can be decomposed in terms of $|S\, M_S\rangle$ eigenstates as

$$|\mathrm{BS}\rangle = \sqrt{\frac{4}{5}}\left|\frac{3}{2}\,\frac{3}{2}\right\rangle + \sqrt{\frac{1}{5}}\left|\frac{5}{2}\,\frac{3}{2}\right\rangle$$

With the calculated energy separation of the BS and the HS states at hand, the exchange coupling parameter J can be estimated. In terms of the phenomenological spin Hamiltonian $\hat{H} = -2J\hat{S}_1 \cdot \hat{S}_1$ it can be demonstrated[227] that for a spin dimer with M and N unpaired spins at site one and two, respectively, the exchange parameter is given by

$$J = -\frac{E_{\mathrm{HS}} - E_{\mathrm{BS}}}{MN}$$

A modification to the above equation has been introduced by Yamaguchi and co-workers,[228] resulting in the following expression

$$J = -\frac{E_{\mathrm{HS}} - E_{\mathrm{BS}}}{\langle S^2 \rangle_{\mathrm{HS}} - \langle S^2 \rangle_{\mathrm{BS}}}$$

in which the expectation values of the squared total spin angular momentum operator appear in the denominator. The Yamaguchi approach has the advantage of being valid over the whole range of coupling strengths, and will be used here. With the values obtained from the optimisation of the HS and BS states of **3**$^-$ ($\Delta E_{\mathrm{HS-BS}}$ = 3.9 kcal mol^{-1}, $\langle S^2 \rangle_{\mathrm{HS}} = 8.78$ and $\langle S^2 \rangle_{\mathrm{BS}} = 4.62$) we obtain J = -328 cm^{-1}. The energy separation between the adjacent sextet and (pure) quartet eigenstate can be calculated from Landé's interval rule[229]

$$E(S) - E(S-1) = -J[S(S+1) - (S-1)S] = -2SJ$$

Using J = -328 cm^{-1} from above, the splitting becomes E(5/2) - E(3/2) = 1640 cm^{-1}, giving rise to the corresponding Heisenberg spin ladder schematically shown in Figure 2.13.

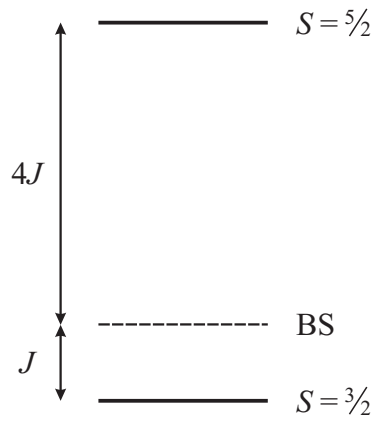

Figure 2.13: The Heisenberg spin ladder indicating the position of the BS state.

The value of J indicates that the exchange coupling is antiferromagnetic, but is not as strong as in related ferrous complexes of α-diimine and iminopyridine radicals studied by Wieghardt and co-workers, where values lie between -440 and -630 cm^{-1}.[224,230] The rather weaker coupling in $\mathbf{3}^-$ probably has the same origins as the elongation of the Fe-C bonds noted above: the key metal-based d_{xz} orbital is also antibonding with respect to the very strong σ-donor mesityl groups, and so exchange coupling and Fe-C bonding are antagonistic.

With the best fit Heisenberg exchange constant of -46.2 cm^{-1} (Figure 2.14), the sextet state lies $\sim$250 cm^{-1} ($5J$) above the ground state quartet and is significantly populated at higher temperatures. In contrast, the computed value of -328 cm^{-1} suggests that the sextet should remain unpopulated even at the highest accessible temperatures. From our point of view it seems therefore unlikely that the

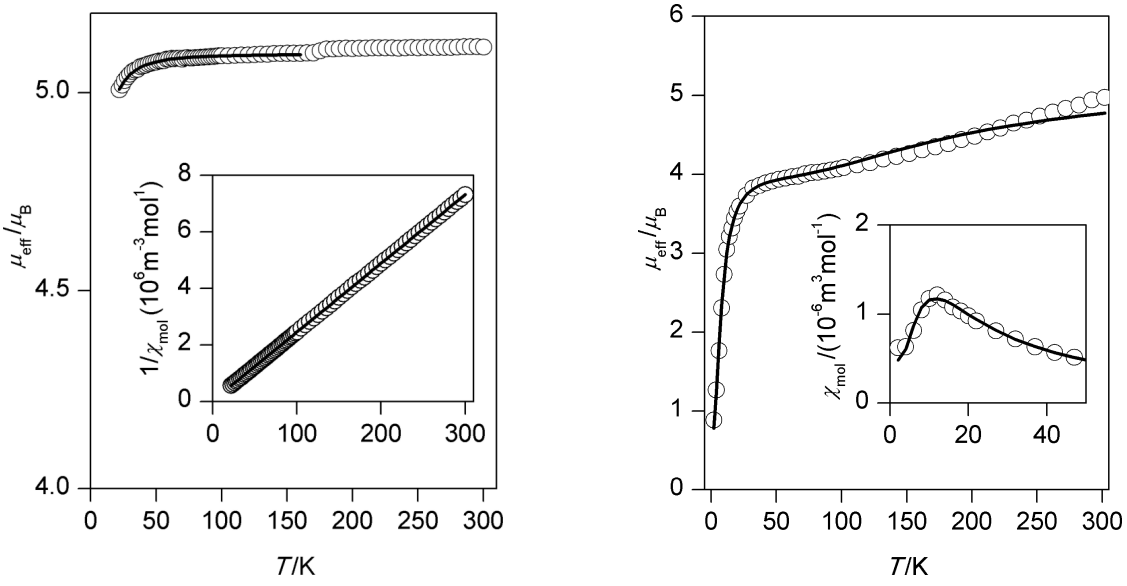

(a) neutral (b) anion

Figure 2.14: Temperature dependence of the effective magnetic moment, μ_{eff}. (a) **3**, (2–300 K). Inset: The temperature dependence of $1/\chi_{\text{mol}}$ (the full line corresponds to a Curie-Weiss fit of the data between 20 and 300 K). (b) $\mathbf{3}^-$, (2–302 K). Inset: low-temperature region of χ_{mol}. Circles, experimental points; lines, calculated data using $J = -46.2\,\text{cm}^{-1}$, $D_{\text{Fe}} = -10.6\,\text{cm}^{-1}$, $g_{\text{Fe}} = 2.05$.

increasing magnetic moment in the anionic complex can be explained with a population of the excited state at elevated temperatures. It is possible that this discrepancy reflects the limitations of the theoretical method,[‡] but it is difficult to calibrate the methodology simply because in the majority of related systems only the ground state is occupied over the temperature range of the experiment, affording only a lower limit to $|J|$.[140] In one of the few cases where the measured μ_{eff} does show temperature dependence (a cobalt(II) complex), the apparent population of the excited state is similarly inconsistent with the large computed J of -794 cm^{-1},[139] suggesting that DFT may indeed systematically overestimate the magnitude of the exchange coupling in this class of system. It should be noted, however, that it is also possible to fit the susceptibility of $\mathbf{3}^-$ to a spin Hamiltonian involving an isolated $S = 3/2$ state (by effectively assuming an infinite J), in which case the rise in χ_{mol} at high temperatures can only be reproduced by invoking a large temperature independent contribution. Despite the discrepancy in computed and experimental values of J for $\mathbf{3}^-$, it is clear that both approaches are consistent in suggesting that the exchange coupling is considerably weaker in $\mathbf{3}^-$ than in comparable systems where strong σ-donor ligands such as mesityl are absent.[224,230]

2.3.3 ^{57}Fe Mössbauer spectroscopy

Mössbauer spectroscopy is a technique which relies on the principle of recoilless nuclear resonant absorption and emission of gamma photons in the solid state. Associated with both these processes are energy level transitions in the atomic nucleus. The energy levels of the nucleus themselves respond to the surrounding environment, both electronic and magnetic in nature. Since such a fingerprint of

[‡]Strictly speaking the Heisenberg spin Hamiltonian formalism is only applicable to orbitally non-degenerate systems, where the orbital angular momentum is quenched. We note this as a possible source of error.

the nuclear energy levels can provide information about the atom's local chemical environment in which it is embedded,[231,232] Mössbauer spectroscopy is widely used to explore the interactions of the probe nucleus with its surrounding.[232–235]

Fundamentals of the Mössbauer effect

The purpose of the following section is to familiarise the reader with the most important aspects of Mössbauer spectroscopy, and also to give an introduction to the computational approach for calculating Mössbauer parameters, which will be of use in the following discussion. A schematic representation of the hyperfine interactions observed in the Mössbauer experiment and their origin[232] is shown in Figure 2.15. The isomer shift (2.15a) arises due to the interaction of the spherical nucleus with a small but discrete volume and the charge density of the s-electrons.

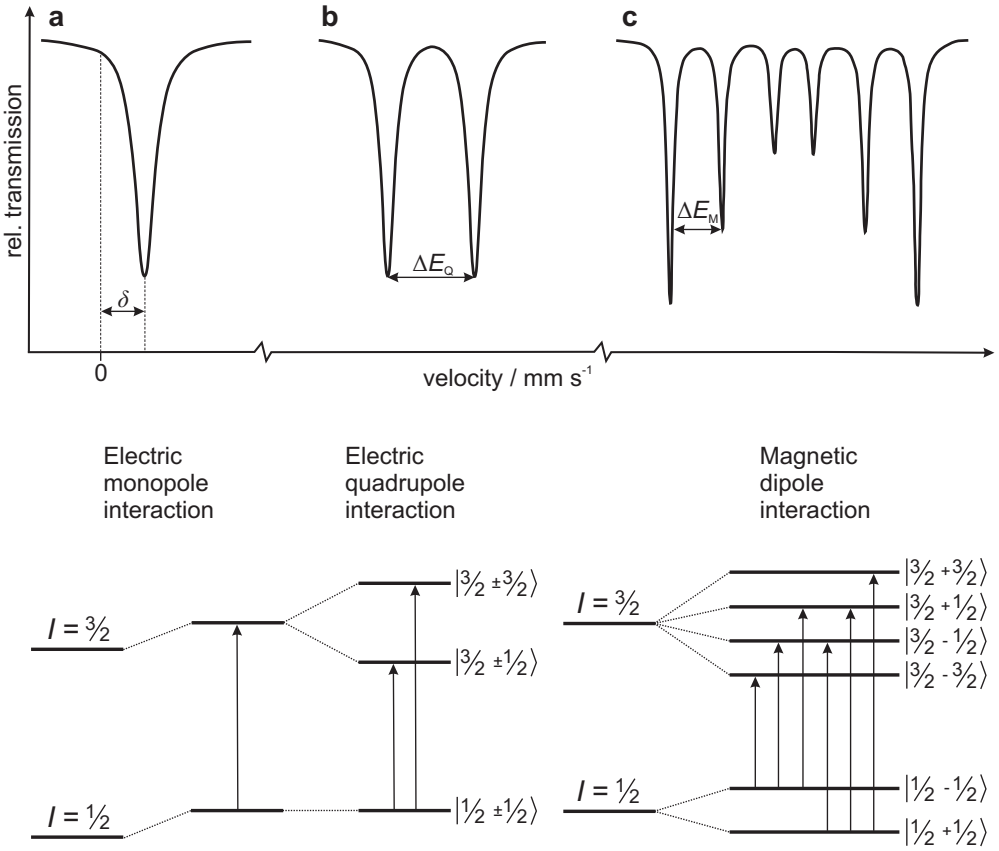

Figure 2.15: Observed hyperfine interactions in a Mössbauer spectrum. Upper panel: schematic representation of the spectrum. Lower panel: involved energy levels. (a) Isomer shift; (b) electric quadrupole splitting; (c) magnetic dipole interaction.

The non-vanishing probability of an s-electron penetrating the nucleus and spending a fraction of time inside it gives rise to an electronic monopole interaction between the nucleus and the electrons at the nuclear site, which alters the nuclear energy levels. The total isomeric shift is expressed as

$$\delta = \frac{4}{5}\pi Z e^2 R^2 \left(\frac{\delta R}{R}\right)\{|\psi_a(0)|^2 - |\psi_s(0)|^2\}$$

where Z is the nuclear charge of the absorber, e the elementary charge, R the nuclear radius, and $\delta R = R_e - R_g$ is the change of the nuclear radius in going from the excited to the ground state. The electronic term $\{|\psi_a(0)|^2 - |\psi_s(0)|^2\}$ is a measure of the electronic density at the absorbing nucleus relative to a given source. Because the nuclear factor is constant for a given Mössbauer atom, the isomer shift is thus only dependent on the differences of the electron densities between absorber and source. The isomer shift, always given relative to a standard, is therefore a sensitive measure for the oxidation and spin state of the probe atom, as well as its bond properties (covalency, ionicity).

Nuclei with a non-spherical charge distribution (requiring $I > 1/2$) possess a nuclear quadrupole moment. In the presence of an asymmetric electronic charge distribution the electric interaction between the quadrupole of the nucleus and the electric field gradient at the nuclear site splits the nuclear energy levels (Figure 2.15b). In the absence of a magnetic interaction the quadrupole splitting results in a doublet in which the two peaks are separated by

$$\Delta E_Q = \frac{1}{2} e Q V_{zz} \left(1 + \frac{\eta^2}{3}\right)^{1/2}$$

where $Q(^{57}\mathrm{Fe})$ is the quadrupole moment of the Mössbauer nucleus and e the proton charge. In the above equation the electric field gradient is described by two

independent parameters, commonly chosen as V_{zz} and the asymmetry parameter $\eta = (V_{xx} - V_{yy})/V_{zz}$, where the V_{ii} $(i = x, y, z)$ are the principal components of the electric field gradient tensor with respect to a defined axis. The quadrupole splitting is highly responsive towards changes in the chemical environment that determine the electric field gradient at the Mössbauer nucleus. This spectral feature thus holds information about the (local) molecular symmetry of the compound as well as bonding properties. Finally, in the presence of a magnetic field (either arising from the electronic environment or from an external magnet) the nuclear spin moment (requiring $I > 0$) experiences a dipolar interaction with the magnetic field. This nuclear Zeeman effect causes a splitting of the nuclear energy states into discrete sublevels $|I\ m_I\rangle$. Due to selection rules ($\Delta m_I = 0, \pm 1$ and $\Delta I = \pm 1$) six transitions are observed, typically having intensities in a 3:2:1:1:2:3 ratio (Figure 2.15c). The magnetic splitting ΔE_M holds information about local magnetic fields at the nucleus.

From a theoretical point of view the two main parameters that can be extracted for a given probe atom in the absence of a magnetic field are the quadrupole-splitting (ΔE_{Q}) and the isomer shift (δ).[209,236–238] The latter Mössbauer parameter is linearly related to the electron density at the nucleus, and the above expression for δ can be cast into the simply form

$$\delta = \alpha(\rho_0 - C) + \beta$$

The regression coefficients α and β are determined by a calibration procedure, in which calculated electron densities are plotted versus experimental isomer shifts. The constant C has been introduced out of convenience. Suitable sets of parameters yielding reliable results for a number of density functionals have been proposed by Neese and co-workers.[239,240]

On the other hand, the quadrupole splitting can be calculated directly from the components of the electric field gradient tensor (see ΔE_Q equation above), which itself is obtained as an expectation value over the ground state electron density. However, it is found that the quality of DFT-predicted quadrupole splittings varies somewhat, and errors of 0.3 to 1.0 $\mathrm{mm\,s^{-1}}$ are common.[237] To complicate things, the computed quadrupole splitting is very sensitive to the chemical environment such as counter ions.[119] Nonetheless, the sign of the computed quadrupole splitting is usually in agreement with experiment, and therefore at least allows for a qualitative interpretation of the results.

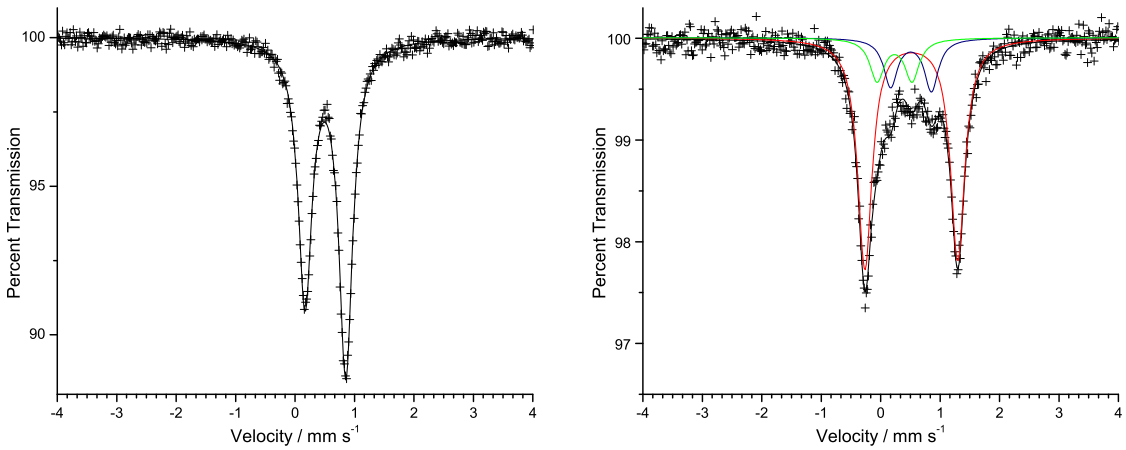

(a) neutral (b) anion

Figure 2.16: ^{57}Fe Mössbauer spectra of **3** (a) and $\mathbf{3}^-$ (b) obtained at 85 K. The red line corresponds to the reduced complex (major component), the blue line to the neutral complex and the green line to a paramagnetic high-spin Fe^{III} impurity.

^{57}Fe Mössbauer spectra of complexes **3** and $\mathbf{3}^-$ have been recorded between 85 K and 295 K, and the 85 K spectra are shown in Figure 2.16. Each spectrum exhibits a major symmetric quadrupole doublet,[§] with $\delta = 0.511\ \mathrm{mm\,s^{-1}}$, $\Delta E_Q = 0.69\ \mathrm{mm\,s^{-1}}$ and $\delta = 0.516\ \mathrm{mm\,s^{-1}}$, $\Delta E_Q = 1.56\ \mathrm{mm\,s^{-1}}$ at 85 K for **3** and $\mathbf{3}^-$,

[§]The difference in the areas of the two components of the observed quadrupole doublet is a result of texture in the absorber that results from the needle-like morphology of the crystals. No attempt has been made to remove this texture because of the high air-sensivity of the complexes and, as a consequence, the spectra have been fit with a quadrupole doublet with a single line width but with different component areas.

respectively. At higher temperature (295 K) the isomer shifts reduce to 0.406 (**3**) and 0.408 $\mathrm{mm\,s^{-1}}$ ($\mathbf{3}^{-}$), while the quadrupole splittings are left unaffected. It should be noted, that for $\mathbf{3}^{-}$ several minor doublets are observed in the spectrum, due to impurities resulting from the air- and moisture-sensitivity of the compound (see the figure caption for details). In contrast to the rather similar isomer shifts of the two complexes, their quadrupole splittings are very different, increasing by a factor of ∼2 to 1.56 $\mathrm{mm\,s^{-1}}$ at 85 K.

Calculated ^{57}Fe Mössbauer parameters

The principal reason for measuring the Mössbauer spectra of $\mathbf{3}^{-}$ was to determine whether the reduction of **3** to yield $\mathbf{3}^{-}$ led to a reduction either of the iron(II) ion or of the bipyridyl ligand, to form a $\mathrm{bpy}^{\bullet -}$ radical anion,[186] and the answer appears to be unambiguous. The isomer shifts of the iron(II) ion in $\mathbf{3}^{-}$ are very similar to those observed in sample **3**, an observation that is apparently inconsistent with a change in metal oxidation state, eliminating the $[\mathrm{Fe^{I}}(2,2'\text{-bpy})(\mathrm{mes})_2]^{-}$ valence tautomer. To further validate this conclusion we have computed the Mössbauer spectral hyperfine parameters (δ and ΔE_{Q}) for $\mathbf{3^0}$ and $\mathbf{3}^{-}$, where our electronic structure analysis is unambiguous in confirming the iron(II) oxidation state in both cases. Table 2.3 compares calculated electron densities at the iron nucleus (ρ_0), isomer shifts (δ) and quadrupole splittings (ΔE_{Q}) of complex $\mathbf{3^0}$, $^{\mathbf{6}}\mathbf{3}^{-}$ and $^{\mathbf{4}}\mathbf{3}^{-}$ for various DFT functionals (B3LYP, BP86, TPSS, TPSSh) in conjunction with both optimised and crystallographic geometries reported in Table 2.3.

Two different sets of fit parameters were used, according to the protocols reported by Sinnecker et al. (A),[239] and Römelt et al. (B).[240] It is apparent that for both the neutral and anionic complex the hybrid density functionals yield isomer shifts closer to the corresponding experimental values, while the pure functionals notably

Table 2.3: Experimental and calculated MB parameters, ρ_0 ($e\,au^{-3}$), δ ($mm\,s^{-1}$) and ΔE_Q ($mm\,s^{-1}$) for complexes $\mathbf{3^0}$, $^6\mathbf{3}^-$ and $^4\mathbf{3}^-$. $\delta\,[mm\,s^{-1}] = \alpha(\rho_0 - C) + \beta$, fitting parameters A taken from Sinnecker et al.,[239] and B from Römelt et al.[240]

		Crystal Structure			Optimised Structure		
	Fit	ρ_0	δ^a	ΔE_Q	ρ_0	δ	ΔE_Q
3 (exp.)			0.511[b]	0.69[b]			
			0.406[c]	0.62[c]			
$\mathbf{3}^-$ (exp.)			0.516[b]	1.56[b]			
			0.408[c]	1.36[c]			
$\mathbf{3^0}$ (calc.)							
B3LYP	A	11816.864	0.361	1.075	11816.833	0.372	0.965
B3LYP	A	11816.958[d]	0.326[d]	2.154[d]			
B3LYP	B	11816.864	0.340	1.075	11816.833	0.351	0.965
BP86	B	11828.103	0.222	-0.916	11828.029	0.254	0.968
TPSS	B	11821.649	0.250	0.923	11821.584	0.277	1.010
TPSSh	B	11820.111	0.328	1.068	11820.072	0.343	0.962
$^6\mathbf{3}^-$ (calc.)							
B3LYP	A	11816.754	0.401	2.075	11816.529	0.484	1.592
B3LYP	B	11816.754	0.380	2.075	11816.529	0.462	1.592
BP86	B	11828.039	0.249	-1.864	11827.736	0.378	1.406
TPSS	B	11821.584	0.277	1.781	11821.311	0.392	1.355
TPSSh	B	11820.016	0.364	1.904	11819.767	0.458	1.491
$^4\mathbf{3}^-$ (calc.)							
B3LYP	A	11816.770	0.396	2.050	11816.565	0.471	1.714
B3LYP	A	11816.732[e]	0.410[e]	1.060[e]			
B3LYP	B	11816.770	0.374	2.050	11816.565	0.449	1.714
BP86	B	11827.966	0.281	2.064	11827.757	0.369	1.509
TPSS	B	11821.552	0.291	1.831	11821.336	0.382	1.401
TPSSh	B	11820.031	0.358	1.884	11819.815	0.440	1.550

[a]Experimental isomer shifts are given relative to 295 K α-iron powder.
[b]Measured at 85 K
[c]Measured at 295 K
[d]Mapping the neutral $S = 2$ state onto the X-ray structure of the anionic complex $\mathbf{3}^-$.
[e]Mapping the anionic $M_S = 3/2$ state onto the X-ray structure of the neutral complex **3**.

underestimate the isomer shift. Moreover, for the anion the results indicate that the isomer shift is largely independent of the chosen electronic configuration (broken-symmetry quartet or high-spin sextet). This is perhaps unsurprising owing to the

fact that the isomer shift is mostly dependent on the immediate electron density at the iron centre, which remains unaffected by the spin-orientation of the electron centred at the bpy ligand. Despite the better performance of B3LYP with respect to prediction of (low-temperature) isomer shifts, the values obtained still remain at the lower end of expected accuracy. Published calibrations yield standard deviations of the order $0.1\,\mathrm{mm\,s^{-1}}$ for isomer shifts.[209,239,240] We conclude that the discrepancy is rather a result of the fitting process than of complications with the electronic structures of both $\mathbf{3^0}$ and $^{\mathbf{4}}\mathbf{3}^-$, which have been unambiguously assigned in the previous section.

Focussing on the optimised structures for the moment, the isomer shift of the anion in each electronic state ($\sim$0.48 $\mathrm{mm\,s^{-1}}$) agrees very well with the experimental low-temperature value ($0.52\,\mathrm{mm\,s^{-1}}$). In contrast, the neutral complex deviates by as much as $0.14\,\mathrm{mm\,s^{-1}}$ from the experimental counterpart at 85 K. Thus in the neutral complex ρ_0 is notably overestimated. This is a direct effect from the presence of the strong σ-donor groups. The Fe-C bond lengths in **3** are almost perfectly reproduced in the optimised structure (Table 2.1), while the same bond length is overestimated by 0.04 Å in $^{\mathbf{4}}\mathbf{3}^-$. Inaccuracies in bond lengths computed by DFT optimisations are a cause of discrepancy between theory and experiment, and the importance of the geometry for calculating MB parameters has been discussed by several authors.[209,241,242] We assume that the high accuracy achieved for the anionic complex is due to the fact that the difference between calculated and observed bond parameters is in the same range typically obtained for the calibration set. On the other hand, the neutral complex shows only a very small deviation from the crystal structure, and therefore can be viewed as an outlier with respect to the training set. In order to gain more insight into the influence of the mesityl groups on the electron density in both the neutral and anionic complex,

we have calculated values of ρ_0 while varying the Fe-C bond distances in $\mathbf{3^0}$ and $^{\mathbf{4}}\mathbf{3}^-$ in the range 2.09-2.20 Å, without further optimisation. The result is plotted in Figure 2.17. The electron density at the iron nucleus reveals a pronounced linear correlation with the Fe-C bond distance, and increases dramatically for decreasing Fe-C bond lengths. Importantly, the trend for $\mathbf{3^0}$ is almost perfectly paralleled by $^{\mathbf{4}}\mathbf{3}^-$. Therefore, when using optimised structures for the calculation of δ, an error is automatically introduced, because the electron densities correspond to different regions of the PES of the Fe-C bond stretch. In contrast, isomer shifts obtained from projecting the corresponding electronic states onto the crystal structures are much more consistent with experiment, because inaccuracies from the optimisation are absent in these structures.

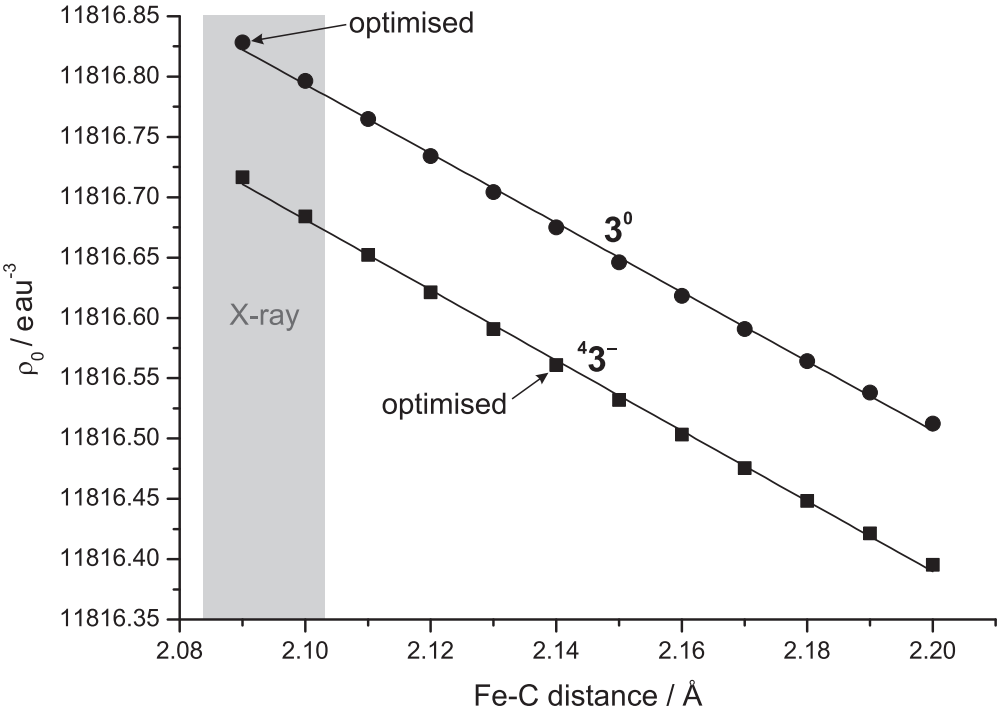

Figure 2.17: Dependency of the calculated electron densities ρ_0 at the iron nucleus on the Fe-C bond distance for $\mathbf{3^0}$ and $^{\mathbf{4}}\mathbf{3}^-$. Each point was calculated at partially optimised geometries, i.e. only the Fe-C distances were varied. The shaded area highlights the range of experimental Fe-C bond lengths from the X-ray structures, while bond lengths of the fully optimised geometries are indicated by arrows.

The crystal structures reveal that the Fe-C bond lengths remain almost constant at around 2.09 Å in both **3** and $\mathbf{3}^{-}$. The computed electron densities, ρ_0, at the ^{57}Fe nucleus for $\mathbf{3^0}$ and $^{\mathbf{4}}\mathbf{3}^{-}$ using the crystal structure geometries in each case, are 11816.86 and 11816.77 electrons au^{-3}, respectively, corresponding to isomer shifts of 0.361 and 0.396 mm s^{-1} using the linear regression curve δ [mm s^{-1}]= $\alpha(\rho_0 - C) + \beta$ ($\alpha = -0.367 \pm 0.015$ au^3 mm s^{-1}, $\beta = 6.55 \pm 0.25$ mm s^{-1} and $C = 11800$ electrons a_0^{-3}) proposed by Sinnecker et al.[239] Within the error limits imposed by the calibration process, the computed values of δ for $\mathbf{3^0}$ and $^{\mathbf{4}}\mathbf{3}^{-}$ are consistent with the experimental (rt) data. Both isomer shifts are very similar in $\mathbf{3^0}$ and $^{\mathbf{4}}\mathbf{3}^{-}$, confirming that the oxidation state of the metal centre remains in the +II oxidation state after reduction. The calculated principal component, V_{zz}, and the asymmetry parameter, η, of the electric field gradient tensor are 0.6538 au, 0.278 and 1.2288 au, 0.413 for $\mathbf{3^0}$ and $^{\mathbf{4}}\mathbf{3}^{-}$, respectively. Using these values and the expression $\Delta E_{\mathrm{Q}} = {}^1\!/_2 eQV_{zz}(1+\eta^2/3)^{1/2}$, with a value of 0.16 barn for $Q(^{57}\mathrm{Fe})$ and a unit conversion of 1 au = 9.717×1021 V m^{-2} = 1.617 mm s^{-1}, the trend in ΔE_{Q} is also reproduced with encouraging accuracy: ΔE_{Q} increases by a factor of 2 from 1.08 mm s^{-1} in $\mathbf{3^0}$ to 2.05 mm s^{-1} in $^{\mathbf{4}}\mathbf{3}^{-}$ compared to experimental values of 0.69 and 1.56 mm s^{-1}, respectively.

In principle, the large quadrupole splitting in $^{\mathbf{4}}\mathbf{3}^{-}$ could arise from a more asymmetric arrangement of the primary coordination sphere, the presence of a strong π-donor 2,2′-bpy radical ligand, or a combination of the two. To distinguish these two distinct possibilities we have recomputed the Mössbauer hyperfine parameters of $\mathbf{3^0}$ using the geometry of $^{\mathbf{4}}\mathbf{3}^{-}$ and *vice versa*. At either geometry, the computed values of δ and ΔE_{Q} for the neutral and anionic species are almost indistinguishable, providing compelling evidence that the shifts in ΔE_{Q} from **3** to $\mathbf{3}^{-}$ are due to the apparently minor changes in geometry, and hence the σ framework (in par-

ticular the Fe-C bonds), and not directly to the presence or absence of an electron in the LUMO of the 2,2′-bpy ligand.

In summary, our DFT analysis of **3** and its one-electron reduced form $\mathbf{3}^{-}$ in combination with structural, magnetic and spectroscopic data has led to an unambiguous assignment of their electronic structures. The neutral complex **3** reveals a high-spin $S = 2$ iron centre embedded in a distorted tetrahedral ligand environment, a situation typically found for iron(II) bis(mesityl) compounds.[243–245] One-electron reduction of **3** yields $\mathbf{3}^{-}$, where the extra electron occupies a π^* antibonding ligand-based orbital. Antiferromagnetic coupling between the iron(II) centre and the 2,2′-bipyridyl radical anion gives rise to a $S = {}^{3}/_{2}$ ground state, and in this way formation of a Fe^{I} alkyl species, known to be relatively rare, is avoided.[225,246]

2.3.4 Further members of the series $[M(2,2'\text{-bpy})(mes)_2]^{0/-}$

After having discussed the example of $[Fe^{II}(2,2'\text{-bpy})(mes)_2]^{0/-}$ complexes in the previous section in detail, we can now proceed to examine further members of the series $M(2,2'\text{-bpy})(mes)_2$ and their anions, where M = Cr, Mn, Co, and Ni. Complexes of chromium, manganese, and nickel in both the neutral and reduced form have been isolated and crystals have proven to be of sufficient quality to allow for a structure determination. We have optimised the geometries of all of the above complexes in their indicated electronic states, which are summarised in Table 2.4 and Scheme 2.9 (the iron complexes are included for completeness).

Perhaps unsurprising, their chemical behaviour is very similar to that of their iron congeners. We therefore refrain from a detailed review of their geometries, but focus on trends and differences among the series instead. A summary of the important optimised bond metric and electronic parameters for the complexes discussed

Table 2.4: Numbering and electronic states of complexes $[M(2,2'\text{-bpy})(mes)_2]^{0/-}$.

	Complex	M_S		Complex	M_S
$\mathbf{1^0}$	$[Cr(2,2'\text{-bpy})(mes)_2]^0$	2	$\mathbf{4^0}$	$[Co(2,2'\text{-bpy})(mes)_2]^0$	3/2
$^{4}\mathbf{1}^-$	$[Cr(2,2'\text{-bpy})(mes)_2]^-$	3/2	$^{3}\mathbf{4}^-$	$[Co(2,2'\text{-bpy})(mes)_2]^-$	1
$^{6}\mathbf{1}^-$	$[Cr(2,2'\text{-bpy})(mes)_2]^-$	5/2	$^{5}\mathbf{4}^-$	$[Co(2,2'\text{-bpy})(mes)_2]^-$	2
$\mathbf{2^0}$	$[Mn(2,2'\text{-bpy})(mes)_2]^0$	5/2	$\mathbf{4^0_{sq}}$	$[Co(2,2'\text{-bpy})(mes)_2]^0$	1/2
$^{5}\mathbf{2}^-$	$[Mn(2,2'\text{-bpy})(mes)_2]^-$	2	$^{1}\mathbf{4}^-_{sq}$	$[Co(2,2'\text{-bpy})(mes)_2]^-$	0
$^{7}\mathbf{2}^-$	$[Mn(2,2'\text{-bpy})(mes)_2]^-$	3	$^{3}\mathbf{4}^-_{sq}$	$[Co(2,2'\text{-bpy})(mes)_2]^-$	1
$\mathbf{3^0}$	$[Fe(2,2'\text{-bpy})(mes)_2]^0$	2	$\mathbf{5^0}$	$[Ni(2,2'\text{-bpy})(mes)_2]^0$	0
$^{4}\mathbf{3}^-$	$[Fe(2,2'\text{-bpy})(mes)_2]^-$	3/2	$^{2}\mathbf{5}^-$	$[Ni(2,2'\text{-bpy})(mes)_2]^-$	1/2
$^{6}\mathbf{3}^-$	$[Fe(2,2'\text{-bpy})(mes)_2]^-$	5/2			

in this section is given in Table 2.5 (parameters for the iron congeners are included for comparison). Among the series, two different coordination geometries are found.

Scheme 2.9: Structural formulas of $[M(2,2'\text{-bpy})(mes)_2]^{0/-}$ complexes.

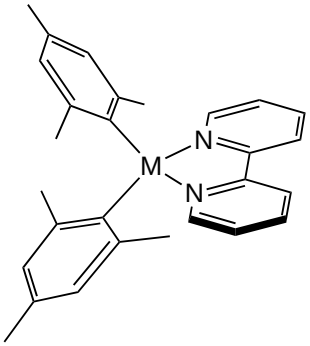

$[Fe^{II}(2,2'\text{-bpy})(mes)_2]^0$ $M_S = 2$
$[Mn^{II}(2,2'\text{-bpy})(mes)_2]^0$ $M_S = 5/2$

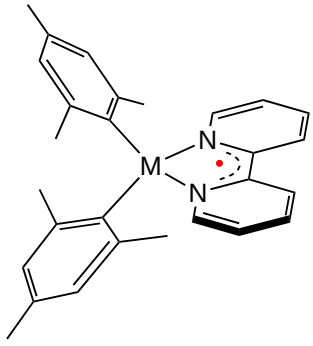

$[Fe^{II}(2,2'\text{-bpy}^{\bullet-})(mes)_2]^-$ $M_S = 3/2$
$[Mn^{II}(2,2'\text{-bpy}^{\bullet-})(mes)_2]^-$ $M_S = 2$

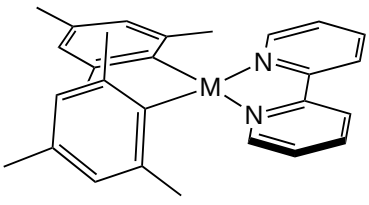

$[Cr^{II}(2,2'\text{-bpy})(mes)_2]^0$ $M_S = 2$
$[Co^{II}(2,2'\text{-bpy})(mes)_2]^0$ $M_S = 1/2$
$[Ni^{II}(2,2'\text{-bpy})(mes)_2]^0$ $M_S = 0$

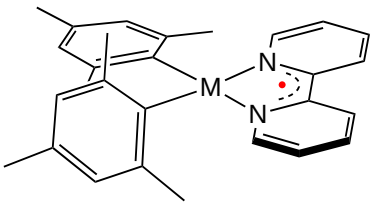

$[Cr^{II}(bpy^{\bullet-})(mes)_2]^-$ $M_S = 3/2$
$[Co^{II}(bpy^{\bullet-})(mes)_2]^-$ $M_S = 1$
$[Ni^{II}(bpy^{\bullet-})(mes)_2]^-$ $M_S = 1/2$

Table 2.5: Optimised geometric and electronic parameters for complexes **1**-**5**.

	Cr			Mn			Fe			Co						Ni	
	$\mathbf{1^0}$	$\mathbf{1^-}$		$\mathbf{2^0}$	$\mathbf{2^-}$		$\mathbf{3^0}$	$\mathbf{3^-}$		$\mathbf{4^0}$	$\mathbf{4^-}$		$\mathbf{4^0_{sq}}$	$\mathbf{4^-_{sq}}$		$\mathbf{5^0}$	$\mathbf{5^-}$
M_S[a]	2	3/2	5/2	5/2	2	3	2	3/2	5/2	3/2	1	2	1/2	0	1	0	1/2
$S_{\mathrm{M}}, S_{\mathrm{bpy}}$[b]	2, 0	2, 1/2		5/2, 0	5/2, 1/2		2, 0	2, 1/2		3/2, 0	3/2, 1/2		1/2, 0	1/2, 1/2		0, 0	0, 1/2
coord[c]	sqpl	sqpl	sqpl	tet	tet	tet	tet	tet	tet	tet	tet	tet	sqpl	sqpl	sqpl	sqpl	sqpl
M-N	2.19	2.14	2.17	2.22	2.19	2.24	2.20	2.13	2.18	2.12	2.07	2.12	2.04	2.03	2.02	2.01	1.99
M-C	2.12	2.17	2.16	2.13	2.20	2.20	2.09	2.14	2.14	2.04	2.09	2.09	1.96	1.98	1.98	1.93	1.95
C(5)-C(6)	1.48	1.43	1.43	1.48	1.43	1.43	1.48	1.43	1.43	1.48	1.43	1.43	1.48	1.43	1.43	1.48	1.43
ϕ[d] / °	18.9	20.1	20.0	63.9	76.0	75.9	67.5	73.8	73.0	69.5	74.8	75.0	17.1	16.7	17.3	17.0	16.8
J[e] / cm^{-1}		-254			-246			-328			-525			+198			
S_{ab}[f]		0.33			0.36			0.39			0.47						
$\langle S^2 \rangle$	6.05	4.69	8.79	8.84	6.89	12.02	6.05	4.62	8.78	3.80	2.80	6.02	0.78	1.02	2.03	0.00	0.76
$S(S+1)+N_\beta$	6.00	4.75	8.75	8.75	7.00	12.00	6.00	4.75	8.75	3.75	3.00	6.00	0.75	1.00	2.00	0.00	0.75
ρ_{M}	4.16	4.19	4.23	4.78	4.87	4.93	3.73	3.74	3.79	2.63	2.66	2.73	1.25	1.16	1.21	0.00	0.03
ρ_{bpy}		-1.00	0.95		-0.88	1.05		-0.86	1.07		-0.80	1.09		-1.03	0.92		0.98

[a]Total M_S value.
[b]Local spin S on metal and ligand centres.
[c]Coordination geometry around the metal centre.
[d]Defined as angle between the C(11)-M-C(21) and N(3)-M-N(4) planes.
[e]Coupling constant J.
[f]Spatial overlap S_{ab} between the two magnetic pairs of metal-ligand orbitals.

The manganese complexes ($\mathbf{2^0}$, $^5\mathbf{2}^-$ and $^7\mathbf{2}^-$) adapt a distorted tetrahedral geometry already found for the iron complexes, with dihedral angles between ligand planes (ϕ) ranging from 64° to 76°. On the other hand, for the nickel complexes ($\mathbf{5^0}$ and $^2\mathbf{5}^-$) a distorted square-planar geometry is found (ϕ ~17°), typical of Ni^{II} with a d^8 electron configuration. Interestingly, the CrN_2C_2 coordination polyhedron in the chromium complexes ($\mathbf{1^0}$, $^4\mathbf{1}^-$ and $^6\mathbf{1}^-$) is also nearly square-planar with dihedral angles around 20° (Figure 2.18).

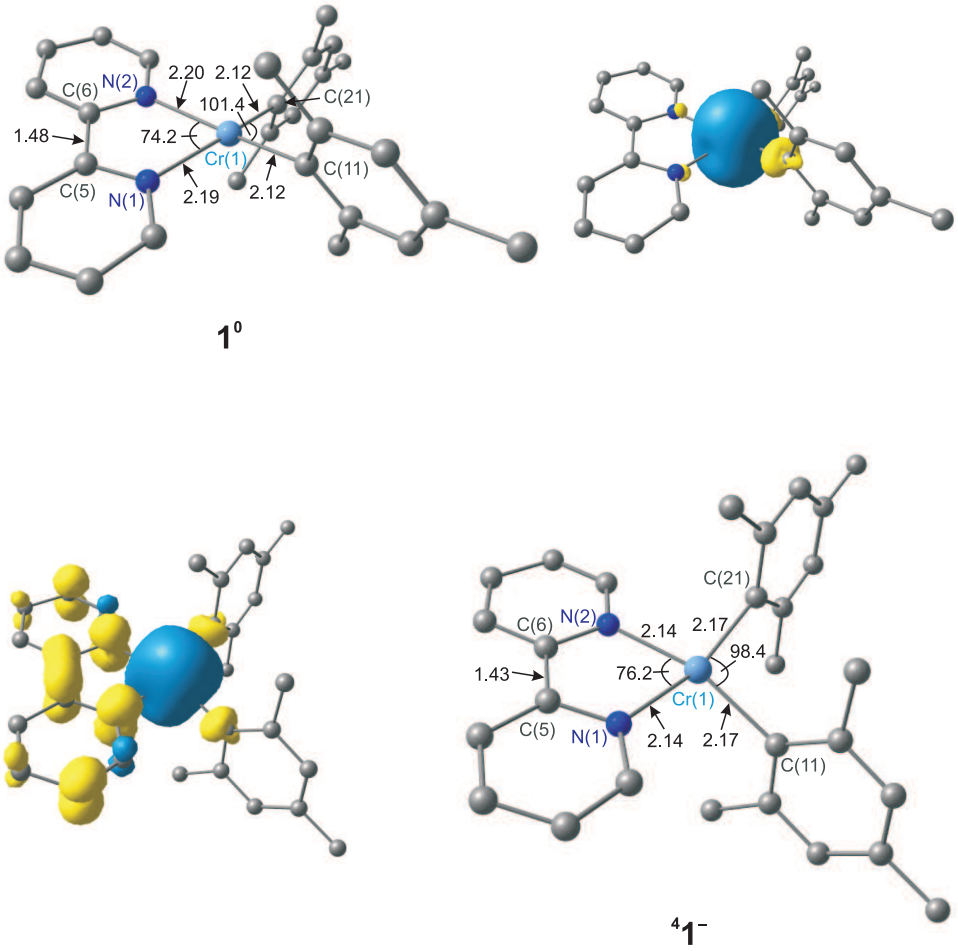

Figure 2.18: Optimised molecular structures (Å, °) of complex $\mathbf{1^0}$ and $^4\mathbf{1}^-$, along with plots of the total spin density (contour value 0.005). [Original in colour]

High-spin Cr^{II} (d^4) complexes with square-planar coordination geometry are less common than their low-spin d^8 counterparts.[247–250] In addition, square-planar geometries can also be adopted by d^7 species. We will return to this point in the

discussion of the cobalt homologues of the present series. Spin densities (Table 2.5) for the neutral complexes unequivocally support a divalent metal centre in each case. Analogous to $\mathbf{3^0}$, the reduction of the neutral complex to yield the anion is a ligand-based process, accompanied by the characteristic contraction of the bridge C-C bond in the ligand (going from 1.48 Å in the neutral to 1.43 Å in the reduced complex). Consequently, addition of an electron to the neutral complex leaves the spin densities on the metal centre unchanged. Thus, in $\mathbf{^2 5^-}$, the closed-shell d^8 configuration of Ni^{II} is conserved by placing the additional electron into the bpy π^* LUMO, retaining a square-planar geometry.

In $\mathbf{^4 1^-}$ and $\mathbf{^5 2^-}$, antiferromagnetic coupling between the ligand radical with $S_{\mathrm{bpy}} = 1/2$ and the metal radical centre ($S_{\mathrm{Cr}} = 2$, $S_{\mathrm{Mn}} = 5/2$) is dominant, stabilising the low-spin state with respect to the high-spin state. The resulting coupling constants J (Table 2.5), again calculated with Yamaguchi's formula, are slightly smaller ($\sim$250 $\mathrm{cm^{-1}}$) compared to the value of the iron congener ($\sim$328 $\mathrm{cm^{-1}}$), indicating that the radical centres interact more weakly in the former.

Turning now to the cobalt members of the series, experimental structures of these complexes are not accessible to this date, and thus we try to predict the most stable geometry of the neutral and anionic complex. The Co system in this set of complexes provides an interesting case, since it seems to lie between two limiting structural formulations. Nickel to its right in the transition metal series favours square-planar geometries, while iron to its left favours a distorted tetrahedral geometry. The central Co^{II} in $Co^{II}(2,2'\text{-bpy})(mes)_2$ is one electron short of a closed-shell d^8 configuration, furnishing some driving force for metal-centred reduction. We have considered distorted tetrahedral as well as square-planar geometries (labelled 'sq') for both oxidation states in the electronic states indicated in Table 2.4. In the neutral oxidation state the square-planar geometry (i.e. $\mathbf{4^0_{sq}}$)

is preferred over the distorted tetrahedral geometry ($\mathbf{4^0}$) by 4 kcal mol^{-1}. Spin densities on each metal centre (Table 2.5) confirm the assignment of the Co^{II} oxidation state. Reduction of both $\mathbf{4^0}$ and $\mathbf{4^0_{sq}}$ is again a solely ligand-based event. The square-planar geometry remains preferred in the high-spin state, thus $^{3}\mathbf{4^-_{sq}}$ is stabilised over $^{5}\mathbf{4}^-$ by 4 kcal mol^{-1}. In contrast, in the broken-symmetry state the energetic order is reversed and the distorted tetrahedral geometry becomes the ground state (-1.5 kcal mol^{-1}). By using a restricted KS formalism, we were also able to optimise a square-planar complex with a closed-shell configuration, corresponding to the Co^{I}(2,2′-bpy) description (spin densities are zero everywhere).

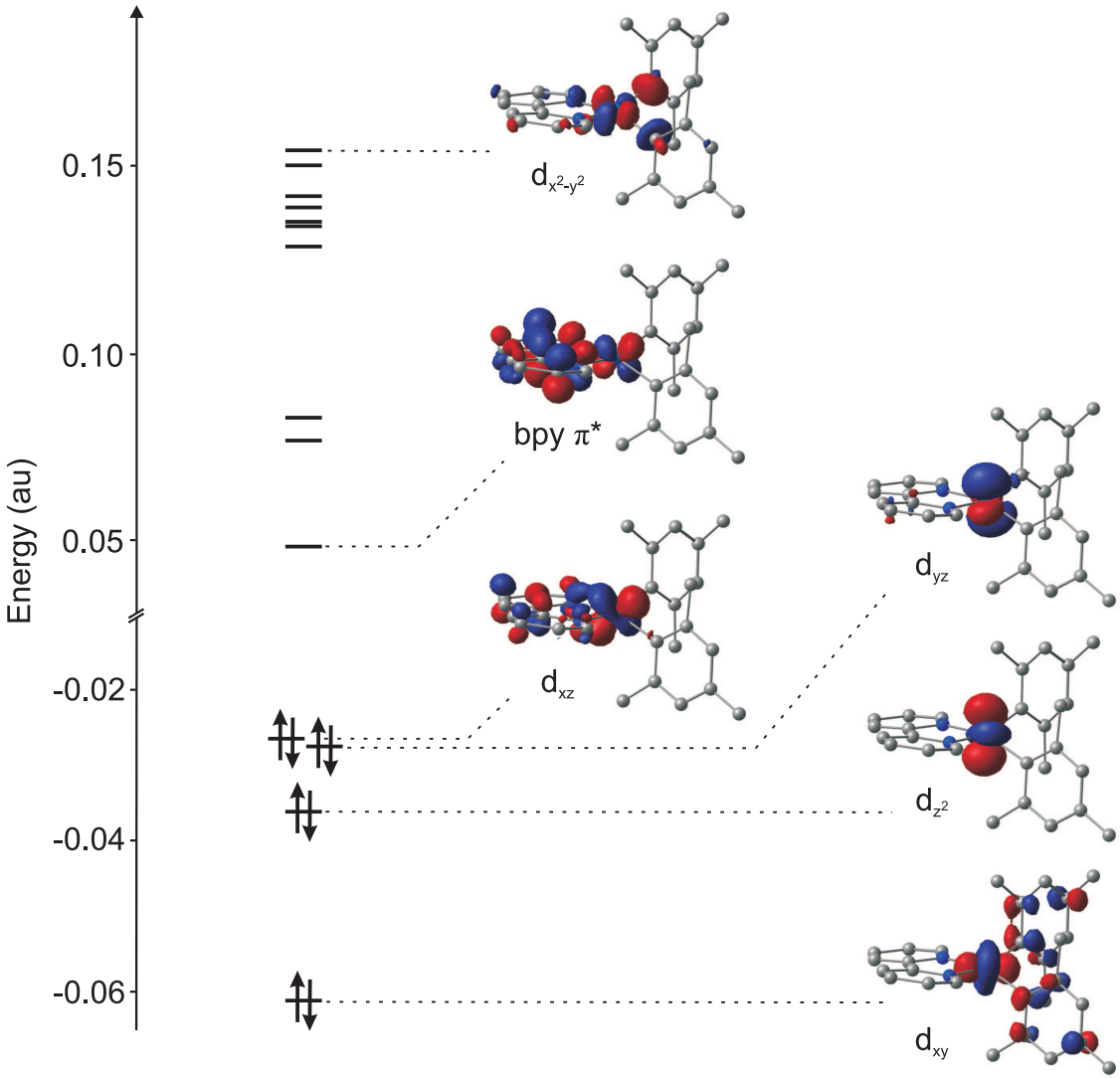

Figure 2.19: Selected canonical Kohn-Sham orbitals for the restricted KS solution for $\mathbf{4^-_{sq}}$ (contour value 0.05). [Original in colour]

In the MO diagram of the canonical KS orbitals shown in Figure 2.19 the presence of both the $d_{x^2-y^2}$ and π^* LUMO of bipyridine in the vacant manifold is unequivocal of an Co^{I} assignment. The contraction of the bridge C-C bond (1.44 Å) is caused by strong d-π^* backdonation from the low-valent metal centre. However, due to the high energy separation (18 kcal mol^{-1}), this electronic state can safely be ruled out.

The exchange coupling constant J for $^{3}\mathbf{4}^{-}$ is much larger (-525 cm^{-1}) compared to the other members of the series, indicating stronger antiferromagnetic coupling. A notable periodic trend is observed for the complexes $^{5}\mathbf{2}^{-}$, $^{4}\mathbf{3}^{-}$ and $^{3}\mathbf{4}^{-}$, in that J and S_{ab} increase dramatically across the series. This observation also reflects an increase of covalency between the metal d and ligand π^* orbitals. Indeed, inspection of the π^* SOMO reveals that the metal contribution gradually increases (Cr: 3.7%, Mn: 4.5%, Fe: 6.8%, Co: 9.6%). Wieghardt et al. have observed the same effect for a series of bis(α-iminopyridine) complexes,[139] and our calculated J values are in line with their reported values. Based on the computed energies, the neutral Co species should adopt a square-planar coordination environement (i.e. structure $\mathbf{4}^{\mathbf{0}}_{\mathbf{sq}}$). Precedent for square-planar d^7 complexes is found in the literature.[251,252] The energy separation between $^{3}\mathbf{4}^{-}$ and $^{1}\mathbf{4}^{-}_{\mathbf{sq}}$ (1.5 kcal mol^{-1}) would suggest a change of the coordination polyhedron from square-planar in the neutral, to tetrahedral in the anionic compound. The latter would be consistent with the structure observed for the Co(α-iminopyridine)$_2$ complex of Wieghardt an co-workers.[139] Nonetheless, the energy separation is small and electronic factors may easily be outbalanced by steric effects in the bulk crystal.

2.4 Complexes of dianionic bipyridine

As mentioned above, bipyridine can be reduced even further to the dianionic form. Such a case is observed independently for the two complexes $[Fe^{II}(2,2'\text{-bipyridine})]^{2-}$ ($\mathbf{6^{2-}}$) and $[Zn_2^{II}(4,4'\text{-bipyridine})(mes)_4]^{2-}$ ($\mathbf{7^{2-}}$). For each complex this becomes most evident from the strongly contracted experimental and calculated bond lengths of the C-C bridge, indicating an even higher degree of double bond character in this bond. However, much like in the case of the previously discussed monoreduced analogues, the determination of correct oxidation states in $\mathbf{6^{2-}}$ is again complicated by the possibility of a low-valent iron centre strongly backbonding into the ligand set.

A comparison of these species serves as another demonstrative example for the importance of quantum chemical modelling of this type of system, in order to distinguish the different scenarios. Here, in both cases the DFT calculations unambiguously show the occupation of the π^* antibonding bpy-based orbital, already familiar to us from the complexes discussed in the previous section. We shall return to the issue of backbonding vs. true radical character in the forthcoming chapter, where we investigate the electronic structure of a dinuclear rhodium complex.

2.4.1 $[Fe^{II}(2,2'\text{-bpy})_2]^{2-}$

The crystal structure of $\mathbf{6^{2-}}$ features the central iron atom in a slightly distorted square-planar ligand environment, in which the two ligand planes form a dihedral angle of 39°. Both ligands reveal bond distances between the carbon bridge atoms significantly shorter (1.38 Å) than those found in free $2,2'\text{-bpy}^{\cdot-}$, but conspicuously close to the ones in free $2,2'\text{-bpy}^{2-}$. Again, two formulations are conceivable to rationalise the observed bonding features in the ligand: a complex containing a

ferrous iron and two dianionic ligands, i.e. $[Fe^{II}(2,2'\text{-bpy}^{2-})_2]^{2-}$, or alternatively, low-valent iron complexed by monoanionic ligands, $[Fe^{0}(bpy^{\cdot-})_2]^{2-}$, with strong metal-to-ligand backbonding. In order to distinguish these possibilities and find the correct ground state we have considered different electronic spin states.

Scheme 2.10: Important possible electronic states for complex $\mathbf{6}^{2-}$.

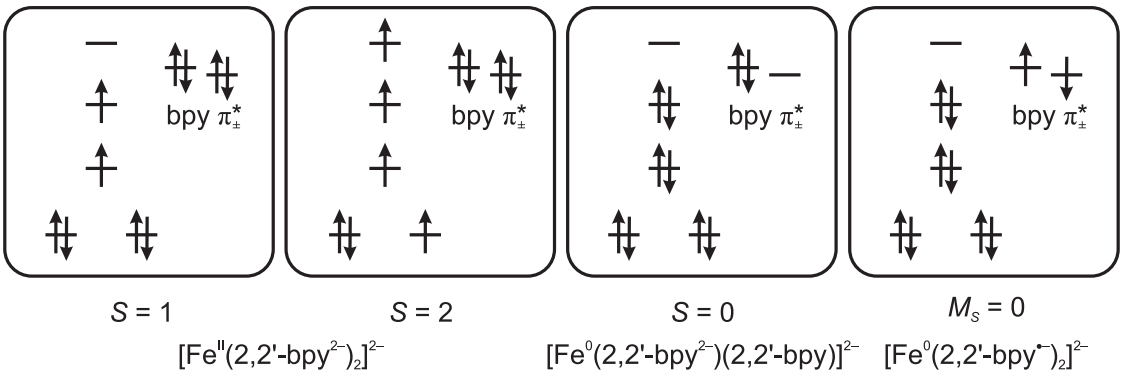

The optimised geometry of the triplet state ($S = 1$), $^{3}\mathbf{6}^{2-}$, corresponding to the lowest-energy structure, is shown in Figure 2.20, and bond metric data of all optimised structures are compared to experimental data in Table 2.6. The bond parameters in $^{3}\mathbf{6}^{2-}$ are in striking agreement with the experimental data, nicely reproducing the dihedral angle ($\phi = 38°$), as well as the short bond distances between the carbon bridge atoms (1.39 Å).

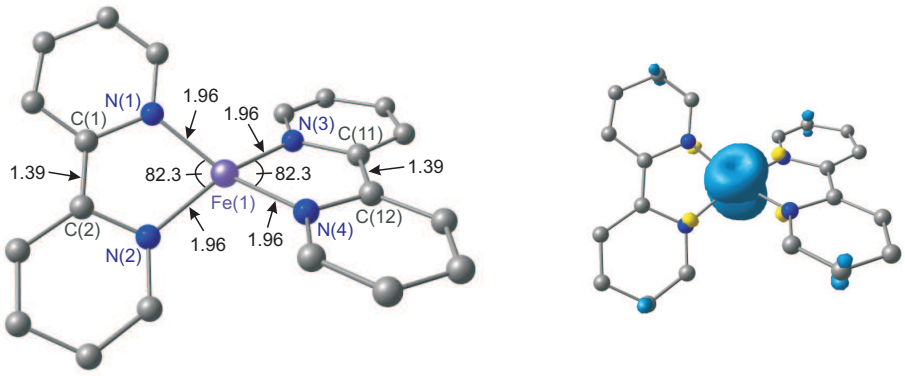

Figure 2.20: Optimised molecular structure (Å, °) of $^{3}\mathbf{6}^{2-}$ with a triplet ground state ($S = 1$), along with a plot of the total spin density (contour value 0.007). [Original in colour]

Table 2.6: Selected experimental and optimised bond lengths (Å) and angles (°) for different electronic states of $\mathbf{6^{2-}}$.

Parameter	$\mathbf{6^{2-}}$ (exp.)	$^{3}\mathbf{6^{2-}}$	$^{5}\mathbf{6^{2-}}$	$^{1}\mathbf{6^{2-}}$
Fe(1)-N(1)	1.917	1.96	2.06	1.91
Fe(1)-N(2)	1.912	1.96	2.06	1.92
Fe(1)-N(3)	1.917	1.96	2.06	1.92
Fe(1)-N(4)	1.912	1.96	2.06	1.91
C(1)-C(2)	1.377	1.39	1.39	1.41
C(11)-C(12)	1.377	1.39	1.39	1.41
N(1)-Fe(1)-N(2)	82.88	82.3	80.4	81.8
N(3)-Fe(1)-N(4)	82.88	82.3	80.4	81.8
N(1)-Fe(1)-N(4)	154.65	155.3	147.5	153.8
N(2)-Fe(1)-N(3)	154.64	155.3	146.9	158.0
ϕ^a	38.7	37.9	51.9	37.3
ρ Fe/2,2′-bpy		1.90	3.64	0.00
$\langle S^2 \rangle$		2.07	6.07	0.00

[a]Defined as angle between the N(1)-Fe-N(2) and N(3)-Fe-N(4) planes.

Analysis of the molecular orbitals (Figure 2.21) allows for an unambiguous assignment of the electronic structure: the intermediate-spin d^6 configuration is typical of a ferrous metal centre, while the doubly reduced state of both bpy ligands is apparent from the full occupation of the in-phase (π^*_+) and out-of-phase (π^*_-) combinations of the bpy π^* LUMO fragment orbitals (Scheme 2.11) in both the α- and β- manifolds. The Mulliken spin density of about 2 electrons on iron and negligible elsewhere (Figure 2.20) further supports this assignment. Hence, this state is distinctive of the $[Fe^{II}(2,2'\text{-bpy}^{\,2-})_2]^{2-}$ formulation.

In the high-spin state, $^{5}\mathbf{6^{2-}}$, occupation of the higher lying α-spin $d_{x^2-y^2}$ orbital leads to a local quintet on iron ($S_{Fe} = 2$, $\rho_{Fe} = 3.64$), leaving the electronic configuration of the ligand set ($(\pi^*_+)^2(\pi^*_-)^2$) otherwise unchanged. Perhaps surprisingly, the quintet state lies only 1 kcal mol^{-1} above the triplet state, and on this basis we conclude that it is very difficult to assign the ground state with confidence based only on energetic criteria.¶

¶Magnetic measurements are not available yet.

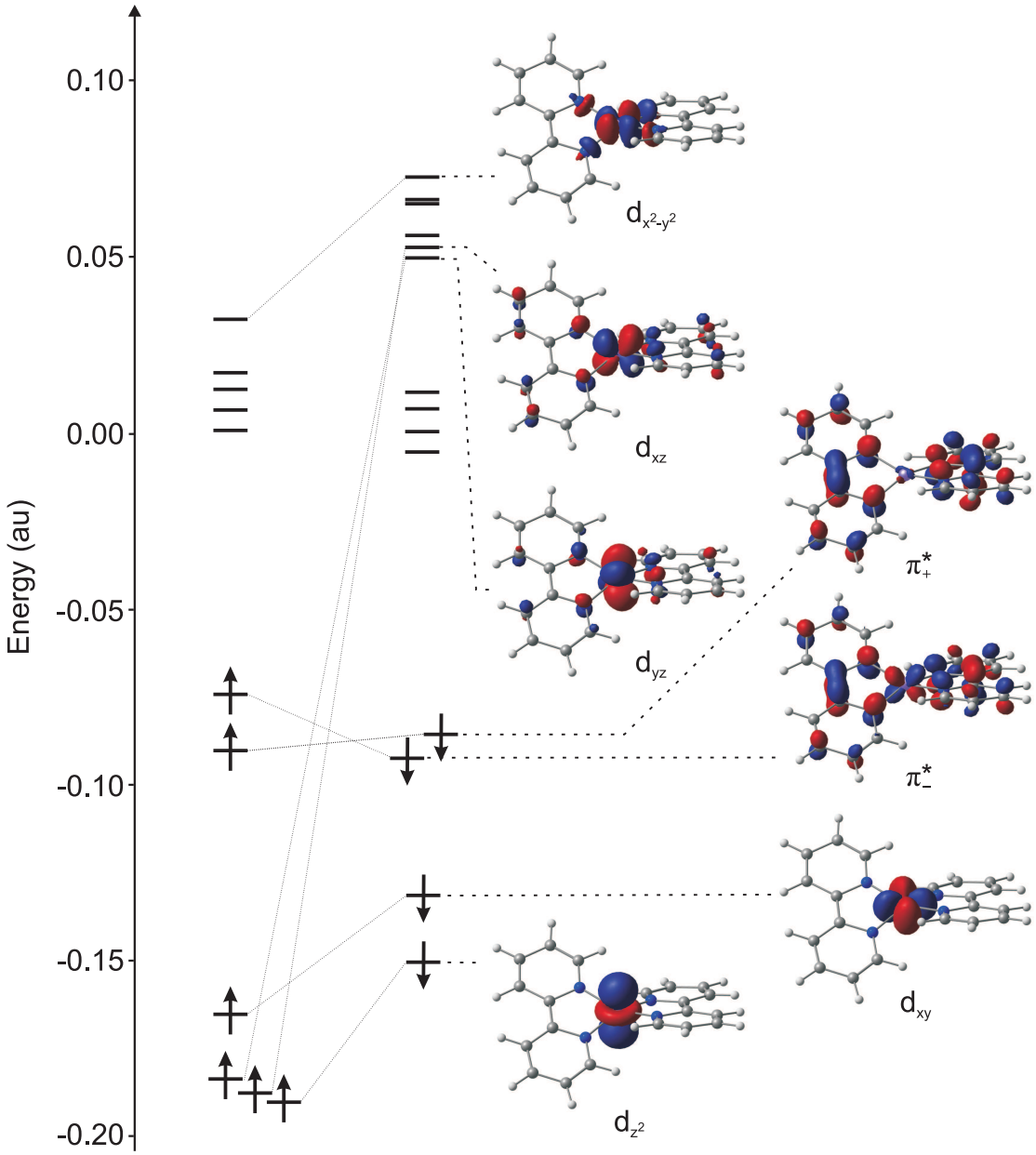

Figure 2.21: Selected canonical Kohn-Sham orbitals in the valence region of complex $^{3}\mathbf{6}^{2-}$ (contour value 0.05). [Original in colour]

Structural data are, in contrast, definitive: due to the single occupation of the $d_{x^2-y^2}$ orbital, with strong antibonding character towards the ligand donor atoms, the Fe-N bonds experience a dramatic elongation (2.06 Å). The obvious structural contradiction with the experimental geometry, also manifested in a much larger dihedral angle ($\phi = 52°$), leads us to reject the quintet state.

We have also optimised the structure of a closed-shell electron density distribu-

Scheme 2.11: Schematic representation of the in-phase (π^*_+) and out-of-phase (π^*_-) combinations, corresponding to the HOMO and HOMO-1 in $^{\mathbf{3}}\mathbf{6}^{\mathbf{2-}}$. Symmetry labels refer to ideal square-planar geometry.

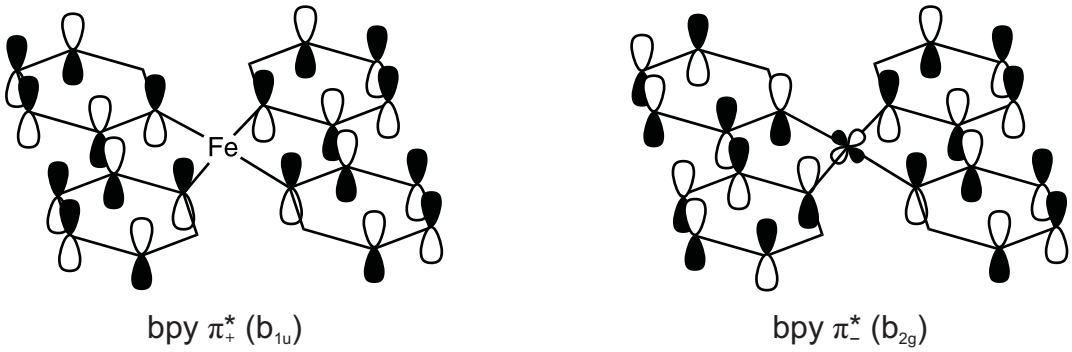

tion ($S = 0$), where the absence of spin polarisation imposes a zero-valent iron (Fe^0). The optimised structure is also in reasonable agreement with the experimental structure (see Table 2.6). Most notably, elongated C-C bonds are also observed in this structure (1.41 Å), although these are markedly longer than in $^{\mathbf{3}}\mathbf{6}^{\mathbf{2-}}$. In this case, the elongation can again only be attributed to strong back-bonding from the Fe^0 d-orbitals to the π^* orbitals of the bpy groups. The MO diagram in Figure 2.22 is characteristic of an electronic structure which is best described as $[Fe^0(2,2'\text{-bpy}^{2-})(2,2'\text{-bpy})]^{2-}$. Four doubly occupied orbitals of mainly metal character confirm the d^8 configuration on iron, while the $d_{x^2-y^2}$ is left unoccupied. The HOMO corresponds to the π^*_- ligand-centred orbital, and the LUMO corresponds to the π^*_+ orbital. This closed-shell state $^{\mathbf{1}}\mathbf{6}^{\mathbf{2-}}$ lies 19 kcal mol^{-1} higher in energy than $^{\mathbf{3}}\mathbf{6}^{\mathbf{2-}}$, and we confidently discard the Fe^0 formulation in favour of the Fe^{II} plus two $(bpy)^{2-}$ alternative.

All attempts to stabilise the broken-symmetry solution with $M_S = 0$ (Scheme 2.10), corresponding to an antiferromagnetically coupled ligand diradical, were unsuccessful. In each case the calculation converged back to a different broken-symmetry singlet state containing the dianionic form of bpy, while concomitantly forming a $(d_{xz})^{\uparrow}(d_{yz})^{\downarrow}$ microconfiguration on the metal centre. In other words, this state represents the broken-symmetry equivalent to the triplet state

of $^{3}\mathbf{6}^{2-}$. This latter state, i.e. $^{3}\mathbf{6}^{2-}$, is also recovered when trying to generate a ferromagnetically coupled ligand diradical. These findings further corroborate the preference for two doubly reduced bpy ligand moieties within the complex, which is also in line with the presence of two closed-shell dianionic ligands in a series of diamagnetic complexes $[M^{II}(L_2^{PDI})]^{2-}$.[253] In these complexes L^{PDI} corresponds to a *o*-diiminocatecholate ligand, coordinated to M = Ni, Pd, or Pt.

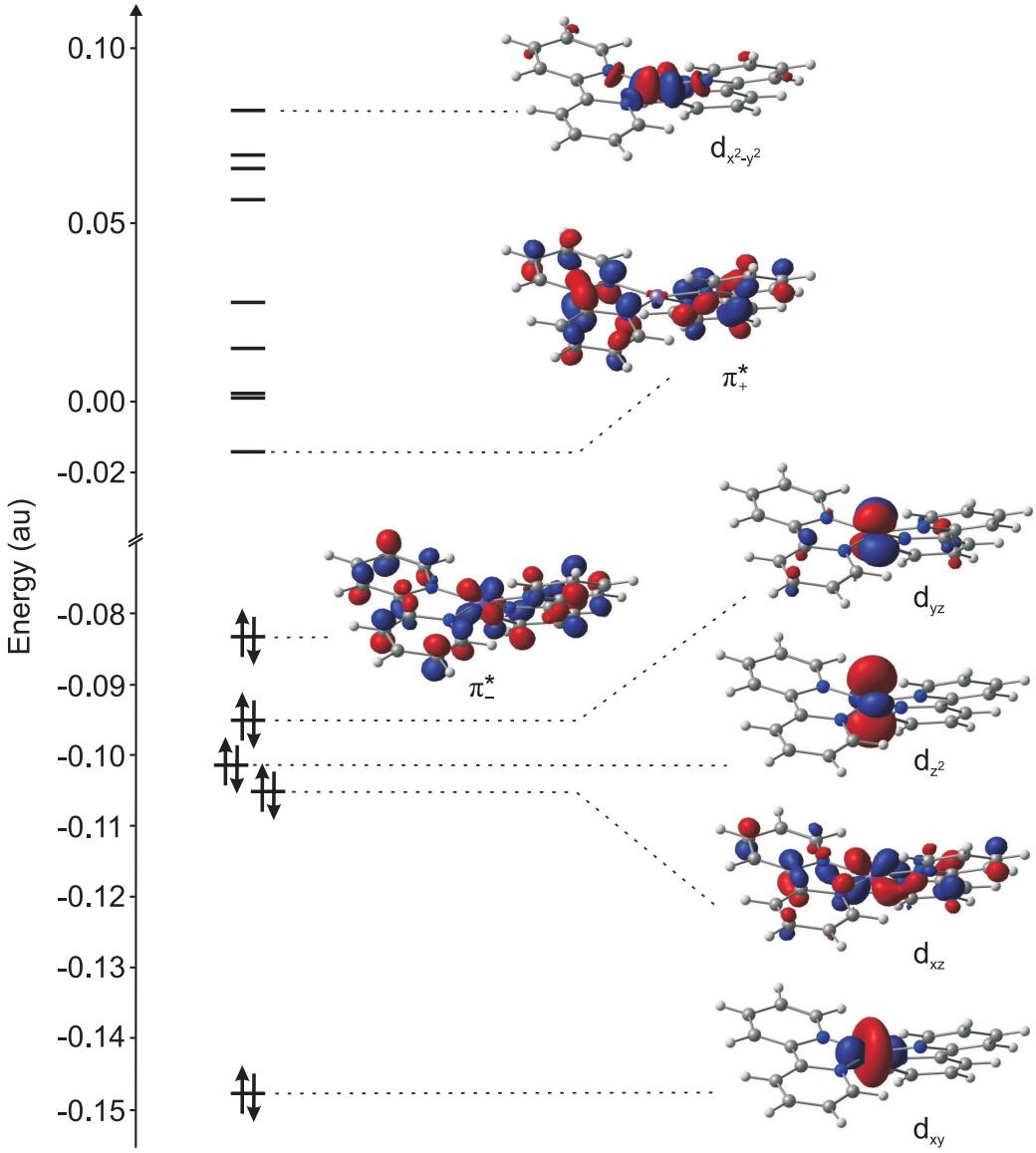

Figure 2.22: Selected canonical Kohn-Sham orbitals for the restricted KS solution for $^{1}\mathbf{6}^{2-}$ (contour value 0.05). [Original in colour]

2.4.2 $[Zn_2^{II}(4,4'\text{-bpy})(mes)_4]^z$ ($z = 0, 1-, 2-$)

We proceed by looking at a homologues series of dinuclear zinc complexes, $[Zn_2^{II}(4,4'\text{-bpy})(mes)_4]^z$ (z = 0, 1-, 2-), for which the assignment of oxidation states to the metal centre and ligand is unequivocal. The complexes are largely isostructural, yet exhibit significant structural variations which arise because of the differences in their electronic structure. Unlike in the previous examples, these complexes feature 4,4′-bipyridine as coligand, which lacks the ability to act as a chelator, but instead bridges between the two dimesitylzinc(II) centres.

We have optimised the geometries of complexes $\mathbf{7^0}$ ($S = 0$), $\mathbf{7^-}$ ($S = 1/2$), and $\mathbf{7^{2-}}$ ($S = 0$) in the indicated electronic states. For complex $\mathbf{7^{2-}}$ we have also located an excited triplet state, which has not been considered further because of the high energy separation (43 kcal mol^{-1}) from the ground state. In all cases, the optimised geometries obtained using DFT were found to be in line with the crystallographically determined data (see Table 2.7). A representative example of the overall structure of the complexes is depicted in Figure 2.23.

Table 2.7: Selected experimental and optimised bond lengths (Å) and angles (°) for complexes $\mathbf{7^0}$, $\mathbf{7^-}$ and $\mathbf{7^{2-}}$.

	neutral		anion		dianion	
Bond	**7** (exp.)	$\mathbf{7^0}$	$\mathbf{7^-}$ (exp.)	$\mathbf{7^-}$	$\mathbf{7^{2-}}$ (exp.)	$\mathbf{7^{2-}}$
1	1.342	1.33	1.361	1.36	1.379	1.38
2	1.383	1.39	1.363	1.37	1.354	1.36
3	1.394	1.40	1.426	1.43	1.465	1.47
4	1.482	1.48	1.417	1.43	1.373	1.38
Zn-N	2.183	2.24	2.043	2.07	1.977	1.97
Zn-C_{mes}	1.975	2.01	1.987	2.03	2.004	2.06
torsion	35.25	38.2	2.83	0.0	0.00	0.0
N-Zn-C	103.32	100.1	111.12	109.6	114.33	117.1
C-Zn-C	153.26	159.8	137.69	140.9	131.33	125.8

Upon reduction of the neutral species to the anionic and dianionic forms, the Zn-N distances contract from 2.24 to 2.07 and 1.97 Å for complexes $\mathbf{7^0}$, $\mathbf{7^-}$ and $\mathbf{7^{2-}}$, respectively. This is consistent with an increased degree of electrostatic character to the Zn-N bond and has the effect of moderately weakening the bonds between the Zn^{II} centres and the strongly σ-donating mesityl substituents, which is manifested in a lengthening of the Zn-C bonds (2.01, 2.03, and 2.06 Å). The second most pronounced structural change, and the most meaningful, relates to the bond distances between pyridyl rings of the 4,4′-bpy moieties. The C-C bridge between the two pyridyl rings of the ligand also contracts considerably upon reduction from 1.48 Å to 1.43 Å and 1.38 Å, as a result of successive occupation of the LUMO of the neutral ligand.

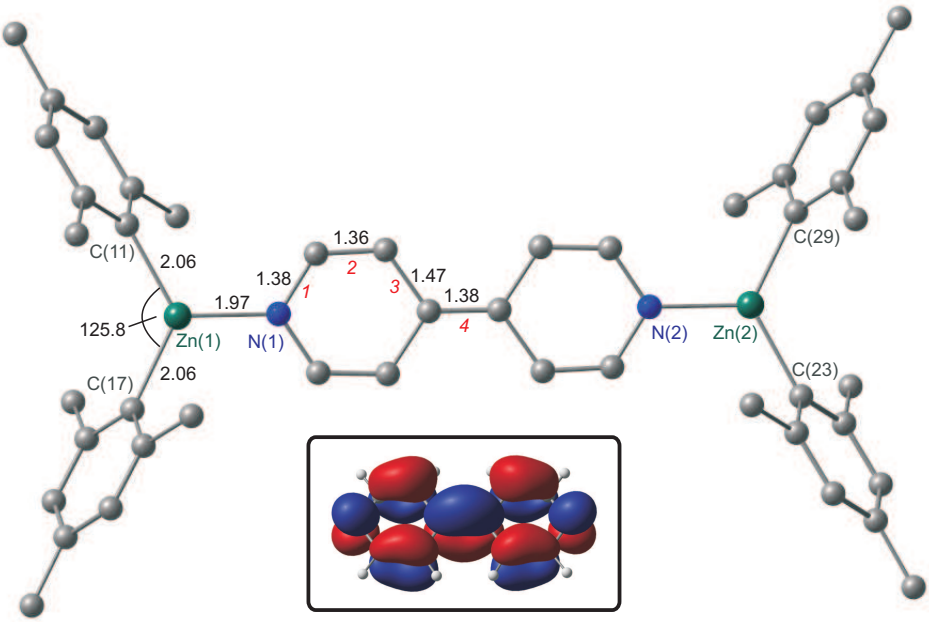

Figure 2.23: Optimised molecular structure (Å, °) of complex $\mathbf{7^{2-}}$. Inset: LUMO of free 4,4′-bipyridine. [Original in colour]

This LUMO (see inset Figure 2.23) reveals a pattern of in-phase/out-of-phase relationships between p orbitals of the ring atoms which is reminiscent of the one in 2,2′-bipyridine. Thus, the character of this central bond changes from a single to a double bond in the dianionic species. The same trend is apparent for bond 2

(according to the numbering scheme employed in Figure 2.23), although the contraction is less pronounced compared to the interpyridyl bond. Conversely, bonds 1 and 3 follow the opposite trend, lengthening upon reduction. Concomitantly, the optimum torsion angle between two pyridyl moieties is being reduced from 38.2° in $\mathbf{7^0}$ to 0.0° in both $\mathbf{7}^-$ and $\mathbf{7^{2-}}$.

^{1}H Magnetic resonance study

The ^{1}H NMR spectrum of a sample of $\mathbf{7^{2-}}$ reveals a significant shift of the 4,4′-bipyridyl resonances with respect to the values observed for the neutral parent compound, from 8.57 and 7.71 ppm to 5.92 and 4.51 ppm for **7** and $\mathbf{7^{2-}}$, respectively. The chemical shift values observed for $\mathbf{7^{2-}}$ are consistent with those previously reported for another complex of the 2,2′-bipyridyl dianion, [{Yb(μ_2-$N_2C_{10}H_8$)(thf)$_2$}$_3$], which were reported at 6.54, 5.28, 5.02, and 4.01 ppm.[254] The lower chemical shift values of the bipyridyl resonances observed in the ^{1}H NMR spectrum of $\mathbf{7^{2-}}$ are consistent with a significant reduction in the aromatic character of the bipyridyl ring system and a greater degree of localised olefinic character to the bond between the carbon atoms to which the protons are bonded. This decrease of aromaticity is illustrated in Figure 2.24, along with the proton numbering scheme. To verify the link between aromaticity and the changes in ^{1}H NMR chemical shifts, we have computed these parameters using DFT, along with the Nucleus Independent Chemical Shifts (NICS), proposed by Schleyer and co-workers.[213] This latter approach is one of the most frequently used magnetic criteria and has become established as a simple and efficient measure of the degree of aromaticity. The NICS corresponds to the absolute magnetic shielding at the point of interest, for example at the geometric centre of a ring or cluster. It is common practice to use the negative of the calculated value in order to adapt to

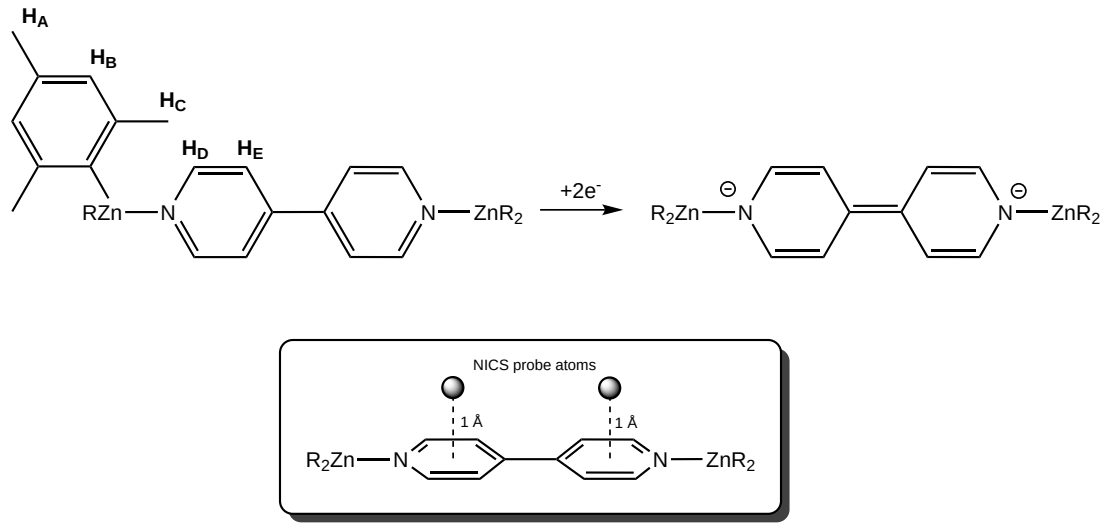

Figure 2.24: Shift of the aromatic character towards olefinic character upon two-electron-reduction of **7**. Labels refer to the proton numbering. Inset: position of the NICS probes (ghost atoms 'Bq') above the ring planes.

experimental convention. Negative NICS values indicate aromaticity, while positive values imply antiaromatic character. The positions of the NICS probes are designated using ghost atoms ('Bq'), and in this case have been placed 1 Å above the centre of the bipyridine rings (inset of Figure 2.24). These so called NICS(1) values are also widely used and largely reflect the influence of π-electrons, and are therefore a better indicator of the ring current (aromaticity) than the values at the centre, where σ-bonding contributions are also of importance.

The calculations reproduce the significant shielding of the aromatic 4,4′-bpy resonances: $\delta_{\mathrm{calc}} = 8.51$ and 7.40 ppm in $\mathbf{7^0}$ and 6.20 and 4.66 ppm in $\mathbf{7^{2-}}$. A full list of computed and measured chemical shifts is given in Table 2.8. For $\mathbf{7^0}$, the strongly negative NICS values calculated for the pyridyl rings, -9.78 ppm, are indicative of substantial aromatic character, and are in fact identical to the values computed for the free ligand at the same level of theory (NICS(1) = -9.82 ppm). The aromaticity as measured by NICS is diminished by the addition of one ($\mathbf{7^-}$, NICS(1) = -1.88 ppm) and two ($\mathbf{7^{2-}}$, NICS(1) = +4.08 ppm) electrons to the π-system of the ligand.

Table 2.8: Experimentally determined and calculated ^{1}H NMR chemical shift and NICS(1) values for complexes $\mathbf{7^0}$, $\mathbf{7^-}$ and $\mathbf{7^{2-}}$.

	δ / ppm		Assignment	NICS(1) / ppm
	exp.	calc.		
	8.57, d	8.51	H_D *ortho*-4,4′-bipyridyl	
	7.71, d	7.40	H_E *meta*-4,4′-bipyridyl	
$\mathbf{7^0}$	6.73, s	6.93	H_B $C_6H_2(CH_3)_3$	-9.78
	2.42, s	2.42	H_C *ortho*-CH_3	
	2.21, s	2.28	H_A *para*-CH_3	
		7.24	H_D	
		6.71	H_B	
$\mathbf{7^-}$		6.28	H_E	-1.88
		2.41	H_C	
		2.15	H_A	
	6.50, s	6.38	H_B	
	5.92, d	6.20	H_D	
$\mathbf{7^{2-}}$	4.51, d	4.66	H_E	+4.08
	2.32, s	2.32	H_C	
	2.21, s	1.96	H_A	

The value for $\mathbf{7^{2-}}$ is in fact close to that for the free dianionic bipyridine (+4.94 ppm), and clearly reflects the antiaromatic character of the rings of the dianion.

Topology of the electron density - AIM analysis

The topology of the electron density in $\mathbf{7^0}$, $\mathbf{7^-}$ and $\mathbf{7^{2-}}$ analysed using the atoms in molecules (AIM) methodology, provides an alternative perspective on the changes in the bonding of the rings. The ellipticity ε at the central C-C bond (4 according to the numbering scheme in Figure 2.23) critical point is a sensitive measure of π-character: values close to zero indicate a cylindrical symmetric (i.e., σ) bond, while deviations away from zero indicate increasing π-character (values in the range 0.18-0.22 are found for aromatic C-C double bonds with partial π-character). The ε value for the bridging bond increases dramatically from 0.04 in $\mathbf{7^0}$ to 0.34 in $\mathbf{7^{2-}}$, again strongly supporting the formulation of the central C-C bridge as double bond. Similarly, the ellipticity of bond 2 within the pyridyl rings increases from

0.22 to 0.37 upon two-electron reduction.

Table 2.9: Computed ellipticity parameters at selected bond critical points for the complexes $\mathbf{7^0}$, $\mathbf{7^-}$ and $\mathbf{7^{2-}}$.

	ε (BCP)			
	N-C (1)	C-C (2)	C-C (3)	C-C (4)
$\mathbf{7^0}$	0.0774	0.2155	0.1847	0.0435
$\mathbf{7^-}$	0.0890	0.2919	0.1480	0.1802
$\mathbf{7^{2-}}$	0.0967	0.3684	0.1203	0.3386

2.5 Conclusions

In this chapter we have reviewed calculations on a wide range of complexes with singly and doubly reduced bpy ligands. In all cases the ligand-based reduction occurs in preference to reduction of the first row transition metal ion. In no case have we found evidence for significant backbonding from metal to ligand, as distinct from ligand radical character. Thus we concur with Wieghardt's recent statement that backbonding is not a significant feature in related M(bpy) complexes.

3

Non-innocent complexes of the 2-(phenylazo)pyridine ligand

In a complementary project performed in collaboration with Prof. Goswami at the Indian Association for the Cultivation of Science (IACS), Kolkata, we have explored the electronic structure of complexes of the 2-(phenylazo)pyridine (pap) ligand. In the first part of this chapter we derive a picture of the electronic structure of the $[Cr(o\text{-Clpap})_3]^n$ (n = 1–, 0, 1+, 2+, 3+) and $[Mo(o\text{-Clpap})_3]^n$ (n = 1–, 0, 1+) electron transfer series from broken-symmetry DFT calculations, MO descriptions and spin density distributions. The results indicate a predominant azo-anion radical description of the ligand in the neutral species $[Cr^{III}(o\text{-Clpap}^{\cdot -})_3]$. All the electrochemical processes are ligand-based, i.e. the half-filled $(t_{2g})^3$ set of the d^3 Cr^{III} ion remains unchanged throughout. The description of the molybdenum analogue is less clear cut, owing to the more significant mixing between metal- and ligand-based orbitals. Based on variations in net spin densities and orbital compositions we argue that the oxidation events are primarily ligand-based, although the electron density at the molybdenum centre is clearly more variable than in the chromium congeners.

An even more intricate situation emerges for the – at least formally – mixed-valent complex $[Rh_2(\mu_2\text{-}p\text{-Clpap})_2(cod)Cl_2]$, whose electronic structure we elucidate

in the second part. The two azo ligands form bridges between the two rhodium centres that have completely different coordination environments. We establish the ligand's ability for strong backbonding, a property that is closely linked to its tendency to form ligand radicals. Hence, the elongated azo bonds of the pap ligand observed in the structure can be attributed to strong d-π^* backdonation from a formally Rh^{-I} centre towards the bridging ligands. The results presented in this chapter have been published in Ref. [316] and [317].

3.1 Introduction

The ligand 2-(phenylazo)pyridine (pap) is formally related to bipyridine by the insertion of an azo group between the two aromatic rings.[131] The azo group is reducible, chemically or electrochemically, and single and double occupation of the low-lying π^* orbital can generate either the radical anion or hydrazido dianion respectively, analogous to bipyridine. The electrochemical series of the pap ligand is shown in Scheme 3.1, along with typical N=N bond lengths in the different oxidation states.[257]

Scheme 3.1: Different redox states of the pap ligand with characteristic bond distances.

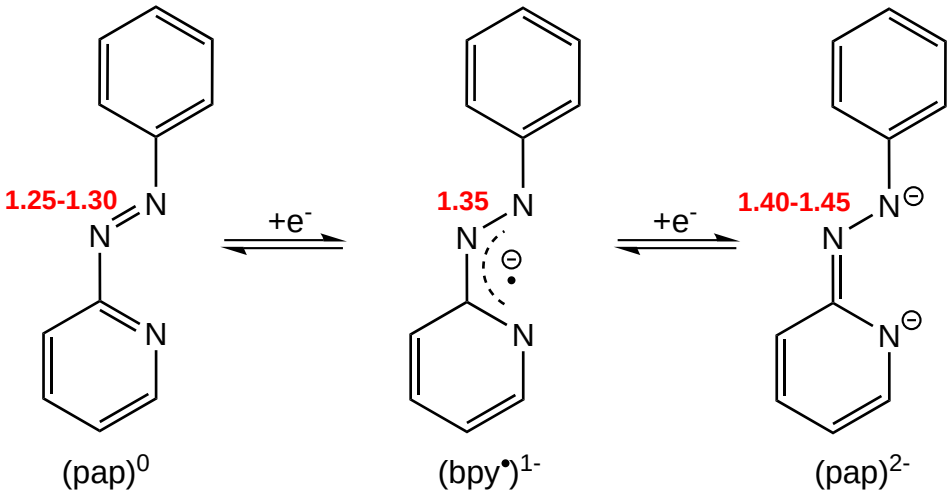

The changes in bond lengths within the ligand skeleton, in particular that of the azo bond, can again be rationalised in terms of the bonding/antibonding overlaps in the lowest unoccupied orbital of the ligand (Figure 3.1).

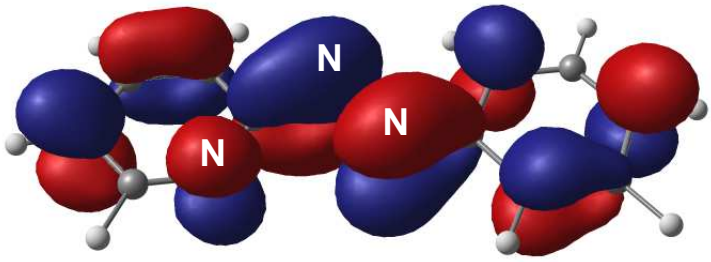

Figure 3.1: Lowest unoccupied molecular orbital of free (2-phenylazo)pyridine.

While the radical azo anion oxidation state has been known in solution for a long time,[258,259] its isolation in the solid state was first reported only in 1998.[260–262] A number of complexes containing azoaromatic ligands in different oxidation states have been reported in the literature.[257,263–273] Some of these undergo unexpected electronic rearrangements through internal electron transfer processes in response to external oxidation. For example, this so called redox-induced electron transfer via internal electron transfer has been observed in the complexes $[M(L)_2]^+$ (M = Ru, Os; L = 2-[(2-N-phenylaminophenyl)azo]pyridine).[270] As a result, ligand-based oxidation of the complexes leads to partial reduction of the metal centre.

The synthesis of neutral octahedral complexes $M(pap)_3$, where M = Cr, Mo or W, has been reported by Ackermann and co-workers.[274] These compounds were primarily characterised by their spectroscopic properties. Subsequent to this study, the crystal structure of a related compound, $Mo(4\text{-}Mepap)_3$ (4-Mepap = 2-[(4-methylphenyl)azo]pyridine), was published.[275] The most prominent features of this structure are the elongated azo bonds (∼1.359 Å), an observation that would be consistent with a radical monoanionic character of the coordinated ligands. The authors ascribed the structural changes in the azo bonds to extensive metal-to-ligand π-backbonding. Thus, the systems were described as complexes of zerovalent

group VI metal ions, and the electrochemical oxidation processes were interpreted as metal-based, whereas the reduction was ligand-based. The ligand radical formulation of the neutral species would necessarily imply the opposite picture, i.e. ligand-based oxidation processes. In view of this controversy we set out to reassess the electronic structures of the trichelate complexes containing both chromium and molybdenum and their accessible redox series (Scheme 3.2).

Scheme 3.2: Complete electron-transfer series for the complexes Cr(*o*-Clpap)$_3$ (**1**) and Mo(*o*-Clpap)$_3$ (**2**).

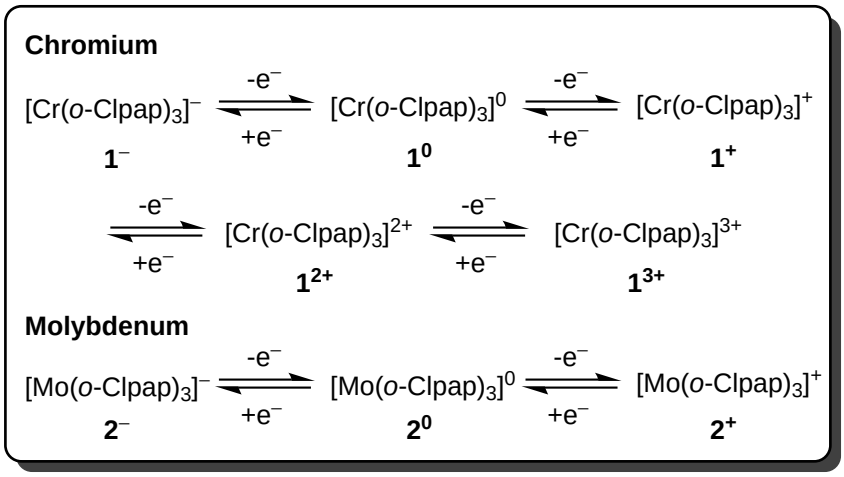

The neutral complexes Cr(*o*-Clpap)$_3$ (**1^0**) and Mo(*o*-Clpap)$_3$ (**2^0**) have been isolated and structurally characterised by single crystal X-ray crystallography (Figure 3.2), along with their chemically oxidised cationic counterparts (**1**$^+$ and **2**$^+$, isolated as their triiodide salts, [**1**]I_3 and [**2**]I_3). In each of these complexes the central ions are coordinated octahedrally by three *o*-Clpap ligands,* revealing notable distortions. Both neutral complexes **1^0** and **2^0** show considerably elongated N-N bonds of the azo chromophores compared to the free ligand, similar to the complex Mo(4-Mepap)$_3$. In complex **1^0** the three N=N bond lengths are 1.345, 1.345 and 1.341 Å, while in **2^0** two of the azo bond lengths are identical at 1.356 Å and the third one is

*The chloro-substituted derivatives of pap are utilised in the synthetic protocols, due to their ability to yield crystals of high quality. Thus, the complexes discussed in this chapter contain either the 2-[(2-chlorophenyl)azo]pyridine (*o*-Clpap) or 2-[(4-chlorophenyl)azo]pyridine (*p*-Clpap) isomer.

1.361 Å. The coordination geometries of the one-electron oxidised complexes [**1**]I_3 and [**2**]I_3 are similar to those of the neutral analogues. The most striking difference between the neutral $\mathbf{1^0}$ and cationic species $\mathbf{1}^+$ is the notable contraction of the N-N bond lengths (1.334, 1.314, 1.316 Å), accompanied by the emergence of a small degree of asymmetry. A similar oxidation-induced contraction of the N-N bonds is observed in the molybdenum homologue, albeit with a larger degree of asymmetry.

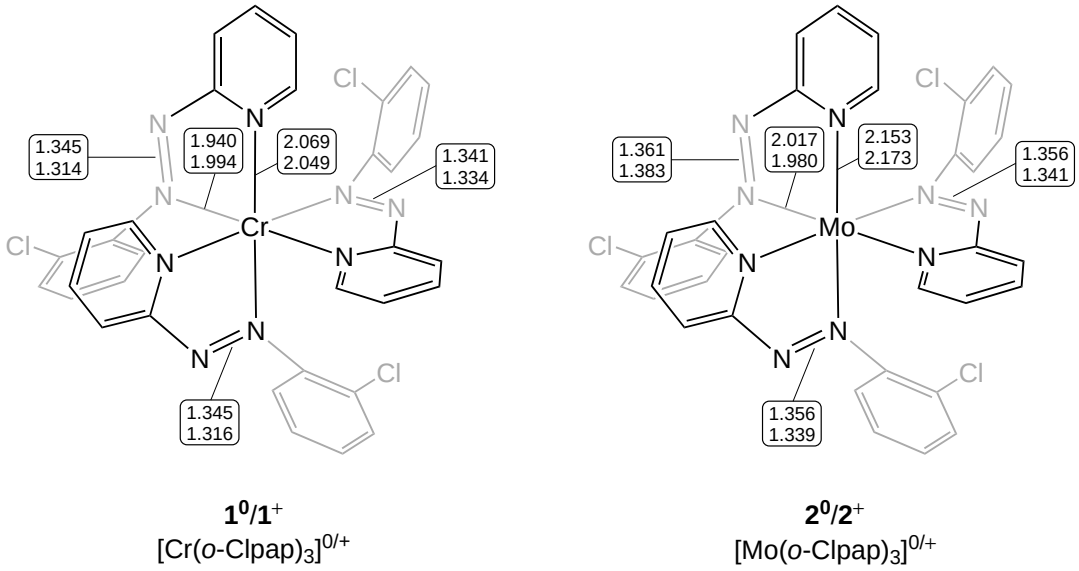

$\mathbf{1^0/1^+}$
$[Cr(o\text{-Clpap})_3]^{0/+}$

$\mathbf{2^0/2^+}$
$[Mo(o\text{-Clpap})_3]^{0/+}$

Figure 3.2: Structure of complexes $\mathbf{1}^{0/+}$ and $\mathbf{2}^{0/+}$, including key bond lengths (Å). The upper value in the boxes refers to the neutral, the lower value to the cationic species in each case.

The N=N bond length pattern in $\mathbf{1}^+$ is suggestive of the possibility of an internal electron transfer process during formation of the cation. Thus, initial ligand-based oxidation of $\mathbf{1^0}$ may be followed by internal electron transfer from a second ligand radical to the metal centre, resulting in intramolecular reduction (Cr^{III} to Cr^{II})[†] of the metal centre (Scheme 3.3). Thus, the formulation of $\mathbf{1}^+$ as $[Cr^{II}(o\text{-Clpap})_2(o\text{-Clpap}^{\cdot-})]^+$ would in principle be consistent with the bond lengths observed in the crystal structure.

Complete electron transfer series $[Cr(o\text{-Clpap})_3]^n$ (n = 1–, 0, 1+, 2+, 3+) and

[†]Albeit unlikely from chemical intuition.

Scheme 3.3: Possible redox-induced internal electron transfer during formation of $\mathbf{1}^{+}$.

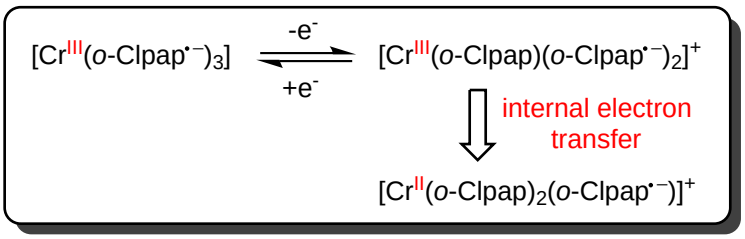

$[\mathrm{Mo}(o\text{-Clpap})_3]^n$ (n = 1–, 0, 1+) have been accessed by cyclovoltammetry, supported by absorption and EPR spectroscopy, amongst others. While both the neutral $\mathbf{1^0}$ and dicationic $\mathbf{1^{2+}}$ complex are EPR-silent, the remaining members of the Cr electron transfer series $\mathbf{1}^-$ (S = ½), $\mathbf{1}^+$ (S = ½) and $\mathbf{1^{3+}}$ (S = ³⁄₂) show characteristic signals in the EPR spectrum, consistent with their indicated ground states. For the molybdenum complexes, both the monocationic $\mathbf{2}^+$ and monoanionic $\mathbf{2}^-$ species are EPR-active, signifying S = ½ ground states in both cases.

The homobimetallic complex $[\mathrm{Rh}_2(p\text{-Clpap})_2(\mathrm{cod})\mathrm{Cl}_2]$ (**3**, cod = 1,5-cyclooctadiene) represents another interesting and challenging example in terms of its electronic structure, combining two separate, yet interlinked, concepts. On one hand, the presence of *p*-Clpap ligands certainly brings about the possibility of redox non-innocence within the compound, which we have already explored for mononuclear species in the previous section. On the other hand, the presence of two discrete rhodium sites adds another interesting aspect, namely that of mixed-valency. Mixed-valence complexes are attractive targets in catalyst design, particularly those in which the oxidation states of the metals differ by two electrons. This feature appears to have a vital role in the catalysis of two-and four-electron transformations, such as those involved in dihydrogen and dioxygen activations.[276–279] Two recent examples of two-electron mixed-valent Rh(-I,I) compounds reported by de Bruin and co-workers[280,281] are particularly relevant for the discussion of the electronic

structure of **3**. Both complexes [{Rh(L)}$_2$(μ-bpi)] (bpi = bis(2-picolyl)imine)[282] are structurally similar and differ only in the nature of the supporting ligand (L = nbd (norbornadiene) or cod). In these complexes, the combination of hard σ-donating and soft π-accepting groups within the same ligand framework generates two distinct coordination environments, facilitating the stabilisation of the different oxidation states.

Complex **3** has been obtained from the reaction of 2-[(4-chlorophenyl)azo]pyridine with [Rh(cod)Cl]$_2$, and its structure was confirmed by single crystal X-ray analysis (Figure 3.3). The striking features within the structure are the two N=N bonds which are elongated appreciably (1.413 and 1.399 Å) compared to typical values for the free diazo ligands (1.25 Å), pointing at the possibility of two azo anion radical bridges. Thus, a formulation as [Cl$_2$Rh^{III}(p-Clpap$^{\cdot -}$)$_2$Rh^{I}(cod)] is a viable option, where the observed EPR silence of the complex necessitates antiferromagnetic coupling of the ligand radicals to yield an overall singlet ($S = 0$) state.

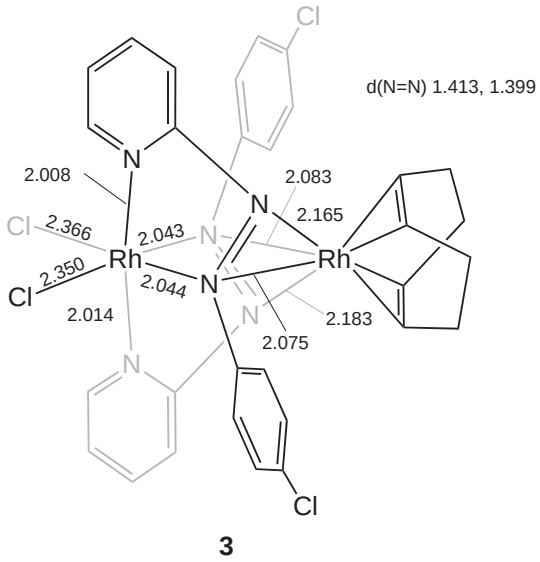

Figure 3.3: Structure of complex **3**, including key bond lengths (Å).

Scheme 3.4: Intramolecular double hydroxylation reaction catalysed by complex **3**. The complete incorporation of dioxygen in the ring hydroxylation process has been unequivocally established by isotope labelling using a $^{18}O_2$ atmosphere.

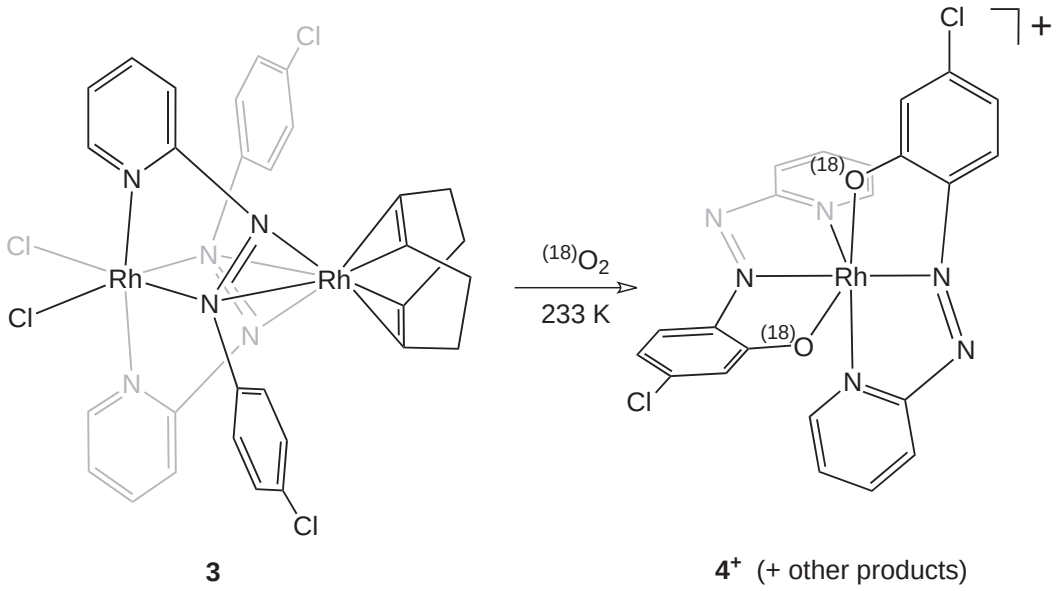

3 **4**$^{+}$ (+ other products)

The above complex is highly air-sensitive and reacts rapidly with O_2, leading to double arene ring hydroxylation of the pendant phenyl groups of the coordinated *p*-Clpap ligands via C-H bond activation (Scheme 3.4). Its ability to activate dioxygen makes the above complex an interesting candidate for the study of this type of reactions, as oxidations involving O_2 activation at metal sites are important in the context of both biological and industrial processes. Related hydroxylation reactions of aromatic rings are known in biological systems for heme-copper oxidases including cytochrome *c* oxidase (CcO) and also for tyrosinase. The presence of an electron rich Rh centre appears to be critical for the observed double aromatic ring hydroxylation. Similar reactions with other less electronically rich Rh^{I} precursors, however, failed to produce the doubly hydroxylated product but yielded the mono-hydroxylated complex instead.

3.2 Methodology

All calculations presented in this chapter were carried out using the Gaussian03 program package.[55] Geometry optimisations were performed without imposing geometric constraints (C_1 symmetry), and obtained stationary points were subsequently confirmed to be minima by vibrational analysis (no imaginary frequencies). All calculations utilised the B3LYP hybrid functional.[19,26,31,32]

Chromium and molybdenum complexes: For the complexes discussed in the first part of the chapter, the TZVP basis set[206] of triple-ζ quality with one set of polarization functions was used on Cr and on N atoms (all except one nitrogen atoms in each of the three azo units are directly coordinating to the metal centre). In case of molybdenum, the def2-TZVP basis set[283] by Weigend and Ahlrichs as obtained from the EMSL Basis Set Library[284,285] was used for the metal centre. This basis set is of triple-ζ quality with an effective core potential (ecp-28, replacing 28 core electrons) for core functions.[61] For the carbon, chlorine and hydrogen atoms slightly smaller polarised split-valence SVP basis sets[207] were used, that are of double-ζ quality in the valence region, and contain a polarising set of d-functions on the non-hydrogen atoms.

It is convenient to adopt the BS(m,n) nomenclature introduced by Neese and coworkers[224] to denote the character of a BS determinant, which has become widely accepted in the field and is common use. The system is formally separated into two fragments. In the BS(m,n) notation, m represents the number of unpaired or partially paired spin-α electrons on one fragment, usually localised on the metal centre, while n stands for the number of unpaired spin-β electrons on the second fragment, essentially localised on the ligand set. It is noted that a high-spin open-shell solution would correspond to a BS($m+n$,0) definition. Generally the BS(m,n)

notation refers to the initial guess wave function, but the variational freedom of the SCF cycle allows convergence to a solution of the form BS($m + n$,0), i.e. the canonical UKS determinant. In this case, the n electrons from one fragment have paired up with the m electrons from the other. To illustrate the usage of the above notation, we return to the example of an iron-nitrosyl complex containing a Fe-NO moiety with otherwise closed-shell coligands. The BS(5,1) solution corresponds to a high-spin Fe^{III} centre antiferromagnetically coupled to a NO doublet radical, while on the other hand a (somewhat arbitrary) BS(0,0) solution would describe a closed-shell low-spin Fe^{II} centre with a coordinated nitrosyl cation in a singlet state.

Rhodium complex: For the dinuclear Rh complex discussed in the second part the SDD basis set (Stuttgart/Dresden ecp-28) was used on Rh,[61] and the TZVP basis[206] on all coordinating atoms (N(1)-N(6), Cl(3), Cl(4), C(22), C(23), C(24), C(25)). The remaining atoms were described by SVP.[207] The topological properties of electron densities, calculated with B3LYP in conjunction with the all-electron DGDZVP basis set on Rh,[286,287] and TZVP and SVP as defined above, were characterised by using the Atoms In Molecules (AIM) theory of Bader[62] with the AIM2000 program package.[63]

3.3 Mononuclear octahedral complexes of 2-[(2-chlorophenyl)azo]pyridine

3.3.1 Electronic structure of chromium compounds

In order to perform a comprehensive search over a range of possible spin states for the considered complexes, we have used a number of conceivable electronic density distributions as starting point for the optimisations. A schematic representation of few selected initial wave functions is given in Scheme 3.5. We will use the notation given in the scheme to denote the different electronic states of a complex, corresponding to the BS(m,n) descriptor for BS determinants introduced by Neese and co-workers.

Scheme 3.5: Important possible spin states for members of the electron transfer series of $[Cr(o\text{-Clpap})_3]^n$ (n = 1–, 0, 1+, 2+, 3+). [Original in colour]

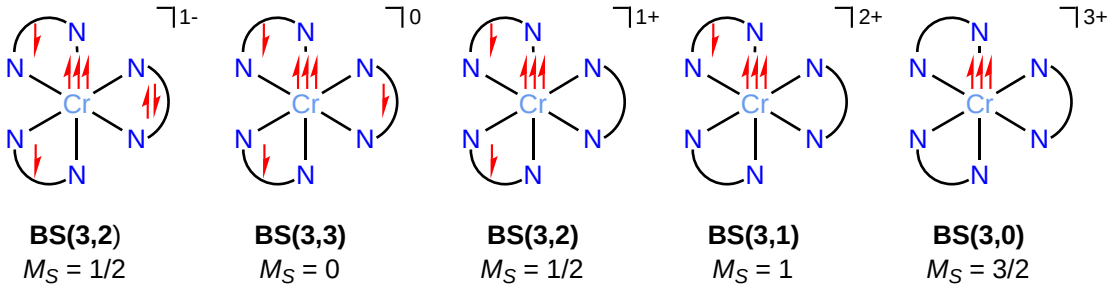

In addition to the states above we have optimised the high-spin states and, where possible, alternative broken-symmetry solutions. We will point these out in the context of the discussion. Optimised structural parameters for the computed ground states of $\mathbf{1}^{\mathbf{0}}$, $\mathbf{1}^{+}$ and $\mathbf{1}^{-}$ ($M_S = 0$, $M_S = {}^1/_2$ and $M_S = {}^1/_2$, respectively) along with net spin densities are collected in Table 3.1. Corresponding geometries of the ground states are depicted in Figure 3.4, along with their net spin densities (isosurface contour 0.006 e au^{-3}).

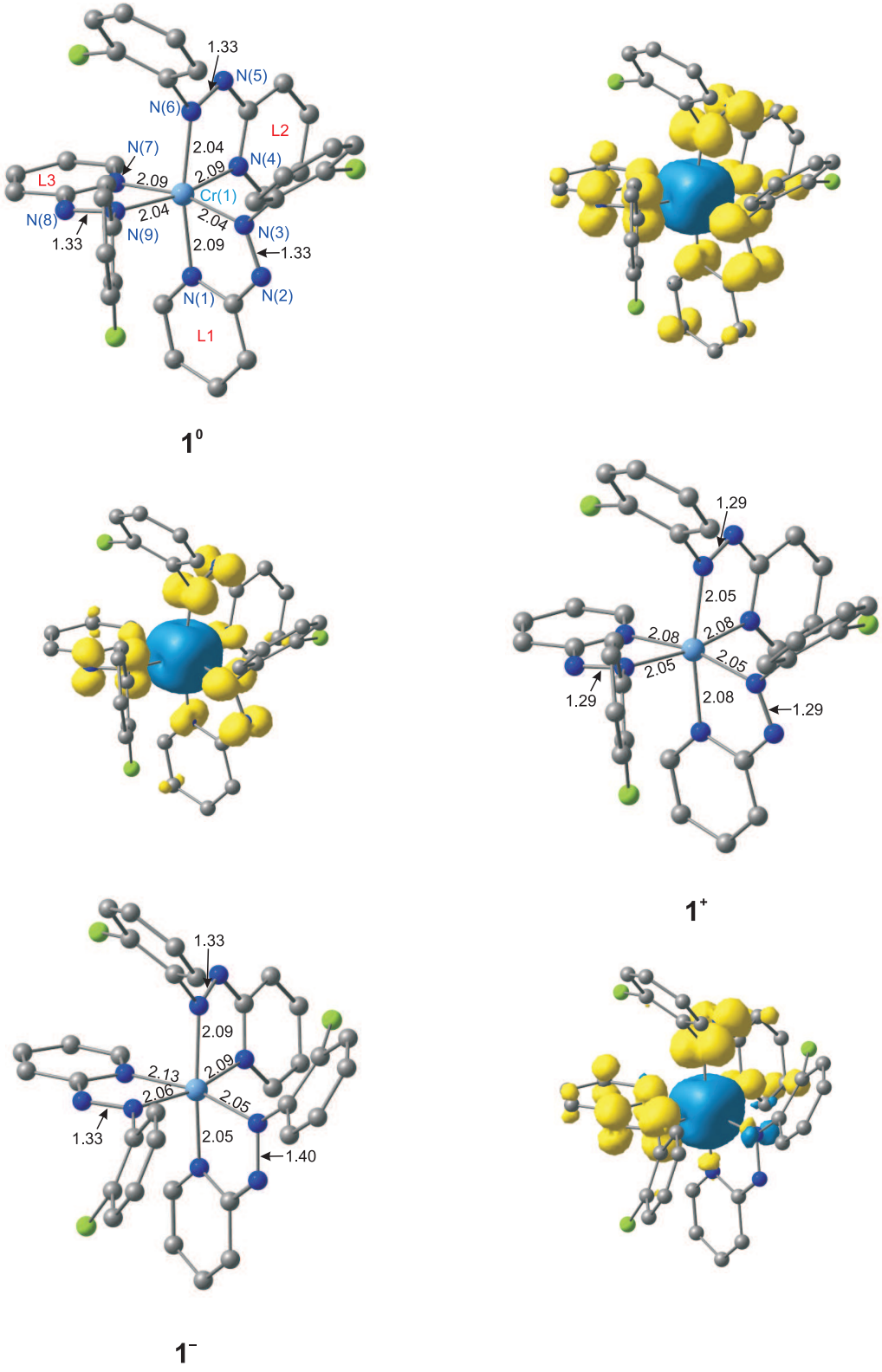

Figure 3.4: Optimised molecular structures (Å) of the ground states of complex $\mathbf{1}^{\mathbf{0}}$ ($M_S = 0$), $\mathbf{1}^{+}$ ($M_S = 1/2$) and $\mathbf{1}^{-}$ ($M_S = 1/2$), along with plots of the total spin density (contour value 0.006). [Original in colour]

Table 3.1: Selected experimental and optimised bond lengths (Å) and angles (°) for complexes $\mathbf{1}^{-/0/+}$ and $\mathbf{2}^{-/0/+}$.

	$\mathbf{1^0}$ (M = Cr)		$\mathbf{1^+}$		$\mathbf{1^-}$	$\mathbf{2^0}$ (M = Mo)		$\mathbf{2^+}$		$\mathbf{2^-}$
Bond	Exp.	Calc.	Exp.	Calc.	Calc.	Exp.	Calc.	Exp.	Calc.	Calc.
M-N1	2.069(2)	2.09	2.049(4)	2.08	2.05	2.153(17)	2.17	2.173(4)	2.17	2.17
M-N3	1.940(2)	2.04	1.994(4)	2.05	2.05	2.017(17)	2.08	1.980(4)	2.09	2.05
M-N4	2.040(2)	2.09	2.059(4)	2.08	2.09	2.160(17)	2.17	2.158(4)	2.17	2.17
M-N6	1.954(2)	2.04	2.023(4)	2.05	2.09	2.017(17)	2.08	2.022(4)	2.09	2.05
M-N7	2.048(2)	2.09	2.059(4)	2.08	2.13	2.160(17)	2.17	2.141(4)	2.17	2.17
M-N9	1.948(2)	2.04	1.979(4)	2.05	2.06	2.021(17)	2.08	2.017(4)	2.09	2.05
N2-N3	1.345(3)	1.33	1.314(5)	1.29	1.40	1.361(2)	1.34	1.383(5)	1.30	1.37
N5-N6	1.345(3)	1.33	1.316(5)	1.29	1.33	1.356(2)	1.34	1.339(6)	1.30	1.37
N8-N9	1.341(3)	1.33	1.334(5)	1.29	1.33	1.356(2)	1.34	1.341(6)	1.30	1.37
N1-M-N6	168.15(9)	166.6	164.86(14)	166.6	167.4	161.33(6)	163.1	161.60(15)	163.4	161.6
N3-M-N7	165.06(8)	166.4	167.90(15)	167.0	166.7	160.92(6)	163.0	165.53(15)	163.5	161.5
N4-M-N9	165.32(9)	166.7	167.24(14)	167.1	164.9	161.81(7)	162.9	160.11(15)	163.3	161.6
$\langle S^2 \rangle$		2.48		2.08	2.51		1.29		0.87	0.79
ρ_{M}		2.98		2.81	2.99		1.86		1.46	1.13
ρ_{L1}		-0.99		-0.61	0.04		-0.62		-0.16	-0.04
ρ_{L2}		-0.99		-0.60	-1.00		-0.62		-0.16	-0.04
ρ_{L3}		-0.99		-0.60	-1.03		-0.62		-0.16	-0.04

Neutral complex $\mathbf{1^0}$

Calculated geometries and metrical parameters are generally found to be in good agreement with their experimental counterparts. The optimised N-N bond lengths of 1.32 Å for the BS(3,3) ($M_S = 0$) ground state of the neutral species are marginally shorter than those obtained from the X-ray experiment (1.342(3) Å) but the elongation relative to the free ligand (calc. d(N-N) = 1.24 Å) is well reproduced. Net spin densities of 2.98 and -0.99 on metal and each ligand, respectively, in $\mathbf{1^0}$ are emphatically in favour of a ligand radical formulation, with the Cr^{III} centre antiferromagnetically coupled to three ligand radicals (see the full spin density plot in Figure 3.4). Successive spin flips on the ligands ($\downarrow\downarrow\downarrow, \uparrow\downarrow\downarrow, \uparrow\uparrow\downarrow, \uparrow\uparrow\uparrow$) result in almost identical energy increases of ∼6 kcal mol^{-1} (Figure 3.5). The ferromagnetically coupled high-spin ($S = 3$) state lies 19 kcal mol^{-1} higher in energy than BS(3,3).

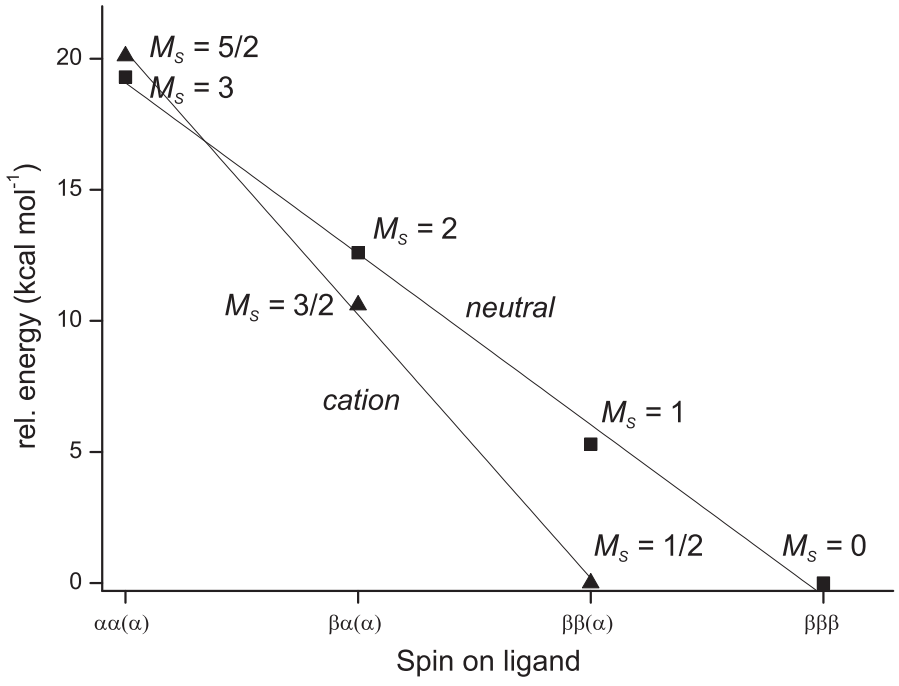

Figure 3.5: Linear relationship of the relative energy on the number of unpaired spin-β electrons residing on the ligand set. The spin in brackets on the abscissa only applies to the neutral species, $\mathbf{1^0}$.

Mapping onto the $\hat{H} = -2J\hat{S}_1 \cdot \hat{S}_1$ Heisenberg exchange Hamiltonian using the Yamaguchi formula, $J = -^{(E_{HS}-E_{BS})}/_{(\langle S^2\rangle_{HS}-\langle S^2\rangle_{BS})}$, yields a value of J = -706 cm^{-1}, a value typical of Cr^{III} ligand radical complexes.[288] This relatively strong exchange coupling is fully consistent with the observed diamagnetism of the compound, and also the substantial overlaps, S_{ab}, between the corresponding orbitals (0.16-0.52, Figure 3.6).

The Cr-N$_{azo}$ bond lengths to a given ligand increase by ∼0.08 Å when the spin of the ligand-based electron is flipped from β (antiferromagnetic) to α (ferromagnetic) and as a result the optimised structure of the high-spin state represents a much poorer match to experiment (Cr-N$_{azo}$ = 2.10-2.14 Å vs. ∼1.95 Å experimentally). These structural changes are a consequence of the slightly antibonding interaction between the ligand LUMOs and metal d orbitals in the α-manifold, while these are bonding in the β-manifold. Thus, each spin flip on a ligand results in a contraction of the corresponding Cr-N$_{azo}$ bond.

We have also optimised the structure of a closed-shell electron density distribution ($S = 0$), where the absence of spin polarisation imposes a zero-valent chromium [Cr^0(o-Clpap)$_3$]. The optimised structure is also in reasonable agreement with the experimental structure. Most notably, elongated N=N bonds are also observed in this structure (1.32 Å), similar to those in BS(3,3). In this case, the elongation can only be attributed to strong backbonding from the Cr^0 d-orbitals to the π^*-orbitals of the azo groups. On this basis we conclude that it is very difficult to distinguish ligand-radical character from metal-based reduction with strong backbonding based on structural data alone. Energetic data are again definitive: the closed-shell state lies 32 kcal mol^{-1} higher in energy than BS(3,3), leading us to reject the Cr^0 formulation in favour of the Cr^{III} plus ligand radical alternative.

It is also important to note that attempts to generate a BS(4,2), BS(2,2), BS(1,1)

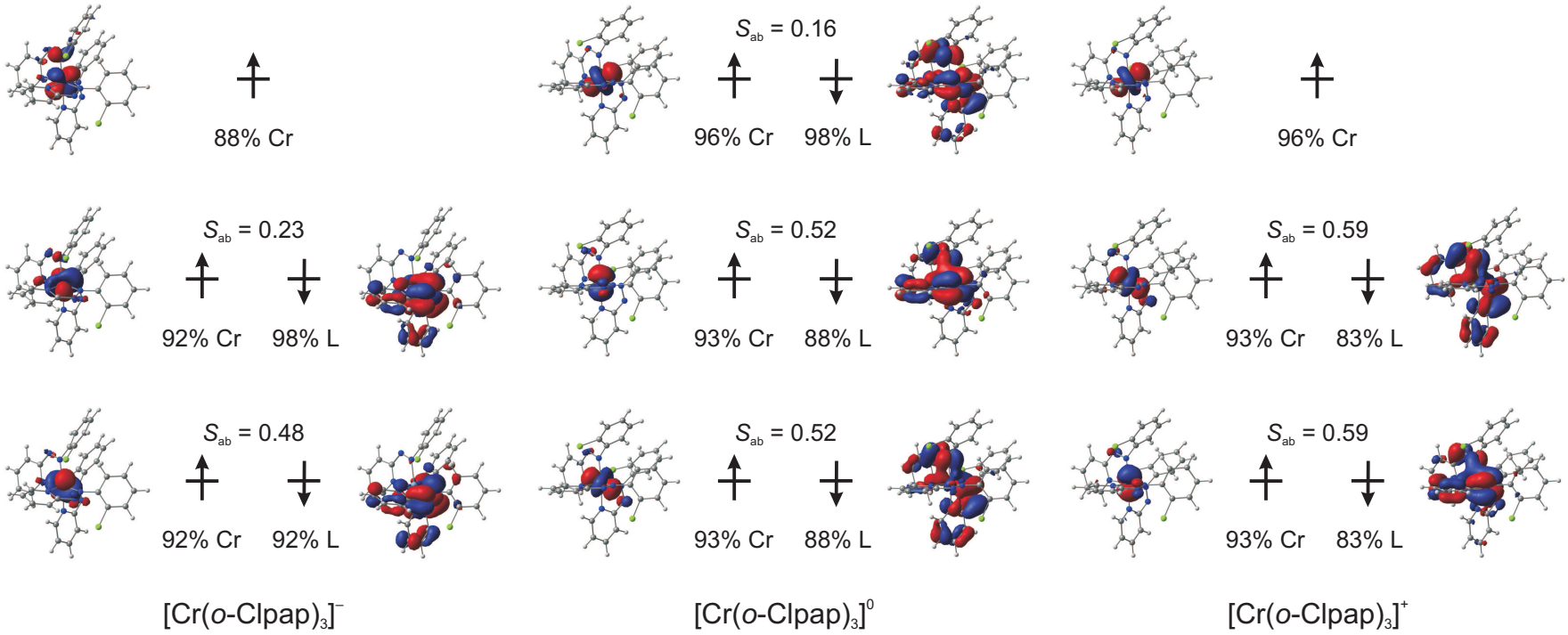

Figure 3.6: Corresponding orbitals for $\mathbf{1^0}$, $\mathbf{1}^+$ and $\mathbf{1}^-$. [Original in colour]

or a spin-unrestricted $S = 0$ solution failed, and all of the mentioned states converged back to the BS(3,3) solution. Thus, electronic structure descriptions such as $[Cr^{II}(o\text{-Clpap}^{\cdot-})_2(o\text{-Clpap})]^0$, $[Cr^{IV}(o\text{-Clpap}^{2-})(o\text{-Clpap}^{\cdot-})_2]^0$ and $[Cr^{V}(o\text{-Clpap}^{2-})_2(o\text{-Clpap}^{\cdot-})]^0$ can be safely ruled out. The basic electronic ground state featuring a Cr^{III} ion ($S_{Cr} = 3/2$) that is strongly antiferromagnetically coupled to three ligand-centred π-radicals ($S_L = 1/2$) has been proposed for related chromium complexes.[288–290]

Cationic complex 1^+

One-electron oxidation of $\mathbf{1^0}$ generates $\mathbf{1}^+$ in a broken-symmetry doublet ($M_S = 1/2$) ground state, BS(3,2), whose geometry is also shown in Figure 3.4. The spin density at the metal is similar in the cation and the neutral species ($\rho_{Cr} = 2.81$, Table 3.1), offering a strong indication that the oxidation is a ligand-based redox event. The unpaired spin-β electrons are equally distributed over three ligands rather than two, evident from the spin densities of -0.60 on each ligand. The structural impact of the oxidation is therefore localised entirely in the ligand array, where the N=N bonds contract by 0.04 Å (c.f. ∼0.03 Å in the X-ray data). Consistent with the delocalisation of the two spin-β electrons, the three Cr-N_{py} (2.08 Å), Cr-N_{azo} (2.05 Å) and N=N bonds (1.29 Å) are equivalent. The energetic cost of the small structural distortions seen in the crystal structure is, however, likely to be very small, and are probably a consequence of the solid-state environment.

The energetic trend upon changing the ligand spinvectors resembles that described for the neutral complex: antiferromagnetic coupling of the ligand radical electrons leads to a strong stabilisation. Flipping spins along the series ($\downarrow\downarrow, \uparrow\downarrow, \uparrow\uparrow$) destabilises the complex by about 10 kcal mol^{-1} at each step (Figure 3.5), indicating that the exchange coupling is somewhat stronger in the oxidised species. The

ferromagnetically coupled counterpart of the ground state of $\mathbf{1}^+$ with $M_S = {}^5/_2$ lies 20 kcal mol^{-1} higher in energy, corresponding to a J value of -1052 cm^{-1}. Higher states on the Heisenberg ladder are therefore clearly inaccessible in the temperature range of the magnetic measurements, in line with the magnetic data.

It is again important to note that despite extensive efforts using initial guess densities with different degrees of spin polarisation, e.g. BS(4,1) and BS(2,1), we have been unable to locate an alternative stable minimum for $\mathbf{1}^+$. Hence, states corresponding to $[Cr^{II}(o\text{-Clpap}^{\cdot-})(o\text{-Clpap})_2]^+$, $[Cr^{IV}(o\text{-Clpap}^{\cdot-})_3]^+$ and $[Cr^{V}(o\text{-Clpap}^{2-})(o\text{-Clpap}^{\cdot-})_2]^+$ formulations can again faithfully be dismissed.

The suitability of TD-DFT based on a broken-symmetry ground state has been debated, but nevertheless excellent agreement between computed ligand-ligand charge transfer excitation energies and features in the near IR spectrum of closely related complexes has been reported.[253,291–293] In the case of $\mathbf{1}^+$ we compute two absorption features at ~0.7 eV (1760 nm) corresponding to transitions within the

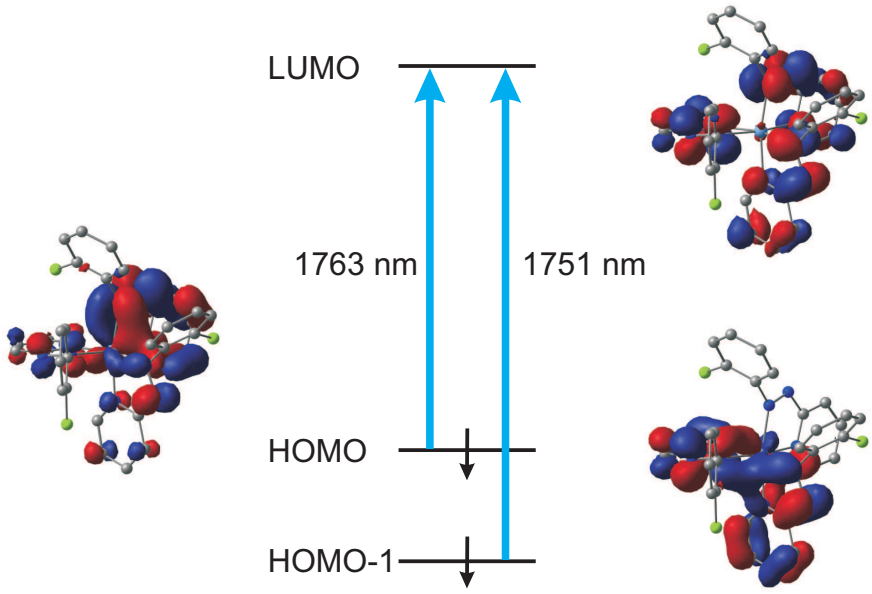

Figure 3.7: Canonical Kohn-Sham orbitals involved in the LLCT transitions in $\mathbf{1}^+$ calculated by TD-DFT, PCM(CH_2Cl_2)/B3LYP/TZVP/SVP.

N=N π^* array (Figure 3.7), in excellent agreement with the weak feature at

∼1500 nm assigned to a ligand-ligand charge transfer (LLCT) band in the UV-vis spectrum of $\mathbf{1}^+$. Such transitions are observed only when both oxidation levels of the ligand are present, and are used as spectroscopic markers to identify mixed-valency within the ligand set.[294] The presence of a LLCT absorption band further corroborates our description of the cation as $[Cr^{III}(o\text{-Clpap}^{\cdot -})_2(o\text{-Clpap})]^+$.

Anionic complex $\mathbf{1}^-$

One-electron reduction to form the anionic species, $\mathbf{1}^-$, also results in negligible changes in the spin density at the metal ($\rho_{Cr} = 2.99$, Table 3.1) and is therefore unambiguously ligand-based, retaining the $(t_{2g})^3$ configuration of the Cr^{III} ion. The lowest-energy solution found for $\mathbf{1}^-$ is the BS(3,2) $M_S = 1/2$ determinant, lying 7.6 kcal mol^{-1} below the corresponding high-spin state with $M_S = 5/2$. The optimised ground state geometry of $\mathbf{1}^-$ is shown in Figure 3.4.

In contrast to $\mathbf{1}^+$, where the negative spin density of -1.81 is evenly dispersed over the three ligand backbones, the situation is somewhat different for $\mathbf{1}^-$. In this case the ligand-centred electrons are more localised, and as a consequence, induce some asymmetry into the N=N bond distances. A vanishingly small spin density (0.04) on one of the ligands combined with a largely elongated N=N bond (1.40 Å) indicates that this ligand is doubly reduced. One occupied orbital of mainly ligand LUMO character is found in both the α- and β-manifold, unequivocally supporting the dianionic character of this ligand. Two unpaired spin-β electrons are localised on the other two ligands, with spin densities of -1.00 and -1.03, respectively (Table 3.1).

We were also able to optimise a high-spin $S = 7/2$ state. Bond metric data in combination with spin densities ($\rho_{Cr} = 4.03, \rho_L = 2.97$), unambiguously support a $[Cr^{II}(o\text{-Clpap}^{\cdot -})_3]^-$ electronic description. However, this state lies 25 kcal mol^{-1}

above the BS(3,2) ground state and therefore has not been considered further. Our calculations also dismiss the presence of a Cr^{V} ion in the surrounding of three closed-shell $(o\text{-Clpap})^{2-}$ ligands.

Our postulated ground state for the anionic complex and its formulation as an $[Cr^{III}(o\text{-Clpap}^{2-})(o\text{-Clpap}^{\cdot-})_2]^{-}$ electromer is in excellent agreement with results by Wieghardt et al. for two chromium complexes carrying ligands based on catechol and benzene-1,2-dithiol.[288,290] The calculated J coupling constant for $\mathbf{1}^{-}$ (-422 cm^{-1}) is somewhat smaller than the ones estimated for the tris(dioxolene)-chromium (-606 cm^{-1}) and tris(dithiolene)chromium (-714 cm^{-1}) complexes.

Dicationic and tricationic complexes $\mathbf{1}^{2+}$ and $\mathbf{1}^{3+}$

The trend of ligand-centred redox processes is continued in the last two members of the electron transfer series. The dication $\mathbf{1}^{2+}$ has a broken-symmetry triplet ground state, BS(3,1), with one spin-β electron delocalised over two of the ligands, while the third ligand has an almost vanishing spin density. This ligand is more loosely bound to the metal centre, with Cr-N distances of 2.10 and 2.22 Å. In contrast, the two radical anion ligands are much more tightly bound to the metal centre. This has already been attributed to the bonding nature of the ligand-metal interaction within the β-spin manifold. Analogous to $\mathbf{1}^{+}$, a LLCT band is observed in the TD-DFT-calculated excitation spectrum of $\mathbf{1}^{2+}$, which is also seen experimentally. It is important to note that such bands are not present in the computed and experimental UV-vis spectra of $\mathbf{1}^{0}$ and $\mathbf{1}^{3+}$, due to the absence of mixed valency in the ligand manifold. Thus, the TD-DFT calculation again supports the formulation of the ground state of $\mathbf{1}^{2+}$ as $[Cr^{III}(o\text{-Clpap}^{\cdot-})(o\text{-Clpap})_2]^{2+}$. In addition, we identified a local minimum on the PES corresponding to a $[Cr^{II}(o\text{-Clpap})_3]^{2+}$ formulation, being destabilised by 9.2 kcal mol^{-1} relative to the $M_S = 1$ ground

state. The geometry of this complex reveals a strong Jahn-Teller distortion.

The tricationic complex $[Cr^{III}(o\text{-Clpap})_3]^{3+}$ ($\mathbf{1}^{\mathbf{3}+}$) is a typical octahedral chromium(III) species, having three singly occupied orbitals in the t_{2g} set, which is notably stabilised due to exchange interaction. The excess of spin density on the metal ($\rho_{Cr} = 3.31$) is caused by spin polarisation effects of metal-ligand σ-bonds having metal e_g character. The calculated N=N bond lengths (1.26 Å) clearly confirm the presence of three neutral ligands. The contour plots of the Mulliken spin densities nicely demonstrate how the spin population on the Cr centre remains unchanged throughout the redox series $\mathbf{1}^{-/\mathbf{0}/+/\mathbf{2}+/\mathbf{3}+}$, preserving the cubic spin density typical for the $(t_{2g})^3$ configuration.[220]

Functional dependence

The functional sensitivity of the Mulliken population analysis of Cr complexes has been pointed out. Significantly different spin densities are obtained for the neutral and anionic complexes with BP86 and B3LYP, and this has implications for the redox state assignment for the metal centre and the ligands. Table 3.2 collects spin densities for the complexes investigated in this work, and catecholate complexes from work by Wieghardt[288] as well as Lay.[295] Indeed, we observe similar trends for some of the complexes that we have studied. As discussed above, the B3LYP calculations yield spin densities of 2.98 / -2.98 (using the notation metal/sum over three ligands) and 2.99 / -1.99 for the neutral and anionic complex, respectively. This is contrasted by the BP86 calculations, which place ∼2 unpaired electrons on the Cr ion in each case, resulting also in reduced spin densities on the ligands (-2.08 and -1.05 for the neutral and anionic complex, respectively). Thus, the latter (BP86) spin distributions would favour a description as $[Cr^{II}(o\text{-Clpap}^{\cdot -})_2(o\text{-Clpap})]^0$ and $[Cr^{II}(o\text{-Clpap}^{2-})(o\text{-Clpap}^{\cdot -})(o\text{-Clpap})]^0$.

Table 3.2: Comparison of calculated Mulliken spin densities for the broken-symmetry states of maximal antiferromagnetic coupling and their corresponding exchange coupling constants.

	S_t	Mulliken spin density B3LYP	BP86	J / cm^{-1} [a]
$\mathbf{1}^{\mathbf{3}+}$	$^3/_2$	3.31 / -0.31		
$\mathbf{1}^{\mathbf{2}+}$	1	2.91 / -0.91	2.66 / -0.66	-1565
$\mathbf{1}^{+}$	$^1/_2$	2.82 / -1.81	2.00 / -1.00	-1052
$\mathbf{1}^{\mathbf{0}}$	0	2.98 / -2.97	2.08 / -2.08	-706
$\mathbf{1}^{-}$	$^1/_2$	2.99 / -1.99	2.05 / -1.05	-422
$[Cr^{III}(L_{cat})_3]^{3-}$ [b]	$^3/_2$	3.03 / 0.00	2.98 / 0.00	
$[Cr^{III}(L_{sq}^{\cdot-})(L_{cat})_2]^{2-}$ [b]	1	2.80 / -0.47	2.34 / -0.34	-527
$[Cr^{III}(L_{sq}^{\cdot-})_2(L_{cat})]^{-}$	$^1/_2$	2.83 / -1.80	1.89 / -0.89	-606
$[Cr^{III}(L_{sq}^{\cdot-})_3]$	0	2.93 / -3.06	2.19 / -2.19	-475
$[Cr^{III}({}^{3,5}L_{S,S}^{\cdot-})_3]$ [c]	0	3.03 / -2.79	-	-732

[a] Coupling constant according to $\hat{H} = -2J\hat{S}_1 \cdot \hat{S}_1$.
[b] L_{cat} = *o*-catecholate, $L_{sq}^{\cdot-}$ = *o*-semiquinonate.
[c] ${}^{3,5}L_{S,S}^{\cdot-}$ = 3,5-di-*tert*-butylbenzene-1,2-dithiolate.

We favour the B3LYP results, owing to the fact that Hartree-Fock exchange is usually important in studies addressing spin state and exchange issues.[296]

3.3.2 Electronic structure of molybdenum compounds

Optimised geometries

Turning to the molybdenum analogues, a comparison of the optimised geometry of $\mathbf{2}^{\mathbf{0}}$ with that of $\mathbf{1}^{\mathbf{0}}$ (Figure 3.8 and Table 3.1) confirms that the more pronounced elongation of the N=N bond in the molybdenum systems is well reproduced, as are the key trends in M-N bond lengths. Thus whilst all Mo-N bonds are longer than their Cr-N counterparts, the elongation is more prominent in M-N_{py} (ΔM-N = 0.10 Å) than in M-N_{azo} (ΔM-N = 0.06 Å).

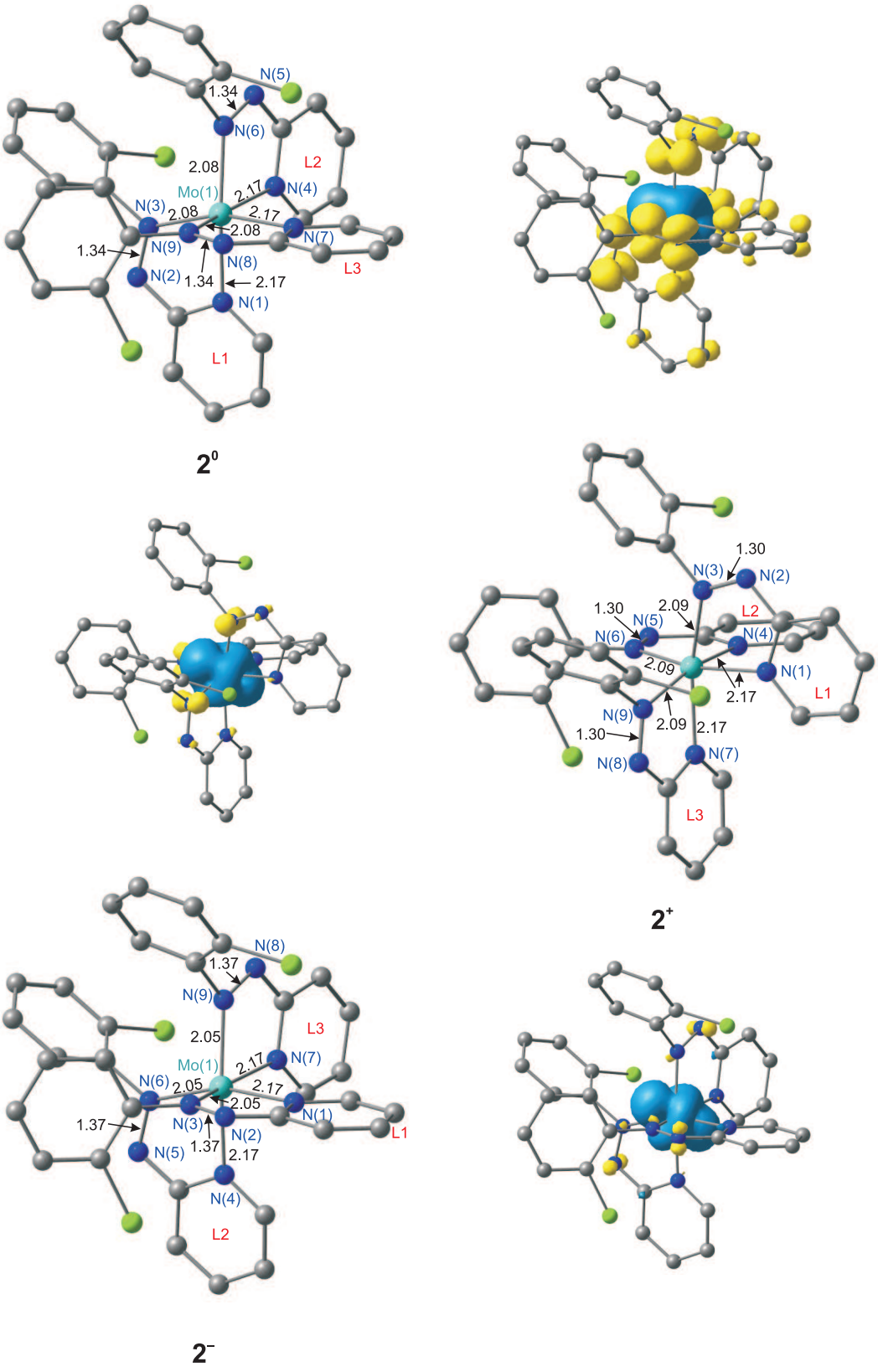

Figure 3.8: Optimised molecular structures (Å) of the ground states of complex $\mathbf{2^0}$ ($M_S = 0$), $\mathbf{2}^+$ ($M_S = 1/2$) and $\mathbf{2}^-$ ($M_S = 1/2$). [Original in colour]

Analysis of the electronic structure

The frontier Kohn-Sham orbitals of $\mathbf{2^0}$ are shown in Figure 3.9, and their compositions, along with those of $\mathbf{2}^+$ and $\mathbf{2}^-$, are collected in Table 3.3. The orbitals of $\mathbf{2^0}$ show the symmetry breaking typical of a metal radical complex, with the spin-α and spin-β components of each orbital localised in different regions of the molecule. Thus the three occupied spin-α orbitals (1a(α) and 1e(α)) are polarised towards the metal centre, and lie ∼3.0 eV below their vacant spin-β counterparts (2a(β) and 2e(β)). Conversely, the three singly occupied spin-β orbitals, (1a(β) and 1e(β)) are linear combinations of N=N π^* orbitals (>80% L), and lie only ∼2.0 eV below their vacant spin-α counterparts (2a(α) and 2e(α)).

The smaller exchange splitting in the ligand-based orbitals reflects the more diffuse nature of the singly-occupied orbitals. The compositions of the 1a(α/β) and 1e(α/β) orbitals also reveal a distinct anisotropy, in so much as the symmetry breaking is much less pronounced in the degenerate e orbitals, 1e(α) and 1e(β) (Mo:L = 51:49 and 20:80) than in 1a(α)/1a(β) (69:31 and 5:95). This anisotropy within the octahedral t_{2g} set has been noted by Ackermann and co-workers,[274] and stems from the presence of only a single orbital of π symmetry on each of the N donor atoms of the N=N unit (as opposed to 2 in a cylindrically symmetric π ligand such as X^- or CO). The result is that, despite sharing the same symmetry (a), the Mo d_{z^2} orbital (z defined here as the trigonal axis) is poorly oriented to overlap with the totally symmetric linear combination of N=N π^* orbitals. This distinction between the orbitals of a and e symmetry is further emphasised by the overlap (S_{ab}) between the corresponding orbitals (Figure 3.10), which is 0.36 for the a-symmetric pair but 0.89 for the e set.

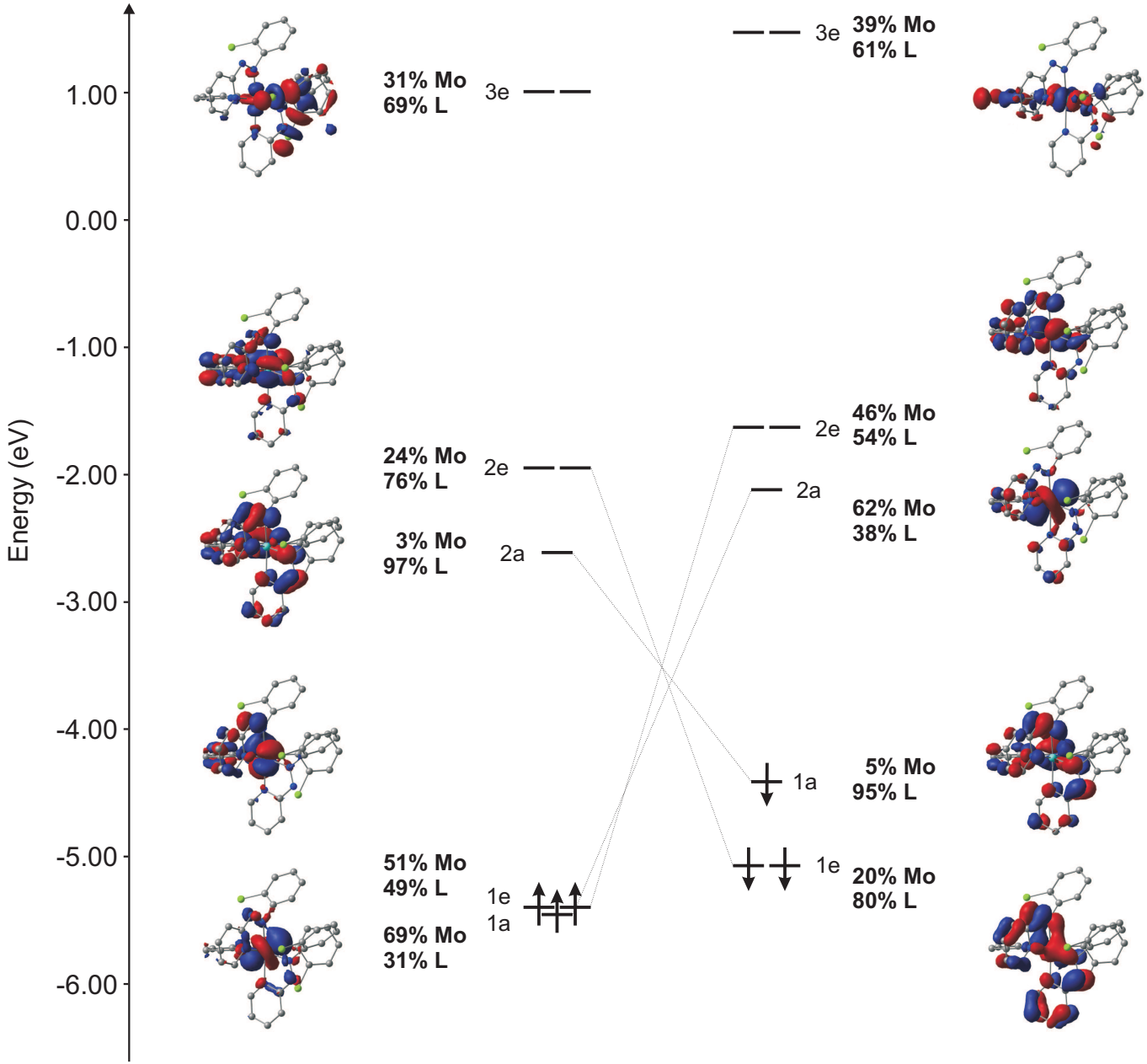

Figure 3.9: Frontier Kohn-Sham orbitals for $\mathbf{2^0}$. [Original in colour]

Table 3.3: Compositions of the frontier Kohn-Sham orbitals for $\mathbf{2}^{+}$, $\mathbf{2}^{\mathbf{0}}$ and $\mathbf{2}^{-}$. The gray shaded area indicates the HOMO in each case.

	$\mathbf{2}^{+}$		$\mathbf{2}^{\mathbf{0}}$		$\mathbf{2}^{-}$	
MO	Mo	L	Mo	L	Mo	L
3e(β)	48	52	39	61	34	66
3e(α)	56	44	31	69	31	69
2e(β)	43	57	46	54	41	59
2a(β)	65	35	62	38	58	42
2e(α)	30	70	24	76	38	62
2a(α)	2	98	3	97	4	96
1a(β)	4	96	5	95	9	91
1e(β)	32	68	20	80	27	73
1e(α)	49	51	51	49	35	65
1a(α)	69	31	69	31	68	32

In the chromium system $\mathbf{1}^{\mathbf{0}}$, the assignment of oxidation state was unambiguous: the spin density pattern, ρ_{M}, $\rho_{\mathrm{L}} \approx +3.0$, -1.0 is clearly consistent only with a $[\mathrm{Cr}^{\mathrm{III}}(\mathrm{L}^{\cdot -})_3]$ formulation. In cases such as $\mathbf{2}^{\mathbf{0}}$ where the radical character is not so pronounced, the oxidation state is more open to debate as it inevitably involves the somewhat arbitrary assignment of the shared electron density to one centre or the other. In the limit of complete symmetry breaking (i.e. where the spatial parts of the two spin components are quite distinct), as they are in $\mathbf{1}^{\mathbf{0}}$ (ρ_{M}, $\rho_{\mathrm{L}} = +3.0$, -1.0), a $[\mathrm{Mo}^{\mathrm{III}}\{\mathrm{L}_3\}^{3-}]$ formulation is clearly appropriate.

However when 1e(α) and 1e(β) are identical, the limiting spin densities of ρ_{M}, $\rho_{\mathrm{L}} = +1.0$, -0.33 could correspond to any point on a $[\mathrm{Mo}^{\mathrm{III}}\{\mathrm{L}_3\}^{3-}] \leftrightarrow [\mathrm{Mo}^{\mathrm{IV}}\{\mathrm{L}_3\}^{4-}] \leftrightarrow [\mathrm{Mo}^{\mathrm{V}}\{\mathrm{L}_3\}^{5-}]$ continuum, depending on whether the four electrons are viewed as being primarily ligand- or primarily metal-based. We note that the localisation of the occupied 1a(α) orbital on the metal centre precludes a $[\mathrm{Mo}^{\mathrm{VI}}\{\mathrm{L}_3\}^{6-}]$ formulation. The computed values of +1.86 and -0.62 for $\mathbf{2}^{\mathbf{0}}$ lie almost exactly midway between the two limits identified above, indicating substantial but not complete symmetry breaking in the 1e(α/β) orbitals. We return to the question of oxidation

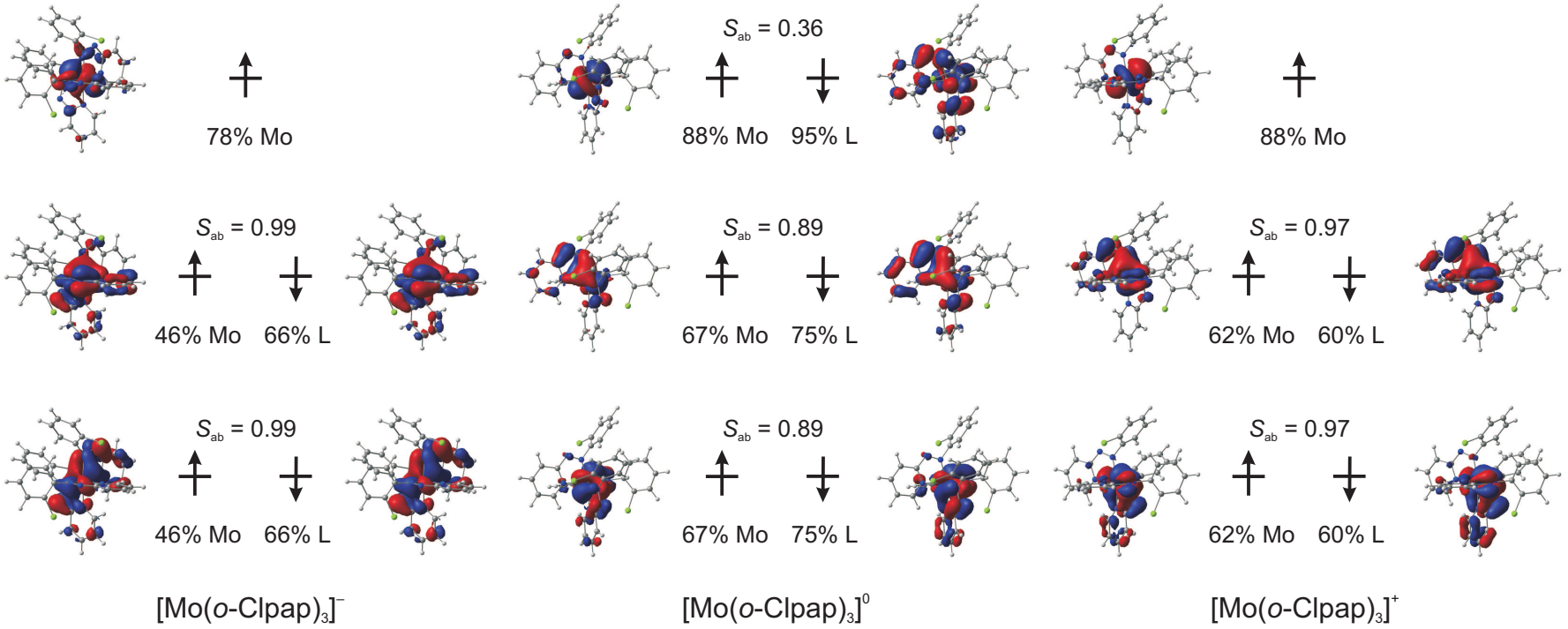

Figure 3.10: Corresponding orbitals for $\mathbf{2^0}$, $\mathbf{2^+}$ and $\mathbf{2^-}$. [Original in colour]

state following a discussion of the related cation and anion.

Oxidation of $\mathbf{2^0}$ generates $\mathbf{2}^+$ in an $M_S = {}^1/_2$ ground state (Figure 3.8), and the redox event can again be considered, at least to first order, as ligand-based because the redox-active orbital, 1a(β), remains strongly localised on the ligand array (96%). However, the changes in spin density at Mo (1.46 vs. 1.86 in $\mathbf{2^0}$, see Figure 3.8)[95] indicate that the metal is far from innocent, and the compositions of the orbitals in Table 3.3 confirm a substantial redox-induced redistribution of charge. Compared to $\mathbf{2^0}$, the occupied spin-β components of the 1e orbital are now much more evenly distributed over Mo (32%) and L (68%), and are spatially rather more similar to their spin-α counterparts (49% Mo, 51% L). The equalisation of the spatial parts of 1e(α) and 1e(β) is reflected in a further increase in the overlap of the corresponding orbitals ($S_{\mathrm{ab}} = 0.97$ vs. 0.89 in $\mathbf{2^0}$). These trends can be interpreted in terms of redox-induced stabilisation of the ligand-based orbitals resulting from removal of the electron in 1a(β), which enhances backbonding from Mo via the orthogonal degenerate e orbitals. Symmetry breaking is therefore less pronounced, and metal and ligand character more evenly distributed amongst 1e(α/β) and 2e(α/β).

We can again use the contrasting limits of complete symmetry breaking and complete delocalisation of the electrons in the 1e orbitals to define the possible range of spin densities. In the case that the spin components of the 1e orbital have identical spatial components, the limiting net spin densities would be +1.0 and 0.0. Complete symmetry breaking (i.e. localisation of 1e(α) and 1e(β) on metal and ligand, respectively), in contrast, would generate limiting spin densities of +3.0 and -0.66, very close to the values computed for $\mathbf{1}^+$. The computed values of 1.46 and -0.16 for $\mathbf{2}^+$ clearly lie much closer to the former limit, reflecting the pronounced backbonding in this case.

The net spin densities for the anion, $\mathbf{2}^{-}$ (M_S = ½ ground state) show striking similarities to the cation (ρ_{M}, ρ_{L} = 1.13 and -0.04 vs. 1.46 and -0.16, see also Figure 3.8), and are quite different from those of the neutral species (ρ_{M}, ρ_{L} = 1.86 and -0.66). The Kohn-Sham orbital compositions summarised in Table 3.3 confirm that the redox-active orbital is again the totally symmetric ligand-based combination, in this case the spin-α component 2a(α), and that this orbital remains almost entirely ligand-based (96% L) in the anion. The degree of symmetry breaking in the occupied 1e orbitals is again lower than in the neutral species: 1e(α), 35% Mo, 65% L; 1e(β), 27% Mo, 73% L, and the overlap of corresponding orbitals approaches unity (S_{ab} = 0.99). The reduced Mo character in the 1e(α) orbital (relative to $\mathbf{2}^{\mathbf{0}}$) is offset by an increase in the vacant 2e(α) (38% Mo vs. 24% in $\mathbf{2}^{\mathbf{0}}$), indicative of more effective backbonding in the anionic case.

The conclusion that a primarily ligand-based oxidation process to form $\mathbf{2}^{+}$ should induce further transfer of electron density from metal-to-ligand via a backbonding mechanism is intuitive, and can readily be rationalised on the basis of stabilisation of the ligand π^* manifold relative to the metal d orbitals. That a one-electron reduction should cause the same effect is somewhat counterintuitive, as we might expect a destabilisation of the ligand π^* manifold to reduce the effectiveness of the backbonding pathway. However, whilst one-electron oxidation and one-electron reduction clearly have very different effects on the total electron density at the ligand, both serve to reduce the net spin density, and therefore by extension the exchange splitting between the occupied spin-β and vacant spin-α components of the ligand π^* manifold. The reduction in spin density that accompanies either redox event therefore enhances the ability of the ligand array to both donate electron density to and accept electron density from the metal through the e orbitals, where overlap is effective.

In this context, the neutral system emerges as the outlier in the series $\mathbf{2}^{-}$ - $\mathbf{2^0}$ - $\mathbf{2}^{+}$ because the half-filled (N=N π^*)^3 shell makes the ligand array unusually resistant to loss or gain of further electron density from the metal.

Throughout the previous paragraphs we have avoided an assignment of formal oxidation states to the molybdenum centres, beyond noting that the neutral species lies somewhere along a continuum linking the three resonance structures $[\mathrm{Mo}^{\mathrm{III}}\{\mathrm{L_3}\}^{3-}] \leftrightarrow [\mathrm{Mo}^{\mathrm{IV}}\{\mathrm{L_3}\}^{4-}] \leftrightarrow [\mathrm{Mo}^{\mathrm{V}}\{\mathrm{L_3}\}^{5-}]$. The redox active orbital is almost entirely ligand-based, and therefore does not have any first-order impact on the physical oxidation state of the metal. The assignment therefore rests on whether the four electrons in the 1e orbital are allocated to the metal or the ligand in each case. In the anion, $\mathbf{2}^{-}$, 1e(α) and 1e(β) are both strongly localised on the ligand (65% and 73%, respectively), and so a limiting Mo^{V} form seems most realistic. The same is true of the cation, $\mathbf{2}^{+}$, although in this case the localisation of the 1e(α) orbitals on L is less clear cut (49:51). Both cation and anion therefore appear to lie towards the Mo^{V} end of the $[\mathrm{Mo}^{\mathrm{III}}\{\mathrm{L_3}\}^{3-}] \leftrightarrow [\mathrm{Mo}^{\mathrm{IV}}\{\mathrm{L_3}\}^{4-}] \leftrightarrow [\mathrm{Mo}^{\mathrm{V}}\{\mathrm{L_3}\}^{5-}]$ spectrum. In neutral $\mathbf{2^0}$ the process is further complicated by the symmetry breaking in the 1e orbital: the spin-β component is substantially localised on the ligand while the spin-α counterpart is delocalised over both metal and ligand (51:49). We noted above that the limit of complete symmetry breaking would correspond to a $[\mathrm{Mo}^{\mathrm{III}}\{\mathrm{L_3}\}^{3-}]$ situation, comparable to $[\mathrm{Cr}^{\mathrm{III}}\{\mathrm{L_3}\}^{3-}]$, $\mathbf{1^0}$. The net spin densities of $\mathbf{2^0}$ are clearly far from this limit, but nevertheless there is a distinct shift to the left in the continuum, with more ligand radical character relative to either $\mathbf{2}^{+}$ or $\mathbf{2}^{-}$. The presence of a half-filled (π^*)^3 shell in the neutral case appears to confer a degree of stability on the ligand array, blocking further electron transfer from the metal via backbonding.

3.4 A dinuclear mixed-valent complex containing 2-(4-chlorophenylazo)pyridine

The structural study of **3** reveals that the azoaromatic ligands host the Rh fragments in two completely different environments separated by 3.15 Å (Scheme 3.6). In the first compartment, Rh(1) is octahedrally coordinated to six strong σ donors: two chloro ligands, two axial pyridines and the lone pairs of the two azo nitrogen atoms, N(3) and N(6).

Scheme 3.6: Possible resonance forms for **3**.

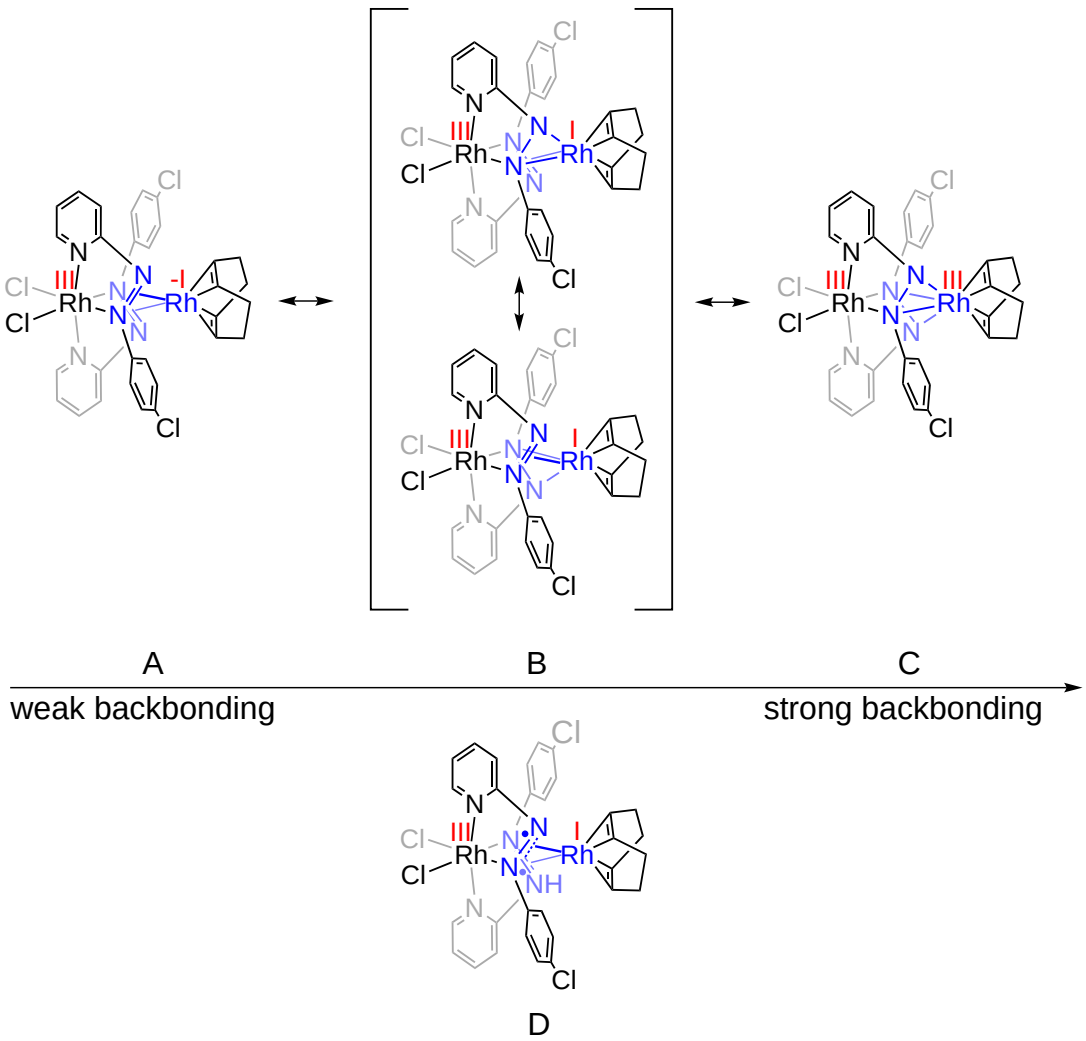

Rh(2), on the other hand, features an almost tetrahedral coordination sphere completed by four strong π-acidic ligands: two C=C double bonds of cod and the two azo functional groups, both coordinated in η^2-fashion. The two N-N bonds are elongated appreciably (1.413(4) and 1.399(4) Å) compared to typical values for the free diazo ligands (∼1.25 Å), or the radical anionic form that we have reviewed in detail in the context of the octahedral Cr and Mo complexes in the previous section.

Thus, the structure of **3** raises a number of important questions concerning the origin of the elongation of the N=N bonds, and related to this, the nature of the mixed valency. The octahedral coordination geometry about Rh(1) points to an unequivocal assignment as Rh^{III} a centre, but the assignment of a distinct oxidation state for the Rh(2) centre is more difficult. The interactions of the rhodium centre with each of the unsaturated ligands can be discussed in terms of two different scenarios. The electronic structure of **3** may be formulated as a $Rh^{I}Rh^{III}$ dimer with a single unpaired electron (α or β) localised on each of the two N=N units, antiferromagnetically coupled to give rise to an overall singlet state ($S = 0$). The latter is an requirement due to the observation that complex **3** is EPR-silent. Alternatively, the bond elongation might also indicate substantial backbonding from the rhodium centre. In this case two limiting resonance forms might be discussed, a Rh^{-I} diazene and a Rh^{I} metalla-azacycle,[297] the two differing in the extent of backbonding from the Rh-based d orbitals into the π^* orbital of the ligand. The different resonance forms for the scenarios described above are shown in Scheme 3.6, where structures A-C correspond to different degrees of backbonding and structure D refers to the diradical formulation.

Optimised geometries

In order to explore the nature of the mixed valency in the dirhodium complex in more detail we have optimised its geometry in different overall spin states. The most stable structure proves to be a closed-shell singlet state (^{1}**3**), shown in Figure 3.11 with optimised structural parameters fully consistent with those obtained crystallographically (Table 3.4). Importantly, the geometry of the Rh_2N_2 diamond core, shown in detail in Figure 3.12, is reproduced with encouraging accuracy.

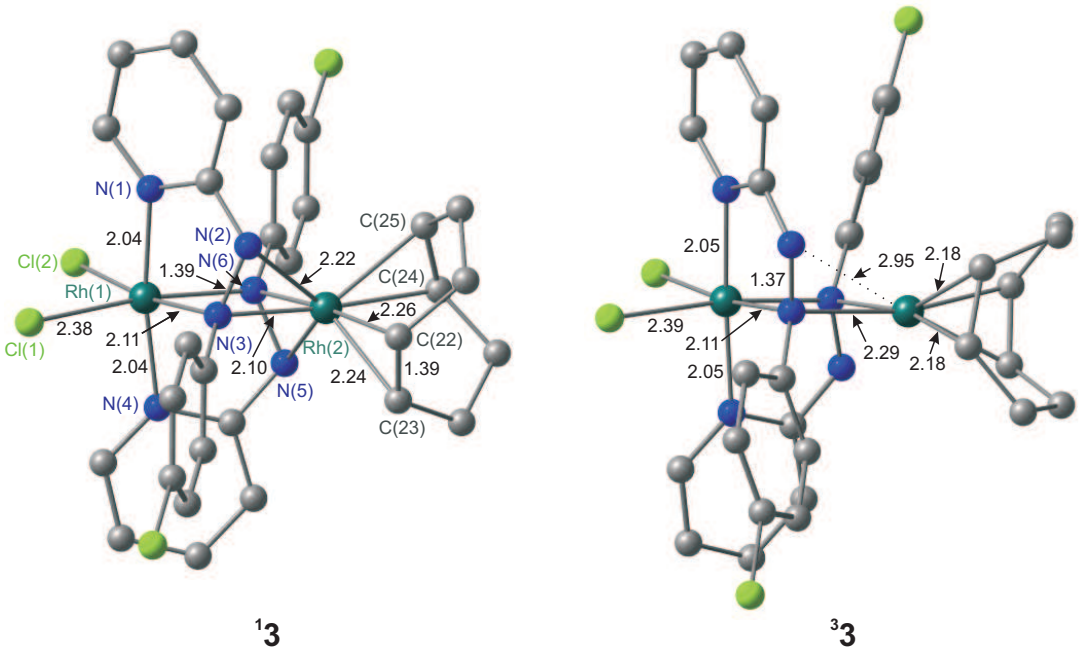

^{1}**3** ^{3}**3**

Figure 3.11: Optimised molecular structures (Å, °) of complex ^{1}**3** ($S = 0$) and ^{3}**3** ($S = 1$). [Original in colour]

The N=N bond lengths are calculated at 1.39 Å, close to the experimental value. The Wiberg bond index[298] of 1.16 for the N=N bonds in ^{1}**3** is substantially reduced from the free-ligand value of 1.77, consistent with the substantial backbonding apparent from the structural data. Within this framework, the electronic structure of ^{1}**3** lies somewhere on a continuum described by the resonance forms $Rh^{III}Rh^{-I}$ (A in Scheme 3.6) ↔ $Rh^{III}Rh^{I}$ (B) ↔ $Rh^{III}Rh^{III}$ (C). The situation in ^{1}**3** is, in

fact, conceptually rather similar to de Bruin's mixed-valent rhodium species noted above, where one of the centres is approximately square planar, implying a Rh^{I} oxidation state, while the second is approximately tetrahedral with an oxidation state of -I or I depending on the extent of backbonding, much like Rh(2) in **^{1}3**.

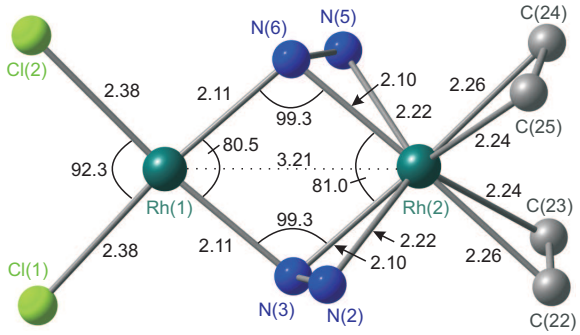

Figure 3.12: Optimised structure (Å, °) of the Rh_2N_2 diamond core of complex **^{1}3**. [Original in colour]

The twist angles $\phi^{\ddagger}$ of the coordinated π-ligands are remarkably similar in all three cases, lying in between those of a tetrahedral (90°) and square-planar (0°) geometry. The angle in **3** (59.8°) falls between those of [{Rh(nbd)}$_2$(μ-bpi)] (66.4°)[280] and [{Rh(cod)}$_2$(μ-bpi)] (56.5°),[281] all of which are clearly greatly distorted from square-planar and closer to the tetrahedral geometry. In the latter two cases the authors favoured a mixed-valent $Rh^{-I}Rh^{I}$ formulation on the grounds that the η^2-coordinated imine unit exhibits limited pyramidalisation and elongation of the C=N bond, both indicative of weak backbonding. In **^{1}3**, the η^2-N=N bonds are more strongly elongated relative to the free ligand and the coordinated nitrogen centres are significantly pyramidalised, suggesting that a metalla-azacycle formulation is more realistic in this case.

Within the confines of unrestricted (broken-symmetry) density functional theory, the diradical structure D is quite distinct from the $Rh^{I}Rh^{III}$ canonical form shown

‡The dihedral angle which is defined by the planes running through the centroids of the double bonds of each ligand and the metal centre.

Table 3.4: Selected experimental and optimised bond lengths (Å) and angles (°), as well as calculated relative energies (kcal mol^{-1}) for complex **3**.

Parameter	**3** (exp.)	^{1}**3**^{a}	^{3}**3**^{a}	^{BS}**3**^{b}
Energy^{c}		0.0 / 0.0	18.8 / 9.1	- / 7.8
Rh(1)-Rh(2)	3.149(4)	3.21	3.23	3.21
Rh(1)-N(3)	2.044(3)	2.11	2.14	2.11
Rh(1)-N(6)	2.043(3)	2.11	2.14	2.11
Rh(2)-N(3)	2.074(3)	2.10	2.29	2.24
Rh(2)-N(6)	2.083(3)	2.10	2.29	2.24
Rh(2)-N(2)	2.164(3)	2.22	2.95	2.89
Rh(2)-N(5)	2.183(3)	2.22	2.95	2.89
N(2)-N(3)	1.413(4)	1.39	1.36	1.35
N(5)-N(6)	1.399(4)	1.39	1.36	1.35
N(3)-Rh(1)-N(6)	81.22(12)	80.5	89.7	88.2
N(3)-Rh(2)-N(6)	79.57(11)	81.0	82.5	82.0
Rh(1)-N(3)-Rh(2)	99.72(13)	99.3	93.9	94.9
Rh(1)-N(6)-Rh(2)	99.47(12)	99.3	93.9	94.9
ϕ^{d}	59.8	56.5	10.1	7.2

[a]Structural data obtained with B3LYP.
[b]Only a minimum on the BHandHLYP PES.
[c]B3LYP / BHandHLYP.
[d]Dihedral angle between the planes defined by Ct(1)-Rh(2)-Ct(2) and Ct(3)-Rh(2)-Ct(4), where Ct1, Ct2, Ct3 and Ct4 are the centroids between N(2) and N(3), N(5) and N(6), C(22) and C(23), and C(24) and C(25), respectively.

in Scheme 3.6, where the electron density transferred to each ligand is not spin polarised. We have searched extensively for broken-symmetry singlet diradical structures using a range of spin-polarised initial guesses designed to mimic the anticipated density of the diradical (i.e. a single unpaired electron on each N=N unit) but in all cases the system converged back to the closed-shell configuration discussed above. A diradical electron density distribution can, however, be enforced with a triplet multiplicity, but this state lies 19 kcal mol^{-1} above the closed-shell singlet. Moreover, its optimised structure, also shown in Figure 3.11 is completely inconsistent with the X-ray structure. The C=C double bonds of the cod ligand rotate by ∼45° about the Rh-Rh axis to impose an approximately square planar coordination about Rh(2), typical of a Rh^{I} configuration. Decoordination of the

out-of-plane nitrogen atoms N(2) and N(5) from the Rh(2) centre increases the Rh-N distance to ∼3 Å. At the same time, the Rh_2N_2 core experiences some distortion, since Rh(2) moves outward and notably increases the distance to the in-plane nitrogen atoms N(2) and N(5) by ∼0.2 Å. We anticipated that functionals with greater HF exchange will stabilise the radical forms relative to their closed-shell alternatives, and indeed with BHandHLYP (50% HF exchange) we have been able to locate the broken-symmetry singlet 1.3 kcal mol^{-1} below the triplet, and with very similar structure (Table 3.4). Contour plots of the spin density in both the triplet and broken-symmetry singlet state are shown in Figure 3.13, confirming the non-innocent radical character of both pap ligands. Figure 3.14 shows the localisation of the frontier molecular orbitals on the two ligands in the broken-symmetry singlet ($M_S = 0$).

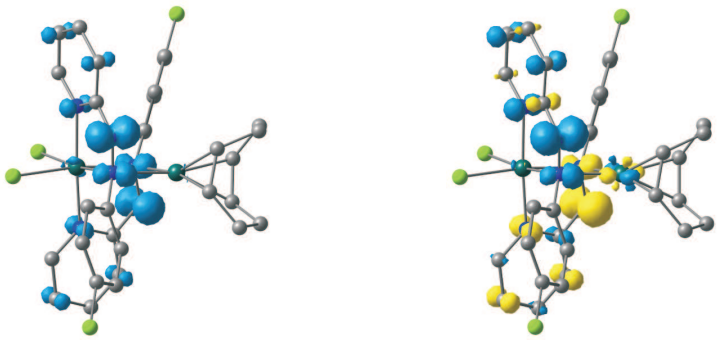

(a) (b)

Figure 3.13: Contour plots of the Mulliken spin density for the (a) triplet and (b) BS singlet. [Original in colour]

However, the broken-symmetry state remains 7.8 kcal mol^{-1} above its closed-shell analogue, and the fact that the diradical state remains relatively unstable even with the most 'forcing' of functionals offers convincing evidence that the $Rh^{III}Rh^{-I}$ formulation is more reasonable, and the computed data therefore lead us to reject the ligand diradical formulation shown in Figure 3.6 D as unrealistic in this case.

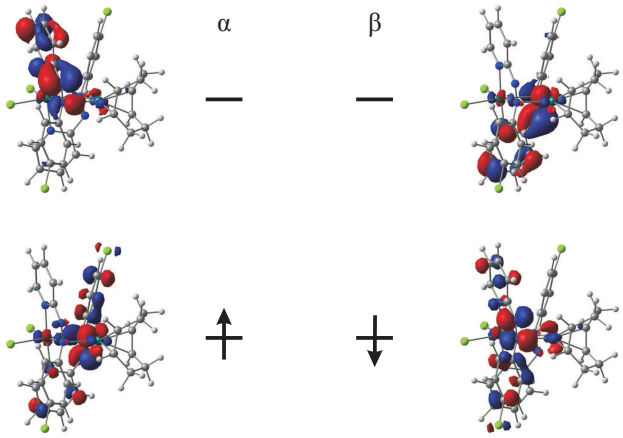

Figure 3.14: Singly occupied MOs of the broken-symmetry singlet minimum (BHandHLYP). [Original in colour]

Topological analysis of the electron density

The closed-shell singlet ground state of complex **3** is in principle consistent with a Rh^{II}-Rh^{0} formulation with a dative metal-metal bond formation. However, this appears inconsistent with the large Rh-Rh separation of 3.21 Å noted earlier.

As a complementary approach we have analysed the topological properties of the calculated electron density $\rho(\mathbf{r})$, using Bader's Atoms In Molecules (AIM) theory. The essence of AIM theory is to represent the main features of the electron density in compact form in terms of critical points, i.e. the points in space where the gradient of the density is zero, $\nabla\rho(\mathbf{r}) = 0$. A critical point that is characterised by one positive and two negative curvatures, termed (3,-1), is referred to as a bond critical point (BCP) and is considered to be diagnostic of the presence of a chemical bond. Critical points characterised by one negative and two positive curvatures, termed (3,+1), are associated with the presence of rings and are referred to as ring critical points (RCP). The topological properties of the electron density $\rho(\mathbf{r})$ and its Laplacian $\nabla^2\rho(\mathbf{r})$ at BCPs allow for the characterisation of chemical interaction between atoms.[299] Large positive values of $\rho(\mathbf{r})$ combined with negative values of $\nabla^2\rho(\mathbf{r})$ are indicative of shared-shell (covalent) interactions, while positive values

for both $\rho(\mathbf{r})$ and $\nabla^2\rho(\mathbf{r})$ are identified with closed-shell (ionic) interactions. It has been stated that the characterisation of bonding interactions based on $\nabla^2\rho(\mathbf{r})$ alone is insufficient.[300] Therefore, in addition to inspecting sign and magnitude of $\rho(\mathbf{r})$ and $\nabla^2\rho(\mathbf{r})$, energetic aspects at BCPs need also to be considered. Several schemes have been suggested based on the total energy density $H(\rho)$, the kinetic energy density $G(\rho)$ and the potential energy density $V(\rho)$.[300–302] Negative values of $H(\rho)$ and $|V(\rho)| > G(\rho)$ are associated with shared-shell (covalent) interactions, as opposed to closed-shell interactions for which $H(\rho)$ is positive and $|V(\rho)| < G(\rho)$.[303–305]

Characteristic topological parameters for selected critical points in complex **[1]3** are collected into Table 3.5. Our analysis confirms that no BCP is present between the Rh centres. Instead, a RCP is located at the centre of the Rh_2N_2 diamond (Figure 3.15a), and the negligible density at this point ($\rho(\mathbf{r}) = 0.03$ e au^{-3}) confirms the absence of direct overlap between the two Rh atomic basins.

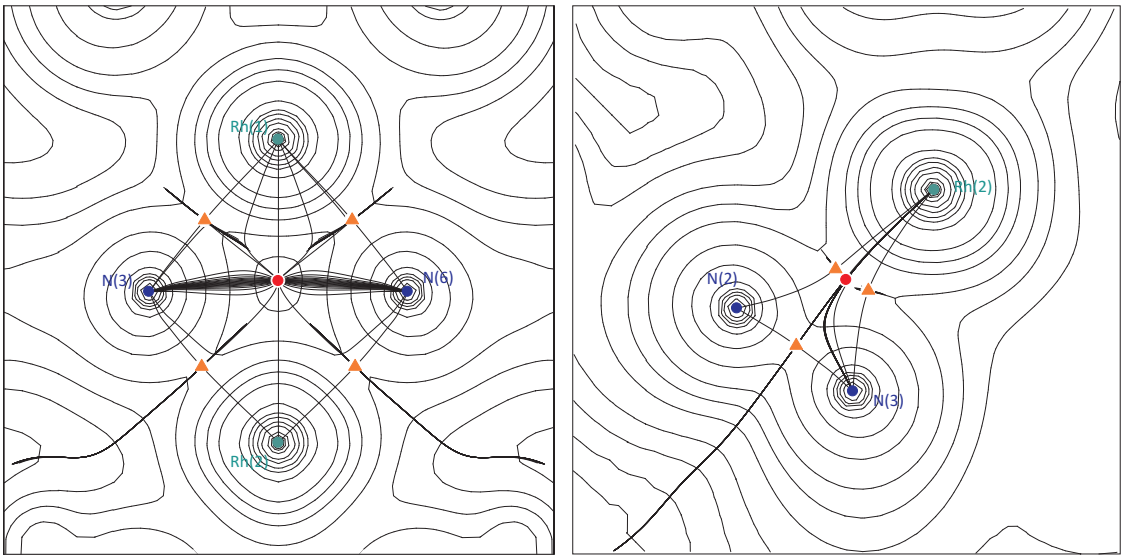

(a) (b)

Figure 3.15: Contour maps of the electron density of $[Rh_2(\mu_2\text{-}p\text{-Clpap})_2(cod)Cl_2]$. (a) Plane defined by Rh(1)Rh(2)N(3)N(6). (b) Plane defined by Rh(2)N(2)N(3). Bond critical points are represented by orange triangles, ring critical points by red circles, bond paths are shown by solid lines.

Table 3.5: Electron density ρ ($\mathrm{e\,au^{-3}}$), Laplacian of the electron density $\nabla^2\rho$ ($\mathrm{e\,au^{-5}}$), ellipticity ε, Hessian eigenvalues λ_i, and energy densities (au) at bond and ring critical points of **1**3. Values obtained using the coordinates from the crystal structure are given in italics.

CP	$\rho(\mathbf{r})$	$\nabla^2\rho(\mathbf{r})$	ε	λ_1	λ_2	λ_3	H(ρ)	G(ρ)	V(ρ)
BCPs									
Rh(1)-N(3)	0.093 *0.106*	0.323 *0.471*	0.440 *0.083*	-0.125 *-0.110*	-0.087 *-0.102*	0.535 *0.684*	-0.016 *-0.018*	0.096 *0.136*	-0.112 *-0.154*
Rh(1)-N(6)	0.093 *0.107*	0.323 *0.476*	0.440 *0.084*	-0.125 *-0.110*	-0.087 *-0.102*	0.535 *0.688*	-0.016 *-0.018*	0.096 *0.137*	-0.112 *-0.155*
Rh(2)-N(3)	0.085 *0.100*	0.375 *0.385*	0.818 *0.067*	-0.050 *-0.118*	-0.028 *-0.110*	0.454 *0.614*	-0.013 *-0.018*	0.107 *0.114*	-0.120 *-0.132*
Rh(2)-N(6)	0.085 *0.099*	0.375 *0.378*	0.818 *0.063*	-0.050 *-0.116*	-0.028 *-0.109*	0.454 *0.602*	-0.013 *-0.017*	0.107 *0.112*	-0.120 *-0.129*
Rh(2)-N(2)	0.084 *0.081*	0.233 *0.319*	1.265 *0.244*	-0.064 *-0.088*	-0.028 *-0.071*	0.325 *0.478*	-0.014 *-0.011*	0.073 *0.092*	-0.087 *-0.103*
Rh(2)-N(3)	0.085 *0.100*	0.375 *0.385*	0.818 *0.067*	-0.050 *-0.118*	-0.028 *-0.110*	0.454 *0.614*	-0.013 *-0.018*	0.107 *0.114*	-0.120 *-0.132*
N(2)-N(3)	0.248 *0.320*	0.335 *-0.548*	0.405 *0.087*	-0.511 *-0.711*	-0.363 *-0.654*	1.209 *0.817*	-0.167 *-0.300*	0.250 *0.163*	-0.417 *-0.463*
Rh(2)-C(22)	0.058 *0.083*	0.235 *0.193*	1.059 *0.389*	-0.035 *-0.077*	-0.017 *-0.055*	0.287 *0.326*	-0.006 *-0.020*	0.066 *0.068*	-0.072 *-0.088*
Rh(2)-C(23)	0.062 *0.085*	0.257 *0.190*	0.993 *0.356*	-0.044 *-0.083*	-0.022 *-0.061*	0.322 *0.334*	-0.007 *-0.021*	0.071 *0.069*	-0.078 *-0.090*
C(22)-C(23)	0.332 *0.316*	-0.925 *-0.872*	0.187 *0.224*	-0.701 *-0.662*	-0.591 *-0.541*	0.366 *0.331*	-0.331 *-0.329*	0.100 *0.112*	-0.431 *-0.441*
Rh(1)-N(1)	0.135 *0.112*	0.420 *0.533*	0.182 *0.138*	-0.202 *-0.120*	-0.171 *-0.105*	0.794 *0.758*	-0.027 *-0.019*	0.132 *0.153*	-0.159 *-0.172*
Rh(1)-N(4)	0.135 *0.111*	0.420 *0.529*	0.182 *0.145*	-0.202 *-0.117*	-0.171 *-0.102*	0.794 *0.748*	-0.027 *-0.019*	0.132 *0.151*	-0.159 *-0.170*
RCPs									
Rh(2)N_2	0.084 *0.076*	0.268 *0.414*		-0.057 *-0.079*	0.019 *0.084*	0.305 *0.409*			
Rh_2N_2	0.032 *0.033*	0.097 *0.136*		-0.014 *-0.028*	0.047 *0.060*	0.064 *0.104*			
Rh(2)C_2	0.057 *0.079*	0.287 *0.307*		-0.035 *-0.067*	0.015 *0.042*	0.307 *0.332*			

In contrast, BCPs were located between each of the nitrogen atoms in the azo groups and the rhodate centre (Figure 3.15b), along with ring critical points at the centre of both N-N-Rh triangles, a situation characteristic of strong Rh-(N=N) backbonding. Examining the data relating to the four types of Rh-N bonds, the topological parameters at the respective BCPs reflect the relative strengths of the interactions, decreasing in the order Rh(1)-N(1)/N(4) (pyridine) > Rh(1)/Rh(2)-N(3)/N(6) (azo) > Rh(2)-N(2)/N(5) (azo). This trend is paralleled by the bond lengths, which increase along this series. The small negative values of $H(\rho)$ and $|V(\rho)| > G(\rho)$ associated with all of the Rh-N interactions suggest that all of them have some degree of shared-shell interaction despite the positive values for the Laplacian. For example, small positive values of $\rho(\mathbf{r})$ ($\sim$0.08 e au^{-3}) and $\nabla^2\rho(\mathbf{r})$ (0.233 and 0.375 e au^{-5}) for the BCPs between Rh(2) and the azo N atoms combined with a negative $H(\rho)$ (-0.014 au) reveal some covalent character in these interactions. The substantially reduced values of $H(\rho)$ for the interactions between Rh(2)-C(22) (-0.006 au) and Rh(2)-C(23) (-0.007 au) are indicative of weaker interactions of the Rh centre with the C=C groups of cod than those with the pap N=N groups. Interestingly, while $\rho(\mathbf{r})$ (0.332 e au^{-3}), $\nabla^2\rho(\mathbf{r})$ (-0.925 e au^{-5}) and $H(\rho)$ (-0.331 au) at the C(22)-C(23) BCP are unequivocal of a strong covalent interaction between the carbon atoms, as one would expect, the Laplacian at the N(2)-N(3) BCP is positive (+0.335 e au^{-5}), which is somewhat counterintuitive. Nonetheless, the large value of $\rho(\mathbf{r})$ (0.248 e au^{-3}) and the pronounced negative value of $H(\rho)$ (-0.167 au) strongly favour a covalent interaction.

The bond path curvature is frequently used to identify the nature of atomic interactions. As an example, the interpretation of bond paths for a silver(I) acetylene complex has been debated in the literature.[306–308] In the limit of a purely ionic interaction a T-shaped bond path geometry would be expected with a BCP between

Rh(2) and the N-N bcp. The presence of some degree of covalency gives rise to the observed concave cyclic structure and the corresponding BCPs and the RCP at the ring centre.[309] The concave curvature of a bond path decreases as the covalency of the interaction increases, eventually leading to a true metallacycle. The curved nature of the Rh(2)-N bond paths suggests that while shared-shell character is present in the interaction, a metalla-azacyle formulation has not been fully approached, which would result in a triangular bond path geometry with straight lines for the Rh-N bond paths. The electron densities $\rho(\mathbf{r})$ at the $Rh(2)N_2$ RCP and Rh(2)-N BCPs do not differ significantly, and are indicative of a rather flat charge density distribution inside the Rh(2)N(2)N(3) cycle. This flatness is also reflected in the high bond ellipticities at the Rh(2)-N BCPs (1.26 and 0.82). It is well known that $\rho(\mathbf{r})$ is sensitive towards small changes in the geometry or the chosen method to model the electron density. As a consequence small changes in the electron density of the Rh(2)N(2)N(3) bonding region have a significant influence on the bond path profile.[310]

We have thus also analysed the topology of $\rho(\mathbf{r})$ using the coordinates of the experimentally determined structure of complex **3**. These results have also been included in Table 3.5, which are given in italics to differentiate them from the computational model. While most topological parameters are largely left unaffected, the most significant change occurs in $\nabla^2\rho(\mathbf{r})$ of the N(2)-N(3) bond, which has now adopted a large negative value (-0.548 $\mathrm{e\,au^{-5}}$), expected for a covalent interaction. Perhaps most strikingly, the bond path profile of the Rh(2)N(2)N(3) ring shown in Figure 3.16a is now less concave, compared to the profile obtained from the optimised geometry of **3**. Thus, the triangular shape suggests a somewhat increased covalent character to the Rh(2)-N bonds, indicating a further advanced transition towards a true metalla-azacycle formulation.

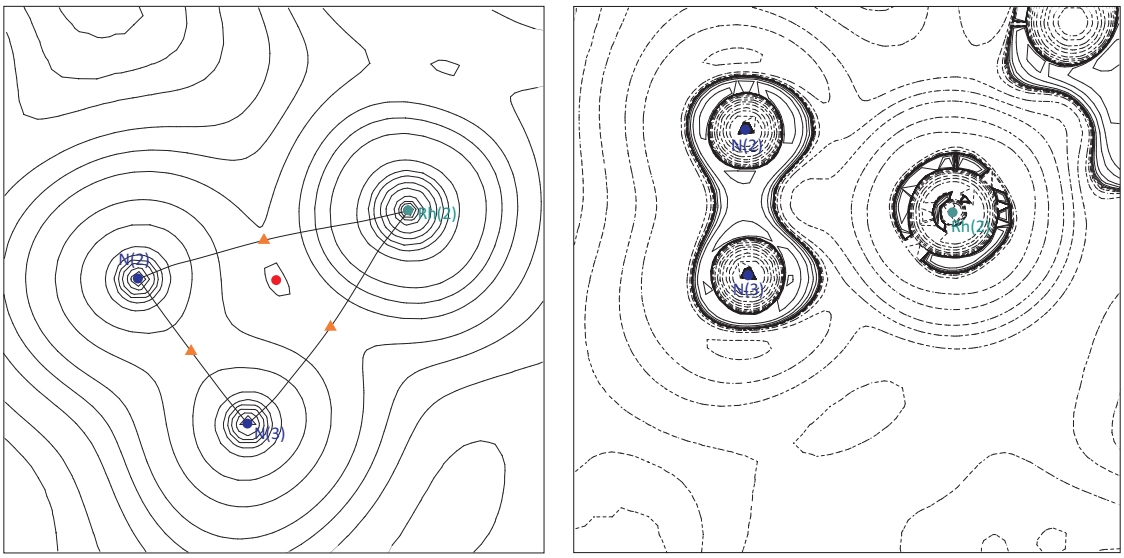

(a) (b)

Figure 3.16: Contour maps in the Rh(2)N(2)N(3) plane for $[Rh_2(\mu_2\text{-}p\text{-Clpap})_2(cod)Cl_2]$ using the X-ray structure. (a) Electron density. Bond critical points are represented by orange triangles, ring critical points by red circles, bond paths are shown by solid lines. (b) Negative Laplacian of the electron density, $L(\mathbf{r}) = -\nabla^2\rho(\mathbf{r})$. Positive contours are represented by solid lines, dashed lines correspond to negative contours.

Examining the plot (Figure 3.16b) of the negative of the Laplacian[§] in the Rh(2)N(2)N(3) plane further corroborates this assertion. The deformation of $L(\mathbf{r})$ on the N atoms indicates some substantial charge concentration directed towards the metal centre along the Rh(2)-N bond vectors.

Comparable topological fingerprints to the one of **3** have been reported in the literature for $Ni(cod)_2$ and $W(CO_5)(C_2H_4)$, for both of which a π-complex has been found.[309,311,312] The energy density characteristics for the $Rh(2)N_2$ unit are very similar to the one for the WC_2 unit in $W(CO_5)(C_2H_4)$. In both cases the energy density $H(\rho)$ at the M-L BCPs are rather small (weak covalency), while $H(\rho)$ for each intraligand bond has a large negative value (strong covalency). In contrast, in the complex $W(Cl_4)(C_2H_4)$, which is considered as metallacycle with covalent W-C bonds, the energy density at the W-L BCPs is clearly more negative.

[§]It is convention to use plots of $L(\mathbf{r}) = -\nabla^2\rho(\mathbf{r})$ instead of the Laplacian itself, because of the more intuitive association of charge depletion and concentration with $L(\mathbf{r}) < 0$ and $L(\mathbf{r}) > 0$, respectively.

Moreover, by visual inspection, the distortion of the Laplacian field in the the Rh(2)N(2)N(3) plane seems to lie somewhere in between the ones found for $Ni(cod)_2$ and $W(CO_5)(C_2H_4)$, but is clearly less pronounced than in $W(Cl_4)(C_2H_4)$.[309,311] Thus, based on the asymmetric energy densities at the Rh-N and N-N BCPs, as well as the Laplacian field, the data appear to favour a donor-acceptor interaction between Rh(2) and the azo group.

In summary, despite the fact that the presence of bond critical points between Rh(2) and each of the four nitrogen centres is consistent with a metalla-azacycle structure, the electron density distribution in $^{\mathbf{1}}\mathbf{3}$ appears to lie somewhere between the $Rh^{I}Rh^{III}$ and $Rh^{III}Rh^{III}$ canonical forms shown in Scheme 3.6. The transfer of substantial electron density to each of the diazene ligands according to the classical Dewar-Chatt-Duncanson model[313,314] is fully consistent with the observed elongation of the N=N bond lengths. The situation in the closed-shell complex may be compared to a series of Rh^{0} radical complexes, including $[Rh^{0}(cod)_2]^{\cdot}$, for which significant delocalisation of spin density towards the ligands has been found, leading to the notion that, "none of these compounds should be regarded as true Rh^{0} d^9 metal centred radicals nor as Rh^{I} complexes of ligand centred radicals".[315]

3.5 Conclusions

A comprehensive survey of redox isomers along the $[M(o\text{-Clpap})_3]^n$ (M = Cr: n = 1–, 0, 1+, 2+, 3+, M = Mo: n = 1–, 0, 1+) electron transfer series has been carried out, using the broken-symmetry DFT formalism. The electronic structure of the neutral chromium complex $[Cr(o\text{-Clpap})_3]^0$ has been unequivocally established. It contains a high-spin chromic ion (S_{Cr} = 3/2) coupled to three ligand-radical anions, leading to an $S = 0$ ground state, and is essentially identical with the well-characterised neutral chromium complexes with catecholate ligands. The

four redox events that connect the electron-transfer series $[Cr(o\text{-Clpap})_3]^n$ (n = 3+, 2+, 1+, 0, 1–) correspond to entirely ligand-based redox processes, with the central chromium ion remaining invariantly in the +III oxidation state throughout (Scheme 3.7). As a result the N=N bond lengths contract upon successive oxidation, and those in the trication ($M_S = {}^3/_2$) approach the values for the free ligand (∼1.24 Å). The robustness of the Cr^{III} centre results largely from the very high exchange energies associated with the $(t_{2g})^3$ configuration.

Scheme 3.7: Electron transfer series of **1**.

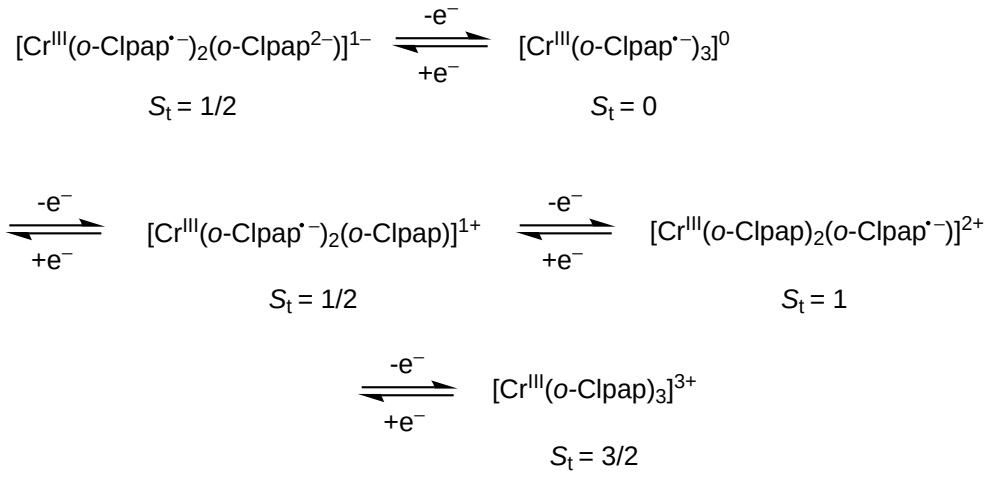

The electronic structure of the molybdenum systems is more complex because of extensive mixing of metal- and ligand-based orbitals of e symmetry. The three redox isomers $[Mo(o\text{-Clpap})_3]^n$ (n = 1+, 0, 1–) lie on a continuum connecting the resonance forms $[Mo^{III}\{L_3\}^{3-n}] \leftrightarrow [Mo^{IV}\{L_3\}^{4-n}] \leftrightarrow [Mo^{V}\{L_3\}^{5-n}]$, with the orbital compositions and spin densities being most consistent with the higher-oxidation-state end of the spectrum. While the electron density distribution in the cation and anion $\mathbf{2}^+$ and $\mathbf{2}^-$ is remarkably similar (differing only in the occupations of the totally symmetric combination of ligand-based π^* orbitals) and is close to the $[Mo^{V}\{L_3\}^{5-n}]$ limit, the intervening neutral species has much more

extensive ligand-radical character.

The assignment of distinct oxidation states within the dinuclear complex $[Rh_2(\mu_2\text{-}p\text{-Clpap})_2(cod)Cl_2]$ is difficult, owing to the possibility of several valence resonances. Certainly there is no evidence for the ligand radical character we observed in the Cr and Mo complexes. An analysis of the topology of the electron density confirms the presence of bond critical points between each pair of atoms in the RhNN entity, suggesting substantial covalence withing the bridge. This data is most consistent with a model involving two limiting resonance forms for each individual RhNN entity, a Rh^{-I} diazene and a Rh^{I} metalla-azacycle, although backbonding from the Rh^{-I} is extensive and the latter metalla-azacycle resonance appears more appropriate. Nonetheless, the two metal centres in the complex can formally be considered as $Rh^{-I}Rh^{III}$.

The implications of the electronic model, however, are clear – the delocalisation of electron density over the $Rh(NN)_2$ unit stabilises a highly reducing environment, apparent from the complex's capability to activate O_2, ultimately leading to the activation of a total of two C-H bonds. Hence, the reactivity of **3** can be viewed to truly fall into the concept of 'non-innocence in catalysis', as the ligands store and release electrons for the hydroxylation reaction. For the reaction itself it is insignificant whether the metal ion is a genuine rhodate in a physical sense, or not, as long as the reducing equivalents are provided by an overall electron-rich metal-ligand unit.

The mechanistic details of the hydroxylation reaction remain unsolved, but a complex reaction coordinate including multiple hypersurfaces (spin crossover) is likely to be involved. Thus, in future work we are seeking to establish a direct causal link between ground state electronic structure, and this remarkable reactivity pattern. The above examples demonstrate that redox non-innocence is a

complex phenomenon, and is not necessarily synonymous with ligand radical character. Establishing patterns in the behaviour of apparently very different classes of molecules is one of the key roles for computational chemistry.

4

Endohedral Zintl Ions

The chemistry of Zintl clusters has long attracted the interest of theoreticians, but has been rejuvenated in the past decade by the disovery of large endohedral clusters containing transition metals, which may act as quantum dots. A number of novel species have been isolated to date, revealing a rich structural variety with surprising electronic configurations. In this chapter we develop a detailed description of the electronic structure of unprecedented open-shell endohedral Zintl anions, including the 12-vertex species $[Mn@Pb_{12}]^{3-}$, as well as the two 10-vertex clusters $[Fe@Ge_{10}]^{3-}$ and $[Fe@Sn_{10}]^{3-}$. This research is done in collaboration with the Goicochea group, who have synthesised and structurally characterised these clusters. The $[Mn@Pb_{10}]^{3-}$ cluster shows strong distortions from perfect I_h symmetry along a D_{2h}-symmetric coordinate. The $[Fe@Ge_{10}]^{3-}$ species adopts an archimedian pentagonal prismatic geometry encapsulating an isolated iron atom core, while the isoelectronic tin homologue, in contrast, contains a deltahedral cage typical of electron deficient clusters. This structural chemistry is difficult to rationalise in terms of any existing bonding theory for clusters, and our aim is to understand the factors that influence the stability of a particular geometry and the interactions between the main group metals within the cages and the ions at the centre of these cages. The results of the first part have been reported in Ref. [430], while those reported in the second part have been submitted to *J. Am. Chem. Soc* recently.

4.1 Introduction

Historical development

Polyatomic anions of the post-transition elements have been known since the early work of Joannis in 1891,[318–320] who discovered that the reduction of elemental lead with sodium in liquid ammonia gave green solutions containing a yet unknown type of lead anion. Following contributions by few other authors,[321–324] the compositions of anionic species such as $[Pb_9]^{4-}$, $[Sn_9]^{4-}$, $[Sb_7]^{3-}$ and $[As_7]^{3-}$ were finally established by Zintl,[325–329] who investigated their chemistry in the early 1930s. Because of his seminal work in the field, bare anionic cluster compounds became subsequently named in his honor. Since their discovery some 100 years ago, a plethora of new Zintl compounds has been isolated and characterised, and the developments in the field have been covered in a number of reviews.[330–335]

Major improvements in Zintl cluster synthesis[336] and crystallisation techniques facilitated their structural characterisation by means of X-ray diffraction methods, making it possible to establish the inter-atomic connectivities within the clusters for the first time. As a result, the existence of Group 14 and Group 15 polyanions was finally verified by the crystal structure determination of a number of clusters, including $[E_9]^{3-}$, $[E_9]^{4-}$ and $[E_5]^{2-}$ (E = Ge, Sn, Pb), $[Pn_7]^{3-}$ and $[Pn_{11}]^{3-}$ (Pn = As, Sb), as well as $[Sb_4]^{2-}$ and $[Bi_4]^{2-}$ (Figure 4.1).[332,334,335,337] This development, driven forward by the studies of Corbett and his co-workers in the 1960s, heralded the dawn of modern Zintl and post-transition element cluster chemistry.

With the crystal structures at hand, it was soon realised that the cluster bonding could not easily be explained in terms of 2-centre-2-electron bonds, and a delocalised model was required. Attempts to establish the relationship between geometry and electronic structure of the polyhedra resulted in the development of

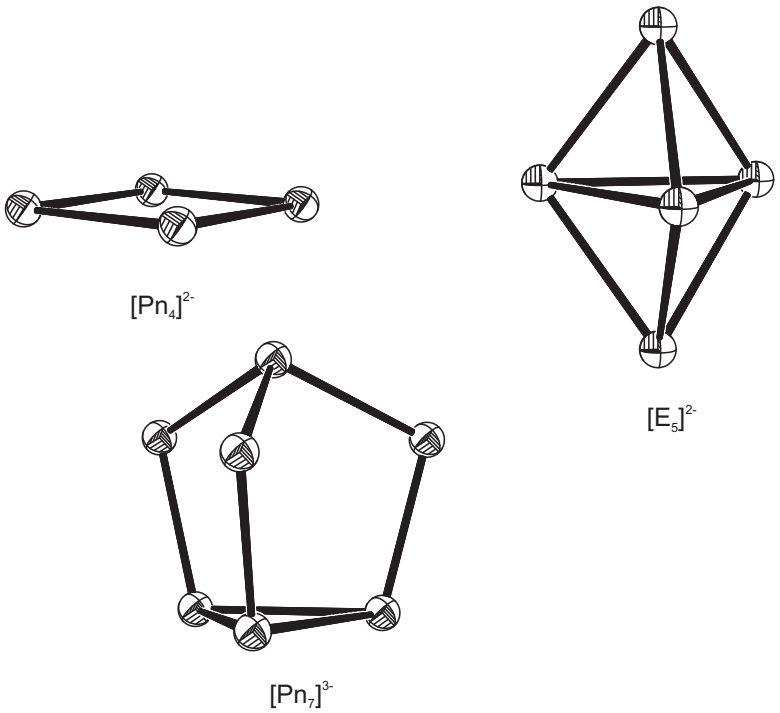

Figure 4.1: Some early examples of Zintl clusters, including $[Pn_4]^{2-}$ (Pn = Sb, Bi), $[E_5]^{2-}$ (E = Ge, Sn, Pb) and $[Pn_7]^{3-}$ (Pn = As, Sb).

several concepts. Perhaps the most successful of these ideas originated when the analogy between the topologies of the bare post-transition metal clusters and the cage-like boranes was recognised.

Wade-Mingos electron counting rules

The Wade-Mingos rules for electron counting,[338–341] originally designed to rationalise the electronic structure of electron deficient boranes, were extrapolated to Zintl clusters. Applied to boranes, the quintessential assertion of the Wade-Mingos formalism is that closed deltahedral (*closo*) boranes with n vertices are stabilised in case that $2n + 2$ valence electrons are available for occupation of $n + 1$ skeletal bonding molecular orbitals. Importantly, the number of bonding skeletal molecular orbitals is not explicitly dependent on whether all vertices of the deltahedral structure are occupied or not. As a consequence, n-atomic *nido* and *arachno* clusters (derived from the *closo* deltahedra by removal of one or two vertices) require

$2n + 4$ and $2n + 6$ skeletal electrons. The origin of these rules can be understood from MO arguments, and the octahedron and square-pyramid (*nido* octahedron) serve as illustrative examples in deriving the relevant molecular orbital schemes.[342,343]

Each vertex (boron atom) of the deltahedron provides a set of two sp hybrid orbitals and two p orbitals. Partitioning these into radial (sp) and tangential (p) components yields two subsets for skeletal bonding. One of the sp hybrid orbitals is used for external bonding (B-H bonds), leaving one radial sp hybrid and two tangential orbitals but only two electrons to participate in the cluster bonding. The molecular orbitals for cluster bonding can be constructed from this basis set of three orbitals per vertex. The skeletal cluster orbitals obtained from the radial subset is shown Figure 4.2a. The important point to notice is that exactly one strongly bonding linear combination (a_1 or a_{1g}, for the square-pyramid and the octahedron, respectively) of radial orbitals is formed, whereas all the others are anti-bonding. Interaction of the capping orbitals and the in-plane orbitals within the tangential component of the octahedron (Figure 4.2b) results in a set of four triply degenerate orbital manifolds (t_{2g}, t_{1u}, t_{2u}, t_{1g}).

Likewise, for the square pyramid the orbitals obtained from the three pairs of doubly degenerate (e) orbitals contributed by the cap and the square split into three sets of doubly degenerate orbitals (e), two of which are bonding and one anti-bonding. It is apparent from the scheme that a total of six low lying tangential orbitals are always present when the square is capped from above and below to give the square pyramid and the octahedron. Combining the radial and tangential components of the individual molecular orbital diagrams yields a total of 7 (in general $n + 1$) bonding skeletal molecular orbitals characteristic for bonding in *closo* and *nido* octahedral borane cluster compounds ($[B_6H_6]^{2-}$ and B_5H_9).

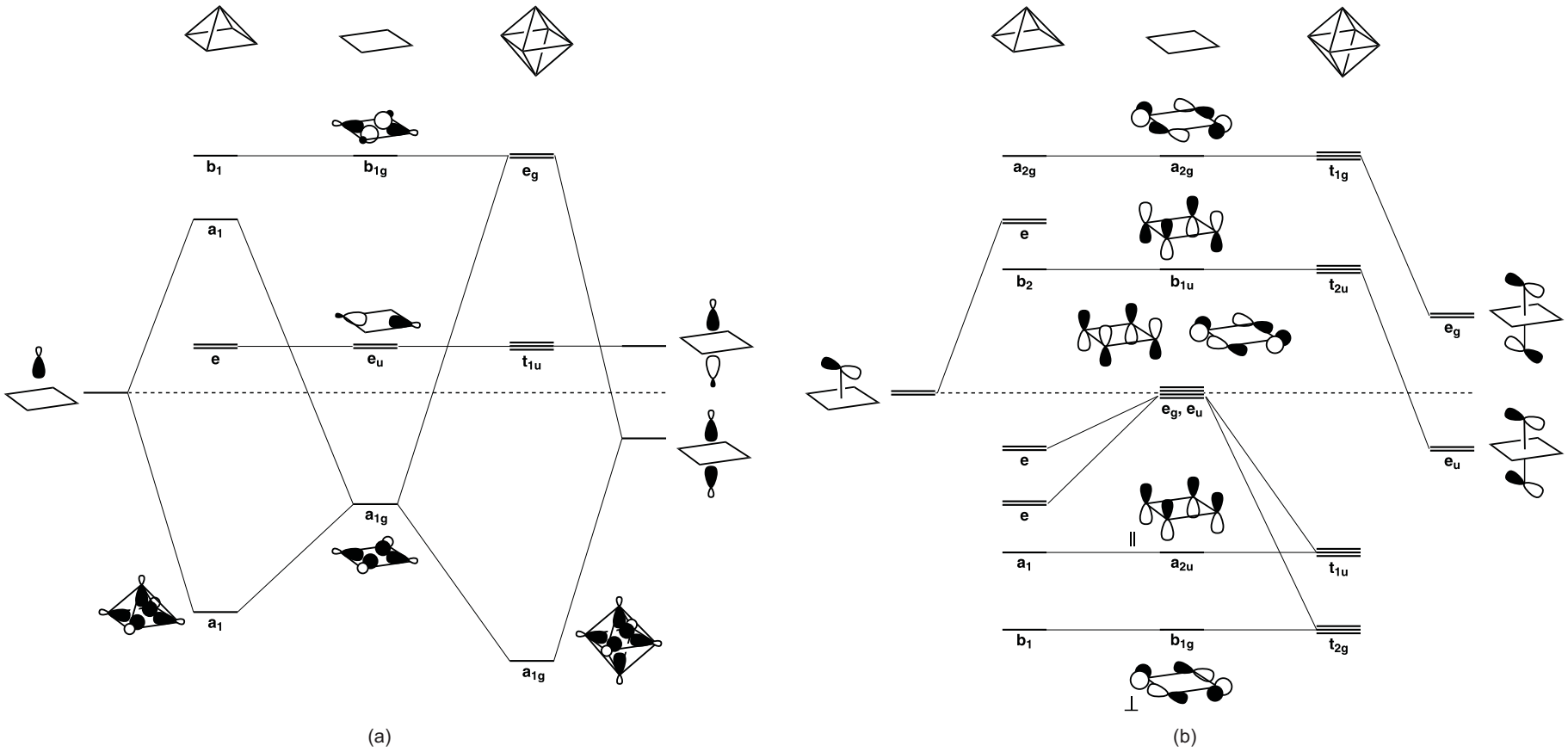

Figure 4.2: Schematic molecular orbital diagrams, built from (a) radial and (b) tangential fragment orbitals for the square pyramid (on the left side in each diagram) and the octahedron (right side). The tangential orbitals form two types, those parallel ($\parallel$) and those perpendicular ($\perp$) to the principle axis of rotation in the molecule. Adapted from Albright, Burdett and Whangbo.[342]

In other words, adding the 5th or 6th vertex does not increase the number of bonding/nonbonding orbitals, but rather the extent to which they are bonding, leaving the optimal electron count unaffected. Extending the Wade-Mingos rules to the homoatomic post-transition metal clusters (we only consider Group 14 element clusters in the following) is achieved by means of the isolobal analogy, and each BH vertex is replaced with an isoelectronic bare Si, Ge, Sn or Pb atom. Therefore, the four valence electrons of each tetrel atom are divided into one lone pair placed in the exo-polyhedral molecular orbital, in analogy to the external B-H bonds in boranes, and two electrons that participate in the skeletal bonding. A comparison of the valence MOs of Group 14 Zintl anions $[E_n]^{2-}$ with those of their valence-isoelectronic boranes $[B_nH_n]^{2-}$ shows that their molecular orbitals are very similar, but the relative energetic ordering of the orbitals is generally different. In $[E_n]^{2-}$ the MOs with lone-pair character correspond to $[B_nH_n]^{2-}$ MOs with B-H bonding character. While in the boranes the B-H bonding orbitals are energetically stabilised with respect to the surface bonding valence MOs, the corresponding MOs in the $[E_n]^{2-}$ anions with lone-pair character are energetically shifted upwards and are found among the highest occupied orbitals.

Besides the Wade-Mingos counting rules, so called spherical models are also used to predict the stability of cluster compounds, including the jellium model[344–346] and tensor surface harmonic theory.[347] These approaches yield cluster wave functions (spherical harmonics) which can be characterised by quantum numbers similar to the ones for atomic orbitals, and their energetic ordering leads to a shell structure. The stability of a cluster results from reaching closed-shell electronic configurations, corresponding to so called magic numbers.

Overview of cluster compounds

Empty homoatomic clusters of Group 14 elements

Having established the counting rules of Wade and Mingos, we proceed by reviewing empty homoatomic clusters of the Group 14 elements, $[E_n]^z$, with a focus on those anions with n = 9, 10 and 12 vertices (Figure 4.3). These clusters are relevant to our later discussion of endohedral clusters, due to their ability to act as receptacles for interstitial transition metals or f-block elements.

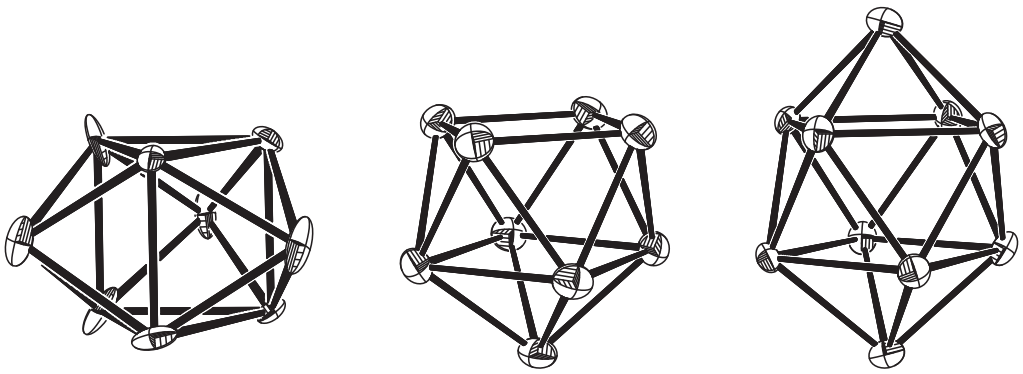

Figure 4.3: Empty cage structures of $[E_9]^{n-}$ and $[E_{10}]^{2-}$ clusters.

Currently, the largest empty cluster with more than nine vertices that has been isolated in solid state and crystallographically characterised is $[Pb_{10}]^{2-}$, which has been obtained as $[K([2.2.2]crypt)]^+$ salt by oxidation of $[Pb_9]^{4-}$ with PPh_3Au^ICl in ethylenediamine (en).[348] More recently, a $[Ge_{10}]^{2-}$ cluster has been captured in the complex $[Ge_{10}Mn(CO)_4]^{3-}$, where it acts as σ-donor ligand coordinated to the $[Mn(CO)_4]^-$ fragment.[349] Both clusters satisfy the Wade-Mingos rules ($2n + 2 = 22$), adopting a bicapped square antiprismatic shape (D_{4d}) expected for a *closo* ten-vertex cluster. Likewise, applying the Wade-Mingos rules to the $[E_{12}]^{2-}$ anions leads to an icosahedral (I_h) *closo* cluster ($2n + 2 = 26$), analogous to $[B_{12}H_{12}]^{2-}$. Although both $[Pb_{12}]^{2-}$ (plumbaspherene) and $[Sn_{12}]^{2-}$ (stannaspherene) have

been identified by photoelectron spectroscopy (PES) in the gas-phase,[350,351] and their stability anticipated by theoretical methods, structural data for these compounds are still unavailable. Nine-atom clusters $[E_9]^{n-}$ are most regularly found as tetraanionic clusters in the intermetallic phases A_4E_9 (A = Na, K, Rb, Cs; E = Ge, Sn, Pb),[352–356] which are frequently used as reagents in Zintl cluster synthesis. These clusters have $2n + 4 = 22$ skeletal electrons required for an $n = 9$ vertex C_{4v} *nido* polyhedron, which corresponds to the capped square antiprism.

Interestingly, distorted polyhedra other than the expected capped square antiprism are also found for the $[E_9]^{4-}$ ions in the solid state. For example, the structure determination of the alkali cryptand or crown ether salts of $[E_9]^{4-}$ clusters revealed that an almost perfect C_{4v} geometry is adopted for E = Si ([Rb[18]crown-6]$Rb_3[Si_9](NH_3)_4$)[357] and Pb ([K[18]crown-6]$_4[Pb_9]$),[358] whereas for $[Sn_9]^{4-}$ ([K[18]crown-6]$_3$K$[Sn_9]$) the symmetry is closer to D_{3h}.[359] On the other hand, Corbett and Edwards have found the predicted capped square antiprismatic geometry for the same cluster anion in the compound [Na([2.2.2]crypt)]$[Sn_9]$.[360] This demonstrates the structural flexibility of the E_9 cage. The rearrangement of cluster atoms follows the diamond-square-diamond mechanism, which represents a low-energy pathway for the interconversion between the different conformers of the empty E_9 cages.[334,335]

The one-electron oxidised homologues $[E_9]^{3-}$ (E = Si, Ge, Sn, and Pb) of the above tetraanions are interesting species from the point of view that the loss of one electron from the degenerate HOMO in the closed-shell $[E_9]^{4-}$ clusters gives rise to a Jahn-Teller distortion. Further, due to their odd skeletal electron count the structures cannot cleanly be explained by the Wade-Mingos rules. All $[E_9]^{3-}$ anions are paramagnetic and have been isolated as $[A([2.2.2]crypt)]^+$ adducts,[361,362] revealing distorted tricapped trigonal prismatic structures with approximate C_{2v} symmetry.

Clusters $[E_9]^{2-}$ with a twofold negative charge have $2n + 2 = 20$ skeletal electrons for cluster bonding, and can build *closo* deltahedra in the form of tricapped trigonal prisms (D_{3h}). Interestingly, in the only example of such a cluster known so far, where the charge assignment of -2 is unambiguous, $[K([18]crown\text{-}6)]_2[Si_9](py)$ (py = pyridine),[363] the structure of $[Si_9]^{2-}$ clearly deviates from this geometry. The cluster is rather a C_{2v}-symmetric distorted tricapped trigonal prism. Only very recently was a *closo* $[Ge_9]^{2-}$ cluster with D_{3h} symmetry crystallographically identified in $[K([2.2.2]crypt)]_2[Ge_9]$, and its topology confirmed by electron localisation function (ELF) analysis.[364]

Endohedral clusters $[M@E_n]^z$ with n = 9, 10, and 12

Having existed as a field of largely academic interest for many years, research into Zintl anions has taken an interesting new direction with the recent discovery of endohedrally filled Zintl clusters, in which a (transition) metal atom is encapsulated by the cluster cage (Figure 4.4). The emergence of this new subclass of Zintl ions and their great potential for interesting future applications has led to a revival of Zintl chemistry, gaining notable attention during the last few years.

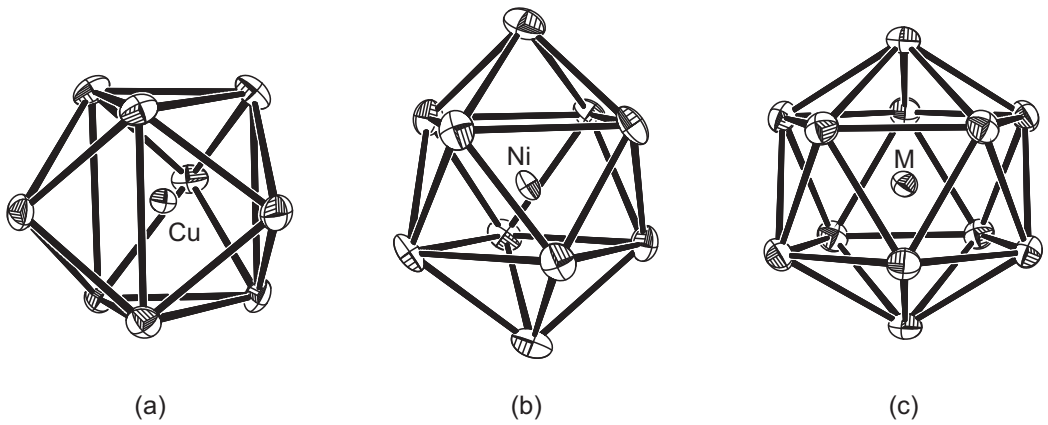

Figure 4.4: Structures of some typical endohedral clusters. (a) $[Cu@Sn_9]^{3-}$, (b) $[Ni@Pb_{10}]^{2-}$ and (c) $[M@Pb_{12}]^{2-}$ (M = Ni, Pd and Pt).

In order to distinguish the metal-centred clusters from their empty cage counter-

parts, the $[M@E_n]^z$ notation has been introduced for the endohedral clusters, where M represents the interstitial metal atom, E_n the surrounding Group 14 element cage and z the cluster charge.

The intermetalloid character of the endohedral Zintl clusters makes them ideal candidates for use as models for doped materials. Some of these species have good prospects of being utilised as building blocks for cluster-based nano materials with tailored electronic, magnetic or chemical properties. In this context the term 'superatom' has emerged as an intriguing new concept,[365,366] based on the idea that an atomic aggregate contributes free electrons to an orbital manifold chemically mimicking an element. Naturally, this idea is strongly interlinked with the Jellium model briefly introduced above. The classic example of a superatom is Al_{13} which mimics the chemical behaviour of halogen atoms ('superhalogen'). Clusters that incorporate open-shell transition metals are of special interest, as these could function as magnetic superatoms being able to support high magnetic moments.

While gas-phase and theoretical studies cover a wide range of cluster sizes n, those clusters $[M@E_n]^z$ obtained from synthetic protocols in solvent phase are found to have cluster sizes of n = 9, 10, 12. These metal-centred clusters appear to form in reactions between Group 14 Zintl anions $[E_9]^{4-}$ (E = Ge, Sn, Pb) and transition metal reagents with labile ligands, acting as a source of a 'naked' metal atom. The first example of a molecular species of this type, the icosahedral cluster $[Pt@Pb_{12}]^{2-}$ was reported by Eichhorn and co-workers, and was obtained by reaction of $[Pb_9]^{4-}$ and $Pt(PPh_3)_4$ (Ph = phenyl).[367] Likewise, related synthetic protocols employing different transition metal reagents have since given rise to a homologues series of isoelectronic icosahedral clusters of the Group 10 triad, $[M@Pb_{12}]^{2-}$ (M = Ni, Pd, Pt).[368] A comparison of their solid state structures revealed that the larger the transition metal is, the less the distortion of the Pb_{12}

skeleton, suggesting some stabilising effect of the interstitial ion on the periphery. There have been no reports of a germanium analogue with a metal-centred Ge_{12} cage to date, but recently an isoelectronic twelve-vertex tin cluster, $[Ir@Sn_{12}]^{3-}$ has been isolated.[369] This icosahedral cluster is obtained from a stepwise reaction starting from an ethylenediamine (en) solution of K_4Sn_9 and $[IrCl(cod)]_2$ (cod = 1,5-cyclooctadiene). The sequence is initiated by the formation of a Ir(cod)-capped Sn_9 cluster, which is transformed into the product $[Ir@Sn_{12}]^{3-}$ upon heating the solution.

Endohedral Zintl ion clusters with nuclearities lower than twelve have also been isolated and structurally characterised. The smallest examples of Zintl clusters accommodating an interstitial transition metal atom are $[Ni@Ge_9]^{3-}$ and $[Cu@E_9]^{3-}$ (E = Sn, Pb).[370–372] Both are obtained from standard procedures, where the first cluster has been isolated from an en solution of K_4Ge_9 and $Ni(cod)_2$, the second formed in dimethylformamide (dmf) solutions of Cu(mes) (mes = mesitylene) and K_4E_9. Two conformers are accessible to the Cu-containing clusters with E = Sn and Pb, both of which have been identified by X-ray crystal structure analysis. In the first isomer the cage atoms form an endohedral tricapped trigonal prism with D_{3h} symmetry, while the second corresponds to an endohedral *nido* cluster with C_{4v} symmetry (a monocapped square antiprism). The fluxional behaviour in solvent within the E_9 cages of the $[Cu@E_9]^{3-}$ anions has been illustrated by NMR measurements, which yield single resonances for both cases. The endohedral ten-vertex cluster $[Ni@Pb_{10}]^{2-}$ was accessible through the reaction of $Ni(cod)_2$ with K_4Pb_9 in ethylenediamine.[373] The zero-valent Ni atom occupies the centre of a bicapped square antiprism (D_{4d}).

Larger non-spherical clusters containing more than one interstitial metal atom such as $[Ni(Ni@Ge_9)_2]^{4-}$,[371] $[Pd_2@Ge_{18}]^{4-}$,[374] $[Pd_2@Sn_{18}]^{4-}$,[375,376] $[Ni_2@Sn_{17}]^{4-}$,[377]

and $[Pt_2@Sn_{17}]^{4-}$[378] have also been reported in the literature.

It is important to note that all of the centred 10- and 12-vertex clusters presented above possess closed-shell electronic configurations and can be rationalised as $[M^z@(E_n)^{2-}]$ species that contain $2n + 2$ skeletal electron $[E_n]^{2-}$ ($n = 10$, 12) units with *closo* structures. The central transition metal atom does not contribute to the skeletal electron count, and maintains a closed-shell d^{10} configuration, thus $z = 0$ for the interstitial Group 10 atoms Ni, Pd, and Pt. The filled subshell can also be reached in case of $[Ir@Sn_{12}]^{3-}$, where the *closo*-$[Sn_{12}]^{2-}$ cage encapsulates an iridium centre in the -I oxidation state ($z = -1$). Likewise, the gas-phase ion $[Cu@Sn_{12}]^-$ has been described as a Cu^+ ion trapped inside stannaspherene, $[Cu^+@Sn_{12}]^{2-}$.[379] Indeed, King has referred to these endohedral d^{10} atoms as pseudo noble gases, analogous to endohedral noble gases in fullerenes such as $He@C_{60}$.[380]

Consequently, deltahedra would be expected for any new endohedral clusters of Group 14. It came as a surprise when two unprecedented germanium clusters were reported almost simultaneously, revealing pentagonal prismatic (D_{5h}) geometries. The first structure, closed-shell $[Co@Ge_{10}]^{3-}$ (22 skeletal electron count = 22 SEC), was isolated by Fässler and co-workers,[381] and shortly thereafter Goicoechea et al. reported the structure of the open-shell Zintl ion $[Fe@Ge_{10}]^{3-}$ (21 SEC, Figure 4.5a).[382]

The bond parameters of both compounds are strikingly similar: the interatomic Ge-Ge distances linking the two pentagons vary over a narrow range between 2.60 to 2.62 Å, the intra-ring distances are slightly shorter (2.50-2.53 Å and 2.53-2.55 Å for Co and Fe, respectively), while the distances between the interstitial metal atom and the Ge atoms are 2.48-2.53 Å for $[Co@Ge_{10}]^{3-}$ and 2.51-2.54 Å for $[Fe@Ge_{10}]^{3-}$. The intra- and inter-ring Ge-Ge-Ge angles are very close to

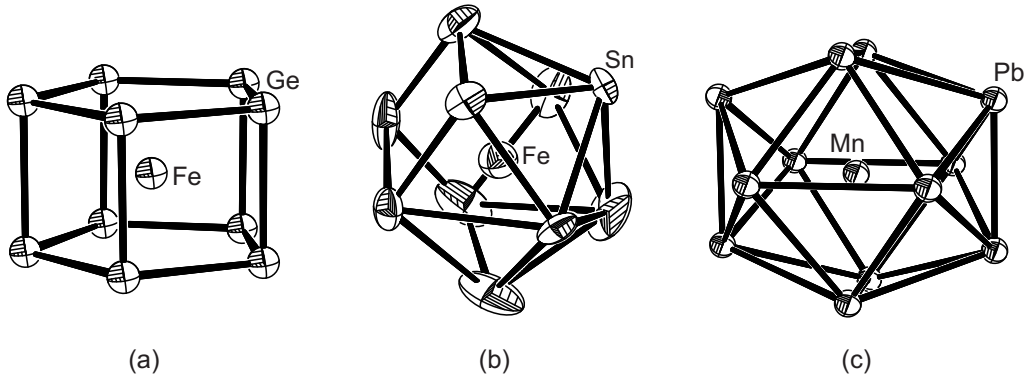

Figure 4.5: Structures of the three paramagnetic members of the endohedral Zintl cluster family. (a) $[Fe@Ge_{10}]^{3-}$, (b) $[Fe@Sn_{10}]^{3-}$ (c) $[Mn@Pb_{12}]^{3-}$.

108° and 90°, required for a perfect pentagonal prism. Therefore both structures are almost ideal Archimedean polyhedra, in stark contrast to the Platonic deltahedral structures found in the other endohedral clusters.[383] The topologies of $[Co@Ge_{10}]^{3-}$ and $[Fe@Ge_{10}]^{3-}$ may be compared only to the D_{5d} pentagonal antiprismatic ion $[Pd@Bi_{10}]^{4+}$,[384] and the organometallic tin compound $Sn_{10}R_{10}$ (R = 2,6-diethylphenyl),[385] also sharing the D_{5h} pentagonal prismatic structure. Surprisingly, the geometry of the cluster $[Fe@Sn_{10}]^{3-}$ (Figure 4.5b), also recently isolated in the Goicoechea group and isosteric with its germanium congener, again falls into the regime of deltahedral structures. Its geometry is marginally distorted away from a bicapped square antiprism (D_{4d}), and is best described as tetracapped trigonal prismatic.

In addition to the paramagnetic 10-vertex clusters $[Fe@E_{10}]^{3-}$ (E = Ge, Sn), the range of endohedral lead clusters was also extended by a further member, $[Mn@Pb_{12}]^{3-}$ (Figure 4.5c), the first example of a synthetic open-shell endohedral 12-vertex lead cluster. Although the cluster suffers from notable disorder, the crystallographic data allowed for identification of a marked low-symmetry distortion from the idealised icosahedral I_h symmetry that is characteristic of related endohedral clusters. Thus, the $[Mn@Pb_{12}]^{3-}$ cluster is D_{2h}-symmetric, and is reached via compression and elongation along two 2-fold rotational axis of the icosahedron.

Theoretical studies on cluster compounds

The experimental data summarised above have been complemented by a large number of theoretical studies, which included both empty and endohedral cluster anions.[350,386–399,399–402] The structures of numerous filled main-group clusters detected by mass spectrometry have been deduced on basis of theoretical calculations. The results of the quantum chemical calculations are commonly analysed by means of electron localisation functions, NBO charges and MO interactions diagrams. Another concept which is often employed is spherical aromaticity, quantified in terms of the nucleus-independent chemical shifts[213,403] at the centre of the cluster, called NICS(0) values. Aromatic, and thus stable clusters, exhibit negative NICS(0) values, whereas antiaromaticity is reflected in positive values.

Empty $[E_n]^z$ cluster anions with n = 10, 12

DFT calculations on the $[E_{10}]^{2-}$ series (E = Si, Ge, Sn, Pb)[404–408] are consistent with the notion that these ions possess 22 skeletal cluster electrons, and they have shown that the bicapped square antiprism invariably corresponds to the global minimum in all cases. King et al. have conducted a comprehensive DFT study on bare ten-vertex $[Ge_{10}]^z$ ($z = 6-, 4-, 2-, 0, 2+, 4+, 6+$) clusters.[406] For $[Ge_{10}]^{2-}$ it was found that the D_{5h} structure also corresponds to a minimum (+41 kcal mol^{-1} above D_{4d}). However, this result seems to be strongly dependent on the chosen method.[404] It has generally been found that the lowest energy structures of bare germanium clusters in the electron-poor or -rich limit are often low-symmetry polyhedra not readily recognisable by the Wade-Mingos rules.[409] For example, the global minimum found for the electron-rich cluster $[Ge_{10}]^{6-}$ corresponds to a slipped pentagonal prism (C_s symmetry), which is favoured over the *arachno* pentagonal antiprism ($2n + 6 = 26$) by 17 kcal mol^{-1}. In the slipped pentagonal

prism the rectangular sides of the ideal pentagonal prism are partially turned into triangular faces, thereby retaining the pentagonal faces.

The presence of I_h-symmetric minima for the $[E_{12}]^{2-}$ series as predicted by the Wade-Mingos rules was confirmed by DFT geometry optimisations. However, the icosahedron only corresponds to the ground state for $[Sn_{12}]^{2-}$ and $[Pb_{12}]^{2-}$, while the situation is more complicated for the lighter congeners of Group 14, where less symmetric structural motifs become the ground state. This case illustrates the delicate balance of electronic effects that direct the cluster geometries and how the electron counting rules become unreliable for certain regions of the cluster conformational space. The differences between the $[E_{12}]^{2-}$ ions also become apparent in the NICS(0) aromaticity criterion, which reveales a change down the group from antiaromatic $[Si_{12}]^{2-}$ to aromatic $[Pb_{12}]^{2-}$.[398] The stability of the D_{4d}-symmetric *closo* $[E_{10}]^{2-}$ cluster anions, on the other hand, is clearly mirrored in large negative NICS(0) values, indicating high aromaticity which decreases down the group.

Intermetalloid endohedral clusters $[M@E_n]^z$ with n = 9, 10, and 12

Theoretical studies on $[M^z@(E_{12})^{2-}]$ clusters typically yield I_h-symmetric geometries as the ground states, although there are exceptions to the rule (E = Si), for which non-deltahedral aggregates are energetically favoured. Indeed, DFT geometry optimisations confirmed the endohedral icosahedral structures found experimentally for the closed-shell species $[Ir@Sn_{12}]^{3-}$,[369] and $[M@Pb_{12}]^{2-}$ (M = Ni, Pd, Pt).[368,405] The calculated bond parameters compare well with those obtained from single crystal structure determination. A natural charge of -1.07 has been found on Ir in $[Ir@Sn_{12}]^{3-}$, justifying the formal description as $[Ir^{-I}@(Sn_{12})^{2-}]^{3-}$. Interaction between the interstitial and cage atoms primarily occurs through mixing of empty metal s and p orbitals with suitable cage orbitals, leaving the d manifold

5-fold degenerate.[367]

In the context of the current study, the recent work by Deng and co-workers on neutral $M@Pb_{12}$ complexes of the first row transition metal series is particularly relevant. $Mn@Pb_{12}$ was reported to have a sextet ground state with 4.34 unpaired electrons on the Mn centre, consistent with a $Mn^{II}@Pb_{12}^{2-}$ formulation.[402] Indeed, Kumar and co-workers have referred to the germanium and tin analogues, $Mn@E_{12}$ (E = Ge, Sn) as 'magnetic superatoms',[391] where the high local moment at the metal centre is shielded from the environment by the E_{12} cluster.

The neutral nickel analogue, $Ni@Pb_{12}$, formally isoelectronic with $[Mn@Pb_{12}]^{3-}$, was reported to have a triplet ground state and only minor deviations (within 0.06 Å) from icosahedral symmetry. The very weak Jahn-Teller distortion in $Ni@Pb_{12}$ contrasts dramatically with the strong prolate distortion observed in $[Mn@Pb_{12}]^{3-}$. An icosahedral structure has also been postulated for the anion $[Co@Pb_{12}]^{-}$, also isoelectronic with $[Mn@Pb_{12}]^{3-}$, which has been generated in vacuum by laser ablation.[410] Endohedral stannaspherene $[M@Sn_{12}]^{-}$ of first row transition metals have also been characterised in gas-phase experiments.[379] The results of DFT calculations on these species match those obtained by Deng and co-workers, i.e. while $[Cu@Sn_{12}]^{-}$ (filled sub-shell) and $[Cr@Sn_{12}]^{-}$ (half-filled sub-shell) both have perfect I_h symmetry, the other members of the set (including $[Co@Sn_{12}]^{-}$) reveal only negligible Jahn-Teller distortions.

Turning to the E_{10} cluster compounds, the centred D_{4d} bicapped square antiprism has been computed to be the ground state geometry for $[Ni@E_{10}]^{2-}$ (E = Ge, Sn, Pb), $[Pd@E_{10}]^{2-}$ (E = Sn, Pb) and $[Pt@Pb_{10}]^{2-}$, all of which have been correlated with the cage's aromaticity.[405] Endohedral 10-vertex germanium clusters $[M@Ge_{10}]^{z}$ have been studied in great detail by King and co-workers at the hybrid B3LYP level.[393,394] Preferences for different structures were explored as a

function of both the central metal and cluster charge. Consistent with the Wade-Mingos rules, $[Ni@Ge_{10}]^{2-}$ adopts a D_{4d} minimum energy structure, which is also a local minimum for $[Pd@Ge_{10}]^{2-}$, but collapses to a C_1-symmetric mushroom-like structure for $[Pt@Ge_{10}]^{2-}$. The centred pentagonal prism (D_{5h}) represents a local minimum for $[Ni@Ge_{10}]^{2-}$ (6 kcal mol^{-1} above D_{4d}), but importantly, is the energetically most favourable structure for the heavier congeners Pd (13 kcal mol^{-1} below D_{4d}) and Pt (>15 kcal mol^{-1} below other structures). For the neutral clusters $M@Ge_{10}$ (M = Ni, Pd and Pt) the global minimum corresponds to the singlet ($S = 0$) bicapped square antiprism in all cases. Ideal pentagonal prisms are stabilised in the triplet state, owing to the doubly degenerate character of the HOMO and LUMO in these species, and they become increasingly stabilised with respect to the ground state on descending Group 10. A number of singlet low-energy unsymmetrical structures are found for the tetraanions $[M@Ge_{10}]^{4-}$. However, for M = Pd the ground state corresponds to an ideal pentagonal prism with $S = 1$, but perhaps surprisingly, for platinum the same D_{5h} structure lies more than 30 kcal mol^{-1} above the global minimum. Based on an analysis of Mulliken charges for all compounds, the authors argue in favour of an $[Ge_{10}]^{z+2}$ cage encapsulating a central M^{-II} anion, with a $d^{10}s^2$ configuration.

In the 20 skeletal electron clusters $Ni@Ge_{10}$, $[Cu@Ge_{10}]^{+}$ and $[Zn@Ge_{10}]^{2+}$ the ground state tetracapped trigonal prism (C_{3v}) and the bicapped square antiprism are very close in energy with a maximum separation of 4.6 kcal mol^{-1} for the nickel derivative. In fact the relative energies are somewhat dependent on the chosen functional. Ahlrichs et al. have found a D_{4d}-symmetric ground state with the BP86 GGA functional for the cluster series $Ni@E_{10}$ and $[Zn@E_{10}]^{2+}$ (E = Ge, Sn, Pb) having the same electron count.[411] For $[Zn@Ge_{10}]^{2+}$ and $[Cu@Ge_{10}]^{+}$ pentagonal prismatic structures have also been obtained as local minima, ~23 kcal mol^{-1} above

the respective ground states. C_{3v} minimum energy geometries are adopted by 24 skeletal electron clusters, and again a pentagonal prismatic structure has been located for zinc ($+12\,\mathrm{kcal\,mol^{-1}}$), albeit somewhat distorted from the ideal D_{5h} symmetry.

For the clusters $[Cu@Ge_{10}]^{5-}$ and $[Zn@Ge_{10}]^{4-}$ (26 skeletal electrons) the D_{5d} pentagonal antiprism predicted by the Wade-Mingos rules and the C_{3v} tetracapped trigonal prism at a somewhat higher energy have been calculated to be lowest in energy overall. For $[Ni@Ge_{10}]^{6-}$, however, the energetic order is reversed.

The effect of the electron count on the geometries of different symmetry has been explained in terms of the bonding/antibonding characteristics of the frontier molecular orbitals. King has reasoned that interactions between the interstitial atom and the surrounding environment are most pronounced in cases when the ns orbital of the central metal functions as an electron donor to the cage. For instance, the nickel atom in $Ni@Ge_{10}$ formally retains a filled d^{10} shell, whereas zinc in $[Zn@Ge_{10}]^{2+}$ is formally ionised to Zn^{2+} and interacts strongly with the cluster fragment orbitals, leading to stabilisations, as quantified by MO interaction diagrams. Beryllium as source of two extra cluster electrons has very recently been shown to have little effect on the structures of several $[Be@Ge_{10}]^{z}$ clusters, thus the same polyhedra were found for isoelectronic pairs of filled $[Be@Ge_{10}]^{z}$ / empty $[Ge_{10}]^{z}$ cages.[412]

As a general result, King and co-workers argue that the internal cage volume available to the interstitial atom can override electronic considerations. Consequently, the Wade-Mingos formalism is most applicable when the E_{10} unit has a large a cavity as possible, e.g. when E is a heavy element such as Pb. However, if the cavity is too small, particularly in the case of Ge, maximising the internal volume of the polyhedral cavity can dominate over electronic effects.

DFT calculations (B3LYP/cc-pVTZ(-NR), PCM) on $[Co@Ge_{10}]^{3-}$ by the Fässler group have confirmed that the D_{5h}-symmetric pentagonal prism indeed corresponds to the ground state.[381] The HOMO-LUMO gap is a substantial 2.27 eV, and a natural charge of -1.05 on cobalt supports the notion of a d^{10} closed-shell configuration on this centre. The D_{5h}- and D_{4d}-symmetric stationary points of the isoelectronic anions $[Co@Ge_{10}]^{3-}$ and $[Ni@Ge_{10}]^{2-}$ differ by +13.3 and -5.33 kcal mol^{-1}, respectively. Thus the energetic separations are small, and a change in the preference for one or the other symmetry seems to occur between Groups 10 and 9. It is worth noting that the D_{4d} stationary state of $[Co@Ge_{10}]^{3-}$ revealed a small (degenerate) imaginary frequency (i43.0 cm^{-1}). The electronic structure of the D_{5h}-symmetric cluster has been further analysed by means of the electron localisation function (ELF), indicating the presence of three types of valence basins. One type is localised on the Ge vertices of the cluster, representing the lone pairs, another was found between neighboring Ge atoms within the 5-membered rings, and finally, smaller basins were located along the five inter-ring bonds. No basins were found for the Co-Ge bond vectors, suggestive of a highly delocalised character of the bonding between the Co and Ge atoms. From the experimental and theoretical data it has been concluded that $[Co@Ge_{10}]^{3-}$ should best be regarded as intermetalloid cluster with highly delocalised bonding. It is interesting to note that $[Co@Ge_{10}]^{-}$ with 20 skeletal electrons has been generated in the gas phase by laser vaporisation as early as 2001,[413] and the minimum energy structure was calculated to be the bicapped square antiprism.[414]

Most of the known synthetic endohedral clusters represent closed-shell systems. The trianionic clusters $[Fe@Ge_{10}]^{3-}$, $[Fe@Sn_{10}]^{3-}$ and $[Mn@Pb_{12}]^{3-}$ from the laboratories of our collaborator Dr. Goicoechea and his co-workers are the first examples that contain odd numbers of electrons, and as such are not readily interpreted in

terms of Wade-Mingos rules. In this chapter we will attempt to address the subtle electronic factors which give rise to the observed structural differences between otherwise isoelectronic species, i.e. $[Mn@Pb_{12}]^{3-}$ vs. $Ni@Pb_{12}$ and $[Fe@Ge_{10}]^{3-}$ vs. $[Fe@Sn_{10}]^{3-}$. Fässler has noted that it is surprising that $[Fe@Ge_{10}]^{3-}$ and $[Co@Ge_{10}]^{3-}$ are both isostructural, as the latter features a degenerate (e_2'') HOMO set, and therefore removal of one electron might be anticipated to induce a Jahn-Teller distortion.[330] In this context we also hope that our electronic structure analysis will shed some light onto this issue.

4.2 Methodology

All calculations described in this chapter were performed with the Amsterdam Density Functional package (ADF2010.02).[56–58] The TZ2P Slater-type basis set of triple-ζ quality, extended with two polarisation functions, was used to describe the 1st row transition metals (M = Mn, Fe, Co, Ni, Cu, Zn) as well as the Group 14 elements (E = Ge, Sn, Pb). Electrons in orbitals up to and including 2p for the transition metals and 3p, 4p and 4d for Ge, Sn, and Pb, respectively, were considered part of the core and treated in accordance with the frozen core approximation (M.2p, Ge.3p, Sn.4p and Pb.4d). All calculations employed the Local Density Approximation (LDA)[8] to the exchange potential, along with the local exchange-correlation potential of Vosko, Wilk and Nusair (VWN)[19] and gradient corrections to non-local exchange and correlation proposed by Becke and Perdew (BP86).[21,22] All calculations were unrestricted. Relativistic effects were incorporated using the Zeroth Order Relativistic Approximation (ZORA).[415–417] The presence of cations in the crystal lattice was modeled by surrounding the clusters with a continuum dielectric model (COSMO).[208] The chosen dielectric constant $\varepsilon = 78.4$ corresponds to that of water, although structural parameters are not strongly dependent on this

choice. All structures were optimised using the gradient algorithm of Versluis and Ziegler.[418] For the discussion of the cluster $[Mn@Pb_{12}]^{3-}$, we note that I_h point symmetry is not supported in ADF, but by using an appropriate sub-group (in this case D_{5d}) and imposing a symmetric electron density distribution with 1 spin-α and $^3/_5$ spin-β electrons in each of the five highest lying orbitals with the symmetries of the 3d set (a_{1g}, e_{1g}, e_{2g}), it is possible to converge on the I_h-symmetric geometries discussed below. Stationary points were characterised by analysis of their harmonic frequencies: true minima and transition states have 0 and 1 imaginary frequencies, respectively. Frequencies were computed by numerical differentiation of energy gradients in slightly displaced geometries.

4.3 The endohedral cluster $[Mn@Pb_{12}]^{3-}$

4.3.1 Optimised geometries

Given the rather low quality of the X-ray data, we have conducted an exhaustive survey of the potential energy surface of the $[Mn@Pb_{12}]^{3-}$ anion to identify all possible isomers. This analysis reveals two almost isoenergetic low-lying stationary points (Figure 4.6 and Table 4.1), one with D_{3d} symmetry, the other D_{2h}, both of which have a triplet multiplicity ($S = 1$). The most stable quintet, in contrast, lies 11.3 kcal mol^{-1} higher in energy and can therefore be eliminated as a candidate for the ground state. Both the D_{2h}- and D_{3d}-symmetric triplets show strongly prolate distortions from the idealised icosahedron, and in fact the D_{2h}-symmetric structure bears a striking resemblance to the X-ray data: the Mn-Pb distances split into three distinct sets of 2.91, 3.15 and 3.35 Å (c.f. 2.90, 3.10 and 3.30 Å from X-ray), while the computed Pb-Pb separations range from 3.16 to 3.76 Å (c.f. 3.10-3.75 Å from X-ray). In the D_{3d}-symmetric structure, in contrast, there are

only two distinct Mn-Pb bond lengths, 2.94 Å and 3.33 Å (in a 6:6 ratio) while the Pb-Pb bond lengths range from 3.16 to 3.64 Å.

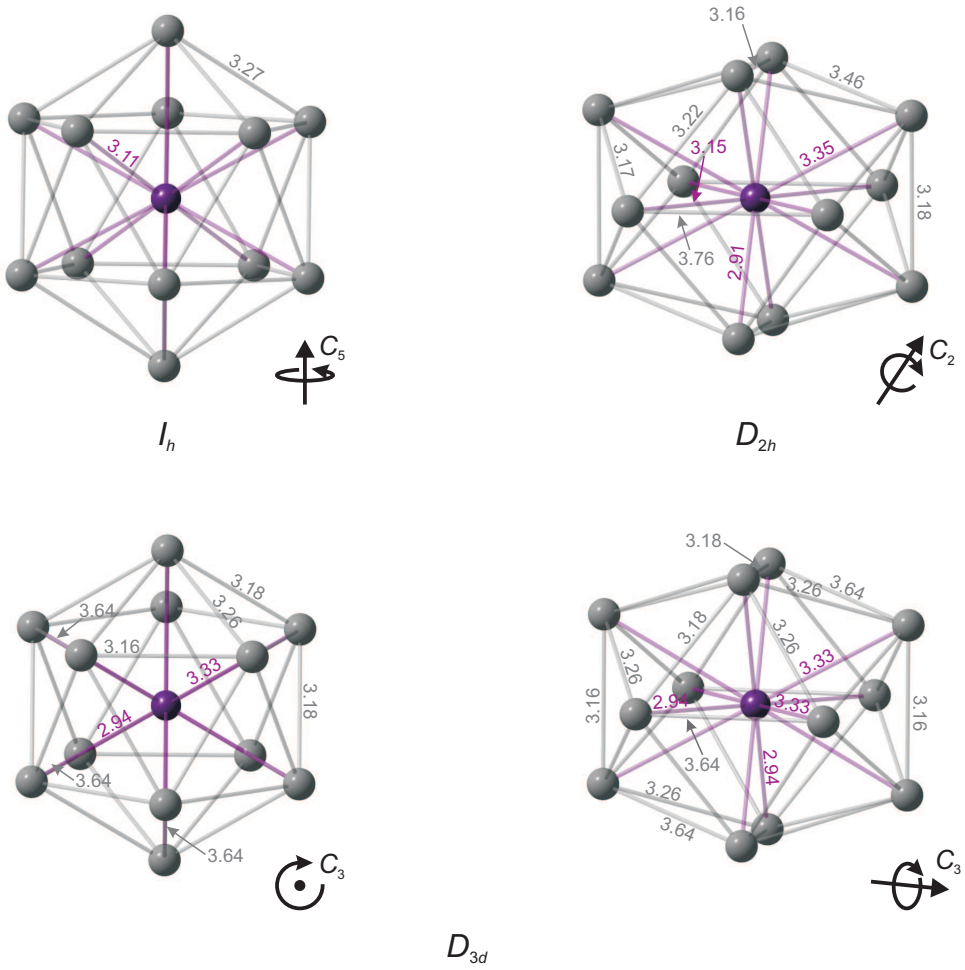

Figure 4.6: Optimised geometries of $[Mn@Pb_{12}]^{3-}$ (I_h, D_{2h} and D_{3d} symmetries). Mn-Pb bonds and distances (Å) in purple, Pb-Pb bonds and distances in grey. The orientation of the principal axis of rotation is indicated. [Original in colour]

Despite the subtle differences between the D_{2h}- and D_{3d}-symmetric structures, the gross features of the prolate distortion are very similar: the span of Pb-Pb and Mn-Pb distances is almost identical, as is the average Pb-Pb separation (∼3.30 Å vs. 3.22 Å from experiment). The second orientation of the D_{3d}-symmetric cluster anion shown in Figure 4.6 emphasises the point that structural differences between the D_{3d} and D_{2h} structures are minimal. The D_{3d} isomer proves to be the global minimum although the D_{2h}-symmetric alternative lies only 0.5 kcal mol^{-1} higher in

energy, well within the anticipated accuracy limits of the computation. In fact, the D_{2h}-symmetric structure is not a true minimum but rather represents a transition state ($i18\,\mathrm{cm}^{-1}$) which connects two equivalent D_{3d}-symmetric geometries. The magnitude of the imaginary frequency is, however, very small, and we conclude only that the potential energy surface is very flat in the region connecting D_{2h}- and D_{3d}-symmetric structures. No C_{2h}-symmetric minima were located - all attempts converged on the nearest D_{2h}-symmetric alternative. We have also located a perfectly icosahedral stationary point (Mn-Pb = 3.11 Å, Pb-Pb = 3.27 Å), which lies $\sim$15 kcal mol^{-1} above the D_{3d}-symmetric global minimum. The large energy gap indicates that the crystallographically observed prolate distortion has a strong intrinsic electronic driving force.

Also included in Table 4.1 are the structural parameters, spin densities and energies of the corresponding stationary points for the isoelectronic species Ni@Pb_{12}. Deng and co-workers have previously reported that the distortions from icosahedral symmetry in this species are small,[402] and our own calculations confirm this to be the case: the shortest and longest Ni-Pb distances differ by only 0.07 Å and the D_{2h}- and D_{3d}-symmetric structures are only 2.3 kcal mol^{-1} more stable than the perfectly icosahedral reference point.

Table 4.1: Calculated bond lengths (Å), relative energies (kcal mol^{-1}) and Mulliken spin densities of $[Mn@Pb_{12}]^{3-}$ and $Ni@Pb_{12}$. Values in parentheses indicate the number of symmetry equivalent bonds of a given length.

	$[Mn@Pb_{12}]^{3-}$				$Ni@Pb_{12}$			
	I_h	D_{2h}	D_{3d}	D_{5d}	I_h	D_{2h}	D_{3d}	D_{5d}
M-Pb	3.11 (12)	2.91, 3.15, 3.35 (4:4:4)	2.94, 3.33 (6:6)	2.92, 3.15 (2:10)	3.10 (12)	3.06, 3.10, 3.13 (4:4:4)	3.08, 3.12 (6:6)	3.09, 3.13 (2:10)
Pb-Pb	3.27 (30)	3.16, 3.17, 3.18, 3.22, 3.46, 3.76 (2:8:2:8:8:2)	3.16, 3.18, 3.26, 3.64 (6:6:12:6)	3.18, 3.28, 3.36 (6:6:6)	3.26 (30)	3.23, 3.25, 3.28, 3.29 (2:18:8:2)	3.24, 3.26, 3.27 (6:6:18)	3.25, 3.27 (20:10)
Spin densities								
M	3.21	3.35	3.33	3.18	0.63	0.68	0.71	0.66
$\sum Pb_{12}$	-1.21	-1.35	-1.33	-1.18	1.37	1.32	1.29	1.34
Rel. energy	+14.8	+0.5	0.00	+7.4	+2.3	0.00	0.00	+0.9

4.3.2 Analysis of the electronic structure

Having established that DFT reproduces the key experimental observables for $[Mn@Pb_{12}]^{3-}$ (viz. the strong prolate distortion and the non-singlet ground state), we are in a position to explore the electronic origins of the distortion. The perfectly icosahedral closed-shell species $[Ni@Pb_{12}]^{2-}$, the Kohn-Sham orbitals of which are shown in Figure 4.7, provides a natural reference point for the discussion. Eichhorn and co-workers have previously discussed the electronic structure of the platinum analogue, which is very similar, qualitatively and quantitatively.[367] The HOMO and HOMO-1, $2h_g$ and $1t_{1u}$, are localised primarily on the Pb_{12} cage, the latter lying just above the five-fold degenerate orbitals with dominant Ni 3d character ($1h_g$). The LUMO and LUMO+1 ($1g_g$ and $3h_g$, respectively) have almost exclusive Pb 6p character, and their spatial properties prove to be critical to the discussion of the low-symmetry distortion in $[Mn@Pb_{12}]^{3-}$: the LUMO is a linear combination of tangentially oriented 6p orbitals on Pb ('surface-only' orbitals in the nomenclature of King and co-workers).[419,420] In contrast the h_g-symmetric LUMO+1 can in principle have both radial and tangential character, but the contour plot in Figure 4.7 confirms that the radial component is dominant.

The removal of two electrons from the h_g-symmetric HOMO of $[Ni@Pb_{12}]^{2-}$ generates a Jahn-Teller instability, and thus distortion from the I_h symmetry of the closed-shell systems is to be anticipated. We note, however, that while this statement is equally true for both $[Mn@Pb_{12}]^{3-}$ and $Ni@Pb_{12}$, the nature and magnitude of the distortion is very different. The Kohn-Sham orbitals for $Ni@Pb_{12}$, in both I_h and D_{2h} symmetry, are shown in Figure 4.8. The two holes are localised in a primarily Pb-based HOMO and the majority of the spin density is therefore distributed over the Pb_{12} cage ($\rho_{Pb_{12}} = 1.37$) with only a small amount transferred

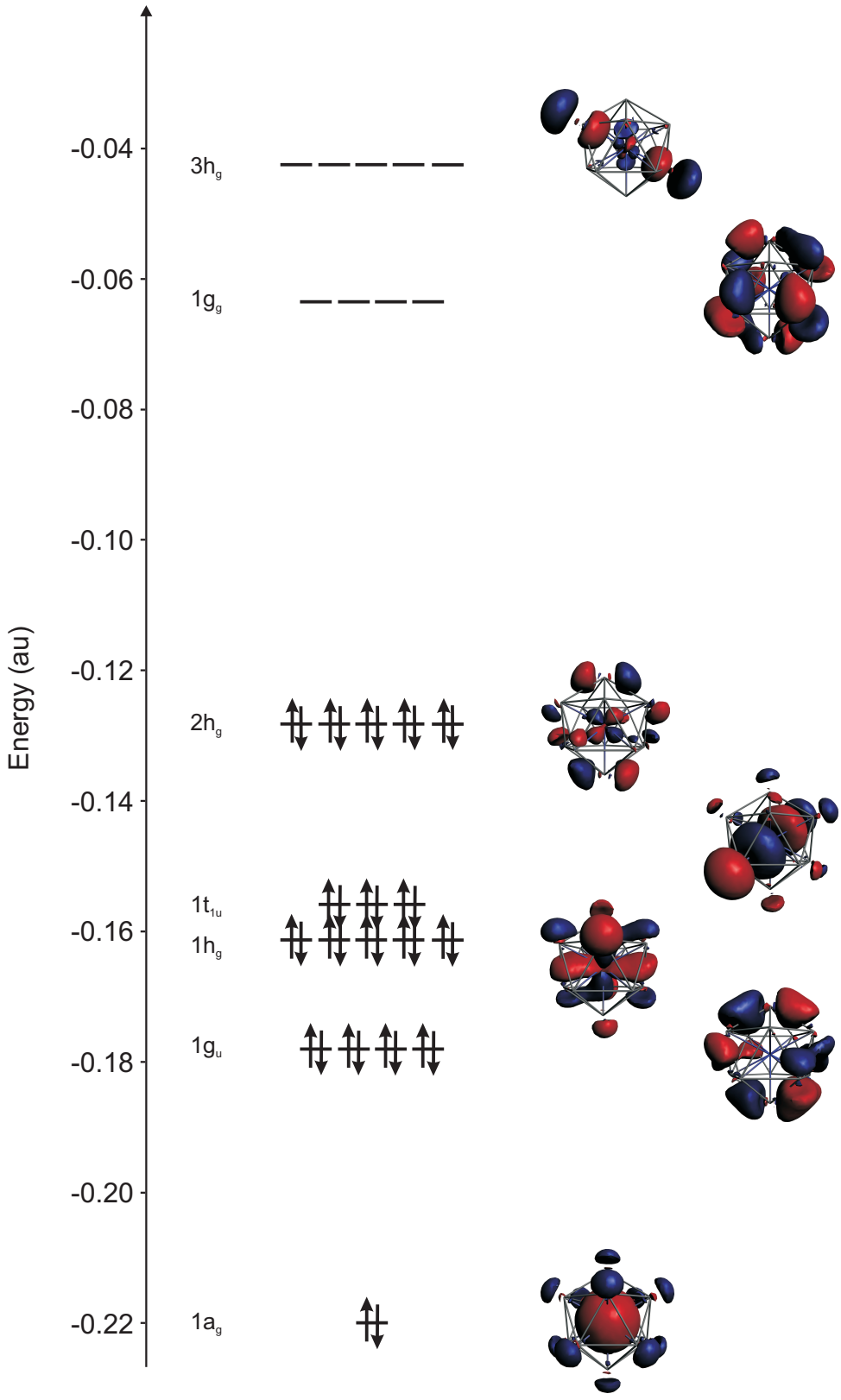

Figure 4.7: Kohn-Sham orbitals for icosahedral $[Ni@Pb_{12}]^{2-}$ (contour value 0.025). Only one component of each degenerate orbital is shown. [Original in colour]

onto the Ni centre ($\rho_{\mathrm{Ni}} = 0.63$). The presence of same-spin (i.e. spin-α) density on *both* metal and ligand (in this case the Pb_{12} cage) is typical of cases where the dominant interaction is between the d orbitals of the metal and an occupied ligand-based donor orbital. The D_{2h}-symmetric form is only marginally more stable, and the frontier orbital domain and spin density distribution are not substantially affected by the distortion: the degeneracy of the $2h_g$ orbital is lifted such that a 3-below-2 pattern emerges, but the magnitude of the splitting is less than 0.01 au.

The frontier Kohn-Sham orbitals (Figure 4.9) and net spin densities (Table 4.1) for $[Mn@Pb_{12}]^{3-}$ (I_h and D_{2h}) indicate a very different electronic situation from the isoelectronic $Ni@Pb_{12}$. The net spin density on the Mn centre (+3.21 in I_h symmetry) is much greater than that in $Ni@Pb_{12}$ (+0.66) and even exceeds the limiting value of 2.0 for an entirely metal-centred triplet. To compensate for this high spin density at Mn, a negative (i.e. spin-β) density of -1.21 is delocalised over the Pb_{12} cage. The accumulation of minority-spin density on the ligand is very typical of ligand-centred radicals, which are most commonly found in combination with first row transition elements near the middle of the d block (Mn, Fe, Co). The dramatically different electron density distributions in the Ni and Mn species can be traced to the relative stabilisation of the 3d orbitals on moving left to right across the transition series. Thus the h_g-symmetric HOMO in I_h symmetry lies considerably higher in $[Mn@Pb_{12}]^{3-}$ than in $Ni@Pb_{12}$, and moreover has dominant Mn 3d rather than Pb 6p character. The complementary Pb 6p character is now localised in the lower-lying $1h_g$ orbital. As a result the holes in the valence shell (and therefore the unpaired electron density) are localised on the Mn centre rather than over twelve Pb atoms, and the exchange splitting between spin-α and spin-β components of the $2h_g$ HOMO is much more pronounced. The combined effects of (i) the lower effective nuclear charge on Mn and (ii) the greater exchange splitting

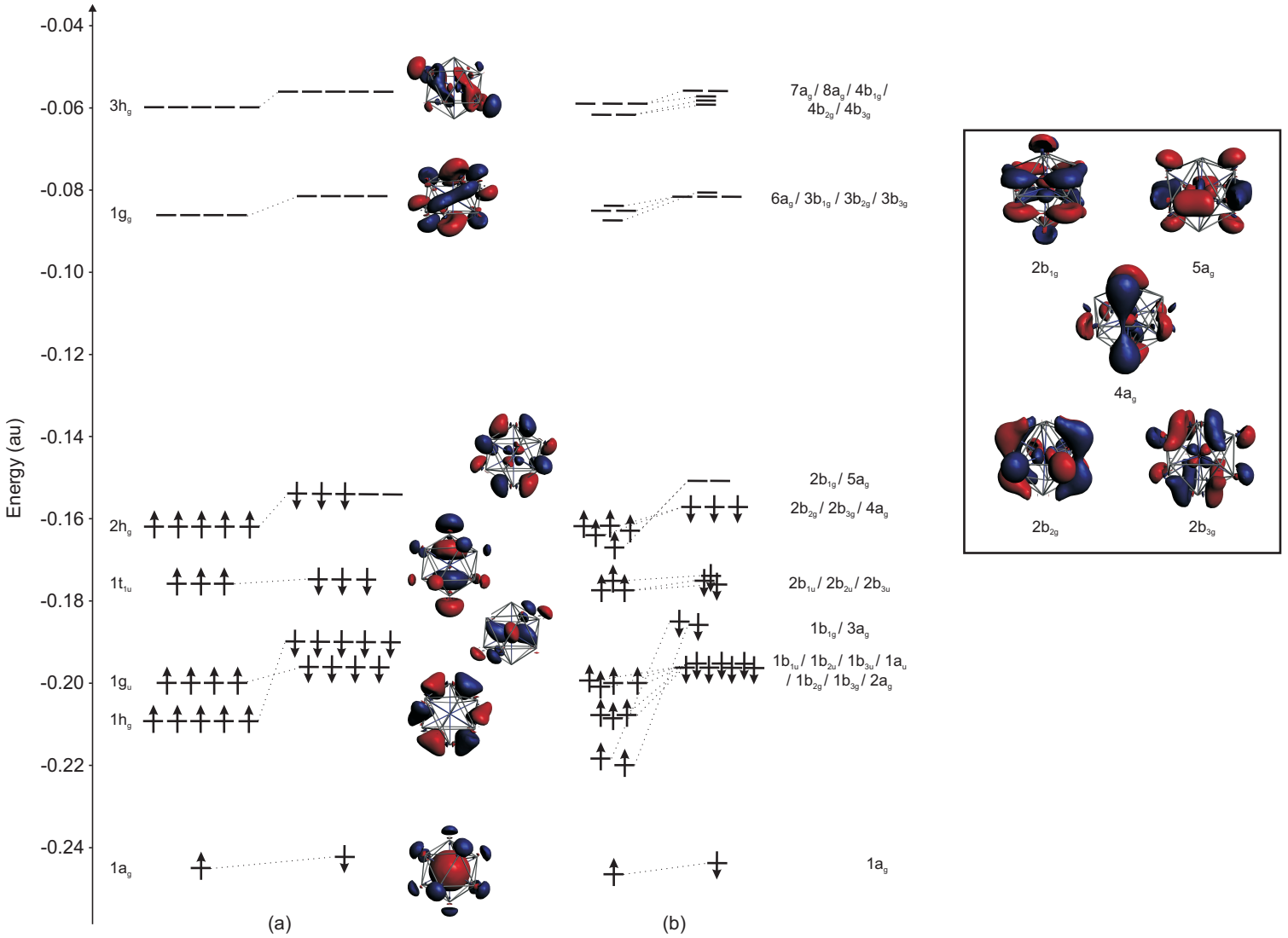

Figure 4.8: Kohn-Sham orbitals (β-spin manifold) for Ni@Pb_{12} in (a) I_h and (b) D_{2h} symmetry (contour value 0.025). Inset are contour plots of the five frontier orbitals (3 occupied, 2 vacant) of the spin-β manifold in D_{2h} symmetry. [Original in colour]

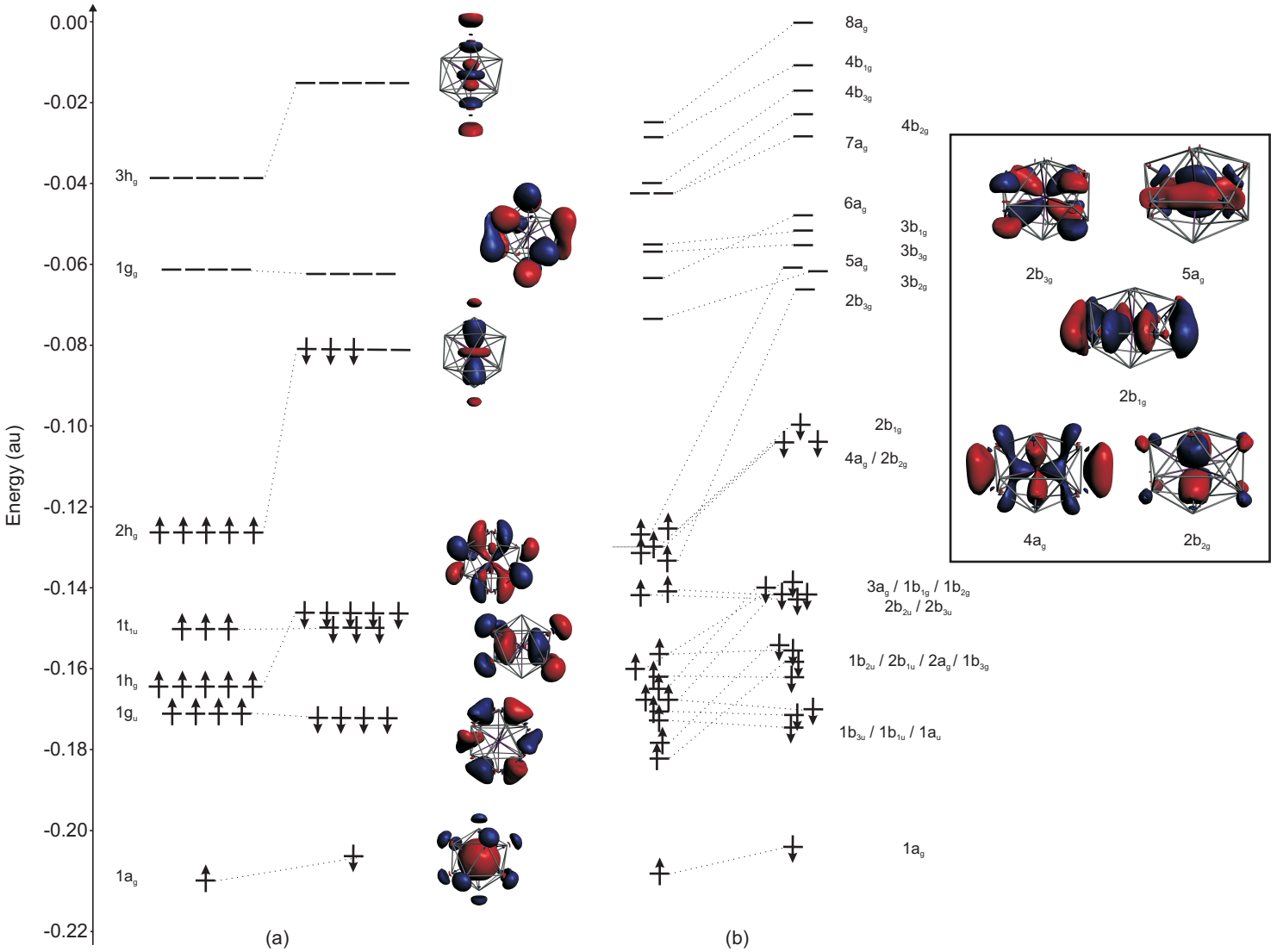

Figure 4.9: Kohn-Sham orbitals (β-spin manifold) for $[Mn@Pb_{12}]^{3-}$ (a) I_h and (b) D_{2h} symmetry (contour value 0.025). Inset are contour plots of the five frontier orbitals (3 occupied, 2 vacant) of the spin-β manifold in D_{2h} symmetry. [Original in colour]

of the HOMO serve to push the spin-β component up, such that it lies in the same energetic window as the LUMO ($1g_g$) and LUMO+1 ($3h_g$) of the $[Pb_{12}]^{2-}$ cage. Symmetry-allowed mixing between the latter and the Mn 3d orbitals therefore results in partial transfer of spin-β electron density from the metal to the cage. The resultant build-up of spin-α density on the metal means that ρ_{Mn} exceeds the value of 2.0 for a pure metal-centred triplet.

The impact of allowing the structure to relax from I_h to D_{2h} symmetry is energetically much more significant in $[Mn@Pb_{12}]^{3-}$ compared to $Ni@Pb_{12}$ (14.3 kcal mol^{-1} vs. 2.3 kcal mol^{-1}), and the perturbations to the frontier orbitals are similarly magnified. Thus three components of the spin-β $2h_g$ HOMO are stabilised by more than 0.02 au while the other two are destabilised by $\sim$0.02 au. The origin of this much enhanced splitting, and hence much more pronounced asymmetry of the cluster, lies in the energetic proximity of the LUMO and LUMO+1 of the cage ($1g_g$ and $2h_g$, respectively). The two orbitals are spatially very different: the former has exclusive tangential Pb 6p character while the 6p orbitals in the latter are aligned primarily in the radial direction. In I_h symmetry, sharing of d-electron density between the metal and the cage occurs exclusively through the h_g orbitals, and the result is the presence of radial Pb 6p character in the partially occupied $2h_g(\beta)$ orbital (Figure 4.9). Low-symmetry distortions, however, allow second-order mixing of one or more components of the closely-separated h_g and g_g sets, the net effect of which is to introduce some strongly Pb-Pb antibonding tangential character from the g_g manifold into the highest lying occupied spin-β orbitals. A comparison of the contour plots of the spin-β HOMOs shown in Figures 4.9a and 4.9b highlights the tangential nature of the Pb_{12}-based components of the HOMO in D_{2h} symmetry. The net effect of this second-order mixing is to further enhance charge transfer from the endohedral manganese centre to the

$[Pb_{12}]^{2-}$ cage, increasing the magnitude of the spin densities by ± 0.14 ($\rho_{Mn} = +3.35$, $\rho_{Pb_{12}} = 1.35$) and allowing the Mn centre to approach more closely the limit of the half-filled shell. The descent in symmetry[421] summarised in Table 4.2 also highlights the fact that the D_{2h} and D_{3d}-symmetric distortions allow for stabilisation of three of the five components of the h_g-symmetric orbital, precisely the situation required for a formal d^8 electron count with three spin-β electrons. A D_{5d}-symmetric distortion, in contrast, allows only for the stabilisation of two (either e_{1g} or e_{2g}) or four (both e_{1g} and e_{2g}) components but not three, and indeed the corresponding optimised structure is stabilised by only 0.32 kcal mol^{-1} relative to the I_h-symmetric reference state. In the isoelectronic $Ni@Pb_{12}$ analogue, where transfer of electron density from the endohedral metal to the Pb_{12} cage is much less pronounced, the energetic distinction between I_h, D_{5d} and D_{2h}/D_{3d} structures is much more marginal.

Table 4.2: Descent in Symmetry $I_h \rightarrow D_{5d} \rightarrow D_{3d} \rightarrow D_{2h}$.

I_h	D_{5d}	D_{3d}	D_{2h}
g_g	$e_{1g} + e_{2g}$	$e_g + a_{1g} + a_{2g}$	$a_g + b_{1g} + b_{2g} + b_{3g}$
h_g	$e_{1g} + e_{2g} + a_{1g}$	$2e_g + a_{1g}$	$2a_g + b_{1g} + b_{2g} + b_{3g}$

The 'broken-symmetry' nature of the wave function for $[Mn@Pb_{12}]^{3-}$, where spin-α and spin-β orbitals differ spatially, is very typical of ligand-centred radicals, which, as noted above, are most common for transition metals near the middle of the 3d block. The reason for this is that the high exchange energies associated with half-filled (or nearly half-filled) shell disfavour the sharing of electron density between metal and ligand. We can therefore identify the driving force pushing spin-β electron density onto the Pb_{12} cage as the increased exchange stabilisation associated with the accumulation of spin-α density at the metal. The limit of complete transfer of the three electrons to the cage corresponds to a $[Mn^{II}@Pb_{12}^{5-}]^{3-}$

distribution with a stable half-filled Mn d shell, consistent with the proposals of Deng[402] and Kumar[392] for $[Mn^{II}@E_{12}^{2-}]$. Alternatively, and by analogy to Fässler's iridium system,[369] the cluster could be formulated as $[Mn^{-I}@Pb_{12}^{2-}]^{3-}$. The net spin densities of +3.21 and -1.21 on Mn and the Pb_{12} cage, respectively (Table 4.1), lie approximately mid-way between the values anticipated for the two limiting forms: $[Mn^{II}@Pb_{12}^{5-}]^{3-}$ (ρ_{Mn} = +5.0, $\rho_{Pb_{12}}$ = -3.0) and $[Mn^{-I}@Pb_{12}^{2-}]^{3-}$ (ρ_{Mn} = +2.0, $\rho_{Pb_{12}}$ = 0.0).

4.4 The clusters $[Fe@Ge_{10}]^{3-}$ and $[Fe@Sn_{10}]^{3-}$

As noted in the introduction the approximately deltahedral structure of the title species $[Fe@Sn_{10}]^{3-}$ is, in isolation, unremarkable, being only marginally distorted from the ideal bicapped square antiprismatic structures typical of the closed-shell group 10 analogue, $[Ni@Pb_{10}]^{2-}$. However, the contrast with the Ge analogue $[Fe@Ge_{10}]^{3-}$, with its pentagonal prismatic geometry, is striking, and presents an opportunity to explore the electronic origins of the structural differences within a well-characterised isoelectronic pair. King and co-workers have argued that the adoption of this D_{5h}-symmetric structure in $[Pd@Ge_{10}]^{2-}$ and $[Pt@Ge_{10}]^{2-}$ but not the nickel analogue simply reflects the larger size of the 4d and 5d elements relative to the cage, which can only be accommodated in the larger pentagonal prism.[345,394] A similar argument can be invoked for the $[Fe@Ge_{10}]^{3-}$ / $[Fe@Sn_{10}]^{3-}$ comparison: the larger volume of a deltahedral Sn_{10} cage might be able to accommodate a formally Fe^{-I} ion where a Ge_{10} cage cannot. However, the fact that qualitatively similar trends are observed in the isoelectronic $[Mn@Pb_{12}]^{3-}$ / $Ni@Pb_{12}$ pair, where different degrees of electron transfer from metal to the cage proves to be the determining factor, suggests that a similar mechanism may be operative here. In this section we aim first to establish that density functional theory can reproduce the

observed structural chemistry (i.e. a preference for a D_{5h}-symmetric geometry in $[Fe@Ge_{10}]^{3-}$ but not its tin analogue), and then go on to explore the electronic origins of the structural differences.

With a view to the second of these goals, it is useful to consider various limiting formulations of the $[Fe@E_{10}]^{3-}$ species and their implications in terms of electron counting. An empty *closo*-$[E_{10}]^{2-}$ cage would require 42 (i.e. $4n + 2$)* valence electrons, so one possible formulation of the 51-electron Fe species is as $[Fe^{-I}@E_{10}^{2-}]^{3-}$: i.e. a formally anionic Fe centre with a d^9 configuration. A similar model has been proposed for $[Co@Ge_{10}]^{3-}$, where the calculated natural charge of -1.05 on the Co ion points towards a $[Co^{-I}@Ge_{10}^{2-}]^{3-}$ formulation with a closed-shell d^{10} configuration. Alternatively, a closed-shell d^{10} configuration at the Fe centre could be achieved by transfer of one electron from the cage to the metal, giving a limiting $[Fe^{-II}@E_{10}^{1-}]^{3-}$ formulation. Conversely, electron transfer from the metal to the cage leads to an $[Fe^{III}@E_{10}^{6-}]^{3-}$ formulation wherein the Fe centre attains a stable half-filled shell (high-spin d^5) configuration. Whilst such a high degree of charge separation is unrealistic, we have argued previously that the exchange stabilisation associated with high spin densities at the metal (the ultimate limit of which is the half-filled shell noted above) contributes to the driving force for the highly distorted structure observed in $[Mn@Pb_{12}]^{3-}$. A rather different perspective comes from noting that the three-connected pentagonal prism is the typical structure for an electron-precise 10-atom cluster, $[E_{10}]^{10-}$ with a total cluster electron count of 50 electrons. As highlighted by Fässler, such a configuration is precisely analogous to the well-known group 14 [n]prismanes, E_nR_n,[385,422–428] although in case of $[Fe@Ge_{10}]^{3-}$ it would imply an extremely polarised limiting $[Fe^{VII}@E_{10}^{10-}]^{3-}$ formulation. We return to a discussion of the electronic structure in terms of the

*This total valence electron count (TVEC) includes the $2n$ external lone pair electrons.

continuum defined by these limiting formulations following a survey of the potential energy surfaces for the two clusters, $[Fe@Ge_{10}]^{3-}$ and $[Fe@Sn_{10}]^{3-}$, computed using density functional theory.

In order to explore the potential energy landscape of both title clusters we used the following strategy, proposed by King and co-workers.[394] The polyhedra shown in Scheme 4.1 with 3-, 4- and 5-fold symmetry provide a convenient starting point for the optimisations. All of these represent common host cages that accomodate interstitial metal atoms. During the initial geometry optimisation of the clusters the indicated symmetries were kept fixed. Symmetry-breaking was then allowed in subsequent optimisation runs, using imaginary vibrational modes to converge to the nearest local minimum. This protocol allows us to probe a large part of the configurational space.[†]

Scheme 4.1: 10-vertex polyhedra used as starting geometries for the optimisations. The central metal ion is not shown.

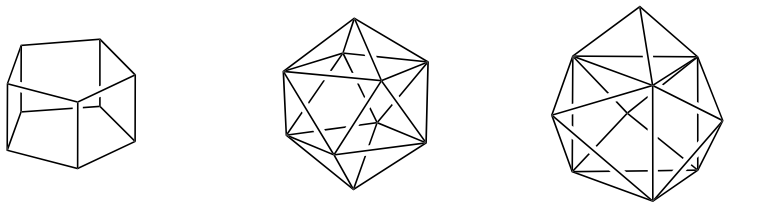

4.4.1 Optimised geometries

The doublet potential energy surface for the $[Fe@Ge_{10}]^{3-}$ cluster features a number of stationary points, illustrated in Figure 4.10. The most stable quartet lies more than 20 kcal mol^{-1} higher in energy and can therefore be safely ruled out as a possible ground state. Bond lengths and Mulliken spin densities for the various minima are also summarised in Table 4.3.

[†]Remaining imaginary frequencies are indicated throughout the text and within figures.

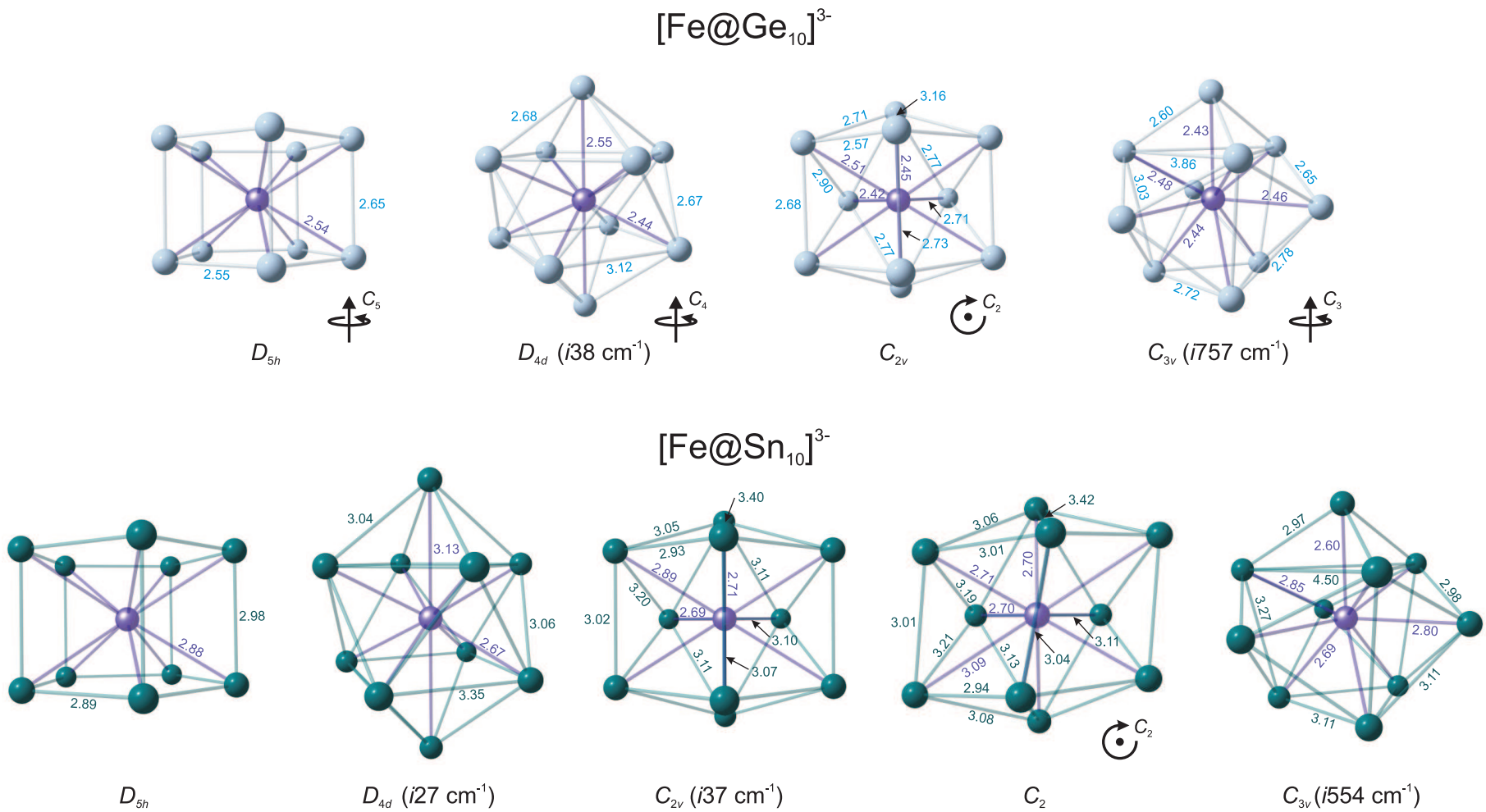

Figure 4.10: Optimised geometries of $[Fe@Ge_{10}]^{3-}$ (D_{5h}, D_{4d}, C_{2v} and C_{3v} symmetries) and $[Fe@Sn_{10}]^{3-}$ (D_{5h}, D_{4d}, C_{2v}, C_2 and C_{3v} symmetries). Fe-E (E = Ge, Sn) bonds and distances (Å) in purple, Ge-Ge bonds in blue and Sn-Sn bonds in green.

Table 4.3: Calculated bond lengths (Å), relative energies (kcal mol^{-1}) and Mulliken spin densities of $[Fe@Ge_{10}]^{3-}$ and $[Fe@Sn_{10}]^{3-}$. Values in parentheses indicate the number of symmetry equivalent bonds of a given length.

	$[Fe@Ge_{10}]^{3-}$				$[Fe@Sn_{10}]^{3-}$				
	D_{5h}	D_{4d}	C_{3v}	C_{2v}	D_{5h}	D_{4d}	C_{3v}	C_{2v}	C_2
M-E	2.54 (10)	2.44, 2.55 (8:2)	2.43, 2.44, 2.46, 2.48 (1:3:3:3)	2.42, 2.42, 2.45, 2.51 (2:2:2:4)	2.88 (10)	2.67, 3.13 (8:2)	2.60, 2.69, 2.80, 2.85 (1:3:3:3)	2.65, 2.69, 2.71, 2.89 (2:2:2:4)	2.64, 2.70, 2.70, 2.71, 3.09 (2:2:2:2:2)
E-E	2.55, 2.65 (10:5)	2.67, 2.68, 3.12 (8:8:8)	2.60, 2.65, 2.72, 2.78, 3.03, 3.86 (3:6:3:6:3:3)	2.57, 2.68, 2.71, 2.71, 2.73, 2.77, 2.90, 3.16 (4:2:4:1:1:4:4:2)	2.89, 2.98 (10:5)	3.04, 3.06, 3.35 (8:8:8)	2.97, 2.98, 3.11, 3.11, 3.27, 4.50 (3:6:3:6:3:3)	2.93, 3.02, 3.05, 3.07, 3.10, 3.11, 3.20, 3.40 (4:2:4:1:1:4:4:2)	2.94-3.42
imag freq. / cm^{-1}	–	*i*38	*i*757	–	–	*i*27	*i*554	i37	–
Spin densities									
M	1.45	0.65	0.36	0.53	1.96	1.16	1.05	1.22	1.28
$\sum E_{10}$	-0.45	0.35	0.64	0.47	-0.96	-0.16	-0.05	-0.22	-0.28
$\langle S^2 \rangle$	0.84	0.77	0.76	0.77	1.09	0.80	0.99	0.94	0.88
Rel. energy	0.0	+8.5	+8.3	+5.9	+7.6	+0.7	+4.5	+0.9	0.0

The global minimum proves to be a $^2A_1'$ state with a pentagonal prismatic structure (D_{5h} symmetry), and the calculated structural parameters are in excellent agreement with their crystallographic counterparts. The ten symmetry-equivalent Fe-Ge separations are 2.54 Å (c.f. 2.51-2.53 Å from X-ray) while the inter-ring (vertical edge, v) and intra-ring (horizontal edge, h) Ge-Ge bond lengths are 2.65 and 2.55 Å, respectively, (c.f. 2.61-2.62 Å and 2.53-2.54 Å). The ratio v/h between the lengths of the vertical and horizontal edges is 1.04, comparable to values of 1.05-1.06 computed for the series $[M@Ge_{10}]^{2-}$ (M = Ni, Pd, Pt)[394] and 1.06 for the $[Co@Ge_{10}]^{3-}$ cluster,[381] all of which exhibit a total valence count of 52. The Ge-Ge bond distances in $[Fe@Ge_{10}]^{3-}$ are however substantially shorter than in the Group 10 analogues, where the edge lengths range from 2.73 Å (v) and 2.61 Å (h) for Ni to 2.83 Å (v) to 2.68 Å (h) for Pt.

Fässler has previously noted that the isostructural relationship between $[Fe@Ge_{10}]^{3-}$ and 52-electron $[Co@Ge_{10}]^{3-}$ is difficult to reconcile with the doubly degenerate nature of the HOMO in the latter (e_2'' symmetry) which, in the absence of electronic rearrangement, would imply a Jahn-Teller active $^2E_2''$ ground state for the Fe compound.[330] Our calculations indicate that this $^2E_2''$ state lies 17 kcal mol^{-1} above the $^2A_1'$ equilibrium structure. Amongst the alternative structural motifs, only the C_{2v}-symmetric structure represents a true minimum, lying 6 kcal mol^{-1} above the D_{5h}-symmetric ground state. The Fe-Ge separations in this case range from 2.42 to 2.51 Å while Ge-Ge bond distances vary between 2.57 to 3.16 Å, substantially longer than those in the pentagonal prism.

The C_{2v}-symmetric structure is very closely related to the deltahedral bicapped-square antiprismatic structure (D_{4d}), which lies only 2.5 kcal mol^{-1} higher in energy. The Fe-Ge bond distances in this case split into two distinct sets, 2.55 Å and 2.44 Å in a 2:8 ratio, while the Ge-Ge bond lengths range from 2.67 to 3.12 Å.

The D_{4d}-symmetric structure is in fact not a minimum but rather a second order saddle point, and following either of the doubly-degenerate imaginary frequencies ($i38$ cm^{-1}) leads to the more stable C_{2v}-symmetric species.

Scheme 4.2: Imaginary modes of the D_{4d}- and C_{3v}-symmetric structures. Viewed along highest axis of rotation.

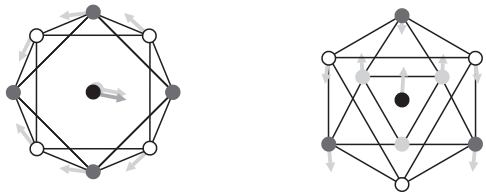

Likewise, optimisation of the tetracapped trigonal prismatic geometry (C_{3v} symmetry) also yields a second order saddle point, almost isoenergetic to the D_{4d} structure and +8.3 kcal mol^{-1} above the D_{5h} global minimum. Following either of the doubly degenerate imaginary modes ($i757$ cm^{-1}) again leads to the C_{2v}-symmetric structure.

Turning to the $[Fe@Sn_{10}]^{3-}$ homologue, a corresponding range of stationary points can be located on the potential energy surface, but the global minimum is now a C_2-symmetric structure with bond lengths remarkably similar to those in the crystal structure. As anticipated in the discussion of the structural data, the C_2-symmetric global minimum is also closely related to the deltahedral D_{4d}-symmetric structure (1 imaginary frequency) which lies only 0.7 kcal mol^{-1} higher in energy, confirming the view that the tin cluster can be viewed as essentially deltahedral. The pentagonal prismatic (D_{5h}) structure is also a local minimum on the potential energy surface, but lies 7.6 kcal mol^{-1} above the global minimum.

4.4.2 Trends along the series Mn Fe Co Ni Cu Zn

The discussion in the previous paragraph establishes that the computed potential energy surfaces faithfully reproduce the known structural chemistry, in so much as the global minimum is approximately deltahedral for $[Fe@Sn_{10}]^{3-}$ but pentagonal prismatic for the Ge analogue. Some insight into the underlying electronic origins of this trend can be gained by considering the variation in relative energies of the various geometries across a more extended isoelectronic series containing the first row transition metal series, $[M@E_{10}]^n$ (Fe: $n = 3-$; Co: $n = 2-$; Ni: $n = 1-$; Cu: $n = 0$; Zn: $n = 1+$, E = Ge, Sn), all of which have a total valence electron count of 51 (Figures 4.11b and 4.11d). We also consider their one-electron reduced homologues with 52 valence electrons (Figures 4.11a and 4.11c), some of which have previously been discussed by Fässler[381] and by King.[393,394] The members of these two isoelectronic series are simply related by the successive addition of protons to the endohedral transition metal centre, so crossing the series from Fe to Zn involves a progressive shift in electron density away from the Ge_{10} cage towards the endohedral metal as well as a decrease in size of the latter. One immediately striking feature is that the trend lines for the D_{4d}, C_{2v} and C_{3v}-symmetric structures lie approximately parallel to each other (note that the reference point is always the D_{5h}-symmetric structure), confirming the fact that all three are closely related electronically as well as structurally (as marginally distorted deltahedra).

For the $[M@Ge_{10}]^n$ group with 52 skeletal electrons (Figure 4.11a), a singlet state with a *closo*-D_{4d} bicapped square antiprism (the structure anticipated by the Wade-Mingos rules) is unambiguously the global minimum for the later transition metals, M = Ni, Cu and Zn. However, the energetic separation between D_{4d}- and D_{5h}-symmetric isomers decreases steadily on moving left from Zn towards Fe, and

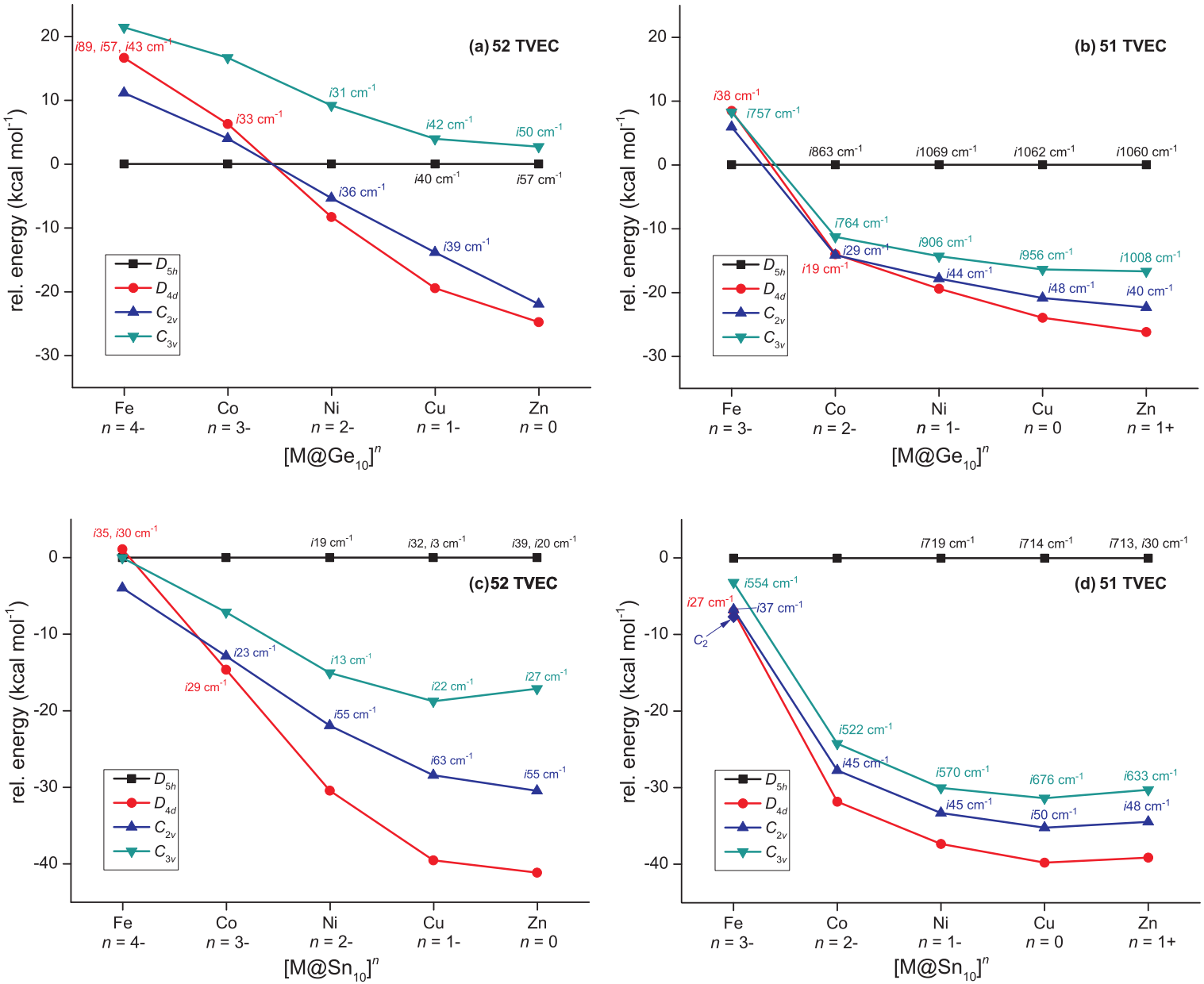

Figure 4.11: Energy profiles for isoelectronic $[M@E_{10}]^n$ (M = Fe, Co, Ni, Cu, Zn) series, comparing different symmetries (D_{5h}, D_{4d}, C_{3v}, C_{2v}). (a) E = Ge, 52 TVEC. (b) E = Ge, 51 TVEC. (c) E = Sn, 52 TVEC. (d) E = Sn, 51 TVEC.

a crossover occurs between Ni and Co, where the global minimum is now the D_{5h}-symmetric structure. Korber has previously noted that, "some kind of border seems to have been crossed when moving from Group 10 to Group 9 endohedral atoms, and the encapsulated transition metal atom clearly is not as innocent a template as it was assumed to be from the earlier results".[429] In this case, the 'border' involves a switch in stability of the D_{5h} and D_{4d} structures, such that the former is the global minimum for Fe and Co. The crossover between D_{5h} and D_{4d} structures also coincides with the emergence of imaginary frequencies in the latter: these imaginary frequencies lead to marginally more stable C_{2v}-symmetric structures, but these still lie well above the D_{5h} global minimum. Our results for this 52-electron series are fully consistent with earlier calculations.[345,381,393,394,412]

Turning to the 51 electron clusters (Figure 4.11b), $[M@Ge_{10}]^n$, the overall picture is very similar, except that the crossover between D_{5h} (early transition metals) and D_{4d} (late transition metals) equilibrium structures is shifted one position to the left, now occurring between Co and Fe. The data in Figure 4.11 are consistent with all available experimental evidence: both $[Fe@Ge_{10}]^{3-}$ and $[Co@Ge_{10}]^{3-}$ adopt the pentagonal prismatic structure but an approximately deltahedral geometry is favoured for $[Fe@Sn_{10}]^{3-}$.

We highlighted previously that the ground state for $[Fe@Ge_{10}]^{3-}$ has $^2A_1'$ symmetry, and hence is not susceptible to first-order Jahn-Teller distortion. For all later transition elements, however, the ground state in D_{5h} symmetry has $^2E_2''$ symmetry, and hence is prone to distortion. The singly occupied orbital in $[Fe@Ge_{10}]^{3-}$ ($3a_1'$, Figure 4.12) has significant metal d_{z^2} character whereas the $1e_2''$ orbital is localised by symmetry on the Ge cage. Thus the switch in ground state from $^2A_1'$ to $^2E_2''$ reflects the relative stabilisation of the d orbitals on crossing the period, and the fact that the d^{10} shell does not participate strongly in bonding from $[Co@Ge_{10}]^{3-}$

onwards. The plots for the 52 and 51-electron Sn analogues, $[M@Sn_{10}]^n$, shown in Figures 4.11c and 4.11d are qualitatively similar to those in Figures 4.11a and 4.11b, but the D_{5h}-symmetric structures are now uniformly destabilised by ca. 20 kcal mol^{-1} relative to the approximately deltahedral alternatives (D_{4d} , C_{3v} and C_{2v}). The result is that in no case is the D_{5h} structure predicted to be the global minimum, and most importantly, the $[Fe@Sn_{10}]^{3-}$ anion prefers the deltahedral D_{4d} geometry.

4.4.3 Analysis of the electronic structure

The trends within the isoelectronic series shown in Figure 4.11 establish a clear preference for D_{5h}-symmetric structures in cases where the metal centre is formally electron rich (or, more precisely, proton-poor), towards the middle of the transition series. The same trend is apparent in the shift in the crossover point from Ni/Co for 52 electron $[M@Ge_{10}]^n$ species to Co/Fe for the less electron rich 51-electron analogues, and also in the switch from a D_{4d}-symmetric structure for $[Ni@Ge_{10}]^{2-}$ to D_{5h} for the more electropositive $[Pt@Ge_{10}]^{2-}$.

It is, of course, difficult to separate arguments based on the electropositivity of the endohedral metal from the steric arguments put forward by King and co-workers: the more electropositive early transition metals are also the largest, the two phenomena (size and electropositivity) simply being different consequences of the variation in effective nuclear charge across the series. However, the computed spin densities and values of $\langle S^2 \rangle$ summarised in Table 4.3 offer strong evidence for a link between structural preference (3-connect D_{5h} vs. deltahedral D_{4d}) and the distribution of electron density between the endohedral metal and the cage. The D_{4d}-symmetric doublet state of $[Fe@Ge_{10}]^{3-}$ shows negligible spin contamination ($\langle S^2 \rangle = 0.77$) and has majority spin density (α) on both metal and ligand, the spin

delocalisation being typical of paramagnetic transition metal complexes where electron transfer from ligand to metal dominates the bonding. In the D_{5h}-symmetric isomer, in contrast, the net spin density on the Fe centre ($\rho_{\mathrm{Fe}} = 1.45$) exceeds the expected value for a metal-centred doublet (1.0), the surplus being offset by an accumulation of minority spin (β) density on the Ge_{10} cage (-0.45). Spin polarisation of this type is commonly found in complexes of non-innocent ligands. The spatial distinction between spin-α and spin-β manifolds is indicative of significant spin contamination, as evidenced by the value of $\langle S^2 \rangle = 0.84$ ($>0.75 = S(S+1)$, the value expected for a pure doublet). At its extreme limit, the shift of spin-β electron density onto the cage would lead to the limiting formulation $[Fe^{III}@Ge_{10}^{6-}]^{3-}$ discussed in the introductory comments. The spin densities suggest that the true situation lies much closer to the $[Fe^{-I}@Ge_{10}^{2-}]^{3-}$ limit, but the tendency to lose spin-β electron density to the cage, and hence enhance the exchange stabilisation of the metal centre, is nevertheless clear. In the previous section we have argued that the strong prolate distortion observed in the $[Mn@Pb_{12}]^{3-}$ cluster is driven by a similar shift in electron density transfer from the endohedral metal to the cage. Thus the structural and electronic contrast between the highly distorted $[Mn@Pb_{12}]^{3-}$ and the approximately deltahedral (and isoelectronic) $Ni@Pb_{12}$ discussed above appears to have similar underlying origins as the $[Fe@Ge_{10}]^{3-}$ / $[Fe@Sn_{10}]^{3-}$ comparison of interest here.

It remains to be resolved why a rather marginal shift in electron density results in such a dramatic change in structure, from an approximately *closo* deltahedron typical of a 42 electron count on the cluster $[Ge_{10}]^{2-}$ to a pentagonal prism which is, as noted above, the archetype for an electron precise $[Ge_{10}]^{10-}$ cluster with 50 valence electrons. A limiting formulation as $[Fe^{VII}@Ge_{10}^{10-}]^{3-}$ is clearly totally unrealistic, so why do the more electron-rich clusters not adopt a somewhat less

distorted *nido* structure that would seem more appropriate for the more marginal accumulation of electron density on the cage suggested by the spin populations? The answer to this question lies in the fact that the electron density is transferred to vacant cluster-based orbitals not as 'free' electrons or electron pairs (the basis of the Wade-Mingos rules), but rather through covalent overlap with occupied metal d orbitals. Thus in cases where backbonding from metal to the cage is significant, the optimal structural form will be that which best stabilises the most available electron density on the metal. In the case of $[Fe@Ge_{10}]^{3-}$ the four spin-β electrons are the most readily available (as they are destabilised relative to the spin-α set by exchange) and indeed the distortion from deltahedral (D_{4d}) to pentagonal prismatic (D_{5h}) structures has the effect of stabilising precisely four cluster-based orbitals. Thus the structural change is exactly the same as that required to accommodate the four additional electron pairs in an electron-precise $[Ge_{10}]^{10-}$ cluster, although the degree of charge transfer to the cage is very much less.

In an exactly parallel argument, the prolate (D_{2h}-symmetric) distortion in $[Mn@Pb_{12}]^{3-}$ discussed above stabilises precisely three vacant cage-based orbitals (relative to the *closo* icosahedral reference) exactly as required to accommodate the three spin-β electrons of the formally Mn^{-I} centre.

These concepts can be placed on a more formal level by referring to the Kohn-Sham orbital array for the D_{5h}-symmetric isomer of $[Fe@Ge_{10}]^{3-}$ shown in Figure 4.12. A symmetry analysis shows that the fifteen Ge-Ge bonding orbitals transform as $a_1' + a_2'' + e_1' + e_1'' + e_2' + e_2''$ (intra-ring) and $a_1' + e_1' + e_2'$ (inter-ring) while the five metal d orbitals transform as $a_1' + e_2' + e_1''$, giving the twenty valence orbitals shown in the Figure. Of the Ge-Ge bonding orbitals, eleven are approximately doubly occupied in the $^2A_1'$ ground state while the other four ($3e_2'$ and $2e_1''$) are unoccupied but overlap strongly with four of the Fe-based 3d orbitals (backbonding).

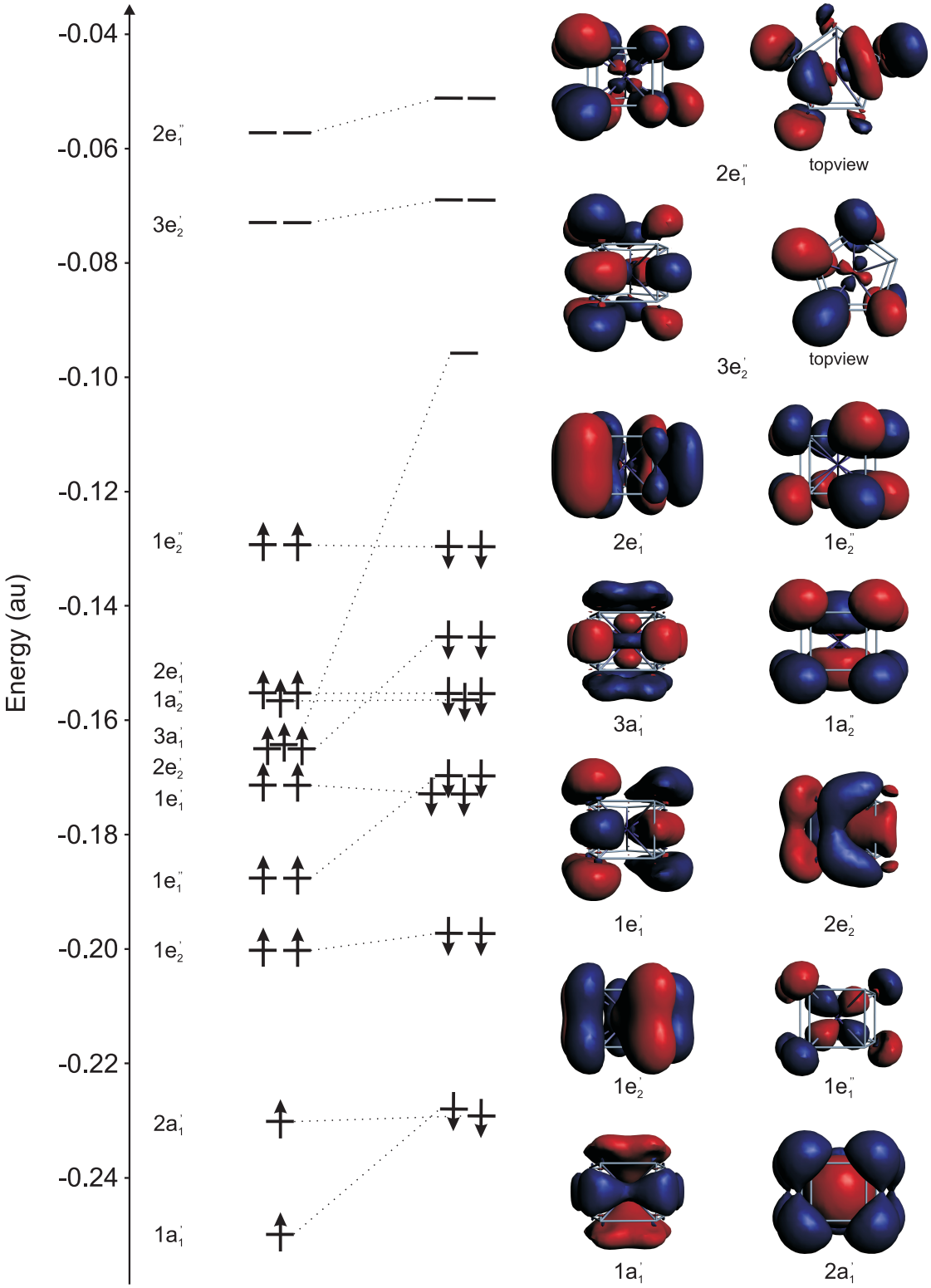

Figure 4.12: Kohn-Sham orbitals (α-spin manifold) for $[Fe@Ge_{10}]^{3-}$ in D_{5h} symmetry (contour value 0.02 au).

This backbonding mechanism will be most significant in the spin-β manifold, and so the transfer of minority spin density to the cage and the deviation of $\langle S^2 \rangle$ from 0.75 are both clear indications of a flow of electron density from the metal to the cage. Based on the distribution of electron density we argue that the nature of the distortion of the cage is determined not by the *total* electron density transferred to the cage via backbonding, but rather by the *number of orbitals over which it is distributed* - we should anticipate the same D_{5h}-symmetric structure for any cluster where electron density needs to be accommodated in four distinct cage-based orbitals. This model neatly rationalises the structure of $[Fe@Ge_{10}]^{3-}$ where there are four high-lying occupied spin-β orbitals, but it is perhaps less obvious why the same structure is adopted by $[Co@Ge_{10}]^{3-}$ where there are five doubly occupied d orbitals, not four (and therefore no spin polarisation). In principle it would be favourable to distort in such a way that five cage orbitals, rather than four, were stabilised but the only way in which this could be achieved would be to expand the cluster while retaining an approximately spherical deltahedral structure. Indeed we note from Table 4.3 that the average E-E bond lengths in the D_{4d}-symmetric structures are longer than those in the pentagonal prisms. This global breathing motion is strongly resisted by the underlying sigma bonding framework that binds the cage atoms, and as a result the D_{5h}-symmetric structure where only four of the five components of the d orbital participate in backbonding, is the best compromise.

How then can we rationalise the different structural preferences for $[Fe@Ge_{10}]^{3-}$ and $[Fe@Sn_{10}]^{3-}$? King and co-workers have argued that the transition from deltahedral to pentagonal prismatic geometries is sterically controlled, the larger endohedral metals requiring the larger but intrinsically less stable D_{5h}-symmetric cluster architecture. The electronic structure model developed here suggests that where the metal is relatively electropositive the D_{5h} structure is strongly stabilised

by backbonding, and this plays a significant role in overcoming the intrinsic preference for a deltahedral geometry. Nevertheless the transition from deltahedral (D_{4d}) to pentagonal prismatic (D_{5h}) architectures is undoubtedly associated with a reduction in strain in the Ge_{10} clusters that is less significant in their Sn_{10} analogues. Thus, although the extent of backbonding (as measured by the spin-β density on the E_{10} cage and by the deviation of $\langle S^2 \rangle$ from 0.75) is actually *greater* for $[Fe@Sn_{10}]^{3-}$ than for $[Fe@Ge_{10}]^{3-}$ (Table 4.3), the absence of steric strain is sufficient to displace the equilibrium in favour of the deltahedral structure. Thus, the differences between $[Fe@Ge_{10}]^{3-}$ and $[Fe@Sn_{10}]^{3-}$ therefore reflect the interplay between backbonding from the electron-rich Fe^{-I} centre to the cage and the intrinsic stability of the deltahedral cage: the former dominates for Ge, the latter for Sn.

4.5 Conclusions

In this chapter we have discussed the electronic structure of a new class of open-shell endohedral clusters, which adopt highly distorted geometries not readily interpreted in terms of the Wade-Mingos rules. In both $[Fe@Ge_{10}]^{3-}$ and $[Mn@Pb_{12}]^{3-}$ backbonding from the encapsulated metal ion to the $E_{10/12}$ cage plays a central role in determining the overall topology. As a result of spin-polarisation, backbonding is most prominent within the spin-β manifold (orbitals are higher in energy), and so includes three electrons in the case of manganese and four electrons for iron. The nature of the distortion (D_{2h} for $[Mn@Pb_{12}]^{3-}$ and D_{5h} for $[Fe@Ge_{10}]^{3-}$) is precisely that which stabilises the corresponding number of formally vacant orbitals on the cluster: three for the $I_h \rightarrow D_{2h}$ distortion and four for the $D_{4d} \rightarrow D_{5h}$ distortion. Thus, the structure is controlled by the number of orbitals over which spin-β electron density is distributed, rather than by the total density transferred.

5

Xenophilic Clusters

The electronic structure of so 'xenophilic' clusters, which contain both organometallic fragments and Werner-type paramagnetic transition metal centres, presents a challenge to simple theories of bonding. Density functional theory shows clearly that the cluster $Mn_2(thf)_4(Fe(CO)_4)_2$ is best described as an exchange-coupled Mn_2^{II} dimer, the closed-shell organometallic $[Fe(CO)_4]^{2-}$ fragments acting simply as bridging ligands. The high-spin configuration of the Mn^{II} ions leads to single occupation of the Mn-Fe σ^* orbitals and therefore substantially weaker metal-metal bonding than in conventional low-valent organometallic clusters. The transition metal fragments are effective mediators of superexchange ($J_{calc} = -44$ cm^{-1}), leading to the measured effective magnetic moment of $\sim$5 μ_B at 300 K, considerably lower than the limiting value of 8.37 μ_B for two uncoupled $S = 5/2$ Mn^{II} centres. The results obtained for the Mn_2^{II} dimer can be extrapolated to the hexagonal cluster $[Mn_7(thf)_6(CO)_{12}]^-$. The overall cluster can be represented by an exchange-coupled tetrameric Mn_2^{II} subsystem. Effective superexchange communicated by $[Mn(CO)_4]^{3-}$ fragments leads to large antiferromagnetic J coupling within the magnetic tetramer, and to a first approximation these pathways can be broken down into those of the dimer. Parts of this study presented in this chapter were published in Ref. [451].

5.1 Introduction

The interactions between metal centres in clusters span a broad spectrum of bond types, from the strong covalent bonds present in low-valent organometallic systems through to the very weak exchange coupling characteristic of collections of high-valent Werner-type paramagnetic centres.[431] In the first class, exemplified by homoleptic carbonyls such as $Mn_2(CO)_{10}$ (a in Scheme 5.1), the bonding is typically discussed within the framework of molecular orbital theory, with an emphasis on the direct overlap between d orbitals on adjacent centres.[347]

Scheme 5.1: Various types of transition metal clusters.

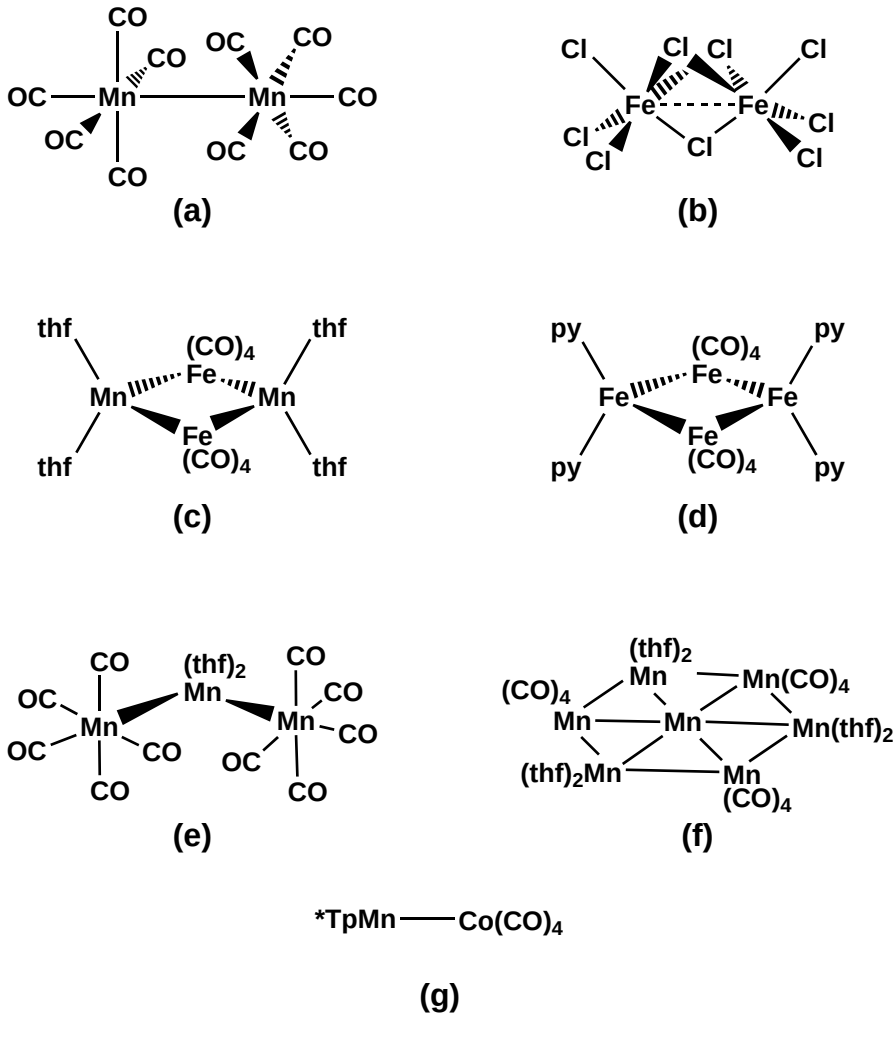

In contrast, the interactions between the paramagnetic metal centres in Werner-type clusters ($[Fe_2Cl_9]^{3-}$, for example, b) are typically mediated by bridging ligands, with direct overlap between the metal-based orbitals making only a minor contribution. In such circumstances, ligand-field-based models are a more natural reference point for describing the bonding.[432] The distinction between the two classes is, of course, not clearcut, and a number of cases that span the boundary have been discussed in the literature. The nonahalides of the chromium triad are a case in point: the chromium system, $[Cr_2Cl_9]^{3-}$, clearly lies in the exchange coupled regime, with a Cr-Cr separation in excess of 3.0 Å, but the larger 5d orbitals in the tungsten congener allow more effective overlap and hence a direct W-W triple bond (W≡W = 2.42 Å).[433] In certain cases, changes in counterion (e.g. $A_3[Mo_2Cl_9]$, A = NH_4^+, K^+, Na^+, Li^+)[434] or even simple crystal packing effects (e.g. $(Cp^*RuCl)_2(\mu\text{-}Cl)_2$)[435,436] can cause a shift from one paradigm to the other. These examples elegantly illustrate the innate flexibility of the metal-metal bond/interaction.

The term 'xenophilic' was coined to describe paramagnetic clusters that contain both low-valent organometallic and Werner-type transition metal centres, and their properties have been reviewed in some detail by both Gade[437] and Whittlesey.[438] Examples of such clusters include $Mn_2(thf)_4(Fe(CO)_4)_2$ (Scheme 5.1c),[439] $Fe_2(py)_4(Fe(CO)_4)_2$ (d),[440] $Mn(thf)_2(Mn(CO)_5)_2$ (e) and $[Mn][Mn_7(thf)_6(CO)_{12}]_2$ (f).[441] The crystal structure of the latter compound is remarkable, as it contains two $[Mn_7(thf)_6(CO)_{12}]^-$ anions, each of which is coordinated to an isolated Mn^{II} cation via three carbonyl oxygens to give an octahedral coordination geometry about the cation. The framework of each $[Mn\{(Mn(thf)_2)_3(Mn(CO)_4)_3\}]^-$ fragment contains a six-membered ring of Mn atoms, built from alternating $Mn(CO)_4$ and $Mn(thf)_2$ units, surrounding a seventh manganese at the ring centre to form a planar Mn_7 disc.

These clusters clearly fall between the two traditional bonding paradigms, and so present an intriguing challenge to theories of bonding. It is clear that xenophilic clusters contain highly polar M-M′ bonds, but it is less clear what the most appropriate reference point is for a discussion of their electronic structure: should they be viewed in the context of molecular orbital theory as polar analogues of low-valent clusters like $Mn_2(CO)_{10}$ or rather as Werner-type clusters of paramagnetic centres, where the low-valent metal centre acts as a ligand? In this chapter, we discuss the nature of the metal-metal bond in the manganese cluster $Mn_2(thf)_4(Fe(CO)_4)_2$, reported in 1996 by Whittlesey and co-workers.[439] This compound has an effective magnetic moment of $\sim$5.0 μ_B at 300 K, close to the spin-only value of 4.47 μ_B expected for a quintet state. It is important to emphasise, however, that no temperature-dependent measurements were reported, so it is not clear, *a priori*, whether this measured moment reflects the properties of an isolated ground state or of thermally populated excited states.

The electronic structure of this compound has been previously discussed from a molecular orbital perspective, and it has been argued that strong overlap of Mn- and Fe-based orbitals destabilises one of the five Mn d orbitals, such that each manganese centre adopts a local $S = 3/2$ configuration.[442] A narrow band of orbitals formed through overlap of the remaining four d orbitals on each manganese centre (mixed to some extent with those on the iron centres) is populated by the 10 valence electrons, yielding a quintet ^5A_g configuration (Figure 5.1), consistent with the available magnetic data.

Similar arguments have been used by the same authors to predict the electronic structure of the heptanuclear cluster $[Mn_7(thf)_6(CO)_{12}]^-$.* Each Mn atom in the $Mn(thf)_2$ fragments again adopts the same local $S = 3/2$ configuration, while two

*The actual calculation has not been performed due to computational limitations.

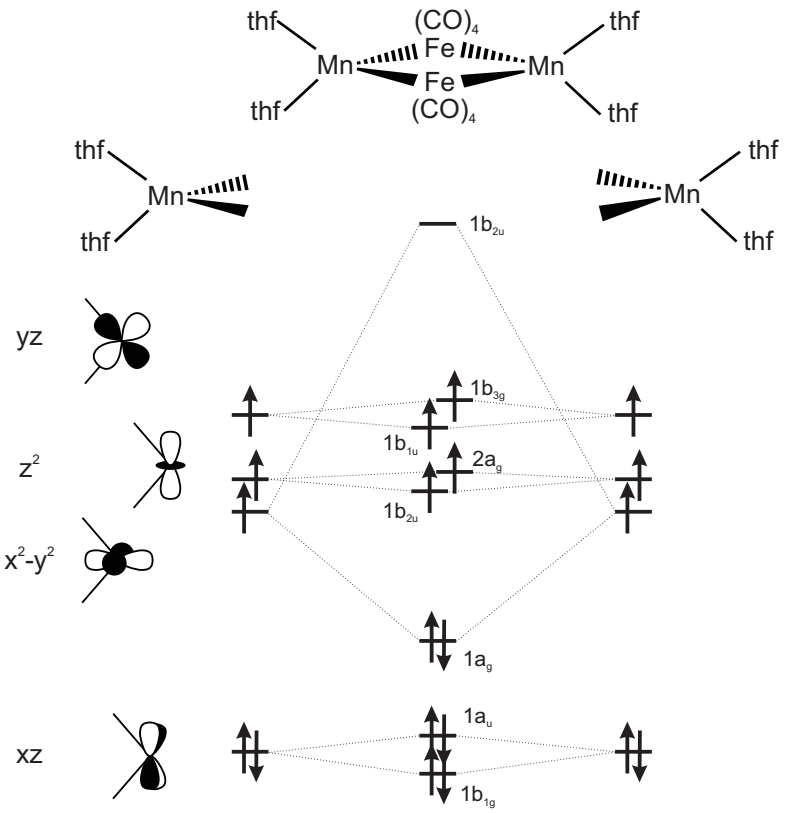

Figure 5.1: Schematic representation of the Mn d-d orbital interactions involved in the bonding in $Mn_2(thf)_4(Fe(CO)_4)_2$, according to Xu and Lin.[442] Note that the d_{xy} orbital has been used for forming Fe-Mn bonds and has been omitted.

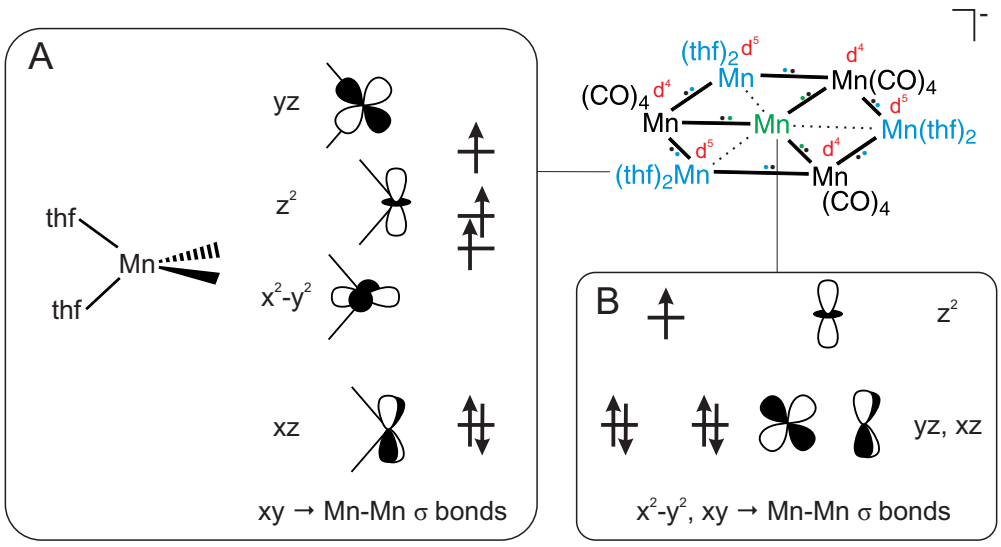

Figure 5.2: Schematic formal bonding model for $[Mn_7(thf)_6(CO)_{12}]^-$, according to Xu and Lin.[442] Panel A: $Mn(thf)_2$ fragment orbitals, panel B: central Mn ion fragment orbitals.

valence electrons are used to form Mn-Mn σ bonds with its ring neighbours (Figure 5.2). The central Mn atom, which has been tentatively assigned the extra electron due to the negative charge, possesses a local $S = 1/2$ configuration. The $Mn(CO)_4$ fragments are assumed to be inactive, being involved in forming three bonds with adjacent Mn sites. On a qualitative basis, it has been concluded that interaction of the three sets of $d_{x^2-y^2}$, d_{yz} and d_{z^2} orbitals from the $Mn(thf)_2$ fragments with the orbitals of the central Mn atom, d_{z^2}, p_x and p_y, could give rise to a set of weakly bonding, non-bonding and antibonding molecular orbitals. Depending on the distribution of the available 10 electrons (3 from each $Mn(thf)_2$, 1 from the central Mn atom), ground states between $S = 2$ and $S = 5$ may result.

More recently, Akita and co-workers have reported the closely related xenophilic bimetallic complex $^{i\mathrm{Pr2}}$TpMn−$Co(CO)_4$ (g in Scheme 5.1), along with its Fe, Co and Ni analogues, and argued that the interaction between metal centres is largely electrostatic, with only a very minor contribution from the direct overlap of the d orbitals on adjacent metals.[443] In this sense, the $[Co(CO)_4]^-$ fragment acts as a diamagnetic ligand, completing the tetrahedral coordination sphere about the manganese centre. The key difference between these two bonding models lies in the population of the Mn-M antibonding orbitals: in the earlier model (Xu and Lin[442]), they are vacant (as in typical organometallic clusters), while in the Akita model,[443] they would be singly-occupied, as in typical exchange coupled clusters of high-spin Mn^{II}. The contrast between these two models has encouraged us to reassess the electronic structure of $Mn_2(thf)_4(Fe(CO)_4)_2$ and $[Mn_7(thf)_6(CO)_{12}]^-$, which is the subject of this chapter. Our revised conclusion is that these systems should be viewed, to a first approximation, as exchange-coupled Mn^{II} dimers and tetramers, with the closed-shell $[Fe(CO)_4]^{2-}$ and $[Mn(CO)_4]^{3-}$ fragments[444,445] playing the role of bridging ligands. The computed value of -44 cm^{-1} for the Heisen-

berg exchange parameter, J, is large for a Mn^{II} dimer, but fully consistent with the reduction in magnetic moment compared to the value of 8.38 μ_B expected for two non-interacting Mn^{II} centres. Likewise, in the Mn^{II} tetramer a J constant of ca. -135 cm^{-1} is indicative of strong antiferromagnetic coupling between the four Mn^{II} centres and results in an overall $S = 5$ ground state for the system.

5.2 Methodology

All geometry optimisations presented in this chapter were carried out using Gaussian09.[54] Both complexes $Mn_2(thf)_4(Fe(CO)_4)_2$ (**1**) and $Mn_2(thf)_4Cl_2$ (**2**) are characterised by two magnetic metal centres (Mn^{II}) with site spins of $S_1 = S_2 = 5/2$, giving rise to total spins of $M_S = 5$ for the high-spin (HS) state and $M_S = 0$ for the broken-symmetry (BS) state due to ferromagnetic and antiferromagnetic coupling of the individual spin sites.

Scheme 5.2: Clusters analysed in this chapter.

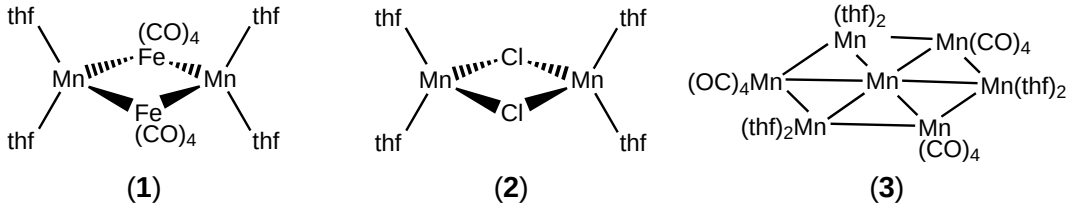

Geometry optimisations of the complexes in their broken-symmetry ($M_S = 0$) states were performed without any geometrical constraints (C_1 symmetry). The stationary points obtained were confirmed to be minima by the absence of imaginary frequencies. All calculations utilised the B3LYP[19,26,31,32] hybrid functional, in combination with the TZVP[206] triple-ζ basis set of Ahlrichs and co-workers on Mn and all coordinating atoms (**1**: Fe(1), Fe(2), O(1), O(2), O(7), O(8), C(9)-C(12), C(21)-C(24); **2**: Cl(1), Cl(2), O(1)-O(4)) and the SVP[207] basis set on the remaining atoms. Using the Heisenberg-Dirac-van Vleck spin Hamiltonian formal-

ism ($\hat{H} = -2J\hat{S}_1 \cdot \hat{S}_1$), the exchange coupling constant, J, can be calculated from the energy differences between the high-spin and broken-symmetry states according to the approaches of Noodleman or Yamaguchi.[52,228] The energies of both broken-symmetry (E_{BS}) and high-spin states (E_{HS}) were calculated at the optimised geometry of the former. Corresponding orbital transformations were performed using the ORCA programme.[60]

Computations on complex $[\mathrm{Mn_7(thf)_6(CO)_{12}}]^-$ (**3**) were performed as single point SCF calculations, using the corresponding unit extracted from the single crystal X-ray structure of $[\mathrm{Mn}][\mathrm{Mn_7(thf)_6(CO)_{12}}]_2$.[441] These calculations also employed the B3LYP functional in conjunction with the TZVP basis set on all atoms. Complex **3** is characterised by four magnetic metal centres ($\mathrm{Mn^{II}}$) with site spins of S_i = 5/2 (i = 1 − 4). The total number of distinct configurations for an n centre system is 2^{n-1}, which in the present tetranuclear array translates into 8 calculations. Parallel and antiparallel coupling of the individual spins yields effective spins of M_S = 10 for the high-spin (HS) state, as well as broken symmetry states with M_S = 5 and M_S = 0. Since the system as defined by the above Hamiltonian is, in principle, overdefined, the set of linear equations was solved by singular value decomposition.[446] This approach guarantees the best possible solution in a least-square sense. However, due to the presence of local C_3 symmetry we arrived at the same result analytically.

5.3 Electronic structure of $\mathrm{Mn_2(thf)_4(Fe(CO)_4)_2}$

5.3.1 Optimised geometry

The optimised geometry of the broken-symmetry (M_S = 0) state of $\mathrm{Mn_2(thf)_4(\mu\text{-}Fe(CO)_4)_2}$ (**1**; thf = tetrahydrofuran) is depicted in Figure 5.3, and selected struc-

tural parameters are summarised in Table 5.1. The single-crystal X-ray diffraction data are also shown for comparison, as are Mulliken spin densities on the manganese centres, ρ_{Mn}, and the expectation values of the squared total spin angular momentum operator $\langle S^2 \rangle$.

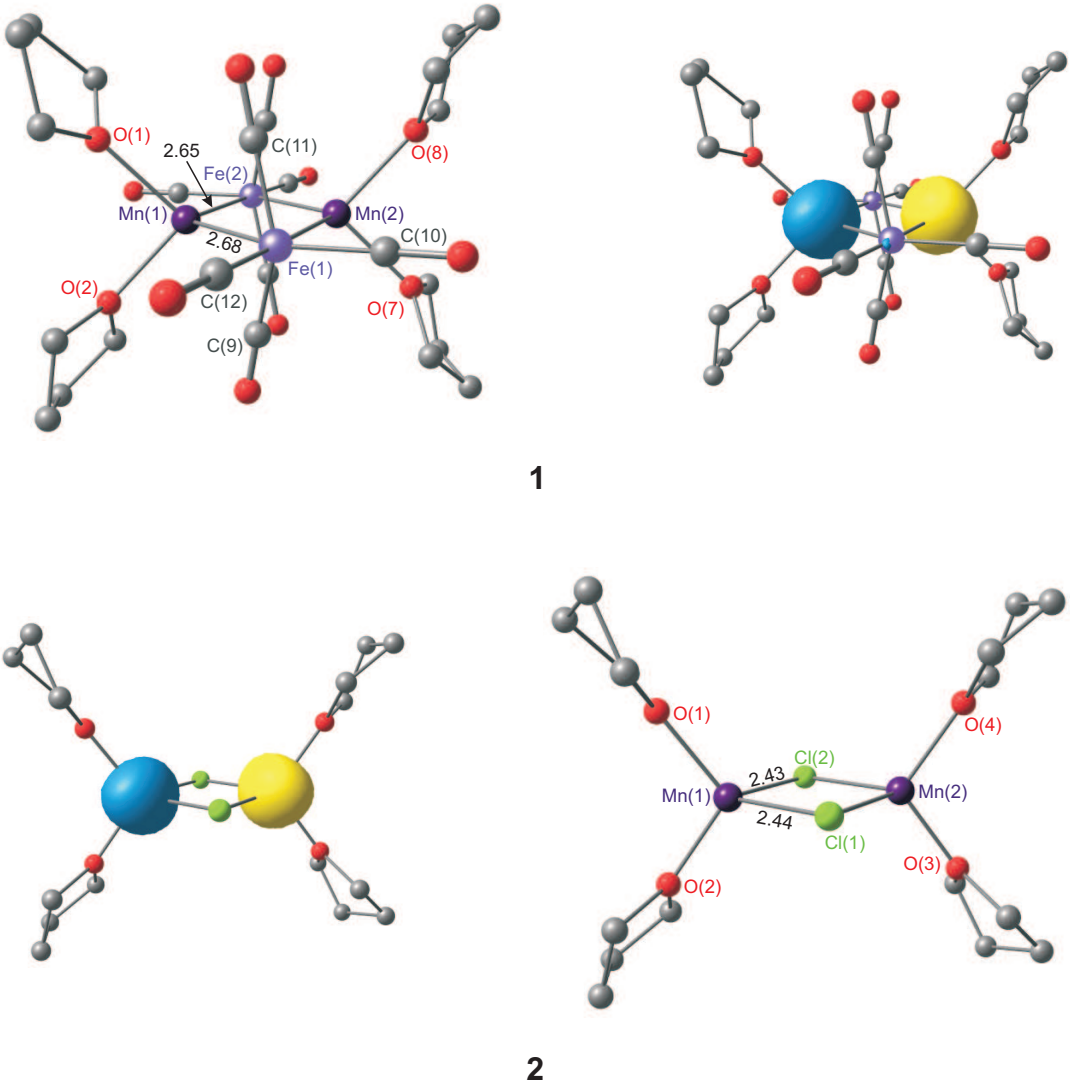

Figure 5.3: Optimised geometries and net spin densities of the broken-symmetry singlet state ($M_s = 0$) of complexes **1** and **2**, including selected bond lengths (Å).

The important structural features of the coordination sphere around the metal centres are well reproduced in the broken-symmetry ($M_S = 0$) state, although the Mn-O bond distances are overestimated by ∼0.10 Å, an error that is not untypical of calculations performed with the B3LYP functional. More importantly, the

Table 5.1: Selected bond lengths (Å) and angles (°) for the $M_s = 0$ states of complexes **1** and **2**. The expectation value of the square of the total spin angular momentum operator ($\langle S^2 \rangle$) and Mulliken spin density (ρ_{Mn}) on the manganese centres are also given.

$Mn_2(thf)_4(Fe(CO)_4)_2$ (**1**)			$Mn_2(thf)_4(Cl)_2$ (**2**)	
	Exp.	DFT		DFT
Mn(1)-Fe(1)	2.63	2.68	Mn(1)-Cl(1)	2.44
Mn(1)-Fe(2)	2.60	2.65	Mn(1)-Cl(2)	2.43
Mn-O (thf) (av.)	2.10	2.20	Mn-O (thf) (av.)	2.07
Mn(1)$\cdots$Mn(2)	2.90	2.91	Mn(1)$\cdots$Mn(2)	3.35
O-Mn-O	91.4	91.3	O-Mn-O	108.2
Mn-Fe-Mn	67.2	66.2	Mn-Cl-Mn	86.8
Fe-Mn-Fe	112.8	113.8	Cl-Mn-Cl	93.2
$\langle S^2 \rangle$		4.97	$\langle S^2 \rangle$	4.99
ρ_{Mn}		$\pm$4.85	ρ_{Mn}	$\pm$4.82

structure of the rhombic Mn_2Fe_2 core is well reproduced, and the Mn$\cdots$Mn separation of 2.91 Å is in excellent agreement with the X-ray value of 2.90 Å. The rather acute Mn-Fe-Mn angle of 67.2° is also well reproduced by theory (calc: 66.2°). The Mn-Fe separations are slightly asymmetric (2.68 and 2.65 Å), causing a distortion of the diamond core that is also apparent in the crystal structure. The $Fe(CO)_4$ units also reorientate such that one of the carbonyl ligands in the Mn_2Fe_2 plane lies approximately *trans* to the longer of the two Mn-Fe bonds (Mn(1)-Fe-C(10) = 145.9°, Mn(1)-Fe-C(11) = 112.1°). The net spin densities for the broken-symmetry state of $Mn_2(thf)_4(Fe(CO)_4)_2$ are typical of an exchange-coupled Mn^{II}/Mn^{II} dimer, as is the $\langle S^2 \rangle$ value of 4.97.

The Kohn-Sham orbitals shown in Figure 5.4 are characteristic of an 'inverted' ligand field scheme, where spin polarisation strongly stabilises the majority spin orbitals (α on the left-hand Mn centre, β on the right), such that the occupied and vacant metal manifolds span the ligand-based levels. Thus, the five occupied spin-α orbitals localised on the left Mn centre are 169-172 and 177a while the vacant spin-α components (on the right) are 188-192a.

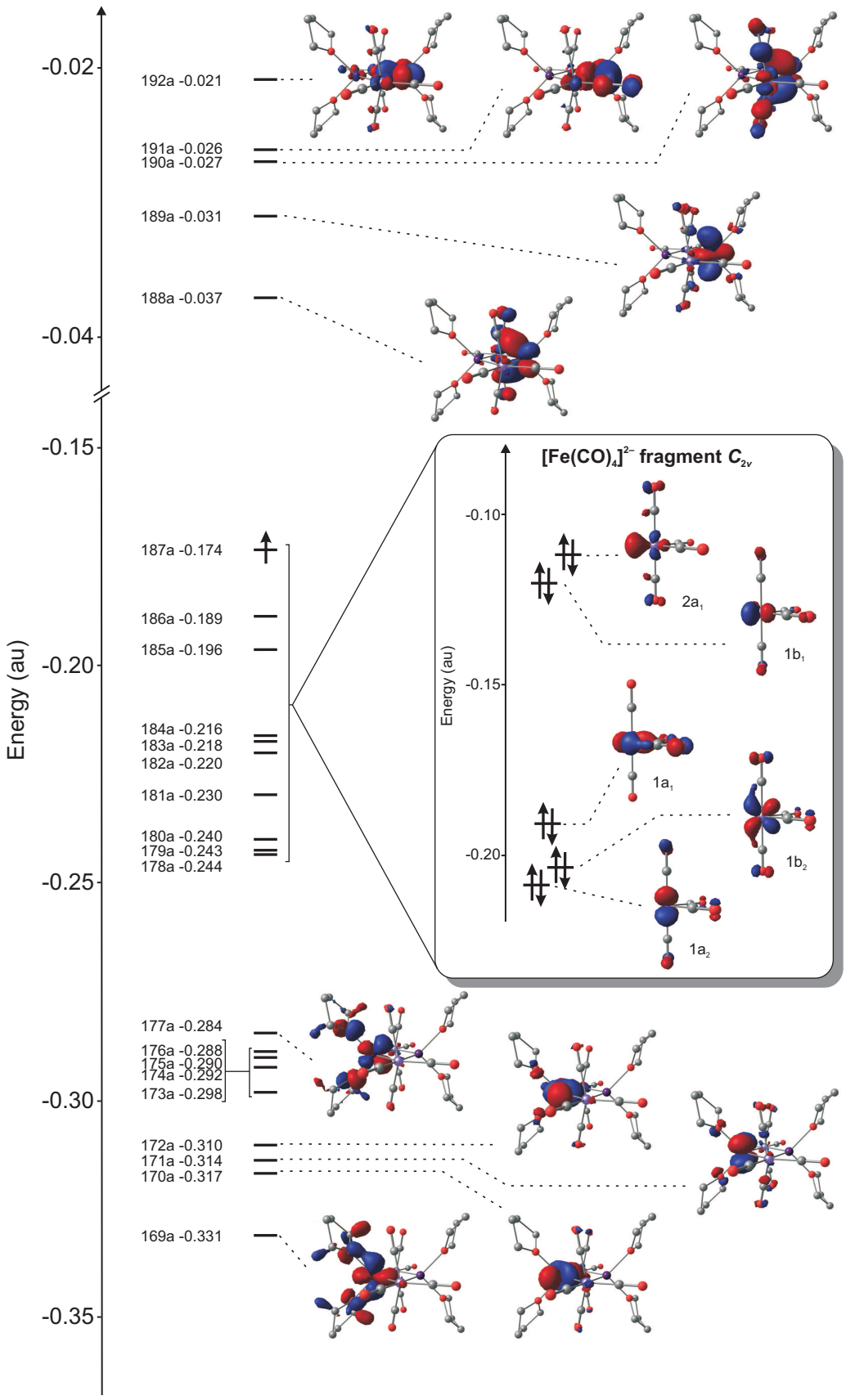

Figure 5.4: Molecular orbital diagram for the broken-symmetry ($M_S = 0$) state of complex **1**. The orbitals of the isolated $[Fe(CO)_4]^{2-}$ ion are shown in the inset.

The corresponding spin-β orbitals are mirror images and are not shown in the figure. The band of ten occupied orbitals 178-187a is made up of linear combinations of the well-documented frontier orbitals of the two $[Fe(CO)_4]^{2-}$ fragments (Figure 5.4, inset).[342] The highest lying of these is an s/p/d hybrid ($2a_1$) aligned along the bisector of the C-Fe-C angle, and a strongly Fe-CO σ antibonding orbital in the equatorial plane ($1b_1$). The remaining three orbitals (per fragment) are related to the octahedral t_{2g} set and lie at a substantially lower energy. Our analysis of the electronic structure of **1** suggests that the $[Fe(CO)_4]^{2-}$ units act as diamagnetic ligands, mediating the exchange coupling between two high-spin Mn^{II} ions. All Fe-Mn σ^* orbitals are therefore singly occupied, leading to weaker bonding than in conventional low-valent organometallic clusters. Much of the superexchange literature has focused on conventional ligands containing main group elements, but interactions mediated by diamagnetic transition metal ions are well known in the context of ligand biradical complexes[291] and also in linear chains of transition metal ions.[447–449]

Following the procedure developed by Noodleman and co-workers, we can map the energies of the broken-symmetry and high-spin states (the latter computed at the broken-symmetry geometry) of **1** onto the diagonal elements of the Heisenberg exchange Hamiltonian ($\hat{H} = -2J\hat{S}_1 \cdot \hat{S}_1$) to calculate the exchange coupling constant, J.[†] The resulting value of $J = -44\ \mathrm{cm}^{-1}$ indicates that the $[Fe(CO)_4]^{2-}$ bridges support moderately strong antiferromagnetic exchange between the manganese centres. The prediction of a singlet ground state can be reconciled with the measured μ_{eff} of $\sim$5.0 μ_{B} at 300 K by incorporating the computed value of J into the Bleaney-Bowers equation for two exchange-coupled $S = 5/2$ centres (Figure 5.5), which predicts a highly temperature-dependent magnetic moment. Thus, a μ_{eff} of

[†]Using $J = -(E_{\mathrm{HS}} - E_{\mathrm{BS}})/(4S_1S_2)$.

5.0 μ_B at 300 K is consistent with a J value in the region of -30 cm^{-1} – we note in this context that the B3LYP functional used here typically overestimates J.

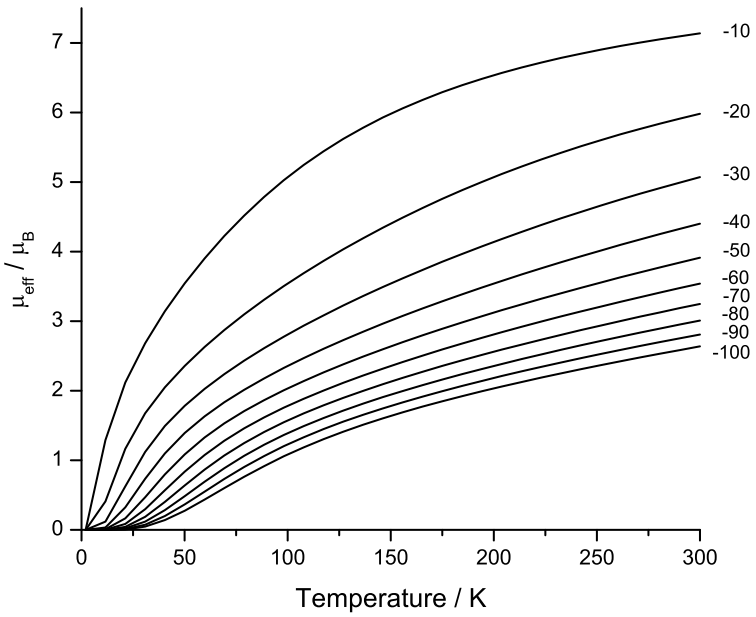

Figure 5.5: The simulated effective magnetic moment, μ_{eff}, of **1** in the temperature range 0-300 K using the Bleaney-Bowers equation (g = 2.00). Values of the isotropic exchange coupling constant J ($\hat{H} = -2J\hat{S}_1 \cdot \hat{S}_1$) are taken at 10 cm^{-1} intervals in the range -10 to -100 cm^{-1}.

The corresponding orbitals[223] for **1** are collected in Figure 5.6: deviations from zero are a measure of the effectiveness of the superexchange pathways. The overlaps indicate that the $J_{x^2-y^2/x^2-y^2}$ (S_{ab} = 0.199) and $J_{xy/xy}$ (S_{ab} = 0.104) pathways, both of which lie in the plane defined by the Mn_2Fe_2 core, dominate the exchange coupling. In order to make a direct comparison with a more conventional (i.e. main-group) ligand set, we have also analysed the exchange coupling in **2**, a direct analogue where the bridging $[Fe(CO)_4]^{2-}$ ligands have been replaced by Cl^-.

The general features of the optimised structure of **2** are very similar to those of **1** (Table 5.1), and the calculated J of -14 cm^{-1} at the optimised geometry suggests that the exchange coupling is considerably weaker than in **1**. However, the magnetostructural correlation shown in Figure 5.7 indicates that the values of J

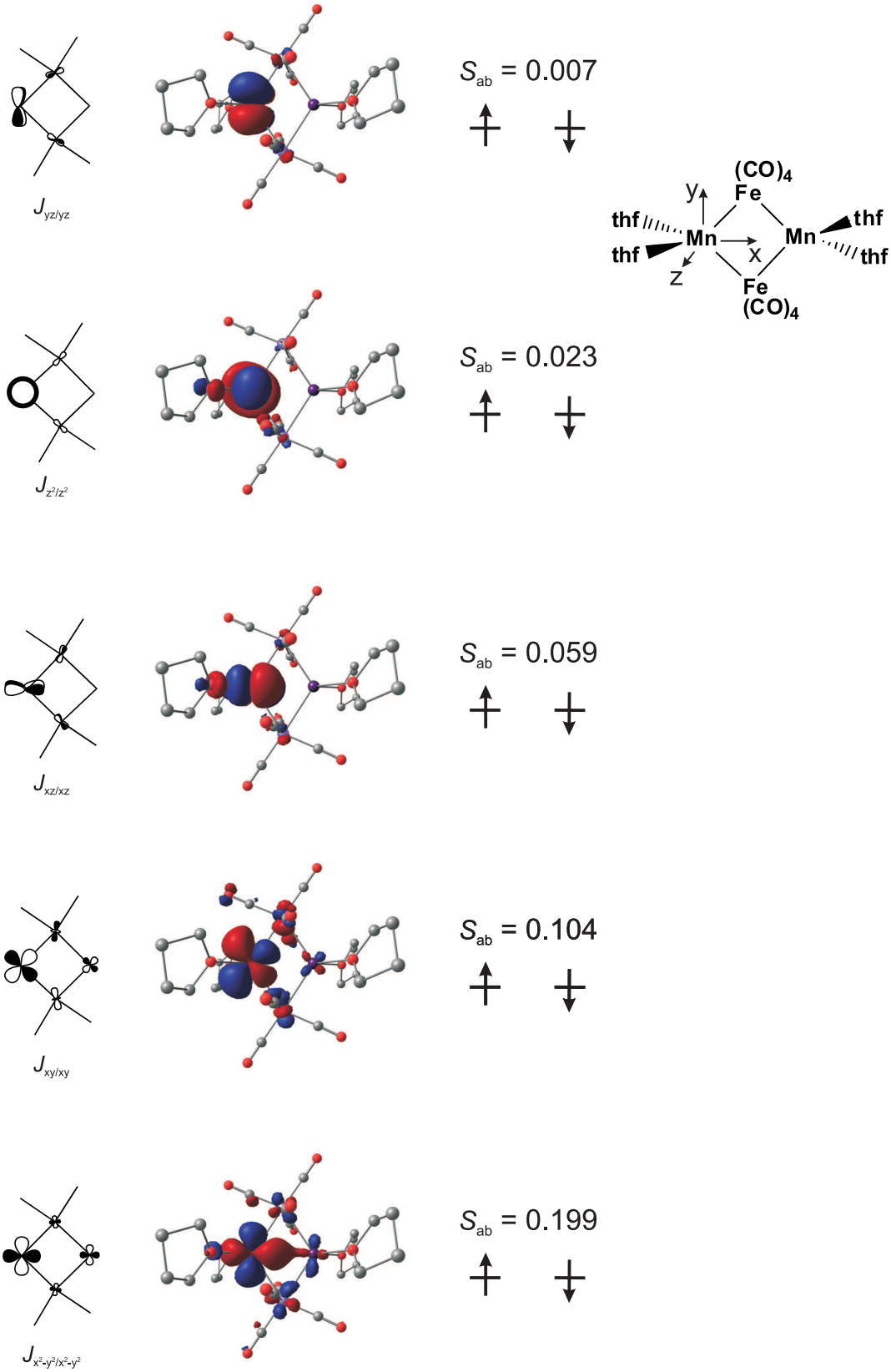

Figure 5.6: Corresponding orbitals of magnetic pairs of **1**.

are highly sensitive to the bridgehead angle, and at any given angle (in the range $60° < \Theta < 90°$), the Cl^- ligand is in fact a better mediator of superexchange than $[Fe(CO)_4]^{2-}$. Thus, the relatively strong exchange coupling in **1** is a direct consequence of the geometric preferences of the bridging ligand, and, in particular, the acute bridgehead angle. The origin of the acute angle can be traced to strong repulsions between the CO and thf ligands that increase dramatically as the $Fe(CO)_4$ units are pulled towards the centre of the cluster at smaller angles. Similar steric factors are likely to be a general feature of xenophilic clusters, imposing narrow bridgehead angles and hence unusually strong superexchange.

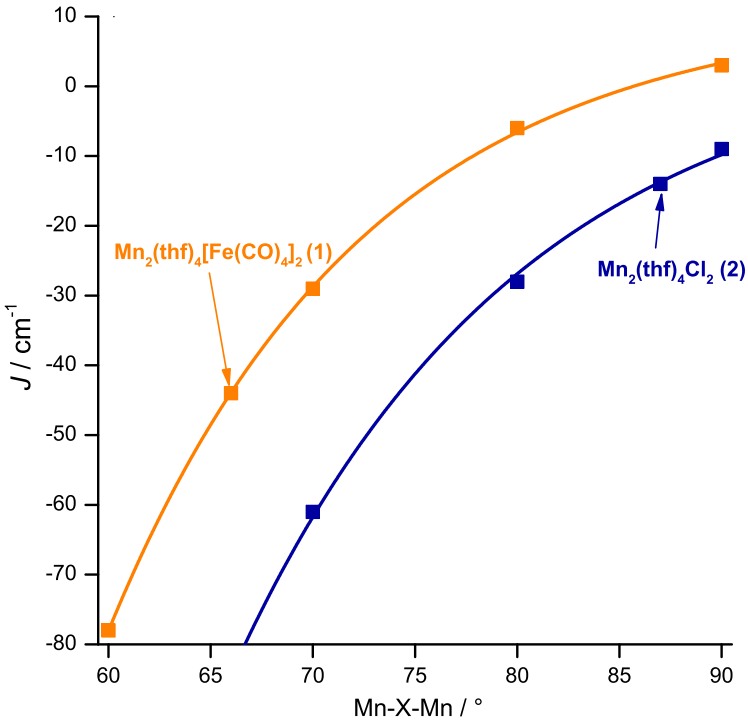

Figure 5.7: The dependence of J on the bridgehead angle for **1** and **2**. Arrows indicate the equilibrium structures of the two systems.

In conclusion, we have shown that the xenophilic cluster **1** is best regarded as an exchange-coupled Mn_2^{II} dimer, with the closed-shell $[Fe(CO)_4]^{2-}$ fragments playing the role of bridging ligands.[‡] Each of the Fe-Mn σ^* orbitals is therefore

[‡]We arrive at the same result for the related cluster $Fe_2(py)_4(Fe(CO)_4)_2$, where two Fe^{II} centres ($S_{loc} = 2$) are antiferromagnetically coupled. The optimised structure with a broken-symmetry ground state ($M_S = 0$) is also in excellent agreement with the X-ray structure.

singly-occupied in a typical high-spin Mn^{II} ligand-field scheme. The steric bulk of the bridging metal unit imposes a rather acute Mn-Fe-Mn bridgehead angle, which in turn leads to relatively strong superexchange between the manganese centres. The computed Heisenberg exchange coupling constant, J, of -44 cm^{-1} is fully consistent with the rather low effective magnetic moment measured at 300 K. The model of electronic structure that emerges is fundamentally different from that developed in earlier work, where the measured moment was erroneously assumed to be characteristic of the ground state.

5.4 Electronic structure of $[Mn_7(thf)_6(CO)_{12}]^-$

The crystal structure of complex $[Mn][Mn_7(thf)_6(CO)_{12}]_2$ is depicted in Figure 5.8, showing the position of the different fragments in a sandwich-like arrangement.

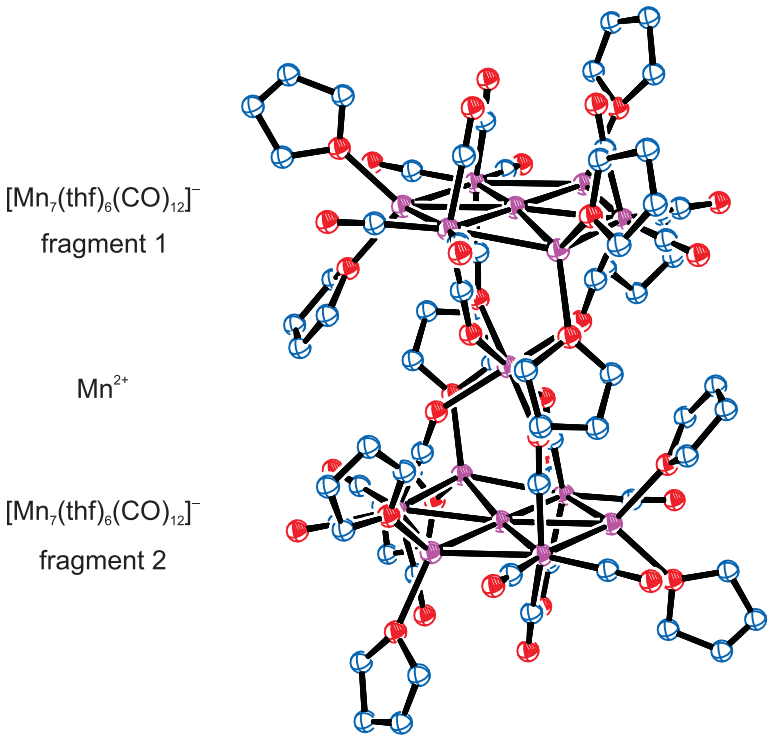

Figure 5.8: Single crystal X-ray structure of $[Mn][Mn_7(thf)_6(CO)_{12}]_2$, indicating the arrangement of the single Mn^{II} atom between the two disc-like fragments, **3**. [Original in colour]

Since we are only interested in a qualitative bonding analysis for the cluster **3**, we have performed single-point calculations on fragment 1, using cartesian coordinates obtained from the single-crystal structure analysis. As in the case of **1**, we can build the spin Hamiltonian by dividing the system into paramagnetic and diamagnetic fragments. Thus, the $Mn(thf)_2$ fragments and the central Mn atom form a tetranuclear subsystem of magnetic Mn^{II} centres with local spin of $S = 5/2$. The $Mn(CO)_4$ units are treated as closed-shell carbonylate ions, i.e. $[Mn(CO)_4]^{3-}$, bridging between the $Mn^{II}(thf)_2$ fragments. In this way, the charges of the three $[Mn(CO)_4]^{3-}$ fragments, three $Mn^{II}(thf)_2$ fragments and one Mn^{II} ion sum up to an overall charge of -1 for the cluster. We proceed by setting up the coupling scheme for the system in the usual way for tetranuclear species, where a central magnetic atom interacts with three peripheral ions.[450] Under the assumption that all pathways are inequivalent (essentially neglecting any local C_3 symmetry), the coupling is characterised by six J_{ij} constants, depicted in Scheme 5.3.

Scheme 5.3: Coupling scheme for the Mn_4^{II} subsystem within the cluster **3**.

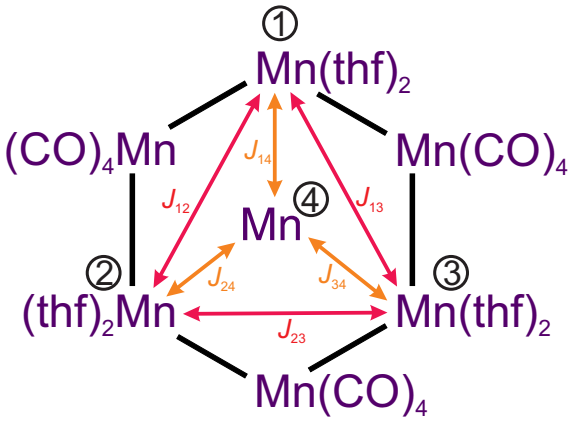

The spin Hamiltonian ($\hat{H} = -\sum J_{ij}\hat{S}_i \cdot \hat{S}_j$) describing the isotropic interaction thus becomes

$$\mathbf{H} = -J_{12}\mathbf{S}_1\mathbf{S}_2 - J_{13}\mathbf{S}_1\mathbf{S}_3 - J_{23}\mathbf{S}_2\mathbf{S}_3 - J_{14}\mathbf{S}_1\mathbf{S}_4 - J_{24}\mathbf{S}_2\mathbf{S}_4 - J_{34}\mathbf{S}_3\mathbf{S}_4 \qquad (5.1)$$

It is anticipated that the 'outer' J coupling along the periphery will be much smaller, owing to the large separation (~4.8 Å) of the magnetic centres, while the 'inner' coupling between the Mn atoms of the ring and the central magnetic atom will be dominant (Mn-Mn ~2.78 Å). The 4 spin centres give rise to 8 unique spin configurations, which we have considered. The different possibilities are illustrated in Scheme 5.4, where each arrow symbolises a local spin of $^5/_2$. There exists one HS state with $M_S = 10$, where all spins are parallel, while antiparallel alignment of one or two spin sites gives rise to four BS solutions with $M_S = 5$ and three with $M_S = 0$, respectively.

Scheme 5.4: Possible HS and BS spinstates for **3**. The magnetic centres (where ⇧ symbolises the local $S = ^5/_2$ spin) correspond to the peripheral $Mn(thf)_2$ units and the central Mn ion, while diamagnetic centres are $Mn(CO)_4$ units.

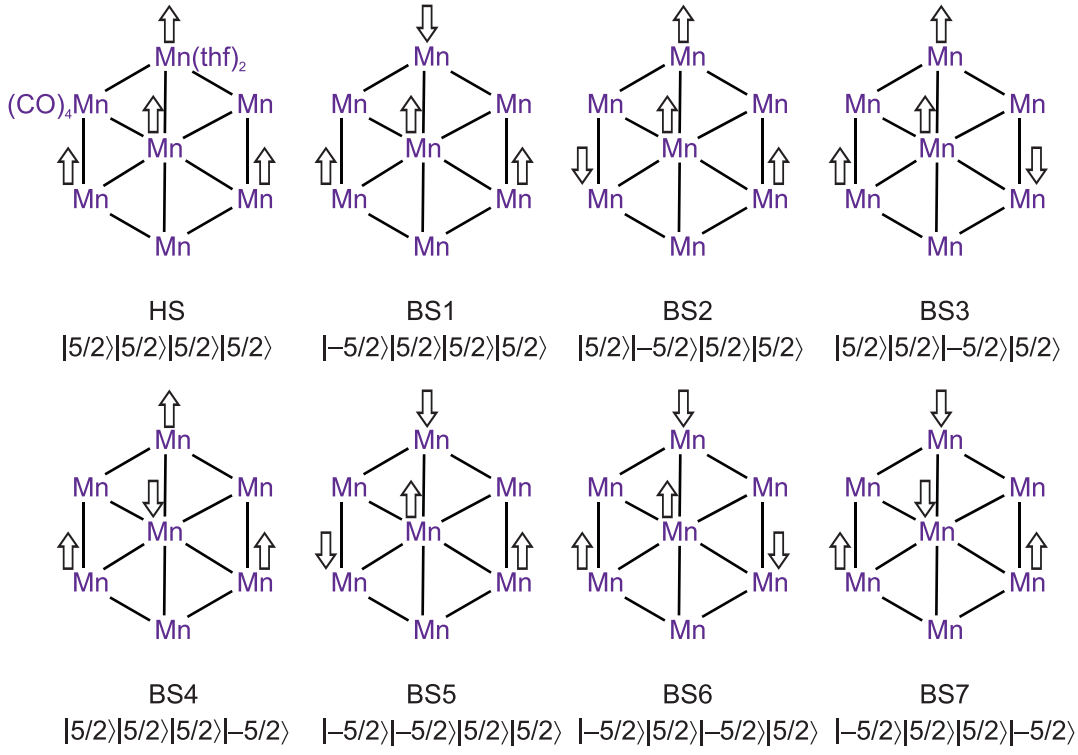

All SCF calculations converged smoothly to the desired states, and calculated net spin densities, $\langle S^2 \rangle$ values and total energies of all spin states are summarised in Table 5.2.

Table 5.2: Calculated Mulliken spin densities (ρ_{Mn}) on the manganese centres, expectation values of the square of the total spin angular momentum operator ($\langle S^2 \rangle$) and total energies.

	ρ_{Mn1}	ρ_{Mn2}	ρ_{Mn3}	ρ_{Mn4}	ρ_{Mn5}	ρ_{Mn6}	ρ_{Mn7}	$\langle S^2 \rangle$	E (au)
HS	4.83	0.23	4.83	0.26	4.83	0.27	4.67	110.07	-10812.7067
BS1	-4.78	0.10	4.84	0.25	4.84	0.11	4.66	34.96	-10812.7151
BS2	4.84	0.09	-4.79	0.11	4.84	0.26	4.65	34.96	-10812.7154
BS3	4.84	0.23	4.84	0.10	-4.79	0.12	4.66	34.96	-10812.7150
BS4	4.79	0.05	4.79	0.05	4.79	0.05	-4.63	34.80	-10812.7300
BS5	-4.78	-0.05	-4.79	0.11	4.84	0.10	4.64	9.86	-10812.7231
BS6	-4.78	0.10	4.84	0.10	-4.79	0.05	4.65	9.87	-10812.7227
BS7	-4.84	-0.09	4.79	0.05	4.79	-0.11	-4.64	9.87	-10812.7230

The HS state reveals a spin α-density on all four Mn centres, with values of the Mulliken spin density close to 5, typical of high-spin Mn^{II} ions (Figure 5.9). In the broken-symmetry states BS1-4 one Mn carries a negative net spin density (spin-β) close to 5, indicative of antiferromagnetic coupling, whereas in BS5-7 a negative spin population is found on two Mn centres. In all cases the spin densities on the remaining metal ions in the $Mn(CO)_4$ fragments is negligible, confirming the closed-shell character of these units. Representative contour plots are shown in Figure 5.9. The calculated $\langle S^2 \rangle$ values are close to the ideal values for the ferromagnetically coupled state ($\langle S^2 \rangle \approx 110$), and states in which one and three ($\langle S^2 \rangle \approx 35$), and two and two centres ($\langle S^2 \rangle \approx 10$) are antiferromagnetically coupled.

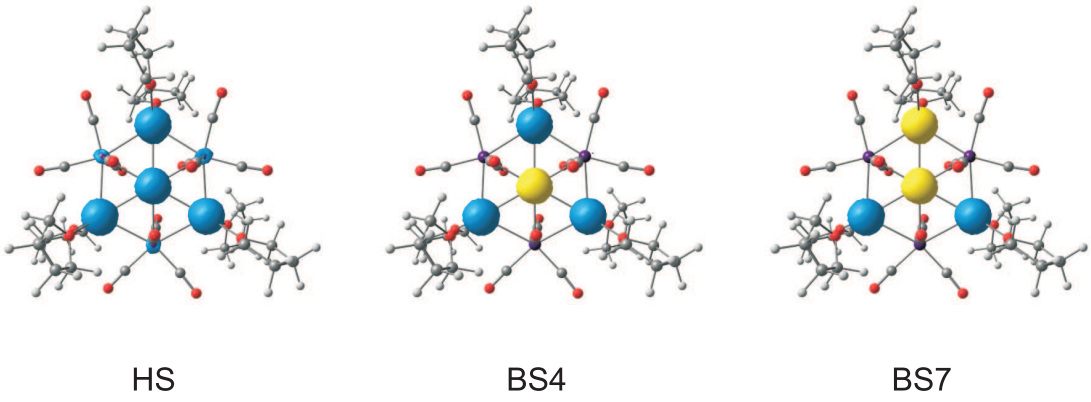

Figure 5.9: Contour plots of the total Mulliken spin density of the HS, BS4 and BS7 states.

The diagonal elements of the spin Hamiltonian can be calculated from the computed total energies of the different states. The following equations can be set up:

$$E_{\mathrm{HS}} = -{}^{25}/_{4}(J_{12} + J_{13} + J_{14}) - {}^{25}/_{4}(J_{14} + J_{24} + J_{34}) \tag{5.2}$$

$$E_{\mathrm{BS1}} = -{}^{25}/_{4}(-J_{12} - J_{13} + J_{14}) - {}^{25}/_{4}(-J_{14} + J_{24} + J_{34}) \tag{5.3}$$

$$E_{\mathrm{BS2}} = -{}^{25}/_{4}(-J_{12} + J_{13} - J_{14}) - {}^{25}/_{4}(J_{14} - J_{24} + J_{34}) \tag{5.4}$$

$$E_{\mathrm{BS3}} = -{}^{25}/_{4}(J_{12} - J_{13} - J_{14}) - {}^{25}/_{4}(J_{14} + J_{24} - J_{34}) \tag{5.5}$$

$$E_{\mathrm{BS4}} = -{}^{25}/_{4}(J_{12} + J_{13} + J_{14}) - {}^{25}/_{4}(-J_{14} - J_{24} - J_{34}) \tag{5.6}$$

$$E_{\mathrm{BS5}} = -{}^{25}/_{4}(J_{12} - J_{13} - J_{14}) - {}^{25}/_{4}(-J_{14} - J_{24} + J_{34}) \tag{5.7}$$

$$E_{\mathrm{BS6}} = -{}^{25}/_{4}(-J_{12} + J_{13} - J_{14}) - {}^{25}/_{4}(-J_{14} + J_{24} - J_{34}) \tag{5.8}$$

$$E_{\mathrm{BS7}} = -{}^{25}/_{4}(-J_{12} - J_{13} + J_{14}) - {}^{25}/_{4}(J_{14} - J_{24} - J_{34}) \tag{5.9}$$

The differences between the above expressions yields the following set of equations, relating the J_{ij} coupling constants to the energy differences of the individual states, which are obtained from the computed single point energies:

$$E_{\mathrm{HS}} - E_{\mathrm{BS1}} = -{}^{25}/_{2}(J_{12} + J_{13} + J_{14}) \tag{5.10}$$

$$E_{\mathrm{HS}} - E_{\mathrm{BS2}} = -{}^{25}/_{2}(J_{12} + J_{23} + J_{24}) \tag{5.11}$$

$$E_{\mathrm{HS}} - E_{\mathrm{BS3}} = -{}^{25}/_{2}(J_{13} + J_{23} + J_{34}) \tag{5.12}$$

$$E_{\mathrm{HS}} - E_{\mathrm{BS4}} = -{}^{25}/_{2}(J_{14} + J_{24} + J_{34}) \tag{5.13}$$

$$E_{\mathrm{HS}} - E_{\mathrm{BS5}} = -{}^{25}/_{2}(J_{13} + J_{14} + J_{23} + J_{24}) \tag{5.14}$$

$$E_{\mathrm{HS}} - E_{\mathrm{BS6}} = -{}^{25}/_{2}(J_{12} + J_{14} + J_{23} + J_{34}) \tag{5.15}$$

$$E_{\mathrm{HS}} - E_{\mathrm{BS7}} = -{}^{25}/_{2}(J_{12} + J_{13} + J_{24} + J_{34}) \tag{5.16}$$

A single value decomposition procedure yields the following values for the individual J_{ij} values:

$$J_{12} = -5.87 \text{ cm}^{-1} \quad J_{14} = -134.16 \text{ cm}^{-1}$$

$$J_{13} = -5.76 \text{ cm}^{-1} \quad J_{24} = -139.54 \text{ cm}^{-1}$$

$$J_{23} = -5.43 \text{ cm}^{-1} \quad J_{34} = -132.12 \text{ cm}^{-1}$$

The obtained values confirm our predictions made above. The 'outer' coupling constants are negligibly small, owing to the large separation of three magnetic Mn atoms lying on the ring, while the 'inner' coupling between peripheral magnetic Mn ions and the central ion is strongly antiferromagnetic. Moreover, the local symmetry intrinsic to the system is reflected in the values, where $J_{12} \approx J_{13} \approx J_{23}$ and $J_{14} \approx J_{24} \approx J_{34}$. Hence, we would have arrived at the same result if we had considered symmetry and used two coupling constants J and J'. Direct 'through space' magnetic coupling between Mn^{II} d electrons tends to be negligible, and thus cannot account for the rather large value of about -130 cm^{-1}. To a first approximation however, the coupling within the magnetic Mn^{II} tetramer can be broken down in terms of effectively di-bridged Mn^{II} dimer interactions (Scheme 5.5).

Scheme 5.5: Possible superexchange pathways present in cluster **3**.

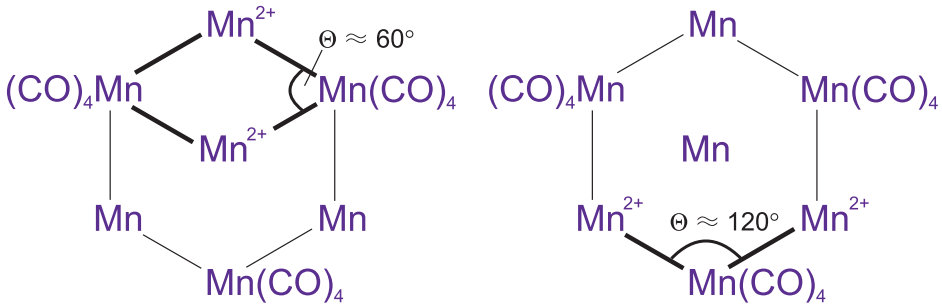

The hexagonal symmetry enforces a bridgehead angle Θ of about 60°, for which one would expect large negative coupling constants from the magnetostructural correlation (Figure 5.7). Thus, this exchange pathway is predominant. Likewise, for the outer $Mn^{II}Mn(CO)_4Mn^{II}$ coupling, $\Theta \approx 120°$, so a small coupling constant would be expected and this is indeed what is observed ($J \approx$-5 cm^{-1}). The energies of the different possible states ($S = 0 - 10$) are obtained by diagonalising the spin Hamiltonian matrix. By using the calculated J values we obtain the energy spectrum shown in Figure 5.10.

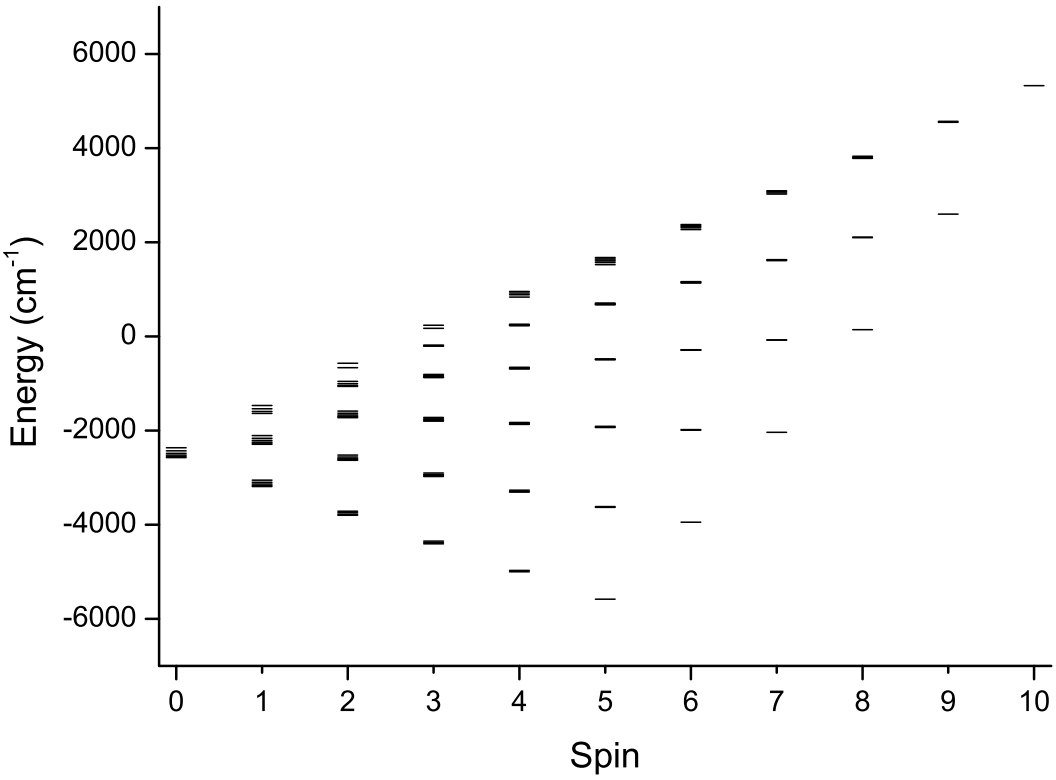

Figure 5.10: Energy spectrum for the spinstates in **3**.

The dominating influence of the antiferromagnetic coupling between a single spin centre and the three other Mn atoms leads to an $S = 5$ ground state for the system, whereas the HS state ($S = 10$) is highly unfavourable.

5.5 Conclusions

In this chapter we have reassessed the electronic structure of a class of 'xenophilic clusters', exemplified by the rhomboidal cluster $Mn_2(thf)_4(Fe(CO)_4)_2$. Contrary to previous models in the literature, these are best viewed as exchanged coupled clusters of Mn^{II}, with the closed-shell units $Fe(CO)_4^{2-}$ acting as effective bridging ligands. The larger Mn_7 cluster can be analysed similarly as an aggregate of four Mn^{II} ($S = 5/2$) and three $Mn(CO)_4^{3-}$ units. The dominant exchange pathways again pass through the $Mn(CO)_4^{3-}$ units and the bridgehead angle imposed by the hexagonal structure determines the values of J. In this case coupling between the central and peripheral Mn^{II} ($\Theta = 60°$) dominates over coupling around the circumference of the ring ($\Theta = 120°$).

6

Study of a model complex of Copper Nitrite Reductase

In this chapter we explore the ability of model copper complexes based on *cis*,*cis*-1,3,5-tris(cinnamylideneamino)cyclohexane (tct) to act as both structural and functional mimics of copper nitrite reductase (CuNiR). The ligand's architecture allows for $\kappa^3 N$ face-capping coordination to a copper centre, mimicking the His_3 environment of the type-2 copper active site in CuNiR. This work is carried out in collaboration with the group of Prof. Walton at the University of York.

Specifically, two complexes are of interest, $[Cu^{I}(tct)(N\text{-}NO_2)$ (**1**) and its cationic Cu^{II} analogue, $\mathbf{2}^+$. The former features an N-bound nitrite coordinated to a cuprous metal centre. In the latter case, the crystallographic structure remains unknown, but density functional theory predicts an O,O-bound geometry for the NO_2 group. Both **1** and $\mathbf{2}^+$ catalyse the reduction of NO_2^- to NO with ascorbate, involving the transfer of an electron and two protons to the substrate. A detailed survey of the reaction coordinate has been performed, revealing possible pathways for the catalytic cycle. The results shed some light on the mechanistic details of the reaction, as well as the electronic structures of the involved intermediates.

6.1 Introduction

6.1.1 Copper NiR

Copper-containing proteins are key players in many biological processes involving electron transfer, dioxygen transport as well as the activation of small molecules such as dioxygen and nitrite.[452,453] Dissimilatory denitrification, the enzymatic reduction of nitrate (NO_3^-) and nitrite (NO_2^-) to gaseous NO, N_2O and N_2, is an anaerobic respiratory process[454] playing a central role within the global nitrogen cycle, which is solely sustained by prokaryotic organisms.[455,456] The denitrification cascade passes through four distinct stages to finally yield dinitrogen, thereby removing 'fixed' inorganic nitrogen from the terrestrial biosphere and returning it into the atmosphere.

The reduction of nitrite to nitric oxide by the enzyme nitrite reductase (NiR) is a critical step within this stepwise reduction process. Two distinct classes of NiRs have been identified, one being multi-copper nitrite reductases (CuNiRs) and the other being cytochrome cd_1 NiRs, the two types differing in the prosthetic groups employed at the catalytic site (copper or heme c and d_1 respectively).[457,458] Very recently, a new class of nitrite reductases from the xanthine oxidase enzyme family has been proposed.[459] Cytochrome cd_1 NiRs are soluble enzymes, present in the periplasmic space. Crystal structures from isolated NiRs (e.g. from *Pseudomonas aeruginosa*[460]) reveal a homodimeric topology built from two 60 kD subunits, each of which contains one heme c cofactor and one heme d_1 group.

CuNiRs have been isolated from a number of denitrifying organisms including *Alcaligenes xylosoxidans*,[461] *Alcaligenes faecalis*,[462] and *Achromobacter cycloclastes*,[463,464] all of which show a high degree of sequence similarity. X-ray studies

of CuNiR from various sources have shown that the enzyme features a typical 110 kD homotrimeric quaternary structure (Figure 6.1), containing two different copper sites (type 1 and type 2)[465] in each monomer, each with a characteristic spectroscopic fingerprint. Depending on the spectral absorption region of the type 1 copper, CuNiRs can be further classified into blue or green reductases. The former (e.g. from *P. aureofaciens*) exhibit a very intense absorption band at ~590 nm and an axial EPR signal, while the latter (e.g. from *A. cycloclastes*) has two intense bands at 460 and 600 nm and rhombic EPR signals.[456]

Figure 6.1: Three-dimensional crystal structure of AfNiR (pdb code 1AS6). [Original in colour]

The type 1 copper site is positioned close to the surface of the protein and is involved in an electron shuttle, accepting electrons from a small electron donor protein (e.g. pseudoazurin) and transferring them to the type 2 copper. Four amino acid residues from the peptide backbone (His95, His145, Cys136 and Met150, re-

ferring to the AcNiR numbering scheme) are ligated to the type 1 copper in a strongly distorted tetrahedral coordination geometry (Figure 6.2). The type 2 site is separated by ∼12.5 Å from the type 1 centre and located at the interface between two proximate monomers. The two copper sites are interlinked by a Cys136-His135 dipeptide bridge which ensures effective electron shuttling between the two sites.[466] The Jahn-Teller-distorted tetrahedral type 2 site is formed from three histidine residues (His100, His135, His306). In the oxidised resting state the fourth coordination site is completed by a water or hydroxide molecule.

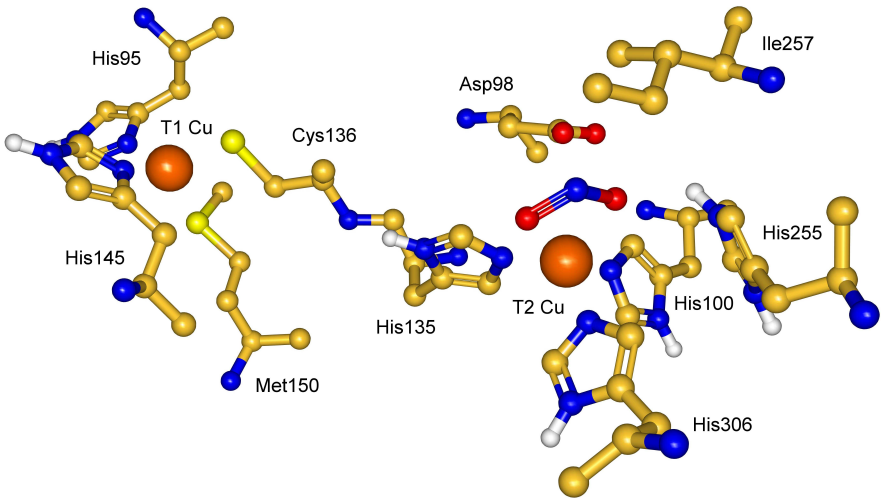

Figure 6.2: Organisation of the T1 and T2 copper centres in the active site of CuNiR (pdb code 1AS6). Non-histidine Hydrogen atoms are omitted for clarity. [Original in colour]

Combined X-ray crystallographic and spectroscopic studies have established that the 'non-blue' type 2 copper is the site of nitrite binding and reduction,[464,467–470] Three highly conserved active site residues (His255, Asp98, Ile257) are situated in close proximity to the type 2 copper and their critical role for the catalytic activity of the enzyme has been implied by both structural and mutagenesis studies.[470,471] The His255 and Asp98 residues participate in a hydrogen bond network involving the bound substrate and water, and eventually mediate proton transfer to nitrite.

The role of hydrophobic and bulky Ile257 is less obvious: Boulanger et al. proposed that Ile257 directs the binding mode of the nitrite such that catalytically essential hydrogen bonds with the side-chain of Asp98 are maintained.[472] Alternatively, the role of a 'gatekeeper' has been ascribed to Ile257, discriminating substrate from other small molecules that might access the type 2 copper site.[473,474] In contrast, Lehnert and Merkle have recently proposed that a steric clash between Ile257 and a coordinated NO ligand may force the adoption of a generally unfavourable side-on coordination mode.[475]

Although both NiR types catalyse the same reaction, $NO_2^- + e^- + 2\,H^+ \longrightarrow NO + H_2O$, their proposed mechanisms of action differ significantly. In the consensus catalytic mechanism for the cytochrome NiRs, the initial step is the binding of nitrite to ferrous d_1 heme. Reduction of the nitrite then leads to cleavage of an N-O bond and formation of a heme iron-nitrosyl intermediate with NO coordinating to the metal centre in an end-on fashion via the nitrogen atom. The product then diffuses out of the active site and an electron transfer from the *c* heme restores the enzyme to its resting state.[476]

For the CuNiR function it is generally recognised that nitrite reduction involves coordination of NO_2^- at the type 2 site followed by protonation and electron transfer events which trigger loss of H_2O to yield a possible (labile) copper nitrosyl,[477–479] which then releases NO (Scheme 6.1). In addition to their physiological role, a second process catalysed by CuNiR is the slow formation of N_2O at high levels of NO, supposably by reaction of an enzyme-bound intermediate with NO or NO_2^-.[478,479] However, while the mechanistic details of the cytochrome cd_1 NiR are well established, the pathways involved for CuNiRs remain somewhat controversial.

A range of questions has emerged in this context, which need to be addressed for a full comprehension of the detailed molecular motions involved in the mechanism

Scheme 6.1: General mechanistic cycle for nitrite reduction by CuNiR (E = enzyme) [Original in colour].

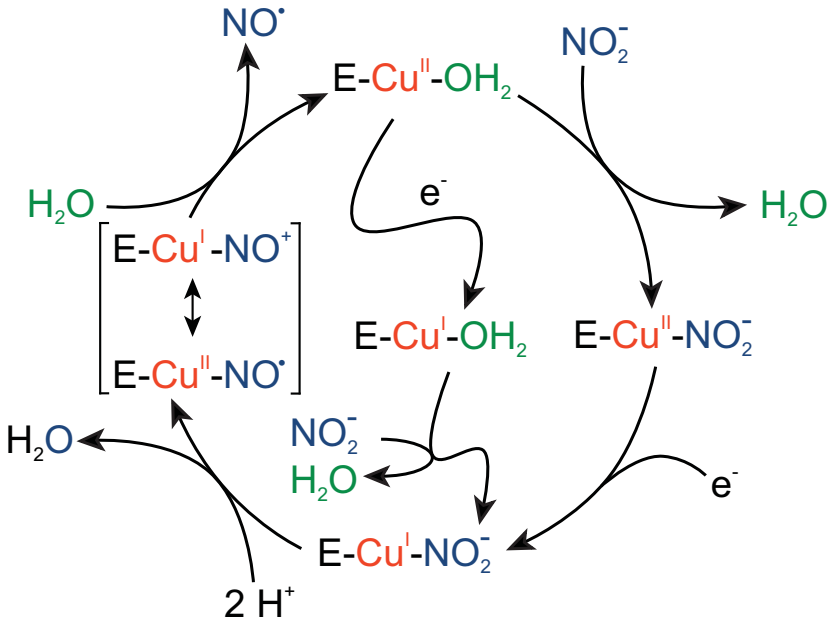

of nitrite reduction. As highlighted in the previous section, the question of the distinct role of the hydrophobic Ile257 residue remains the subject of debate. Another question concerns the catalytically active mode of binding of the substrate at copper. Nitrite shows a variability of binding modes (linkage isomerism) and may coordinate to a mononuclear metal centre in one of the ways shown in Scheme 6.2. Monodentate coordination of nitrite may occur through either nitrogen, $\kappa^1 N$ (**A**) or oxygen, $\kappa^1 O$ (**B**). Binding of nitrite in a bidentate fashion to a metal ion would yield either an oxygen-bound species, $\kappa^2 O, O'$ (**C**) or a mixed nitrogen/oxygen-coordinated complex $\kappa^2 N, O$ (**D**). Additionally, the possibility of an asymmetric O,O′-bound moiety (**C′**) must be considered, which contains only one formal M-O bond and a second longer M-O interaction (generally with a Cu-O bond length >2.5 Å).

On the basis of the hard-soft acid-base (HSAB) theory one would predict a preference for N-ligation by Cu^{I}, while the harder Cu^{II} would prefer O-ligation. Crystallographic structures of nitrite-soaked CuNiRs[480–482] and spectroscopic studies[483]

Scheme 6.2: Bonding modes of copper nitrite and nitrito complexes.

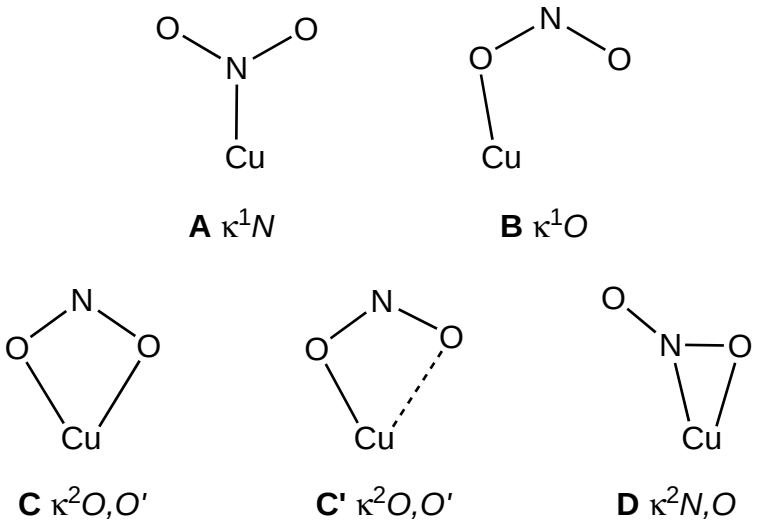

confirm the binding of nitrite to the oxidised type 2 copper site in the $\kappa^2 O, O'$-mode. The structure also suggests that the $CuNO_2$ unit in the enzyme is not planar, but rather that the dihedral angle between the NO_2 and CuO_2 planes is approximately 75°. Consequently, owing to the binding situation found, one is confronted with the paradox of how a presumed N-bound nitrosyl can subsequently be generated from a O,O′-coordinated substrate. One possibility is that reduction of the Cu centre facilitates isomerisation of the nitrite to an N-bound form. Related to this issue is the question of the exact electronic structure and geometry of the proposed Cu-NO intermediate. Under normal conditions coordination of NO occurs through the nitrogen atom, and either of the metal binding modes shown in Scheme 6.3 can be adopted when NO binds as a terminal ligand.[484]

The binding mode is predominantly determined by electronic factors, i.e. it depends on the availability of low-lying metal-based orbitals for accepting an electron pair from NO. For electron poor systems NO functions as an sp σ donor with π-backbonding from the metal, leading to linear NO, while in cases where the metal-centred orbitals are filled, the nitrogen has to accommodate a lone pair, re-

Scheme 6.3: Bonding modes of nitrosyl to copper.

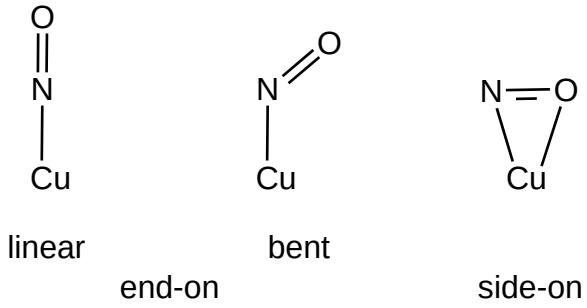

quiring sp^2 hybridisation and bending. While side-on $Cu-O_2$ complexes have been characterised structurally,[485–487] complexes featuring the κ^2-M(NO) side-on binding mode are relatively rare. A ferric side-on heme-NO complex has been identified in nitrophorin,[488] and some examples are also known from non-biological systems, e.g. photolytically induced generation in Fe and Ru nitrosyl complexes.[489] These findings have been further supported by DFT calculations on model species.[490,491]

6.1.2 Mechanistic studies

Two distinct models have been proposed for the detailed mechanism. The first of these is rather similar to that for cytochrome cd_1 NiR, in that nitrite binds to reduced copper of the type 2 centre through the nitrogen atom to form an *N*-nitrito isomer and an N-bound NO is generated subsequently after protonation and dehydration.[492] This view finds support in model studies, where copper(I) complexes with N-bound nitrite, e.g. the complex $[Cu(^{i}Pr_3tacn)(\kappa^1 N\text{-}NO_2)]$ (tacn = 1,4,7-triazocyclononane) from Tolman's group (*vide infra*),[493] evolve NO gas (and water) under acidic conditions. A recent report by Murphy and co-workers[480] suggests that the NO in the active site may be coordinated to the copper centre in an unprecedented side-on fashion (cf. Scheme 6.3), evident from an X-ray structure of the NO-soaked native enzyme. Although additional crystal structures have confirmed this result,[494] it is not clear whether such a structure is part of the catalytic

pathway or a dead-end. The electronic structure of this species has been subject of much debate, and contradictory findings have been made.

On the basis of EPR measurements on solutions of ascorbate reduced CuNiR and NO under anaerobic conditions, the crystallographically obtained $\{CuNO\}^{11}$ species (using Enemark-Feltham notation*) was assigned an unusual Cu^{II}-NO^- electronic structure.[494] However, Solomon and co-workers have disproved this conclusion by demonstrating that the solution species obtained by Murphy and co-workers is in fact a Cu^{II}-NO_2^- complex.[495] They concluded that the crystallographically observed side-on species most likely has no relevance for the catalytic cycle, owing to the fact that it is only generated in the crystal but not in solution phase. Moreover, they argued that the electronic structure of the Cu-NO moiety in the crystal structure is best described as Cu^{I}-$NO^{\cdot}$.

In a separate study, Scholes and co-workers have shown that a solution phase $\{CuNO\}^{11}$ species can in fact be generated by CuNiR by using a fully reduced enzyme in the presence of limited amounts of NO,[496] but the binding-mode of NO to the Cu atom remained unclear.

Evidence for a strongly bent Cu-NO unit ($\sim$135°) present in the enzyme was presented by Lehnert and co-workers, based on the correlation between the Cu-NO bond angle and the **g** tensor.[497] DFT treatments of Cu-NO model complexes as well as active site models indicate that both $\{CuNO\}^{10}$ and $\{CuNO\}^{11}$ species may exhibit side-on coordination of NO,[475,495,498] although this mode is generally energetically disfavoured with respect to the end-on isomers, showing some dependence on the choice of ligand set. The calculations also strongly corroborate a Cu^{I}-$NO^{\cdot}$ description of the $\{CuNO\}^{11}$ species in both the side-on and end-on forms.

*The Enemark-Feltham formalism[91] treats the metal nitrosyl as a single unit, $\{MNO\}^n$, where the superscript n represents the total number of electrons associated with the metal d and π^*(NO) orbitals.

In a detailed study of the decomposition of Tolman's complex [Cu(^{i}Pr$_3$tacn)(κ^1*N*-NO$_2$)] to nitric oxide and [(^{i}Pr$_3$tacn)Cu$^{\mathrm{II}}$(H$_2$O)] with trifluoroacetic acid (TFA), Kujime and Fujii[499] were able to detect two distinct intermediates in a stopped-flow experiment with absorption maxima at 350 and 423 nm in the UV-vis absorption spectrum. The time course for the three-step reaction was fitted to a biexponential function with k_{fast} and k_{slow}. While the initial step was too fast to be measured, the rate constant for the second step, (k_{fast} = 6.54×10^3 M^{-1} s^{-1}), was found to be linearly dependent on the TFA concentration. On the other hand, the third step rate constant (k_{slow} = 6.82×10^{-1} s^{-1}) is independent on the TFA concentration. Kinetic isotope studies using deuterium-labelled TFA indicated a KIE of $k_{\mathrm{H}}/k_{\mathrm{D}}$ ≈1.4 for the fast step at 203 K while no KIE was observed for the third step, confirming that TFA is not involved in the final step of the mechanism. Activation parameters obtained from Eyring plots for T = 193-223 K (k_{fast}: $\Delta^{\ddagger}H$ = 28.4±3.2 kJ mol^{-1} and $\Delta^{\ddagger}S$ = -27.1±2.4 J mol^{-1} K^{-1}, k_{slow}: $\Delta^{\ddagger}H$ = 18.9±1.5 kJ mol^{-1} and $\Delta^{\ddagger}S$ = -151.0±24.7 J mol^{-1} K^{-1}) indicated associative transition states in both cases. Further, the oxidation states of the first and second intermediate have been confirmed to be Cu$^{\mathrm{I}}$ and Cu$^{\mathrm{II}}$, respectively, by trapping the intermediates with oxygen. On the basis of these experiments the authors proposed a stepwise proton transfer mechanism where an initial [(^{i}Pr$_3$tacn)Cu$^{\mathrm{I}}$(NO$_2$H)]$^+$ intermediate subsequently reacts with a second equivalent of TFA, inducing N-O bond cleavage and formation of the second intermediate, a Cu$^{\mathrm{I}}$–NO$^+$ complex. The latter then decays to the final product and nitric oxide.

A second pathway for CuNiR, has been proposed by Suzuki and co-workers,[471] where nitrite displaces a water ligand at the type 2 copper site and binds via the two oxygen centres in a $\kappa^2 O, O'$-mode. The released water then protonates the nearby Asp98 residue, generating an OH$^-$ moiety. One-electron reduction of

the type 2 centre then triggers a linkage isomerism reaction, wherein the NO_2^- rearranges from O,O′-coordination to N-coordination. Donation of a proton from the His255 residue to the oxygen of N-coordinated nitrite leads to the formation of a nitrous acid complex which is reduced by 1-electron transfer from the reduced type 2 copper. Transfer of a second proton then induces N-O bond cleavage to produce NO via a $Cu^{I}-NO^{+}$ intermediate. The cycle is closed by release of NO and aquation to regenerate the initial aqua complex. It has been argued that the proximity of the nitrogen atom of the NO_2^- ligand to Cu due to the 75°-tilt in the native enzyme facilitates the rearrangement of the nitrite after electron transfer has occurred.[480]

Siegbahn and co-workers proposed a subtly different mechanism based on models of the CuNiR active site including the first and secondary coordination sphere and solvent water.[500] In their proposed pathway, coordination of the nitrite ligand again occurs via oxygen, but now in a monodentate *O*-nitrito mode rather than the $\kappa^2 O, O'$-alternative suggested by Suzuki. Coordination of the nitrite induces protonation of an Asp92 residue, increasing the redox potential of the type 2 copper and so inducing electron transfer from the type 1 copper site. Uptake of a second proton then yields two distinct isomers of a nitrous acid complex, one of which shows a significant elongation of the N-OH bond, reducing the activation barrier for the bond cleavage. Protonation occurs at the oxygen bound to the metal centre, so cleavage of the N-O bond which follows the transfer of a second proton results in direct release of NO without formation of an intermediate nitrosyl complex.

In a related study,[501] Burton and co-workers proposed that a change of substrate coordination mode from O- to N-bound occurs upon reduction and protonation, due to the increased stability of N-bound protonated nitrite compared to the O-bound isomer (2.4-8.0 $\mathrm{kcal\,mol^{-1}}$). This process is associated with a very low barrier

(4-13 $\mathrm{kcal\,mol^{-1}}$), and hence is not rate limiting. The N-coordination of the nitrite means that the NO molecule produced on N-O bond cleavage is trapped by the metal centre, generating a transient five-coordinate nitrosyl complex, in contrast to Siegbahn's model where NO was released directly.

Solomon et al.[502] have also recently reported a combined spectroscopic and DFT study of the geometric and electronic structure of the nitrite bound type 2 copper site at high and low pH in nitrite reductase. For the computational survey of the potential energy surface for nitrite reduction, a model of the active site taken from a pdb structure of the native enzyme was employed, incorporating critical second sphere residues (Asp98, His255, Ile257) and water. The authors propose bidentate nitrite binding to copper which facilitates the reductive cleavage of the nitrite bond though backbonding combined with stabilisation of OH^- by coordination to Cu^{2+}. Different binding modes of HNO_2 towards the metal centre were investigated with respect to their influence on the energetics of electron transfer and ON-OH bond scission. The authors pointed out that the single proton transfer does not lead to spontaneous HO-NO bond cleavage, but the activation energy strongly depends on the coordination mode of HNO_2. It was lowest ($\Delta^{\ddagger}E = 16\,\mathrm{kcal\,mol^{-1}}$) for the bidentate O,O′-bound case and highest ($\Delta^{\ddagger}E = 50\,\mathrm{kcal\,mol^{-1}}$) for N-bound HNO_2. The authors give evidence that the bidentate coordination allows good configurational interaction between the donor Cu^+ $d_{x^2-y^2}$ orbital and the acceptor HO-NO σ^* orbital. The availability of both oxygen atoms of the HNO_2 enables efficient backbonding and thus electron transfer. The authors concluded that the overall reduction step is best described as a proton transfer triggered electron transfer.

6.1.3 Model studies

The controversies surrounding the mechanism in the enzyme itself have driven an extensive body of work investigating structural and functional mimics of the CuNiR type 2 copper site. A range of structural and spectroscopic $CuNO_2$ and CuNO models for both cupric (Cu^{II})[502–514] and cuprous (Cu^{I})[496,497,504,507,508,515–521] forms of copper nitrite reductase have been reported. The experimental data has been complemented by a number of computational studies on model complexes of type 2 copper sites as well as on type 2 sites embedded in the enzymatic environment.[475,500–503,522–524] Some typical structures of $CuNO_2$ model complexes are summarised in Figure 6.3, which have also been included in recent review articles.[525–527]

The first structurally characterised mononuclear Cu^{II} complex was $[(Tp^{tBu,H})Cu^{II}(NO_2)]$ (Tp = tris(pyrazolyl)hydroborate (tpzb), **I** in Figure 6.3), in which the scorpionate ligand mimics histidine binding. The crystal structure reveals that nitrite coordinates as the O,O'-isomer to the copper ion, in line with the findings for the oxidised enzyme. In fact, the majority of known crystal structures of inorganic $Cu^{II}NO_2^-$ model complexes contain an O,O'-bonded nitrito moiety. It is also interesting, that the coordination geometry of the $CuNO_2$ unit is influenced by the surrounding ligand environment.[510] Depending on the steric bulk of the substituents R in $[(Tp^{R,R'})Cu(NO_2)]$, one either finds a trigonal-bipyramidal (R = ^{t}Bu, R′ = H) or square-pyramidal (R = Me, R′ = Me) coordination geometry. As a result the Cu-O bond lengths are asymmetric in the former, while they are symmetric in the latter. Remarkably, all cupric model complexes are nonmimetic[528] as exemplified by the reaction of $[(Tp^{tBu,H})Cu(NO_2)]$ with either (PPN)Cl or Me_3SiOTf ($^-$OTf = $^-O_3SCF_3$). These reactions afford the respective $[(Tp^{tBu,H})Cu^{II}(Cl)]$ or

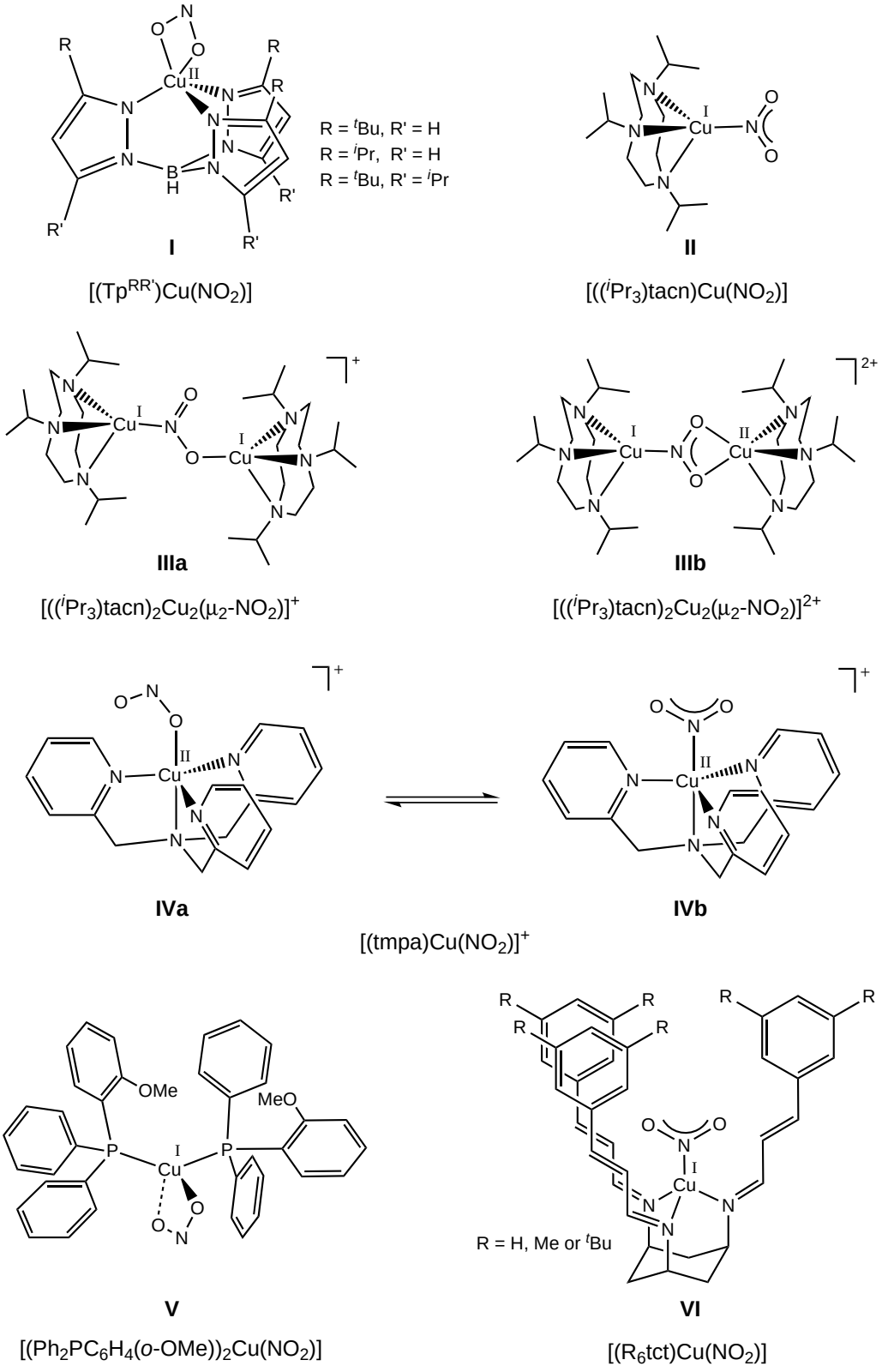

Figure 6.3: Selected synthetic Cu^{I}- and Cu^{II}-NO_2 model complexes featuring different ligand systems.

[(Tp^{tBu,H})Cu^{II}(OTf)] complexes, indicating that the nitrite ligand is quite labile in the parent complex.[514] On the other hand, the first structurally characterised Cu^{I} nitrite complex with biomimetic activity was the previously mentioned complex [(^{i}Pr$_3$tacn)Cu($\kappa^1 N$-NO$_2$)] (**II**),[493] in which nitrite binds through the nitrogen atom. Indeed this compound reacts with acetic acid or Lewis acid Me$_3$SiOTf to yield [(^{i}Pr$_3$tacn)Cu(OAc)$_2$] and nitric oxide (and water), via an oxidised Cu^{II}-nitrosyl complex that dissociates NO. A somewhat unusual dinuclear Cu^{I}Cu^{I}-complex (**IIIa**) is formed at the initial stage of the synthesis of **II**, in which a nitrite bridges two metal centres as μ_2-NO$_2$-κN:κO ligand. Therefore, nitrite exhibits both monodentate O- and N-coordination to the metal centres within the same complex. This binding mode has also been noted for another dimeric complex, although in this case containing two copper(II) ions.[529] Interestingly, the O and N atoms of the bridging nitrite involved in binding occupy apical positions of the two square-pyramidal copper centres. Subsequent reaction of the dimer with PPh$_3$ affords the monomeric complexes [(^{i}Pr$_3$tacn)Cu(PPh$_3$)] and [(^{i}Pr$_3$tacn)Cu(NO$_2$)]. Moreover, the Cu^{I}Cu^{I} dimer may be converted to the mixed-valent Cu^{I}Cu^{II} species (**IIIb**) by electrochemical oxidation or chemical oxidation using ferrocenium, upon which nitrite switches from monodentate κO to bidentate $\kappa^2 O, O'$ coordination mode.

The complex [(^{i}Pr$_3$tacn)Cu($\kappa^1 N$-NO$_2$)] can be viewed as the prototype for a functional biomimetic complex of CuNiR, and its discovery has triggered the synthesis of a range of Cu^{I}-κN-NO$_2$ compounds, all of which reveal nitrite reductase reactivity.[504,507,526] These results underline the inherent reactivity of the κN-coordination in these complexes and the potential role as key reaction intermediates of CuNiR.

In contrast, mononuclear Cu^{I} model complexes which feature O-coordinated nitrite are rare. The only three known examples reported to date include

$[(PPh_3)_2Cu(NO_2)]$,[520] $[(2,6\text{-}(Ph_2P(o\text{-}C_6H_4)CH{=}N)_2C_5H_3N)Cu(NO_2)]$,[515] and $[(Ph_2PC_6H_4(o\text{-}OMe))_2Cu(NO_2)]$ (**V**),[516] all containing soft-base phosphine ligands. In these complexes, the binding of nitrite ranges from symmetric to asymmetric κ^2O,O' (structures **C** and **C′** in Scheme 6.2). The latter two complexes are of interest, because both generate NO from the reaction with acetic acid, therefore representing models for potential intermediate reactants in the nitrite reduction cycle. Thus, these examples seem to provide some support for the proposed importance of bidentate nitrite binding for the activation of the nitrite bond,[502] although the character of the reaction intermediates remains unknown so far.

Despite the apparent preferences for O- or N-binding of nitrite, the energetic difference between the various binding modes is relatively small. This is illustrated in an example by Tanaka et al., who have demonstrated that solvent-dependent interconversion between N- and O-ligation modes occurs for the complex $[(tmpa)Cu^{II}(NO_2)]^+$ (tmpa = tris(2-pyridylmethyl)amine, **IVa** and **IVb**).[511] In the context of the enzymatic reaction, these results strongly suggest that modulations of the nitrite binding mode by the protein environment play an important role within the mechanistic cycle.

In light of the mechanistical significance of a copper-nitrosyl intermediate, it is surprising that only a few biomimetic complexes featuring a Cu-NO moiety have been reported so far. The majority of these complexes fall into the $\{CuNO\}^{11}$ regime, and contain $Tp^{RR'}$ as the coligand (cf. **VII** in Figure 6.4), where R = 3-^{t}Bu, Ph, CF_3, or mesityl (Mes), and R′ = 5-H, Ph or CH_3.[521,530,531]

Their adducts with NO have been studied in detail by means of FT-IR, EPR, NMR and UV-vis spectroscopy. In contrast to the comprehensive amount of spectroscopic data, the number of crystallographically characterised complexes within this series is limited to three, including $[(Tp^{tBu,H})Cu(NO)]$, and the more recent

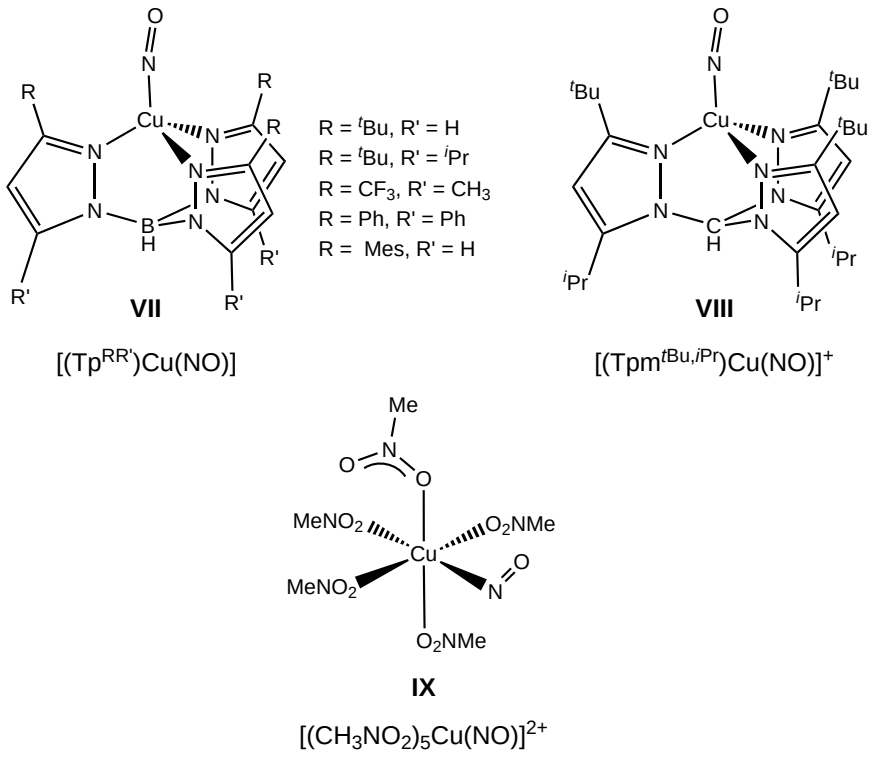

Figure 6.4: Synthetic Cu^{I}- and Cu^{II}-NO model complexes featuring different ligand systems.

$[(Tp^{tBu,iPr})Cu(NO)]$ and $[(Tpm^{tBu,iPr})Cu(NO)]^{+}$ complexes.[497] The latter contains a tris(pyrazolyl)methane (Tpm) ligand (**VIII**), the neutral congener of Tp. These complexes exhibit nearly linear copper-nitrosyl units (172° and 176°), while in $[(Tp^{tBu,H})Cu(NO)]$ the Cu-N-O angle is significantly smaller (163°). Although electronic effects usually predominate among the factors that induce nitrosyl bending, the authors hold steric effects responsible for the differences in bond angles. All three complexes have short Cu-N bond lengths (1.76-1.79 Å), and are considered to have a Cu^{I}-$NO^{\cdot}$ electronic structure.

Synthesis and structural characterisation of a rare example of a $\{CuNO\}^{10}$ complex, $[(CH_3NO_2)_5Cu(NO)]^{2+}$ (**IX**), has been achieved by Hayton and co-workers.[532] The structure reveals a Jahn-Teller-distorted octahedral geometry around copper, with a bent NO ligand ($\angle Cu{-}N{-}O = 121.0°$) coordinated at an equatorial site. The Cu-N bond length (1.955 Å) in this complex is significantly longer than in

the previous examples. To account for the observed Jahn-Teller distortion and the bond metric parameters of the NO ligand, the authors favour a Cu^{II}-$NO^{\cdot}$ description of the electronic structure. Evidence for antiferromagnetic coupling between the Cu^{II} ion and NO ligand has been obtained from EPR measurements.

The chemistry of model compounds has focussed largely on mimicking the first coordination sphere of the copper, and attempts to replicate more remote regions of the enzyme active site have been limited to copper nitrite and nitrosyl complexes of the hydrotris(pyrazolyl)borate,[503,530] tris(pyrazolyl)methane, and tris(imidazolyl)carbinol series.[517] Some examples of dinuclear model complexes exist, which either exhibit nitrite reducing functionality[533] or aim to reproduce the "CuHisCysCu" array in the enzyme's active site by utilising organic linkers to arrange the copper atoms at distances close to 12.5 Å.[534]

The work in this chapter is based on a different model system developed by Walton and co-workers. They reported the synthesis and characterisation of a series of copper *N*-nitrito complexes (**VI**, Figure 6.3) which are based on the *cis*,*cis*-1,3,5-triaminocyclohexane ligand system.[518,535] The face-capping $\kappa^3 N$ motif is common in bioinorganic chemistry, making the tach family of ligands an ideal candidate for use in small molecule metalloenzyme models. Complexes of the ligand *cis*,*cis*-1,3,5-tri-[(*E*,*E*)-cinnamylideneamino]cyclohexane (tct) with zinc as the metal centre have been previously used as mimics of carbonic anhydrase,[536] while the copper-based redox chemistry of a benzylideneamino derivative of tach has been explored in the context of galactose oxidase mimicry.[537] One of the major advantages of the tach architecture is that it can be easily modified to introduce features that mimic the second coordination spheres of active sites. For example, in the tris-(3,5-di-*tert*-butyl) derivative, the bulky groups in the 3-positions of the aromatic rings lie in the region of space occupied by the alkyl chain of the isoleucine residue of the native

enzyme. The experiments show that all of the biomimetic copper complexes of the above tct ligand system catalyse the reduction of nitrite at high reaction rates, dependent on the ring substituents.† However, the mechanistic details remain unknown. We thus used density functional calculations in order to unveil possible reaction pathways, using complexes of the unsubstituted tct ligand as model. In doing so we hope to shed some light on the basic underlying mechanistic details. In future work we aim to consider the perturbations caused by the introduction of ^{t}Bu groups.

6.2 Methodology

All geometry optimisations described in this chapter were performed without symmetry constraints (C_1 symmetry), and stationary points were confirmed to be minima (no imaginary frequency) or transition states (one imaginary frequency) by vibrational analysis. The calculations employed the hybrid B3LYP exchange-correlation functional.[19,26,31,32] This functional was chosen for its recognised good accuracy for a variety of chemical systems, including transition metals.[538,539] In the context of CuNiR model chemistry, B3LYP has been successfully used by a number of authors. Ahlrichs' triple-ζ valence basis set (TZV) was utilised for Cu, N and O extended by one polarisation function (p-function for Cu, d-function for O and N).[206] A slightly smaller basis set (SVP) was employed for C and H.[207] This basis set is of double-ζ quality in the valence region, and is supplemented by one polarisation function (d-function for C, p-function for H). All calculations utilised a model complex containing the unsubstituted tct ligand (Scheme 6.4).

Solvation energies, $\Delta_{\text{solv}}G^\circ$, were computed by means of the self-consistent reaction field scheme (SCRF). The solvent was approximated by the integral equation

†Personal communication.

Scheme 6.4: Model ligand used in this study, L = *cis*,*cis*-1,3,5-tri-[(*E*,*E*)-cinnamylideneamino]cyclohexane (tct).

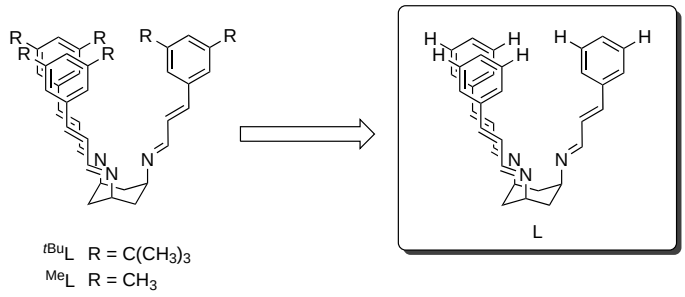

formalism of the dielectric continuum model (IEF-PCM),[540–543] with a dielectric constant for methanol of $\varepsilon = 32.63$, together with UAHF radii. For the larger copper complexes, $\Delta_{\mathrm{solv}}G^{\circ}$ was taken from single point calculations (using tight SCF convergence and an ultrafine integration grid) on the gas phase optimised structures. Small molecules (NO_2^-, NO, H_2O, H_3O^+, ascorbic acid, dehydroascorbic acid) were fully optimised in the continuum solvent model.

For the catalytic cycles, the Gibbs free energies are reported for methanol solution at a standard state of 1 M and 298.15 K, denoted $\Delta G^{\circ\prime}$. Ascorbic acid was used in order to provide the proton equivalents as well as the electron equivalents, and so the energies of the reduction steps are referenced to the computed energy of the two-electron oxidation of ascorbic acid (AA) to dehydroascorbate (DHAA), the potential of which has been established experimentally ($\mathrm{AA} \longrightarrow \mathrm{DHAA} + 2\,\mathrm{H}^+ + 2\,\mathrm{e}^-$, $E^{\circ} = 0.390\,\mathrm{V}$ vs. SHE at pH = 0).

For protonation steps, the gas phase Gibbs free energy of the proton was taken to be -7.76 kcal mol^{-1} + 5/2 RT = -6.28 kcal mol^{-1} at 298 K and 1 atm pressure,[‡] where the first term represents the entropic part of the free energy obtained with the Sackur-Tetrode equation,[544] and the second term comprises the translational

[‡]The energies obtained with the 'free' proton are congruent with results obtained using the hydronium ion as proton donor, yielding one molecule of water as the corresponding base (thereby using fully SCRF-optimised structures in combination with UAHF radii for H_3O^+ and H_2O in order to obtain good approximations to the free solvation energy). We chose the former method of 'free' H^+ for calculating protonation energies.

energy plus RT.[545] For the free solvation energy of the proton in methanol we used the value determined by Hwang and Chung ($\Delta_{\mathrm{solv}}G^{\circ}$ = -263.4 kcal mol^{-1}).[546] The Gaussian03 program[55] has been used throughout in the present study.

6.3 Molecular structures of nitrite adducts

6.3.1 Copper(I) complexes

Geometry optimisations of the model complex [Cu$^{\mathrm{I}}$(L)(κN-NO$_2$)] (**1**) yielded the structure shown in Figure 6.5, and relevant bond lengths and angles are collected in Table 6.1, where data for their experimental counterparts are also shown for comparison.

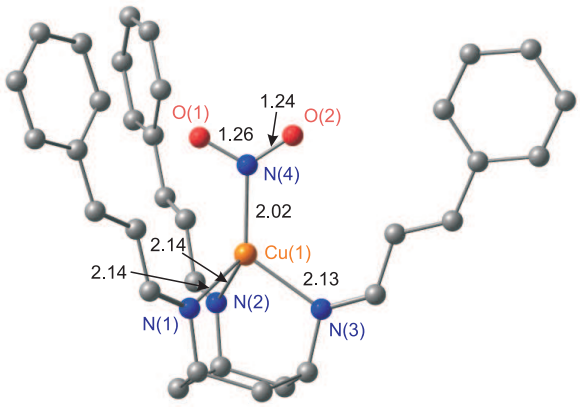

1

Figure 6.5: Optimised molecular structure of complex **1**. [Original in colour]

The calculations reproduce the principal features of the coordination spheres complex with encouraging accuracy. **1** has a closed-shell singlet ground state, with optimised Cu-N bond lengths only marginally larger than the experimental values (Table 6.1). The copper centre in **1** shows the apical nitrite in the N-coordination mode, with the tridentate basal ligand completing the Cu coordination sphere in a $\kappa^3 N$ face-capping fashion. Small basal intraligand N$_{\mathrm{L}}$-Cu-N$_{\mathrm{L}}$ angles (L = coligand

nitrogen, 89.0-93.6°, exp. 91.6-95.8°) and large N_L-Cu-N(4) angles around 124° (exp. 120.0-125.8°) are characteristic of a C_{3v}-distorted tetrahedral (i.e. trigonal-pyramidal) geometry at the metal centre. The Cu-NO_2 bond length is 2.02 Å. The bond parameters for the $CuNO_2$ unit are also in faithful agreement with experi-

Table 6.1: Selected structural parameters for nitrite complexes.

	bond lengths (Å)					
	Cu-N_L	Cu-N(4)	Cu-O(1)	Cu-O(2)	N(4)-O(1)	N(4)-O(2)
1	2.13-2.14	2.02	2.83	2.90	1.26	1.24
1 (exp.)	2.05-2.10	2.01	2.78	2.88	1.24	1.22
$\mathbf{2}^+$	2.03-2.21	2.52	2.07	2.10	1.26	1.26

	bond angles (°)		
	N_L-Cu-N_L	N_L-Cu-N(4)	O(1)-N(4)-O(2)
1	89.0-93.6	123.6-124.0	118.0
1 (exp.)	91.9-94.4	120.0-125.8	119.1
$\mathbf{2}^+$	91.7-94.8	-	111.1

mental data reported for other $Cu^I(N\text{-}NO_2)$ model compounds, for which Cu-$N_{nitrite}$ bond lengths of 1.90 Å[493] and 1.89-2.03 Å[517] have been found, although a somewhat longer Cu-$N_{nitrite}$ bond length (2.09 Å) has been reported by Suzuki and co-workers[504] for a copper(I) nitrite complex with bis(6-methyl-2-pyridylmethyl)-amine as coligand.

The cinnamylidene arms form a cavity in which the $CuNO_2$ unit is tightly embedded. In the crystal structure of **1**, one of the oxygen atoms points directly towards the central C-H bond of the propenyl unit of one cinnamyl group, giving a rather short O···H−C contact of 2.30 Å (N···C distance of 3.25 Å).[518] The nitrite anion is slightly tilted as a result, with Cu···O distances of 2.78 and 2.88 Å. As indicated by the similar N_L-Cu-N(4) angles, the nitrite anion adapts a more symmetric position in the computational model of **1** than in the X-ray structure, in which the three angles are unequal (120-126°) and nitrite is tilted towards the N(3)

cinnamyl arm. The slightly unsymmetrical Cu···O distances found in the crystal structure are reproduced by the calculations (2.83 and 2.90 Å), as well as the short contacts between nitrite and the propylidene residue (O···H−C = 2.13 Å, N···C = 3.73 Å). The conformational preference of the NO_2 group is well reproduced by the calculations. In summary, the calculation accurately reproduces the experimental geometries with deviations lying in the normal range expected for the method.

6.3.2 Copper(II) complexes

Addition of NO_2^- to a solution of copper(II)triflate in methanol yielded crystals of $\mathbf{2}^+$, but these have proved to be of insufficient quality to allow a structure determination. However, the optimised structure of the doublet ground state of $\mathbf{2}^+$ shown in Figure 6.6 confirms that the basic features of the $\kappa^3 N$ face-capping architecture are retained, but the two oxygens of the nitrite ligand are now coordinated to Cu^{II} (Cu-O distances of 2.07 and 2.10 Å) completing an approximately square-pyramidal coordination sphere about the metal centre. The small value of the geometry descriptor τ[§] for this complex (0.09) is indicative of a symmetrical coordination geometry around the copper atom. The calculated Cu-O bond lengths are in the range of experimental and calculated bond lengths reported for copper(II) nitrite models of same coordination symmetry (2.03 / 2.09 Å and 2.02 / 2.13 Å,[502] 2.02 / 2.03 Å,[503] 2.03 / 2.03 Å[510]).

The frontier molecular orbitals of $\mathbf{2}^+$ are typical of a square-pyramidal Cu^{II} complex with the single vacancy in the Cu $d_{x^2-y^2}$ orbital, giving a net spin density of 0.63 on Cu and an apical Cu-N distance (2.21 Å) substantially longer than its basal counterparts (2.03 Å). A similar electronic situation has also been reported

[§]The structural parameter $\tau = (\alpha - \beta)/60°$, where α and β are the largest angles ($\alpha > \beta$) around a five-coordinate metal centre. For an ideal trigonal-bipyramidal geometry τ is equal to 1, while for an ideal square-planar geometry it becomes 0.[547]

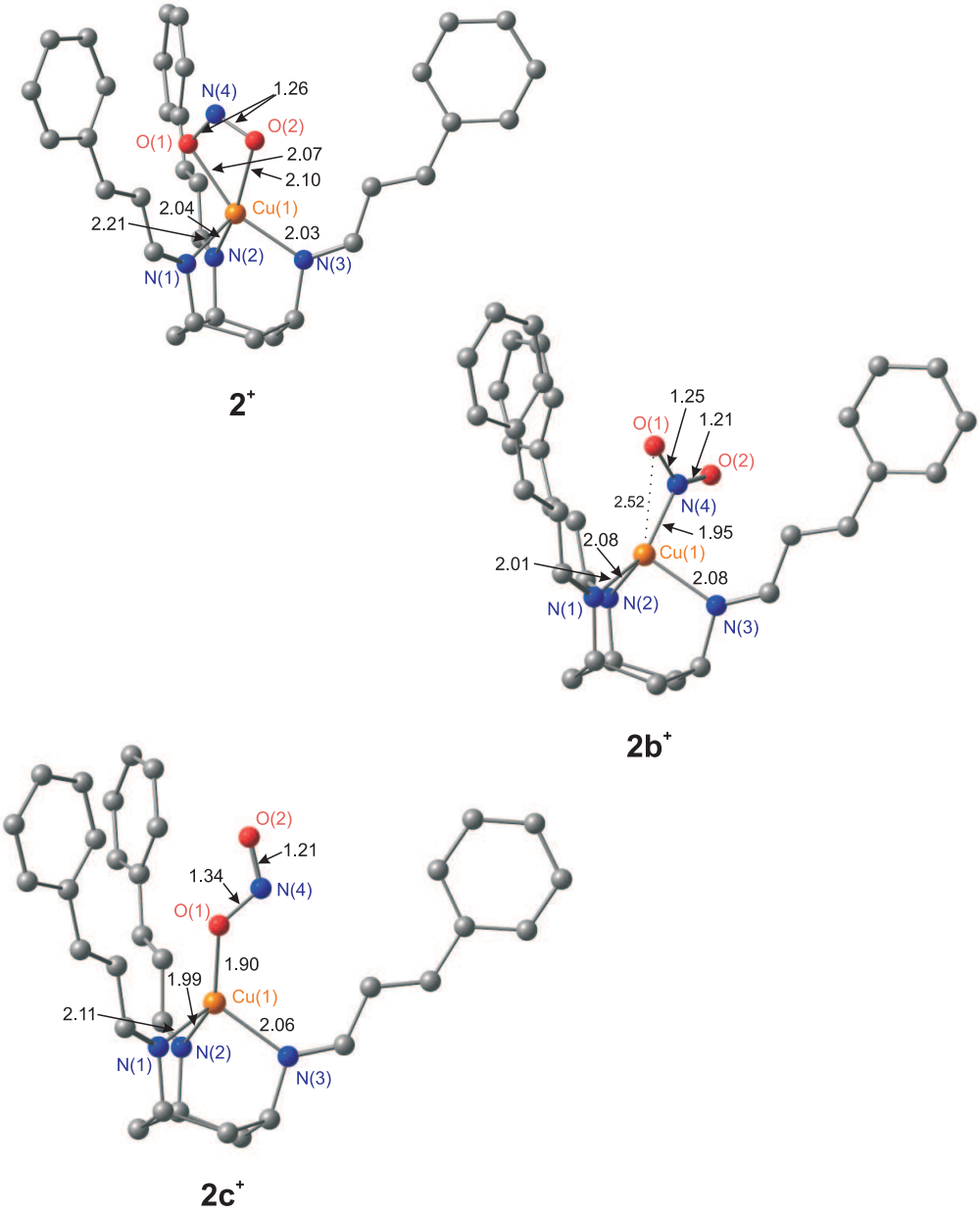

Figure 6.6: Optimised molecular structures of complex $\mathbf{2}^{+}$, $\mathbf{2b}^{+}$ and $\mathbf{2c}^{+}$. [Original in colour]

for related copper(II) models with a N_3O_2 ligand environment.[502,503,537] The N(4)-O bond lengths of 1.26 Å resemble those of the free nitrite anion (1.25±0.02 Å[548]), but the chelating bridging mode clearly introduces some strain as the O(1)-N(4)-O(2) bond angle is more acute (111.1°) than in the free ligand (117.5±2.0°[548]). It has been reported that the nitrite ONO plane is tilted by 75° relative to the OCuO plane in the structure of nitrite soaked native CuNiR, prompting suggestions that

the π-system of the NO_2^- ligand may interact with the metal centre.[480] We see no evidence for a similar distortion here: the copper, N(4), O(1) and O(2) atoms are almost coplanar in **2**, and any attempts to optimise a structure starting with a tilted $CuNO_2$ unit reverted back to this structure.

The possibility of facile linkage isomerism has been extensively discussed in the context of the nitrite reductases because it is clear that the different Cu oxidation states involved in the cycle demand rather different coordination modes. This is neatly illustrated by the comparison of **1** and $\mathbf{2}^+$, where the preferred coordination mode in the ground state switches from N to O,O. In the Cu^{II} complex, however, the N-bound isomer, $\mathbf{2b}^+$, lies only 3.2 kcal mol^{-1} higher in energy. The structure is somewhat similar to the ground state of **1**, although the coordination geometry is distorted from ideal C_{3v} symmetry and the Cu-N(4) bond length is decreased from 2.01 Å to 1.95 Å.[549] The two minima are connected by an intermediate *trans* O-bound nitrite complex ($\mathbf{2c}^+$), with a barrier of 5.1 kcal mol^{-1}. On this basis, we conclude that linkage isomerism between the O- and N- bound forms of nitrite is kinetically and thermodynamically facile at Cu^{II}, and is therefore unlikely to be the rate-limiting step in the overall one-electron reduction of nitrite to NO. We return to the question of linkage isomerism in the Cu^{I} system in the discussion of the reaction mechanism.

6.4 Reaction profile for the catalytic cycle

Having discussed the electronic structures of **1** and $\mathbf{2}^+$ previously, we now take these two complexes as a basis for constructing a catalytic cycle for nitrite reduction. Here we focus on the simplified ligand system (**1** and $\mathbf{2}^+$) to map out the basic possible pathways available to the system.

The free energy surface for the reduction of nitrite to yield nitric oxide and water

is shown in Figure 6.7 and the overall reaction, $NO_2^- + e^- + 2\,H^+ \longrightarrow NO + H_2O$, is exergonic ($\Delta G^{\circ\prime}$ = -23.5 kcal mol^{-1}) at this level of theory.

Optimised structures of all key stationary points are illustrated in Figure 6.8. By analogy to previously proposed mechanisms for the enzyme system copper nitrite reductase, and also to related computational studies,[500] we take the diaqua complex $[Cu^{II}(L)(H_2O)_2]^{2+}$, $\mathbf{3}^{2+}$, as the starting point for the catalytic cycle. We note that the experimental conditions involved methanol as the solvent, for which water is an appropriate substitute. Like $\mathbf{2}^+$, $\mathbf{3}^{2+}$ has a doublet ground state (S = ½) and a distorted square-pyramidal coordination geometry with the apical Cu-N distance (2.16 Å) rather longer than the other two (Cu-N: 2.00 Å). The two oxygen atoms (Cu-O: 2.14 and 2.20 Å) form part of the distorted basal plane. All attempts to obtain a stable molecular structure for a triaqua complex with an octahedral coordination geometry failed, as the additional water molecule was expelled into the secondary solvation sphere, further confirming the diaqua complex as a reasonable starting point in the cycle. The first phase of the catalytic cycle then involves coordination of the nitrite ion to form $\mathbf{2}^+$, with the nitrite bound in the κ^2O,O'-NO_2 mode as discussed above. The reaction is highly exergonic ($\Delta G^{\circ\prime}$ = -37.2 kcal mol^{-1}) due to the very favourable electrostatic component, and indeed substantially *more* exergonic than the overall reduction of NO_2^- to NO ($\Delta G^{\circ\prime}$ = -23.5 kcal mol^{-1}). The remainder of the catalytic cycle must therefore be endergonic by +13.7 kcal mol^{-1}, the necessary driving force being provided by the reducing agent (ascorbate in this case). This energetic comparison highlights an important point: if the initial $Cu^{II}(NO_2)$ complex is too stable, it may become a thermodynamic sink, retarding the catalytic reduction.

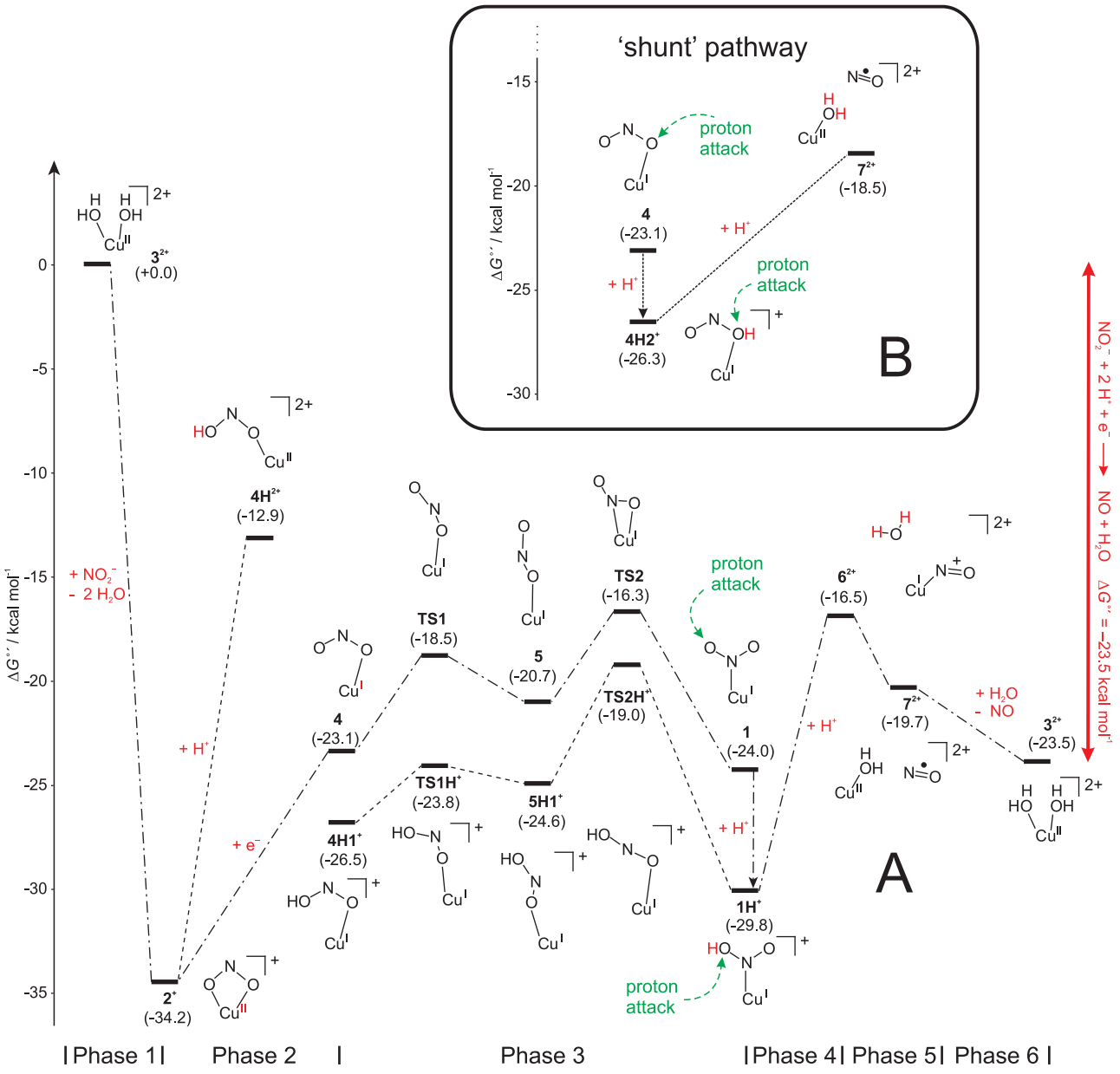

Figure 6.7: Reaction energy profile for the nitrite reduction starting from $\mathbf{3}^{2+}$, showing pathway A and B (inset). [Original in colour]

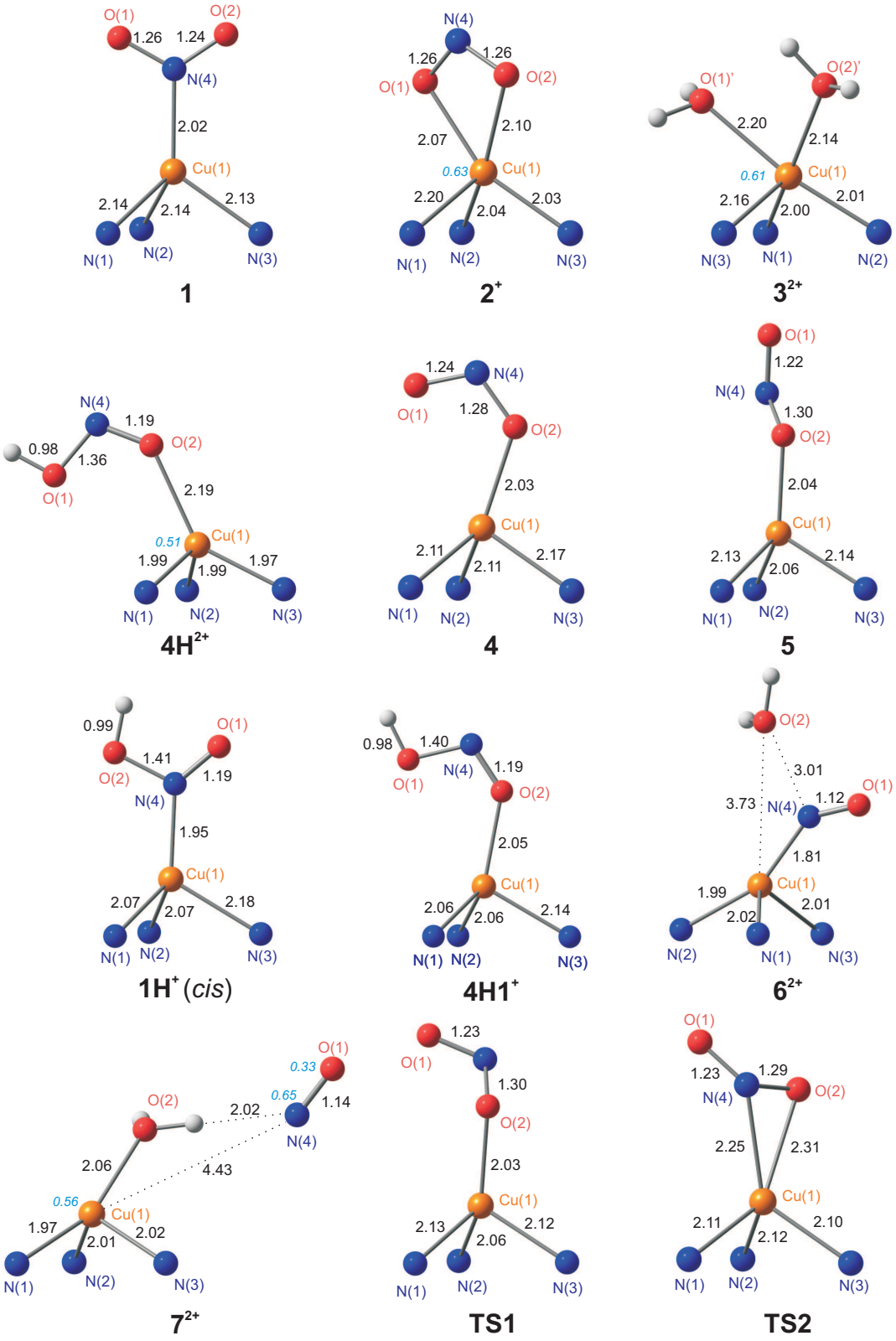

Figure 6.8: Optimised structural parameters (Å) and Mulliken spin populations (italics) for key stationary points described in Figure 6.7. The bulk of the ligand has been removed for clarity. [Original in colour]

Coordination of the nitrite could, in principle, be followed either by protonation or by one-electron reduction of the copper(II) centre. Both possibilities are shown in Figure 6.7 (phase 2) from which it is clear that protonation of nitrite O(1), yielding the tetrahedrally distorted Cu^{II}-HONO complex ($\mathbf{4H}^{2+}$), is strongly disfavoured ($\Delta G^{\circ\prime} = +21.3\,\mathrm{kcal\,mol^{-1}}$), due to the electrostatic repulsion between the positive charges in the complex and the proton. The large value for the Gibbs free energy equates to a pK_a value of ∼16, which underlines the low basicity of $\mathbf{2}^+$.¶ In contrast, the reduction of the copper(II) complex to give **4** (corresponding to the reaction $\mathbf{2}^+ + \frac{1}{2}\mathrm{AA} \longrightarrow \mathbf{4} + \frac{1}{2}\mathrm{DHAA} + \mathrm{H}^+$) is considerably less endergonic ($\Delta G^{\circ\prime} = +11.1\,\mathrm{kcal\,mol^{-1}}$), and therefore provides a more viable pathway.

Intermediate **4** is, of course, simply a linkage isomer of the N-bound global minimum, **1**, discussed above, and the subsequent step (phase 3) in the cycle involves a change in coordination mode. In fact, **4** lies only $0.9\,\mathrm{kcal\,mol^{-1}}$ above **1**, suggesting that the soft Cu^{I} centre does not differentiate strongly between N- and O-donor coordination modes. Although examples for the former are far more numerous,[493,504,517] an O-coordinated nitrite has been reported in the dinuclear complex $[(^{i}\mathrm{Pr}_3\mathrm{tacn})_2\mathrm{Cu}_2(\mu_2\text{-}\kappa N{:}\kappa O)\text{-}\mathrm{NO}_2]\mathrm{PF}_6$ of Tolman et al.,[550] reported above, where the bridging nitrite ion coordinates to one Cu^{I} centre via its N atom (bond distance 1.899 Å) and to the other Cu^{I} atom via a single O atom (1.968 Å). **1** and **4** are interconverted via a second O-nitrito isomer, **5**, where the non-coordinated oxygen is now directed away from the copper along the pseudo-C_3 axis. Details of the copper coordination environment are otherwise very similar to those in **4**. Transition states linking **4** with **5** (**TS1**) and **5** with **1** (**TS2**) (the latter featuring an η^2-NO bound nitrito group) are relatively low-lying, and the maximum barrier for the linkage isomerism process is $\Delta^{\ddagger}G^{\circ\prime} = 6.8\,\mathrm{kcal\,mol^{-1}}$. The activa-

¶The calculated free energy of this protonation step represents an upper bound to the true value, as the presence of an ionic atmosphere will stabilise the dication somewhat.

tion barrier can be compared to the one reported by Burton et al. for a copper tris(imidazolyl)carbinol complex.[501] Interestingly, in this case the barrier shows a dependency on the protonation state of the substrate and is larger in the unprotonated case (13 kcal mol^{-1}) compared to the protonated one (4 kcal mol^{-1}). The rearrangement from O- to N-bound form should therefore be kinetically facile as well as thermodynamically feasible ($\Delta G^{\circ\prime}$ = -0.9 kcal mol^{-1}).[‖]

Following the initial sequence of the catalytic cycle, protonation of Cu^{I}-bound nitrite to generate a nitrous acid complex appears to be a logical step forward within the mechanism. These HONO complexes are of particular importance, owing to their role as precursors for the N-O bond breaking step. From this perspective, they can be seen as a mechanistic junction. Geometries of various nitrous acid adducts with Cu^{I} are summarised in Figure 6.9. As for the nitrite complexes, two coordination modes for binding of nitrous acid need to be considered. Following rearrangement of **4** to **1**, protonation generates the nitrous acid complex, $\mathbf{1H^{+}}$, in which HONO is N-coordinated. We have in fact optimised two distinct structures of $\mathbf{1H^{+}}$, one where the proton lies *cis* to the non-protonated oxygen and is directed into the centre of the cavity, the other where it lies *trans* to the O and is directed between two of the cinnamylidene arms. The N-OH bond length is considerably longer in the latter (1.43 Å), probably due to the absence of intramolecular hydrogen bonding. The lower Wiberg bond order (1.002 vs. 1.031 for the *cis* isomer) suggests that the *trans* isomer is more activated towards N-O bond cleavage. The *cis*-form is slightly more stable than its *trans*-isomer, but the energetic differences are very small and have negligible impact on the overall shape of the potential energy surface.

[‖] We have also considered the possibility that linkage isomerism occurs at the Cu^{II} stage (i.e. before the reduction). At this oxidation level, isomerisation to the N-bound form is endergonic by 3.5 kcal mol^{-1}, suggesting that equilibrium concentrations of the latter will be very small.

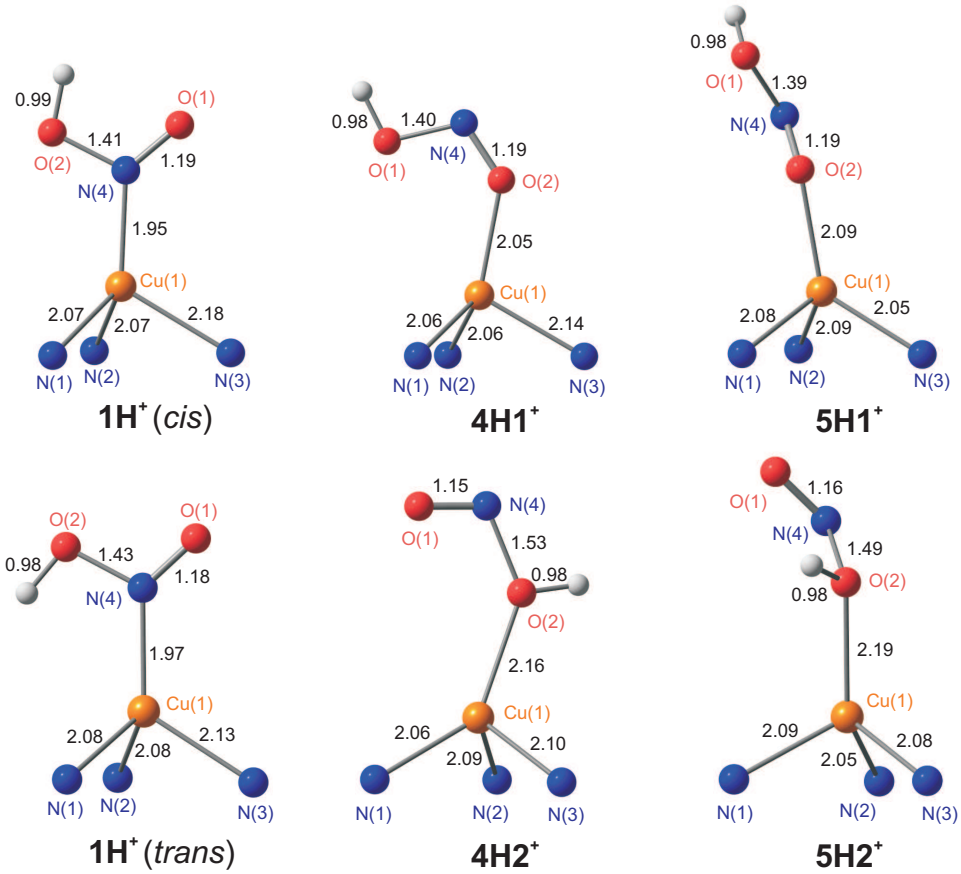

Figure 6.9: Optimised geometries (Å) of nitrous acid adducts relevant to the catalytic cycle. The bulk of the ligand has been removed for clarity. [Original in colour]

Considering O-bound coordination of nitrous acid, the free energy change for the protonation of **4** at O(1) to yield **4H1**$^+$ ($\Delta G^{\circ\prime}$ = -3.4 kcal mol^{-1}) equates to a pK_a of 4.25, a value that is similar to that for the first dissociation of ascorbic acid (4.17), suggesting that protonation at this stage of the pathway is reasonable. In fact, the more favourable protonation of **1** relative to **2**$^+$ is simply a consequence of the additional positive charge in the latter, and so it is possible that protonation could occur at any stage following the initial reduction of **2**$^+$ to **4**.

In Figure 6.7 (phase 3) we show linkage isomerism pathways for both unprotonated (**4** to **1**) and protonated (**4H**$^+$ to **1H**$^+$) forms, and it is clear that the presence of the proton does not change the free energy profile to any great extent. The linkage isomerism is marginally more exergonic for the protonated species sim-

ply because the oxygen atom that bonds to H^+ carries a formal negative charge in the N-bound isomer, but the surfaces remain approximately parallel, with no significant barriers. Another possible target of protonation is O(2) in **4**, which leads to the formation of $\mathbf{4H2}^+$, almost isoenergetic to $\mathbf{4H1}^+$ ($\Delta G^{\circ\prime}$ = -3.2 kcal mol^{-1}). The optimised structure of $\mathbf{4H2}^+$ shows an even more activated HO(2)-NO bond (1.53 Å) compared to the N-coordinated $\mathbf{1H}^+$, suggesting easy formation of NO and a cupric hydroxo or aqua complex. The same trends, although less pronounced, are observed for $\mathbf{5H1}^+$ and $\mathbf{5H2}^+$, which simply represent rotameric forms of $\mathbf{4H1}^+$ and $\mathbf{4H2}^+$ (Figure 6.9). Consistent with experimental results, N-coordination is thermodynamically favoured over the O-coordination mode, for both nitrite and nitrous acid. Thus regardless of exactly which point in phase 3 the protonation event takes place, this region of the potential energy surface is unlikely to be rate-limiting. Moving on now to the NO generation step, several scenarios for the transfer of the second proton can be envisaged.

NO generation in the N-coordination mode

From $\mathbf{1H}^+$, further protonation at O(2)H (phase 4, $\Delta G^{\circ\prime}$ = +13.3 kcal mol^{-1}), leads to spontaneous cleavage of the N-O bond, generating the Cu^I species $\mathbf{6}^{2+}$. The distorted tetrahedral environment of the copper centre features an NO ligand and a weakly coordinated water. At this point, our surface resembles that proposed by Burton et al. for the enzyme system, in so much as the NO species generated by N-O bond cleavage is trapped by the metal centre. The electronic structure of formally Cu^I-NO^+ species such as $\mathbf{6}^{2+}$ has been debated extensively, as they could, in principle, be described as a biradical, Cu^{II}-$NO^{\cdot}$. We favour the Cu^I-NO^+ formulation in the case of $\mathbf{6}^{2+}$ because it has a closed-shell singlet ground state although we note that a broken-symmetry singlet with Mulliken spin densi-

ties of ±1.0 on Cu and NO, respectively, lies only 2.7 kcal mol^{-1} higher in energy. Thus a definite assertion cannot be made. The Cu-N-O unit is distinctly bent in $\mathbf{6}^{2+}$ (N(2)-Cu-N(4) angle = 156°) but this is a consequence of the interaction of the loosely bound water with the π^* orbital of the NO rather than any biradical character. Finally, exchange of the water and NO ligands (phase 5) is exergonic, forming first the monoaqua Cu$^{\mathrm{II}}$ complex with weakly bound NO$^{\cdot}$ in the second coordination sphere ($\mathbf{7}^{2+}$, $\Delta G^{\circ\prime}$ = -3.2 kcal mol^{-1}) and then the starting complex $\mathbf{7}^{2+}$, with complete release of NO ($\Delta G^{\circ\prime}$ = -3.8 kcal mol^{-1}). We denote this route as pathway A.

NO generation in the O-coordination mode

It is not unreasonable that the cleavage of the N-O bond takes place before linkage isomerism has set in, and therefore could also occur from the O-coordinated species $\mathbf{4H2}^{+}$ or $\mathbf{5H2}^{+}$. The energetic profile for the former case can be used to exemplify this point, shown in the inset of Figure 6.7. Indeed, proton transfer to O(2)H leads to bond breaking, and interestingly, the optimisation converged to a broken-symmetry singlet state ($\langle S^2 \rangle$ = 1.00), with spin densities indicating formation of a Cu$^{\mathrm{II}}$ aqua complex and released NO$^{\cdot}$ (0.56 and -0.97 on Cu and NO, respectively). Having said that, the strongly elongated HO(2)-NO bond could also facilitate formation of a Cu$^{\mathrm{II}}$ hydroxo complex, with subsequent protonation of the OH group to yield the aqua complex. The triplet state (S = 1) of $\mathbf{4H2}^{+}$ forces bond rupture and release of NO, and the resulting Cu$^{\mathrm{II}}$ hydroxo complex with loosely bound NO lies only 5.2 kcal mol^{-1} above the starting structure. In comparison with the longer pathway A, including the linkage isomerisation sequence to form the N-coordinated Cu-(H)NO$_2$ isomer, this pathway (denoted B) can be viewed as a shunt, as it bypasses the formation of a copper nitrosyl intermediate.

Hence, release of NO and recovery of the starting complex are direct.

Unproductive proton attacks

The second protonation could, in principle, occur at the unprotonated oxygen atom in any of the Cu-HONO complexes presented above (e.g. O(1) rather than O(2) in $\mathbf{1H}^+$). However, this leads to energetically unfavourable complexes with protonated nitrous acid, $H_2NO_2^+$, and therefore proton transfer to the unprotonated oxygen is not productive.

Formation of isonitrosyl

Transfer of the additional proton to the O(1)H group in either of the isomeric complexes $\mathbf{4H1}^+$ (i.e. before linkage isomerism) or $\mathbf{5H1}^+$ does lead to N-O bond cleavage, but in each case the reaction is unlikely to occur, as the products being formed are highly destabilised (ΔE $\sim$20 kcal mol^{-1}) copper isonitrosyl complexes (Cu-ON). Therefore this route does not represent a viable pathway, and a proposed[482,551] Cu^{I}-ON^+ transient species appears to be highly unlikely and without chemical precedent.

The catalytic cycle described above involves initial substrate coordination followed by one-electron reduction to generate the intermediate **4**. The remainder of the cycle involves a complex sequence of steps including protonation, linkage isomerism, cleavage of the O-N bond, dissociation of the NO ligand and coordination of two further water ligands leading to the final products. Thereby the nature of the activation products crucially depends on the point on the energy surface at which the bond scission is initialised. While some of the pathways pose to be a dead-end to the cycle and can almost certainly be excluded, based on thermodynamic arguments, it is difficult to discriminate between the two pathways A and

B, which lead to product formation. From our analysis it is clear that both catalytically productive pathways, leading either to direct release of NO via O-bound HONO (B) or a copper nitrosyl intermediate via a N-bound HONO (A), are thermodynamically feasible. A distinct differentiation, however, is only meaningful when being based on activation barriers. Because of the difficulty associated with locating transition states for proton transfer reactions in our chosen model, it is not possible to give a final answer to the question which mechanism is operative, and we leave both options open. Nonetheless, we have devised viable reaction channels for the catalytic reduction of nitrite. Our results closely parallel the findings of previous computational studies,[501,552] and are also consistent with experimental data.[499,504,517,553] Both catalytically productive pathways have been discussed in the literature. Pathway A is identical to the reaction sequence proposed for the mechanism by Suzuki and co-workers.[471,504] The final steps in this mechanism (phase 4-6) match well with the experimental findings by Fujii and Kujime[499] and Suzuki et al.,[504] who have reasoned for a stepwise two-proton transfer mechanism, involving formation of a N-bound HONO intermediate and a tentative Cu-NO complex during the catalytic cycle. A copper-nitrosyl intermediate has been proposed,[492,554] to account for the ability of the enzyme to form N_2O. The recent report of Wright and co-workers[532] on the isolation of a Cu^{II}-NO complex provides more support for the possibility of such an intermediate. However, we note again that our calculations do not allow for an exact electronic structure determination of the CuNO complex. The low barriers associated with the linkage isomerisation from O,O- to N-coordinated nitrite imply that traversing from one to the other is a fast process at room temperature. On the other hand, several authors have argued in favour of direct release of NO and formation of a $Cu^{II}(H_2O)$ complex, thereby regenerating the metal centre for further catalysis.[455]

6.5 Conclusions

We have mapped out the potential energy surface for the reduction of nitrite to nitric oxide, which is catalysed by Cu complexes of the tct ligand. A series of complex reaction steps is found to lie on a flat surface. In one pathway one-electron reduction of $[Cu^{II}(tct)(\eta^2\text{-}O,O'\text{-}NO_2)]^+$ is followed by a sequence of linkage isomerisation, resulting in N-bound nitrite. Subsequent two-fold protonation of the nitrite ion leads to N-O bond scission and formation of an intermediate $Cu^{II}NO$ complex and water. Replacement of NO by water closes the cycle and restores the initial state. Alternatively, protonation of an O-coordinated nitrous acid complex, $[Cu^{I}(tct)(O\text{-}HONO)]^+$, leads to direct release of NO and formation of an cupric aqua complex. Both the former ('indirect') and latter ('shunt') pathways are thermodynamically and kinetically viable, and we argue that both would be operative during the reaction. In future work we aim to investigate the influence (steric and/or electronic) of substituents attached to the ligand's benzyl rings (e.g. *tert*-butyl) on the mechanism, ultimately hoping to obtain some insight into the possible role of the Ile257 residue present in the native enzyme.

7

Appendix

7.1 Units

Table 7.1: Atomic units (from IUPAC, I. Mills, *Quantities, Units and Symbols in Physical Chemistry*, Blackwell Science, Oxford, 1988.)

Physical quantity	Name of unit	Symbol and definition	Value in SI units
Mass	electron rest mass	m_e	$\approx 9.1094 \times 10^{-}31$ kg
Charge	elementary charge	e	$\approx 1.6022 \times 10^{-}19$ C
Action	Planck constant/(2π)	$\hbar = h/(2\pi)$	$\approx 1.0546 \times 10^{-}34$ J s
Length	Bohr	$a_0 = 4\pi\varepsilon_0\hbar^2/(m_e e^2)$	$\approx 5.2918 \times 10^{-}11$ m
Energy	Hartree	$E_h = \hbar^2/(m_e a_0^2)$	$\approx 4.3598 \times 10^{-}18$ J

Table 7.2: Conversion factors for energy units (from IUPAC, I. Mills, *Quantities, Units and Symbols in Physical Chemistry*, Blackwell Science, Oxford, 1988).

Name of unit	Conversions			
Hartree	1 E_h	27.21 eV	2.1947×10^5 cm^{-1}	627.51 kcal mol^{-1}
Electronvolt	1 eV	$3.675 \times 10^{-2} E_h$	8065.54 cm^{-1}	23.06 kcal mol^{-1}
Wavenumber	1 cm^{-1}	$4.556 \times 10^{-6} E_h$	1.240×10^{-4} eV	2.859×10^{-3} kcal mol^{-1}
Kilocalorie / mole	1 kcal mol^{-1}	$1.594 \times 10^{-3} E_h$	4.336×10^{-2} eV	349.76 cm^{-1}

7.2 List of Acronyms

Table 7.3: Abbreviations and ligand names used in this thesis.

AA	ascorbic acid
AIM	atoms in molecules
AO	atomic orbital
Asp	aspartic acid
BCP	bond critical point
BO	Born-Oppenheimer
bpi	bis(2-picolyl)imine
bpy	bipyridine
2,2′-bpy, 4,4′-bpy	2,2′-bipyridine, 4,4′-bipyridine
BS	broken-symmetry
CASSCF	complete active space self-consistent field
CC (CCSD, CCSDT)	coupled cluster (including singles and doubles or
CCSD(T)	singles, doubles and triples from a perturbative treatment)
CGF	contracted Gaussian function
CI (CISD and CISDT)	configuration interaction (including doubles and doubles and triples)
o-Clpap, *p*-Clpap	2-[(2-chlorophenyl)azo]pyridine, 2-[(4-chlorophenyl)azo]pyridine
cod	1,5-cyclooctadiene
COSMO	conductor-like screening model
COT	corresponding orbital transformation
CP	critical point
Cp	cyclopentadienyl (C_5H_5)
Cp^*	pentamethylcyclopentadienyl (C_5Me_5)
[18]crown-6	1,4,7,10,13,16-hexaoxacyclooctadecane
[2.2.2]crypt	1,10-diaza-4,7,13,16,21,24-hexaoxabicyclo[8.8.8]hexacosane
CuNiR	Copper Nitrite Reductase
Cys	cysteine
3,5-DBQ	3,5-di-*tert*-butylquinone
DFT	density functional theory
DHAA	dehydroascorbate
DZ	double-zeta
ECP	effective core potential
ELF	electron localisation function
ESR	electron spin resonance
FOS	formal oxidation state
FT-IR	Fourier-transform infrared
GGA	generalised gradient approximation
GIAO	gauge-independent atomic orbital
GTO	Gaussian-type orbital
HF	Hartree-Fock
His	histidine
HK	Hohenberg-Kohn
^{1}H NMR	proton nuclear magnetic resonance
HOMO	highest occupied molecular orbital
HS	high-spin
HSAB	hard-soft acid base
IEF-PCM	integral equation formalism of the polarizable continuum model
Ile	isoleucine
IR	infrared

Table 7.4: Abbreviations and ligand names used in this thesis (continued).

KIE	kinetic isotope effect
KS	Kohn-Sham
LCAO-MO	linear combination of atomic orbitals to give molecular orbitals
LLCT	ligand-to-ligand charge transfer
LS	low-spin
L(S)DA	local (spin) density approximation
LUMO	lowest unoccupied molecular orbital
MB	Mössbauer
MCSCF	multi-configurational self-consistent field
4-Mepap	2-[(4-methylphenyl)azo]pyridine
mes	mesityl (2,4,6-$Me_3C_6H_2$)
Met	methionine
MO	molecular orbital
MP2, MP3, MP4	Møller-Plesset perturbation theory up to second, third, fourth order
nbd	norbornadiene
NICS	nuclear independent chemical shift
NIL	non-innocent ligand
OTf	trifluoromethane sulfonate
pap	2-(phenylazo)pyridine
PCM	polarizable continuum model
PDI	pyridine-2,6-diimine
PES	potential energy surface
Ph	Phenyl (C_6H_5-)
POS	physical oxidation state
(PPN)Cl	bis(triphenylphosphine)iminium chloride
PT	perturbation theory
py	pyridine
RCP	ring critical point
rt	room temperature
SCF	self-consistent field
SCRF	self-consistent reaction field
SEC	skeletal electron count
SHE	standard hydrogen electrode
SOMO	singly occupied molecular orbital
SQUID	superconducting quantum interference device
STO	Slater-type orbital
SZ	single-zeta
SV	split valence
tacn	1,4,7-triazacyclononane
TCNE	tetracyanoethylene
TCNQ	tetracyanoquinodimethane
tct	*cis*,*cis*-1,3,5-tri-[(*E*,*E*)-cinnamylideneamino]cyclohexane
TD-DFT	time-dependent density functional theory
TFA	trifluoroacetic acid
thf	tetrahydrofuran
tmpa	tris(2-pyridylmethyl)amine
Tp	hydrotris(pyrazolyl)borate ($[HB(C_3N_2H_3)_3]^-$)
Tp^*	hexamethylhydrotris(pyrazolyl)borate ($[HB(C_3N_2Me_2H)_3]^-$)
tpm	tris(pyrazolyl)methane
TVEC	total valence electron count
TZ	triple-zeta
UAHF	united atom for Hartree-Fock
UV-vis	ultraviolet/visual
XAS	X-ray absorption spectroscopy
ZORA	zeroth order regular approximation

References

[1] A. Szabo and N. S. Ostlund, *Modern Quantum Chemistry: Introduction to Advanced Electronic Structure Theory*, Dover Publications, New York, 1996.

[2] W. J. Hehre, L. Radom, P. von Ragué Schleyer, and J. A. Pople, *Ab Initio Molecular Orbital Theory*, John Wiley & Sons, New York, 1986.

[3] P. Atkins and R. Friedman, *Molecular Quantum Mechanics*, Oxford University Press, Oxford, 2007.

[4] I. N. Levine, *Quantum Chemistry*, Prentice Hall, New York, 2009.

[5] C. J. Cramer, *Essentials of Computational Chemistry: Theories and Models*, John Wiley & Sons, Chichester, 2009.

[6] F. Jensen, *Introduction to Computational Chemistry*, John Wiley & Sons, Chichester, 2007.

[7] W. Koch and M. C. Holthausen, *A Chemist's Guide to Density Functional Theory*, Wiley-VCH, Weinheim, 2001.

[8] R. G. Parr and W. Yang, *Density-Functional Theory of Atoms and Molecules*, Oxford University Press, New York, 1989.

[9] E. Schrödinger, *Ann. Phys.*, 1926, **79**, 361–376.

[10] E. Schrödinger, *Ann. Phys.*, 1926, **79**, 489–527.

[11] E. Schrödinger, *Ann. Phys.*, 1926, **80**, 437–490.

[12] E. Schrödinger, *Ann. Phys.*, 1926, **81**, 109–139.

[13] L. H. Thomas, *Proc. Camb. Phil. Soc.*, 1927, **23**, 542–548.

[14] E. Fermi, *Rend. Accad. Lincei*, 1927, **6**, 602–607.

[15] J. C. Slater, *Phys. Rev.*, 1951, **81**, 385–390.

[16] P. Hohenberg and W. Kohn, *Phys. Rev. B*, 1964, **136**, 864–871.

[17] W. Kohn and L. J. Sham, *Phys. Rev. A*, 1965, **140**, 1133–1138.

[18] D. M. Ceperley and B. J. Alder, *Phys. Rev. Lett.*, 1980, **45**, 566–569.

[19] S. H. Vosko, L. Wilk, and M. Nusair, *Can. J. Phys.*, 1980, **58**, 1200–1211.

[20] J. P. Perdew and Y. Wang, *Phys. Rev. B*, 1992, **45**, 13244–13249.

[21] A. D. Becke, *Phys. Rev. A*, 1988, **38**, 3098–3100.

[22] J. P. Perdew, *Phys. Rev. B*, 1986, **33**, 8822–8824.

[23] J. P. Perdew, in *Electronic Structure of Solids*, ed. P. Ziesche and H. Eschrig, Akademie Verlag, Berlin, 1991.

[24] J. P. Perdew, J. A. Chevary, S. H. Vosko, K. A. Jackson, M. R. Pederson, D. J. Singh, and C. Fiolhais, *Phys. Rev. B*, 1992, **46**, 6671–6687.

[25] J. P. Perdew, K. Burke, and Y. Wang, *Phys. Rev. B*, 1996, **54**, 16533–16539.

[26] C. Lee, W. Yang, and R. G. Parr, *Phys. Rev. B*, 1988, **37**, 785–789.

[27] B. Miehlich, A. Savin, H. Stoll, and H. Preuss, *Chem. Phys. Lett.*, 1989, **157**, 200–206.

[28] J. P. Perdew, K. Burke, and M. Ernzerhof, *Phys. Rev. Lett.*, 1996, **77**, 3865–3868.

[29] A. D. Becke, *J. Chem. Phys.*, 1996, **104**, 1040–1046.

[30] J. Tao, J. P. Perdew, V. N. Staroverov, and G. E. Scuseria, *Phys. Rev. Lett.*, 2003, **91**, 146401.

[31] A. D. Becke, *J. Chem. Phys.*, 1993, **98**, 5648–5652.

[32] P. J. Stephens, F. J. Devlin, C. F. Chabalowski, and M. J. Frisch, *J. Phys. Chem.*, 1994, **98**, 11623–11627.

[33] J. P. Perdew, M. Ernzerhof, and K. Burke, *J. Chem. Phys.*, 1996, **105**, 9982–9985.

[34] C. Adamo and V. Barone, *J. Chem. Phys.*, 1999, **110**, 6158–6170.

[35] M. Ernzerhof and G. E. Scuseria, *J. Chem. Phys.*, 1999, **110**, 5029–5036.

[36] V. N. Staroverov, G. E. Scuseria, J. Tao, and J. P. Perdew, *J. Chem. Phys.*, 2003, **119**, 12129–12137.

[37] Y. Zhao and D. G. Truhlar, *Acc. Chem. Res.*, 2008, **41**, 157–167.

[38] Y. Zhao and D. G. Truhlar, *J. Phys. Chem. A*, 2006, **110**, 5121–5129.

[39] Y. Zhao and D. G. Truhlar, *J. Phys. Chem. A*, 2006, **110**, 13126–13130.

[40] Y. Zhao, N. E. Schultz, and D. G. Truhlar, *J. Chem. Phys.*, 2005, **123**, 161103.

[41] Y. Zhao and D. G. Truhlar, *Theor. Chem. Acc.*, 2008, **120**, 215–241.

[42] Y. Zhao, N. E. Schultz, and D. G. Truhlar, *J. Chem. Theory Comput.*, 2006, **2**, 364–382.

[43] S. Grimme, *J. Chem. Phys.*, 2006, **124**, 34108.

[44] T. Benighaus, R. A. DiStasio Jr., R. C. Lochan, J.-D. Chai, and M. Head-Gordon, *J. Phys. Chem. A*, 2008, **112**, 2702–2712.

[45] T. Schwabe and S. Grimme, *Phys. Chem. Chem. Phys.*, 2006, **8**, 4398–4401.

[46] T. Schwabe and S. Grimme, *Phys. Chem. Chem. Phys.*, 2007, **9**, 3397–3406.

[47] G. Frenking and T. Wagener, in *Encyclopedia of Computational Chemistry*, ed. P. von Ragué Schleyer, John Wiley & Sons, Chichester, 1998, 3073–3084.

[48] A. P. Ginsberg, *J. Am. Chem. Soc.*, 1980, **102**, 111–117.

[49] L. Noodleman, D. A. Case, and A. Aizman, *J. Am. Chem. Soc.*, 1988, **110**, 1001–1005.

[50] L. Noodleman and E. R. Davidson, *Chem. Phys.*, 1986, **109**, 131–143.

[51] L. Noodleman, J. G. Norman Jr., J. H. Osborne, A. Aizman, and D. A. Case, *J. Am. Chem. Soc.*, 1985, **107**, 3418–3426.

[52] L. Noodleman, *J. Chem. Phys.*, 1981, **74**, 5737–5743.

[53] J. A. Pople, P. M. W. Gill, and N. C. Handy, *Int. J. Quant. Chem.*, 1995, **56**, 303–305.

[54] Gaussian 09, Revision A.02, M. J. Frisch, G. W. Trucks, H. B. Schlegel, G. E. Scuseria, M. A. Robb, J. R. Cheeseman, G. Scalmani, V. Barone, B. Mennucci, G. A. Petersson, H. Nakatsuji, M. Caricato, X. Li, H. P. Hratchian, A. F. Izmaylov, J. Bloino, G. Zheng, J. L. Sonnenberg, M. Hada, M. Ehara, K. Toyota, R. Fukuda, J. Hasegawa, M. Ishida, T. Nakajima, Y. Honda, O. Kitao, H. Nakai, T. Vreven, J. A. Montgomery, Jr., J. E. Peralta, F. Ogliaro, M. Bearpark, J. J. Heyd, E. Brothers, K. N. Kudin, V. N. Staroverov, R. Kobayashi, J. Normand, K. Raghavachari, A. Rendell, J. C. Burant, S. S. Iyengar, J. Tomasi, M. Cossi, N. Rega, J. M. Millam, M. Klene, J. E. Knox, J. B. Cross, V. Bakken, C. Adamo, J. Jaramillo, R. Gomperts, R. E. Stratmann, O. Yazyev, A. J. Austin, R. Cammi, C. Pomelli, J. W. Ochterski, R. L. Martin, K. Morokuma, V. G. Zakrzewski, G. A. Voth, P. Salvador, J. J. Dannenberg, S. Dapprich, A. D. Daniels, Ö. Farkas, J. B. Foresman, J. V. Ortiz, J. Cioslowski, and D. J. Fox, Gaussian, Inc., Wallingford CT, 2009.

[55] Gaussian 03, Revision D.02/E.01, M. J. Frisch, G. W. Trucks, H. B. Schlegel, G. E. Scuseria, M. A. Robb, J. R. Cheeseman, J. A. Montgomery Jr., T. Vreven, K. N. Kudin, J. C. Burant, J. M. Millam, S. S. Iyengar, J. Tomasi, V. Barone, B. Mennucci, M. Cossi, G. Scalmani, N. Rega, G. A. Petersson, H. Nakatsuji, M. Hada, M. Ehara, K. Toyota, R. Fukuda, J. Hasegawa, M. Ishida, T. Nakajima, Y. Honda, O. Kitao, H. Nakai, M. Klene, X. Li, J. E. Knox, H. P. Hratchian, J. B. Cross, V. Bakken, C. Adamo, J. Jaramillo, R. Gomperts, R. E. Stratmann, O. Yazyev, A. J. Austin, R. Cammi, C. Pomelli, J. W. Ochterski, P. Y. Ayala, K. Morokuma, G. A. Voth, P. Salvador, J. J. Dannenberg, V. G. Zakrzewski, S. Dapprich, A. D. Daniels, M. C. Strain, O. Farkas, D. K. Malick, A. D. Rabuck, K. Raghavachari, J. B. Foresman, J. V. Ortiz, Q. Cui, A. G. Baboul, S. Clifford, J. Cioslowski, B. B. Stefanov, G. Liu, A. Liashenko, P. Piskorz, I. Komaromi, R. L. Martin, D. J. Fox, T. Keith, M. A. Al-Laham, C. Y. Peng, A. Nanayakkara, M. Challacombe, P. M. W. Gill, B. Johnson, W. Chen, M. W. Wong, C. Gonzalez, and J. A. Pople, Gaussian, Inc., Wallingford CT, 2004.

[56] ADF2010, SCM, Theoretical Chemistry, Vrije Universiteit, Amsterdam, The Netherlands, http://www.scm.com, E. J. Baerends, T. Ziegler, J. Autschbach, D. Bashford, A. Bérces, F. M. Bickelhaupt, C. Bo, P. M. Boerrigter, L. Cavallo, D. P. Chong, L. Deng, R. M. Dickson, D. E. Ellis, M. van Faassen, L. Fan, T. H.

Fischer, C. Fonseca Guerra, A. Ghysels, A. Giammona, S. J. A. van Gisbergen, A. W. Götz, J. A. Groeneveld, O. V. Gritsenko, M. Grüning, S. Gusarov, F. E. Harris, P. van den Hoek, C. R. Jacob, H. Jacobsen, L. Jensen, J. W. Kaminski, G. van Kessel, F. Kootstra, A. Kovalenko, M. V. Krykunov, E. van Lenthe, D. A. McCormack, A. Michalak, M. Mitoraj, J. Neugebauer, V. P. Nicu, L. Noodleman, V. P. Osinga, S. Patchkovskii, P. H. T. Philipsen, D. Post, C. C. Pye, W. Ravenek, J. I. Rodríguez, P. Ros, P. R. T. Schipper, G. Schreckenbach, J. S. Seldenthuis, M. Seth, J. G. Snijders, M. Solà, M. Swart, D. Swerhone, G. te Velde, P. Vernooijs, L. Versluis, L. Visscher, O. Visser, F. Wang, T. A. Wesolowski, E. M. van Wezenbeek, G. Wiesenekker, S. K. Wolff, T. K. Woo, and A. L. Yakovlev.

[57] G. te Velde, F. M. Bickelhaupt, S. J. A. van Gisbergen, C. Fonseca Guerra, E. J. Baerends, J. G. Snijders, and T. Ziegler, *J. Comp. Chem.*, 2001, **22**, 931–967.

[58] C. Fonseca Guerra, J. G. Snijders, G. te Velde, and E. J. Baerends, *Theor. Chem. Acc.*, 1998, **99**, 391–403.

[59] Jaguar, version 7.6, Schödinger, LLC, New York, NY, 2009.

[60] F. Neese, ORCA - *an ab initio, density functional and semiempirical program package*, version 2.6, revision 35; University of Bonn: Bonn, Germany, Feb 2008 (http://www.thch.uni-bonn.de/tc/orca/).

[61] D. Andrae, U. Häußermann, M. Dolg, H. Stoll, and H. Preuß, *Theor. Chim. Acta*, 1990, **77**, 123–141.

[62] R. F. W. Bader, *Atoms in Molecules. A Quantum Theory*, Oxford University Press, Oxford, 1990.

[63] F. Biegler-König and J. Schönbohm, AIM2000, version 2.0, Büro für Innovative Software, 2002.

[64] S. I. Gorelsky, AOMix: Program for Molecular Orbital Analysis, University of Ottawa, (http://www.sg-chem.net), 2010.

[65] S. I. Gorelsky and A. B. P. Lever, *J. Organomet. Chem.*, 2001, **635**, 187–196.

[66] R. S. Mulliken, *J. Chem. Phys.*, 1955, **23**, 1833–1840.

[67] R. S. Mulliken, *J. Chem. Phys.*, 1955, **23**, 1841–1846.

[68] R. S. Mulliken, *J. Chem. Phys.*, 1955, **23**, 2338–2342.

[69] R. S. Mulliken, *J. Chem. Phys.*, 1955, **23**, 2343–2346.

[70] G. A. Zhurko and D. A. Zhurko, Chemcraft, version 1.6, build 342, (http://www.chemcraftprog.com), 2011.

[71] ADF-GUI2010, SCM, Amsterdam, The Netherlands, http://www.scm.com, O. Visser, P. Leyronnas, W.-J. van Zeist, and M. Luppi.

[72] H. Grützmacher, *Angew. Chem. Int. Ed.*, 2008, **47**, 1814–1818.

[73] K. Ray, T. Petrenko, K. Wieghardt, and F. Neese, *Dalton Trans.*, 2007, 1552–1566.

[74] Q. Knijnenburg, S. Gambarotta, and P. H. M. Budzelaar, *Dalton Trans.*, 2006, 5442–5448.

[75] W. Kaim, *Inorg. Chem.*, 2011, **50**, 9752–9765.

[76] W. Kaim and B. Schwederski, *Coord. Chem. Rev.*, 2010, **254**, 1580–1588.

[77] R. Eisenberg, *Coord. Chem. Rev.*, 2011, **255**, 825–836.

[78] S. Sproules and K. Wieghardt, *Coord. Chem. Rev.*, 2010, **254**, 1358–1382.

[79] J. L. Boyer, J. Rochford, M.-K. Tsai, J. T. Muckerman, and E. Fujita, *Coord. Chem. Rev.*, 2010, **254**, 309–330.

[80] K. P. Butin, E. K. Beloglazkina, and N. V. Zyk, *Russ. Chem. Rev.*, 2005, **74**, 531–553.

[81] M. D. Ward and J. A. McCleverty, *J. Chem. Soc., Dalton Trans.*, 2002, 275–288.

[82] W. Kaim, *Coord. Chem. Rev.*, 1987, **76**, 187–235.

[83] C. G. Pierpont and C. W. Lange, *Prog. Inorg. Chem.*, 1994, **41**, 331–442.

[84] C. G. Pierpont, *Coord. Chem. Rev.*, 2001, **216**, 99–125.

[85] A. B. P. Lever, *Coord. Chem. Rev.*, 2010, **254**, 1397–1405.

[86] S. Záliš, R. F. Winter, and W. Kaim, *Coord. Chem. Rev.*, 2010, **254**, 1383–1396.

[87] P. Deplano, L. Pilia, D. Espa, M. L. Mercuri, and A. Serpe, *Coord. Chem. Rev.*, 2010, **254**, 1434–1447.

[88] D. N. Hendrickson and C. G. Pierpont, in *Spin Crossover in Transition Metal Compounds II*, ed. P. Gütlich and H. A. Goodwin, Springer, Berlin, 2004, 63–96.

[89] R. K. Szilagy, in *Computational Inorganic and Bioinorganic Chemistry*, ed. E. I. Solomon, R. A. Scott and R. B. King, Wiley & Sons, Chichester, 2009, 411–423.

[90] C. K. Jørgensen, *Coord. Chem. Rev.*, 1966, **2**, 164–178.

[91] J. H. Enemark and R. D. Feltham, *Coord. Chem. Rev.*, 1974, **13**, 339–406.

[92] A. Wanat, T. Schneppensieper, G. Stochel, R. van Eldik, E. Bill, and K. Wieghardt, *Inorg. Chem.*, 2002, **41**, 4–10.

[93] G. N. Schrauzer and V. Mayweg, *J. Am. Chem. Soc.*, 1962, **84**, 3221.

[94] S. Sproules and K. Wieghardt, *Coord. Chem. Rev.*, 2011, **255**, 837–860.

[95] M. M. Khusniyarov, E. Bill, T. Weyhermüller, E. Bothe, and K. Wieghardt, *Angew. Chem. Int. Ed.*, 2011, **50**, 1652–1655.

[96] R. K. Szilagyi, B. S. Lim, T. Glaser, R. H. Holm, B. Hedman, K. O. Hodgson, and E. I. Solomon, *J. Am. Chem. Soc.*, 2003, **125**, 9158–9169.

[97] G. Parkin, *J. Chem. Edu.*, 2006, **83**, 791–799.

[98] P. Chaudhuri, C. N. Verani, E. Bill, E. Bothe, T. Weyhermüller, and K. Wieghardt, *J. Am. Chem. Soc.*, 2001, **123**, 2213–2223.

[99] B. Kirchner, F. Wennmohs, S. Ye, and F. Neese, *Curr. Opin. Chem. Biol.*, 2007, **11**, 134–141.

[100] C. K. Jørgensen, *Oxidation Numbers and Oxidation States*, Springer, Heidelberg, 1969.

[101] M. B. Robin and P. Day, *Adv. Inorg. Chem. Radiochem.*, 1967, **10**, 247–422.

[102] E. Evangelio and D. Ruiz-Molina, *Eur. J. Inorg. Chem.*, 2005, 2957–2971.

[103] H. Ohtsu and K. Tanaka, *Angew. Chem. Int. Ed.*, 2004, **43**, 6301–6303.

[104] R. M. Buchanan and C. G. Pierpont, *J. Am. Chem. Soc.*, 1980, **102**, 4951–4957.

[105] W. P. Griffith, *Transition Met. Chem.*, 1993, **18**, 250–256.

[106] A. L. Balch, *J. Am. Chem. Soc.*, 1973, **95**, 2723–2724.

[107] S. Bhattacharya, P. Gupta, F. Basuli, and C. G. Pierpont, *Inorg. Chem.*, 2002, **41**, 5810–5816.

[108] O. Carugo, K. Djinovi, M. Rizzi, and C. B. Castellani, *J. Chem. Soc., Dalton Trans.*, 1991, 1551–1555.

[109] E. Rijnberg, B. Richter, K.-H. Thiele, J. Boersma, N. Veldman, A. L. Spek, and G. van Koten, *Inorg. Chem.*, 1998, **37**, 56–53.

[110] C. W. Lange, B. J. Conklin, and C. G. Pierpont, *Inorg. Chem.*, 1994, **33**, 1276–1283.

[111] A. S. Attia and C. G. Pierpont, *Inorg. Chem.*, 1997, **36**, 6184–6187.

[112] O. Sato, A. Cui, R. Matsuda, J. Tao, and S. Hayami, *Acc. Chem. Res.*, 2007, **40**, 361–369.

[113] G. Bruno, M. Almeida, F. Artizzu, J. C. Dias, M. L. Mercuri, L. Pilia, C. Rovira, X. Ribas, A. Serpec, and P. Deplano, *Dalton Trans.*, 2010, **39**, 4566–4574.

[114] K. Wang and E. I. Stiefel, *Science*, 2001, **291**, 106–110.

[115] D. J. Harrison, N. Nguyen, A. J. Lough, and U. Fekl, *J. Am. Chem. Soc.*, 2006, **128**, 11026–11027.

[116] R. R. Kapre, E. Bothe, T. Weyhermüller, S. DeBeer George, and K. Wieghardt, *Inorg. Chem.*, 2007, **46**, 5642–5650.

[117] R. Kapre, K. Ray, I. Sylvestre, T. Weyhermüller, S. DeBeer George, F. Neese, and K. Wieghardt, *Inorg. Chem.*, 2006, **45**, 3499–3509.

[118] K. Ray, S. DeBeer George, E. I. Solomon, K. Wieghardt, and F. Neese, *Chem. Eur. J.*, 2007, **13**, 2783–2797.

[119] K. Ray, A. Begum, T. Weyhermüller, S. Piligkos, J. van Slageren, F. Neese, and K. Wieghardt, *J. Am. Chem. Soc.*, 2005, **127**, 4403–4415.

[120] K. Ray, E. Bill, T. Weyhermüller, and K. Wieghardt, *J. Am. Chem. Soc.*, 2005, **127**, 5641–5654.

[121] K. Ray, T. Weyhermüller, F. Neese, and K. Wieghardt, *Inorg. Chem.*, 2005, **44**, 5345–5360.

[122] A. K. Patra, E. Bill, T. Weyhermüller, K. Stobie, Z. Bell, M. D. Ward, J. A. McCleverty, and K. Wieghardt, *Inorg. Chem.*, 2006, **45**, 6541–6548.

[123] T. Petrenko, K. Ray, K. E. Wieghardt, and F. Neese, *J. Am. Chem. Soc.*, 2006, **128**, 4422–4436.

[124] K. Ray, T. Weyhermüller, A. Goossens, M. W. J. Crajé, and K. Wieghardt, *Inorg. Chem.*, 2003, **42**, 4082–4087.

[125] P. Chaudhuri and K. Wieghardt, *Prog. Inorg. Chem.*, 2001, **50**, 151–216.

[126] P. Clopath and A. von Zelewsky, *J. Chem. Soc. D, Chem. Commun.*, 1971, 47–48.

[127] H. Bock and H. tom Dieck, *Angew. Chem. Int. Ed.*, 1966, **5**, 520–522.

[128] S. Richter, C. Daul, and A. von Zalewsky, *Inorg. Chem.*, 1976, **15**, 943–948.

[129] G. van Koten and K. Vrieze, *Adv. Organomet. Chem.*, 1982, **21**, 151–239.

[130] W. Kaim, M. Sieger, S. Greulich, B. Sarkar, J. Fiedler, and S. Záliš, *J. Organomet. Chem.*, 2010, **695**, 1052–1058.

[131] W. Kaim, *Coord. Chem. Rev.*, 2001, **219**, 463–488.

[132] W. Kaim and M. Moscherosch, *Coord. Chem. Rev.*, 1994, **129**, 157–193.

[133] W. Kaim, *Coord. Chem. Rev.*, 2002, **230**, 127–139.

[134] R. E. Cowley, E. Bill, F. Neese, W. W. Brennessel, and P. L. Holland, *Inorg. Chem.*, 2009, **48**, 4828–4836.

[135] M. H. Chisholm, J. C. Huffman, I. P. Rothwell, P. G. Bradley, N. Kress, and W. H. Woodruff, *J. Am. Chem. Soc.*, 1981, **103**, 4945–4947.

[136] W. Kaim, R. Reinhardt, and M. Sieger, *Inorg. Chem.*, 1994, **33**, 4453–4459.

[137] S. Záliš, M. Sieger, S. Greulich, H. Stoll, and W. Kaim, *Inorg. Chem.*, 2003, **42**, 5185–5191.

[138] M. Sieger, W. Kaim, D. J. Stufkens, T. L. Snoeck, H. Stoll, and S. Záliš, *Dalton Trans.*, 2004, 3815–3821.

[139] C. C. Lu, E. Bill, T. Weyhermüller, E. Bothe, and K. Wieghardt, *J. Am. Chem. Soc.*, 2008, **130**, 3181–3197.

[140] B. M. Wile, R. J. Trovitch, S. C. Bart, A. M. Tondreau, E. Lobkovsky, C. Milsmann, E. Bill, K. Wieghardt, and P. J. Chirik, *Inorg. Chem.*, 2009, **48**, 4190–4200.

[141] C. C. Lu, E. Bill, T. Weyhermüller, E. Bothe, and K. Wieghardt, *Inorg. Chem.*, 2007, **46**, 7880–7889.

[142] K. J. Blackmore, N. Lal, J. W. Ziller, and A. F. Heyduk, *J. Am. Chem. Soc.*, 2008, **130**, 2728–2729.

[143] M. R. Haneline and A. F. Heyduk, *J. Am. Chem. Soc.*, 2006, **128**, 8410–8411.

[144] H. Chun, C. N. Verani, P. Chaudhuri, E. Bothe, E. Bill, T. Weyhermüller, and K. Wieghardt, *Inorg. Chem.*, 2001, **40**, 4157–4166.

[145] C. N. Verani, S. Gallert, E. Bill, T. Weyhermüller, K. Wieghardt, and P. Chaudhuri, *Chem. Commun.*, 1999, 1747-1748.

[146] H. Chun, T. Weyhermüller, E. Bill, and K. Wieghardt, *Angew. Chem. Int. Ed.*, 2001, **40**, 2489–2492.

[147] S. Kokatam, T. Weyhermüller, E. Bothe, P. Chaudhuri, and K. Wieghardt, *Inorg. Chem.*, 2005, **44**, 3709–3717.

[148] X. Sun, H. Chun, K. Hildenbrand, E. Bothe, T. Weyhermüller, F. Neese, and K. Wieghardt, *Inorg. Chem.*, 2002, **41**, 4295–4303.

[149] J. I. van der Vlugt and J. N. H. Reek, *Angew. Chem. Int. Ed.*, 2009, **48**, 8832–8846.

[150] R. C. Bauer, Y. Gloaguen, M. Lutz, J. N. H. Reek, B. de Bruin, and J. I. van der Vlugt, *Dalton Trans.*, 2011, **40**, 8022–8029.

[151] T. Büttner, J. Geier, G. Frison, J. Harmer, C. Calle, A. Schweiger, H. Schönberg, and H. Grützmacher, *Science*, 2005, **307**, 235–238.

[152] N. P. Mankad, W. E. Antholine, R. K. Szilagyi, and J. C. Peters, *J. Am. Chem. Soc.*, 2009, **131**, 3878–3880.

[153] Y. Miyazato, T. Wada, J. T. Muckerman, E. Fujita, and K. Tanaka, *Angew. Chem. Int. Ed.*, 2007, **46**, 5728–5730.

[154] P. Hemmerich, *Proc. R. Soc. Lond. A*, 1968, **302**, 335–350.

[155] W. Kaim, B. Schwederski, O. Heilmann, and F. M. Hornung, *Coord. Chem. Rev.*, 1999, **182**, 323–342.

[156] J.-H. Fuhrhop, *Angew. Chem. Int. Ed.*, 1974, **13**, 321–335.

[157] K. Pierloot, H. Zhao, and S. Vancoillie, *Inorg. Chem.*, 2010, **49**, 10316–10329.

[158] O. Zakharieva, V. Schünemann, M. Gerdan, S. Licoccia, S. Cai, F. A. Walker, and A. X. Trautwein, *J. Am. Chem. Soc.*, 2002, **124**, 6636–6648.

[159] B. A. Jazdzewski and W. B. Tolman, *Coord. Chem. Rev.*, 2000, **200**, 633–685.

[160] Y. Shimazaki and O. Yamauchi, *Ind. J. Chem. A*, 2011, **50**, 383–394.

[161] J. W. Whittaker, *Arch. Biochem. Biophys.*, 2005, **433**, 227–239.

[162] W. I. Dzik, J. I. van der Vlugt, J. N. H. Reek, and B. de Bruin, *Angew. Chem. Int. Ed.*, 2011, **50**, 3356–3358.

[163] B. de Bruin, E. Bill, E. Bothe, T. Weyhermüller, and K. Wieghardt, *Inorg. Chem.*, 2000, **39**, 2936–2947.

[164] M. W. Bouwkamp, A. C. Bowman, E. Lobkovsky, and P. J. Chirik, *J. Am. Chem. Soc.*, 2006, **128**, 13340–13341.

[165] A. L. Smith, K. I. Hardcastle, and J. D. Soper, *J. Am. Chem. Soc.*, 2010, **132**, 14358–14360.

[166] P. J. Chirik and K. Wieghardt, *Science*, 2010, **327**, 794–795.

[167] W. I. Dzik, X. P. Zhang, and B. de Bruin, *Inorg. Chem.*, 2011, **50**, 9896–9903.

[168] W. I. Dzik, X. Xu, X. P. Zhang, J. N. H. Reek, and B. de Bruin, *J. Am. Chem. Soc.*, 2010, **132**, 10891–10902.

[169] O. Sato, J. Tao, and Y.-Z. Zhang, *Angew. Chem. Int. Ed.*, 2007, **46**, 2152–2187.

[170] E. C. Constable, *Adv. Inorg. Chem.*, 1989, **34**, 1–63.

[171] C. Creutz, *Comments Inorg. Chem.*, 1982, **1**, 293–311.

[172] Y. Saito, J. Takemoto, B. Hutchinson, and K. Nakamoto, *Inorg. Chem.*, 1972, **11**, 2003–2011.

[173] H. Kawashima, T. Kato, and T. Shida, *J. Raman Spectrosc.*, 1991, **22**, 187–190.

[174] M. Castellà-Ventura, E. Kassab, G. Buntinx, and O. Poizat, *Phys. Chem. Chem. Phys.*, 2000, **2**, 4682–4689.

[175] G. D. Danzer, J. A. Golus, D. P. Strommen, and J. R. Kincaid, *J. Raman Spectrosc.*, 1990, **21**, 3–8.

[176] P. G. Bradley, N. Kress, B. A. Homberger, R. F. Dallinger, and W. H. Woodruff, *J. Am. Chem. Soc.*, 1981, **103**, 7441–7446.

[177] E. König and S. Herzog, *J. Inorg. Nucl. Chem.*, 1970, **32**, 585–599.

[178] E. König and S. Kremer, *Chem. Phys. Lett.*, 1970, **5**, 87–90.

[179] C. Mahon and W. L. Reynolds, *Inorg. Chem.*, 1967, **6**, 1927–1928.

[180] A. Zahlan, F. W. Heineken, M. Bruin, and F. Bruin, *J. Chem. Phys.*, 1962, **37**, 683–684.

[181] J. Dos Santos Veiga, W. L. Reynolds, and J. R. Bolton, *J. Chem. Phys.*, 1966, **44**, 2214–2216.

[182] J. C. M. Henning, *J. Chem. Phys.*, 1966, **44**, 2139–2155.

[183] J. D. W. van Voorst, W. G. Zijlstra, and R. Sitters, *Chem. Phys. Lett.*, 1967, **1**, 321–322.

[184] E. König and H. Fischer, *Z. Naturforsch.*, 1962, **37**, 1063–1066.

[185] W. Kaim, *Chem. Ber.*, 1981, **114**, 3789–3800.

[186] E. Gore-Randall, M. Irwin, M. S. Denning, and J. M. Goicoechea, *Inorg. Chem.*, 2009, **48**, 8304–8316.

[187] L. Echegoyen, A. DeCian, J. Fischer, and J.-M. Lehn, *Angew. Chem. Int. Ed.*, 1991, **30**, 838–840.

[188] P. L. Bellavance, E. R. Corey, J. Y. Corey, and G. W. Hey, *Inorg. Chem.*, 1977, **16**, 462–467.

[189] G. B. Nikiforov, H. W. Roesky, M. Noltemeyer, and H.-G. Schmidt, *Polyhedron*, 2004, **23**, 561–566.

[190] W. J. Evans, S. L. Gonzales, and J. W. Ziller, *J. Am. Chem. Soc.*, 1994, **116**, 2600–2608.

[191] W. J. Evans and D. K. Drummond, *J. Am. Chem. Soc.*, 1989, **111**, 3329–3335.

[192] M. Schultz, J. M. Boncella, D. J. Berg, T. D. Tilley, and R. A. Andersen, *Organometallics*, 2002, **21**, 460–472.

[193] C. H. Booth, M. D. Walter, D. Kazhdan, Y.-J. Hu, W. W. Lukens, E. D. Bauer, L. Maron, O. Eisenstein, and R. A. Andersen, *J. Am. Chem. Soc.*, 2009, **131**, 6480–6491.

[194] S. J. Kraft, P. E. Fanwick, and S. C. Bart, *Inorg. Chem.*, 2010, **49**, 1103–1110.

[195] S. R. Batten, K. S. Murray, and N. J. Sinclair, *Acta Cryst. C*, 2000, **56**, E320.

[196] M. Biner, H.-B. Bürgi, A. Ludi, and C. Röhr, *J. Am. Chem. Soc.*, 1992, **114**, 5197–5203.

[197] E. C. Constable, P. R. Raithby, and D. N. Smit, *Polyhedron*, 1989, **36**, 367–369.

[198] A. Mootz McPherson, B. F. Fieselmann, D. L. Lichtenberger, G. L. McPherson, and G. D. Stucky, *J. Am. Chem. Soc.*, 1979, **101**, 3425–3430.

[199] L. J. Radonovich, M. W. Eyring, T. J. Croshens, and K. J. Klabunde, *J. Am. Chem. Soc.*, 1982, **104**, 2816–2819.

[200] E. E. Pérez-Cordero, C. Campana, and L. Echegoyen, *Angew. Chem. Int. Ed.*, 1997, **36**, 137–140.

[201] P. Rosa, N. Mézailles, L. Ricard, F. Mathey, and P. Le Floch, *Angew. Chem. Int. Ed.*, 2000, **39**, 1823–1826.

[202] B. V. Mork, A. McMillan, H. Yuen, and T. D. Tilley, *Organometallics*, 2004, **23**, 2855–2859.

[203] C. P. Lenges, P. S. White, W. J. Marshall, and M. Brookhart, *Organometallics*, 2000, **19**, 1247–1254.

[204] D. Roitershtein, Â. Domingos, L. C. J. Pereira, J. R. Ascenso, and N. Marques, *Inorg. Chem.*, 2003, **42**, 7666–7673.

[205] C. C. Scarborough and K. Wieghardt, *Inorg. Chem.*, 2011, **50**, 9773–9793.

[206] A. Schäfer, C. Huber, and R. Ahlrichs, *J. Chem. Phys.*, 1994, **100**, 5829–5835.

[207] A. Schäfer, H. Horn, and R. Ahlrichs, *J. Chem. Phys.*, 1992, **97**, 2571–2577.

[208] A. Klamt, *J. Phys. Chem.*, 1995, **99**, 2224–2235.

[209] F. Neese, *Inorg. Chim. Acta*, 2002, **337**, 181–192.

[210] R. Ditchfield, *Mol. Phys.*, 1974, **27**, 789–807.

[211] K. Wolinski, J. F. Hinton, and P. Pulay, *J. Am. Chem. Soc.*, 1990, **112**, 8251–8260.

[212] F. Jensen, *J. Chem. Theory Comput.*, 2008, **4**, 719–727.

[213] P. von Ragué Schleyer, C. Maerker, A. Dransfeld, H. Jiao, and N. J. R. van Eikema Hommes, *J. Am. Chem. Soc.*, 1996, **118**, 6317–6318.

[214] H. Jiao and P. von Ragué Schleyer, *J. Phys. Org. Chem.*, 1998, **11**, 655–662.

[215] M. S. Henry and M. Z. Hoffman, *J. Phys. Chem.*, 1979, **83**, 618–625.

[216] F. Labat, P. P. Lainé, I. Ciofini, and C. Adamo, *Chem. Phys. Lett.*, 2006, **417**, 445–451.

[217] C. Blanchet-Boiteux, P. Friant-Michel, A. Marsura, J.-B. Regnouf-de-Vains, and M. F. Ruiz-López, *J. Mol. Struct.: THEOCHEM*, 2007, **811**, 169–174.

[218] M. S. Denning, M. Irwin, and J. M. Goicoechea, *Inorg. Chem.*, 2008, **47**, 6118–6120.

[219] B. N. Williams, W. Huang, K. L. Miller, and P. L. Diaconescu, *Inorg. Chem.*, 2010, **49**, 11493–11498.

[220] E. Ruiz, J. Cirera, and S. Alvarez, *Coord. Chem. Rev.*, 2005, **249**, 2649–2660.

[221] A. T. Amos and G. G. Hall, *Proc. R. Soc. Lond. A*, 1961, **263**, 483–493.

[222] H. F. King, R. E. Stanton, H. Kim, R. E. Wyatt, and R. G. Parr, *J. Chem. Phys.*, 1967, **47**, 1936–1941.

[223] F. Neese, *J. Phys. Chem. Solids*, 2004, **65**, 781–785.

[224] S. C. Bart, K. Chłopek, E. Bill, M. W. Bouwkamp, E. Lobkovsky, F. Neese, K. Wieghardt, and P. J. Chirik, *J. Am. Chem. Soc.*, 2006, **128**, 13901–13912.

[225] A. M. Tondreau, C. Milsmann, A. D. Patrick, H. M. Hoyt, E. Lobkovsky, K. Wieghardt, and P. J. Chirik, *J. Am. Chem. Soc.*, 2010, **132**, 15046–15059.

[226] D. Dai and M.-H. Whangbo, *J. Chem. Phys.*, 2003, **118**, 29–39.

[227] D. Dai and M.-H. Whangbo, *J. Chem. Phys.*, 2001, **114**, 2887–2893.

[228] T. Soda, Y. Kitagawa, T. Onishi, Y. Takano, Y. Shigeta, H. Nagao, Y. Yoshioka, and K. Yamaguchi, *Chem. Phys. Lett.*, 2000, **319**, 223–230.

[229] J. C. Slater, *Quantum Theory of Atomic Structure*, McGraw-Hill, New York, 1960.

[230] N. Muresan, C. C. Lu, M. Ghosh, J. C. Peters, M. Abe, L. M. Henling, T. Weyhermüller, E. Bill, and K. Wieghardt, *Inorg. Chem.*, 2008, **47**, 4579–4590.

[231] M. D. Dyar, D. G. Agresti, M. W. Schaefer, C. A. Grant, and E. C. Sklute, *Annu. Rev. Earth Planet. Sci.*, 2006, **34**, 83–125.

[232] E. I. Solomon and A. B. P. Lever (ed.), *Inorganic Electronic Structure and Spectroscopy, Volume I: Methodology*, John Wiley & Sons, Hoboken, 2006.

[233] T. C. Gibb, *Principles of Mössbauer Spectroscopy*, Chapman & Hall, London, 1976.

[234] N. N. Greenwood and T. C. Gibb, *Mössbauer Spectroscopy*, Chapman & Hall, London, 1971.

[235] T. E. Cranshaw, B. W. Dale, G. O. Longworth, and C. E. Johnson, *Mössbauer Spectroscopy and its Applications*, Cambridge University Press, Cambridge, 1985.

[236] F. Neese, *Curr. Opin. Chem. Biol.*, 2003, **7**, 125–135.

[237] F. Neese, *Coord. Chem. Rev.*, 2009, **253**, 526–563.

[238] M. Filatov, *Coord. Chem. Rev.*, 2009, **253**, 594–605.

[239] S. Sinnecker, L. D. Slep, E. Bill, and F. Neese, *Inorg. Chem.*, 2005, **44**, 2245–2254.

[240] M. Römelt, S. Ye, and F. Neese, *Inorg. Chem.*, 2009, **48**, 784–785.

[241] G. M. Sandala, K. H. Hopmann, A. Ghosh, and L. Noodleman, *J. Chem. Theory Comput.*, 2011, **7**, 3232–3247.

[242] V. Vrajmasu, E. Münck, and E. L. Bominaar, *Inorg. Chem.*, 2003, **42**, 5974–5988.

[243] E. J. Hawrelak, W. H. Bernskoetter, E. Lobkovsky, G. T. Yee, E. Bill, and P. J. Chirik, *Inorg. Chem.*, 2005, **44**, 3103–3111.

[244] C. P. Magill, C. Floriani, A. Chiesi-Villa, and C. Rizzoli, *Inorg. Chem.*, 1994, **33**, 1928–1933.

[245] A. Klose, E. Solari, C. Floriani, A. Chiesi-Villa, C. Rizzoli, and N. Rea, *J. Am. Chem. Soc.*, 1994, **116**, 9123–9135.

[246] P. L. Holland, *Acc. Chem. Res.*, 2008, **41**, 905–914.

[247] M. Ghosh, S. Sproules, T. Weyhermüller, and K. Wieghardt, *Inorg. Chem.*, 2008, **47**, 5963–5970.

[248] A. R. Hermes, R. J. Morris, and G. S. Girolami, *Organometallics*, 1988, **7**, 2372–2379.

[249] J. J. H. Edema, S. Gambarotta, F. van Bolhuis, W. J. J. Smeets, A. L. Spek, and M. Y. Chiang, *J. Organomet. Chem.*, 1990, **389**, 47–59.

[250] J. C. Brewer, T. J. Collins, M. R. Smith, and B. D. Santarsiero, *J. Am. Chem. Soc.*, 1988, **110**, 423–428.

[251] J. Chatt and B. L. Shaw, *J. Chem. Soc.*, 1961, 258–290.

[252] M. Cibian, S. Derossi, and G. S. Hanan, *Dalton Trans.*, 2011, **40**, 1038–1040.

[253] D. Herebian, E. Bothe, F. Neese, T. Weyhermüller, and K. Wieghardt, *J. Am. Chem. Soc.*, 2003, **125**, 9116–9128.

[254] I. L. Fedushkin, T. V. Petrovskaya, F. Girgsdies, R. D. Köhn, M. N. Bochkarev, and H. Schumann, *Angew. Chem. Int. Ed.*, 1999, **38**, 2262–2264.

[255] M. Irwin, R. K. Jenkins, M. S. Denning, T. Krämer, F. Grandjean, G. J. Long, R. Herchel, J. E. McGrady, and J. M. Goicoechea, *Inorg. Chem.*, 2010, **49**, 6160–6171.

[256] M. Irwin, T. Krämer, J. E. McGrady, and J. M. Goicoechea, *Inorg. Chem.*, 2011, **50**, 5006–5014.

[257] B. Sarkar, S. Patra, J. Fiedler, R. B. Sunoj, D. Janardanan, S. M. Mobin, M. Niemeyer, G. K. Lahiri, and W. Kaim, *Angew. Chem. Int. Ed.*, 2005, **44**, 5655–5658.

[258] J. L. Sadler and A. J. Bard, *J. Am. Chem. Soc.*, 1968, **90**, 1979–1989.

[259] S. Goswami, R. Mukherjee, and A. Chakravorty, *Inorg. Chem.*, 1983, **22**, 2825–2832.

[260] M. Shivakumar, K. Pramanik, P. Ghosh, and A. Chakravorty, *Inorg. Chem.*, 1998, **37**, 5968–5969.

[261] M. Shivakumar, K. Pramanik, P. Ghosh, and A. Chakravorty, *J. Chem. Soc., Dalton Trans.*, 1998, 2103–2104.

[262] N. Doslik, T. Sixt, and W. Kaim, *Angew. Chem. Int. Ed.*, 1998, **37**, 2403–2404.

[263] M. N. Ackermann, J. W. Naylor, E. J. Smith, G. A. Mines, N. S. Amin, and M. L. Kerns, *Organometallics*, 1992, **11**, 1919–1926.

[264] B. Sarkar, S. Patra, J. Fiedler, R. B. Sunoj, D. Janardanan, G. K. Lahiri, and W. Kaim, *J. Am. Chem. Soc.*, 2008, **130**, 3532–3542.

[265] S. Blanchard, F. Neese, E. Bothe, E. Bill, T. Weyhermüller, and K. Wieghardt, *Inorg. Chem.*, 2005, **44**, 3636–3656.

[266] S. Ye, B. Sarkar, F. Lissner, T. Schleid, J. van Slageren, J. Fiedler, and W. Kaim, *Angew. Chem. Int. Ed.*, 2005, **44**, 2103–2106.

[267] N. Paul, S. Samanta, and S. Goswami, *Inorg. Chem.*, 2010, **49**, 2649–2655.

[268] A. Sanyal, S. Chatterjee, A. Castiñeiras, B. Sarkar, P. Singh, J. Fiedler, S. Záliš, W. Kaim, and S. Goswami, *Inorg. Chem.*, 2007, **46**, 8584–8593.

[269] A. Sanyal, P. Banerjee, G.-H. Lee, S.-M. Peng, C.-H. Hung, and S. Goswami, *Inorg. Chem.*, 2004, **43**, 7456–7462.

[270] S. Samanta, P. Singh, J. Fiedler, S. Záliš, W. Kaim, and S. Goswami, *Inorg. Chem.*, 2008, **47**, 1625–1633.

[271] K. Pramanik, M. Shivakumar, P. Ghosh, and A. Chakravorty, *Inorg. Chem.*, 2000, **39**, 195–199.

[272] B. Sarkar, S. Konar, C. J. Gómez-García, and A. Ghosh, *Inorg. Chem.*, 2008, **47**, 11611–11619.

[273] D. Das, T. K. Mondal, S. M. Mobin, and G. K. Lahiri, *Inorg. Chem.*, 2009, **48**, 9800–9810.

[274] M. N. Ackermann, C. R. Barton, C. J. Deodene, E. M. Specht, S. C. Keill, W. E. Schreiber, and H. Kim, *Inorg. Chem.*, 1989, **28**, 397–403.

[275] M. N. Ackermann, S. R. Kiihne, P. A. Saunders, C. E. Barnes, S. C. Stallings, H. Kim, C. Woods, and M. Lagunoff, *Inorg. Chim. Acta*, 2002, **334**, 193–203.

[276] A. F. Heyduk and D. G. Nocera, *Science*, 2001, **293**, 1639–1641.

[277] J. Rosenthal, J. Bachman, J. L. Dempsey, A. J. Esswein, T. G. Gray, J. M. Hodgkiss, D. R. Manke, T. D. Luckett, B. J. Pistorio, A. S. Veige, and D. G. Nocera, *Coord. Chem. Rev.*, 2005, **249**, 1316–1326.

[278] J. Rosenthal and D. G. Nocera, *Acc. Chem. Res.*, 2007, **40**, 543–553.

[279] A. J. Esswein and D. G. Nocera, *Chem. Rev.*, 2007, **107**, 4022–4047.

[280] C. Tejel, M. A. Ciriano, M. P. del Río, F. J. van den Bruele, D. G. H. Hetterscheid, N. Tsichlis i Spithas, and B. de Bruin, *J. Am. Chem. Soc.*, 2008, **130**, 5844–5845.

[281] C. Tejel, M. P. del Río, L. Asensio, F. J. van den Bruele, M. A. Ciriano, N. Tsichlis i Spithas, D. G. H. Hetterscheid, and B. de Bruin, *Inorg. Chem.*, 2011, **50**, 7524–7534.

[282] C. Tejel, L. Asensio, M. P. del Río, B. de Bruin, J. A. López, and M. A. Ciriano, *Angew. Chem. Int. Ed.*, 2011, **50**, 8839–8843.

[283] F. Weigend and R. Ahlrichs, *Phys. Chem. Chem. Phys.*, 2005, **7**, 3297–3305.

[284] K. L. Schuchardt, B. T. Didier, T. Elsethagen, L. Sun, V. Gurumoorthi, J. Chase, J. Li, and T. L. Windus, *J. Chem. Inf. Model.*, 2007, **47**, 1045–1052.

[285] D. Feller, *J. Comp. Chem.*, 1996, **17**, 1571–1586.

[286] N. Godbout, D. R. Salahub, J. Andzelm, and E. Wimmer, *Can. J. Chem.*, 1992, **70**, 560–571.

[287] C. Sosa, J. Andzelm, B. C. Elkin, E. Wimmer, K. D. Dobbs, and D. A. Dixon, *J. Phys. Chem.*, 1992, **96**, 6630–6636.

[288] R. R. Kapre, E. Bothe, T. Weyhermüller, S. DeBeer George, N. Muresan, and K. Wieghardt, *Inorg. Chem.*, 2007, **46**, 7827–7839.

[289] G. H. Spikes, S. Sproules, E. Bill, T. Weyhermüller, and K. Wieghardt, *Inorg. Chem.*, 2008, **47**, 10935–10944.

[290] P. Banerjee, S. Sproules, T. Weyhermüller, S. DeBeer George, and K. Wieghardt, *Inorg. Chem.*, 2009, **48**, 5929–5847.

[291] D. Herebian, K. E. Wieghardt, and F. Neese, *J. Am. Chem. Soc.*, 2003, **125**, 10997–11005.

[292] M. M. Khusniyarov, T. Weyhermüller, E. Bill, and K. Wieghardt, *J. Am. Chem. Soc.*, 2009, **131**, 1208–1221.

[293] F. Neese, *J. Biol. Inorg. Chem.*, 2006, **11**, 702–711.

[294] H.-C. Chang, H. Miyasaka, and S. Kitagawa, *Inorg. Chem.*, 2001, **40**, 146–156.

[295] C. Milsmann, A. Levina, H. H. Harris, G. J. Foran, P. Turner, and P. A. Lay, *Inorg. Chem.*, 2006, **45**, 4743–4754.

[296] E. Ruiz, *Struct. Bond.*, 2004, **113**, 71–102.

[297] P. Maire, A. Sreekanth, T. Büttner, J. Harmer, I. Gromov, H. Rüegger, F. Breher, A. Schweiger, and H. Grützmacher, *Angew. Chem. Int. Ed.*, 2006, **45**, 3265–3269.

[298] K. B. Wiberg, *Tetrahedron*, 1968, **24**, 1083–1096.

[299] R. F. W. Bader and H. Essén, *J. Chem. Phys.*, 1984, **80**, 1943–1960.

[300] D. Cremer and E. Kraka, *Angew. Chem. Int. Ed.*, 1984, **23**, 627–628.

[301] D. Cremer and E. Kraka, *Croat. Chem. Acta*, 1984, **57**, 1265–1287.

[302] D. Cremer and E. Kraka, *J. Am. Chem. Soc.*, 1985, **107**, 3800–3810.

[303] P. Macchi, D. M. Proserpio, and A. Sironi, *J. Am. Chem. Soc.*, 1998, **120**, 13429–13435.

[304] H. A. Sparkes, S. K. Brayshaw, A. S. Weller, and J. A. K. Howarda, *Acta Cryst. B*, 2008, **64**, 550–557.

[305] H. A. Sparkes, T. Krämer, S. K. Brayshaw, J. C. Green, A. S. Weller, and J. A. K. Howard, *Dalton Trans.*, 2011, **40**, 10708–10718.

[306] A. Reisinger, N. Trapp, I. Krossing, S. Altmannshofer, M. P. Verena Herz, and W. Scherer, *Angew. Chem. Int. Ed.*, 2007, **46**, 8295–8298.

[307] A. Krapp and G. Frenking, *Angew. Chem. Int. Ed.*, 2008, **47**, 7796–7797.

[308] D. Himmel, N. Trapp, I. Krossing, S. Altmannshofer, V. Herz, G. Eickerling, and W. Scherer, *Angew. Chem. Int. Ed.*, 2008, **47**, 7798–7801.

[309] P. Macchi, D. M. Proserpio, and A. Sironi, *J. Am. Chem. Soc.*, 1998, **120**, 1447–1455.

[310] W. Scherer, G. Eickerling, D. Shorokhov, E. Gullo, G. S. McGrady, and P. Sirsch, *New J. Chem.*, 2006, **30**, 309–312.

[311] G. Frenking and U. Pidun, *J. Chem. Soc., Dalton Trans.*, 1997, 1653–1662.

[312] U. Pidun and G. Frenking, *Organometallics*, 1995, **14**, 5325–5336.

[313] J. S. Dewar, *Bull. Soc. Chim. Fr.*, 1951, **18**, C71–79.

[314] J. Chatt and L. A. Duncanson, *J. Chem. Soc.*, 1953, 2939–2947.

[315] B. de Bruin, J. C. Russcher, and H. Grützmacher, *J. Organomet. Chem.*, 2007, **692**, 3167–3173.

[316] N. D. Paul, T. Krämer, J. E. McGrady, and S. Goswami, *Chem. Commun.*, 2010, **46**, 7124–7126.

[317] S. Joy, T. Krämer, N. D. Paul, P. Banerjee, J. E. McGrady, and S. Goswami, *Inorg. Chem.*, 2011, **50**, 9993–10004.

[318] A. C. Joannis, *R. Hebd. Seances Acad. Sci.*, 1891, **113**, 795–798.

[319] A. C. Joannis, *R. Hebd. Seances Acad. Sci.*, 1892, **113**, 587.

[320] A. C. Joannis, *Ann. Chim. Phys.*, 1906, **7**, 75–84.

[321] C. A. Kraus, *J. Am. Chem. Soc.*, 1908, **29**, 1556–1571.

[322] F. H. Smyth, *J. Am. Chem. Soc.*, 1917, **39**, 1299–1312.

[323] E. B. Peck, *J. Am. Chem. Soc.*, 1918, **40**, 335–347.

[324] C. A. Kraus, *J. Am. Chem. Soc.*, 1922, **44**, 1216–1239.

[325] E. Zintl, J. Goubeau, and W. Dullenkopf, *Z. Phys. Chem, Abt. A*, 1931, **154**, 1–46.

[326] E. Zintl and A. Harder, *Z. Phys. Chem, Abt. A*, 1931, **154**, 47–91.

[327] E. Zintl and W. Dullenkopf, *Z. Phys. Chem, Abt. B*, 1932, **16**, 183–194.

[328] E. Zintl and H. Kaiser, *Z. Allg. Anorg. Chem.*, 1933, **211**, 113–131.

[329] E. Zintl, A. Harder, and S. Neumayr, *Z. Phys. Chem, Abt. A*, 1931, **154**, 92–96.

[330] S. Scharfe, F. Kraus, S. Stegmaier, A. Schier, and T. F. Fässler, *Angew. Chem. Int. Ed.*, 2011, **50**, 3630–3670.

[331] S. C. Sevov and J. M. Goicoechea, *Organometallics*, 2006, **25**, 5678–5692.

[332] J. D. Corbett, *Angew. Chem. Int. Ed.*, 2000, **39**, 670–690.

[333] T. F. Fässler and S. D. Hoffmann, *Angew. Chem. Int. Ed.*, 2004, **43**, 6242–6247.

[334] T. F. Fässler, *Coord. Chem. Rev.*, 2001, **215**, 347–377.

[335] J. D. Corbett, *Chem. Rev.*, 1985, **85**, 383–397.

[336] J. D. Corbett, D. G. Adolphson, D. J. Merryman, P. A. Edwards, and F. J. Armatis, *J. Am. Chem. Soc.*, 1975, **97**, 6267–6268.

[337] J. D. Corbett, *Struct. Bond.*, 1997, **87**, 157–193.

[338] K. Wade, *J. Chem. Soc. D, Chem. Commun.*, 1971, 792–793.

[339] K. Wade, *Adv. Inorg. Chem. Radiochem.*, 1976, **18**, 1–66.

[340] D. M. P. Mingos, *Acc. Chem. Res.*, 1984, **17**, 311–319.

[341] D. M. P. Mingos and R. L. Johnston, *Struct. Bond.*, 1987, **68**, 29–87.

[342] T. A. Albright, J. K. Burdett, and M.-H. Whangbo, *Orbital Interactions in Chemistry*, John Wiley & Sons, New York, 1985.

[343] D. M. P. Mingos, *Essential Trends in Inorganic Chemistry*, Oxford University Press, Oxford, 1998.

[344] R. B. King and I. Silaghi-Dumitrescu, *Dalton Trans.*, 2008, 6083–6088.

[345] R. B. King, *Struct. Bond.*, 2011, **140**, 1–24.

[346] E. Janssens, S. Neukermans, and P. Lievens, *Curr. Opin. Solid St. M.*, 2004, **8**, 185–193.

[347] D. M. P. Mingos and D. J. Wales, *Introduction to Cluster Chemistry*, Prentice Hall, Englewood Cliffs, 1990.

[348] A. Spiekermann, S. D. Hoffmann, and T. F. Fässler, *Angew. Chem. Int. Ed.*, 2006, **45**, 3459–3462.

[349] D. Rios and S. C. Sevov, *Inorg. Chem.*, 2010, **49**, 6396–6398.

[350] L.-F. Cui, X. Huang, L.-M. Wang, J. Li, and L.-S. Wang, *J. Phys. Chem. A*, 2006, **110**, 10169–10172.

[351] L.-F. Cui, X. Huang, L.-M. Wang, D. Y. Zubarev, A. I. Boldyrev, J. Li, and L.-S. Wang, *J. Am. Chem. Soc.*, 2006, **128**, 8390–8391.

[352] V. Queneau and S. C. Sevov, *Inorg. Chem.*, 1998, **37**, 1358–1360.

[353] E. Todorov and S. C. Sevov, *Inorg. Chem.*, 1998, **37**, 3889–3891.

[354] C. Hoch, M. Wendorff, and C. Rohr, *Acta Cryst. C*, 2002, **58**, I45–I46.

[355] C. Hoch, M. Wendorff, and C. Rohr, *J. Alloys Compd.*, 2003, **361**, 206–221.

[356] S. Ponou and T. F. Fässler, *Z. Allg. Anorg. Chem.*, 2007, **633**, 393–397.

[357] S. Joseph, C. Suchentrunk, F. Kraus, and N. Korber, *Eur. J. Inorg. Chem.*, 2009, 4641-4647.

[358] T. F. Fässler and R. Hoffmann, *J. Chem. Soc., Dalton Trans.*, 1999, 3339–3340.

[359] T. F. Fässler and R. Hoffmann, *Angew. Chem. Int. Ed.*, 1999, **38**, 543–546.

[360] J. D. Corbett and P. A. Edwards, *J. Am. Chem. Soc.*, 1977, **99**, 3313–3317.

[361] J. M. Goicoechea and S. C. Sevov, *J. Am. Chem. Soc.*, 2004, **126**, 6860–6861.

[362] T. F. Fässler, M. Hunziker, M. E. Spahr, H. Lueken, and H. Schilder, *Z. Allg. Anorg. Chem.*, 2000, **626**, 692–700.

[363] J. M. Goicoechea and S. C. Sevov, *Inorg. Chem.*, 2005, **44**, 2654–2658.

[364] J. Åkerstedt, S. Ponou, L. Kloo, and S. Lidin, *Eur. J. Inorg. Chem.*, 2011, 3999–4005.

[365] J. U. Reveles, P. A. Clayborne, A. C. Reber, S. N. Khanna, K. Pradhan, P. Sen, and M. R. Pederson, *Nat. Chem.*, 2009, **1**, 310–315.

[366] A. W. Castleman Jr., *J. Phys. Chem. Lett.*, 2011, **2**, 1062–1069.

[367] E. N. Esenturk, J. Fettinger, Y.-F. Lam, and B. Eichhorn, *Angew. Chem. Int. Ed.*, 2004, **43**, 2132–2134.

[368] E. N. Esenturk, J. Fettinger, and B. Eichhorn, *J. Am. Chem. Soc.*, 2006, **128**, 9178–9186.

[369] J.-Q. Wang, S. Stegmaier, B. Wahl, and T. F. Fässler, *Chem. Eur. J.*, 2010, **16**, 1793–1798.

[370] J. M. Goicoechea and S. C. Sevov, *J. Am. Chem. Soc.*, 2006, **128**, 4155–4161.

[371] J. M. Goicoechea and S. C. Sevov, *Angew. Chem. Int. Ed.*, 2005, **44**, 4026–4028.

[372] S. Scharfe, T. F. Fässler, S. Stegmaier, S. D. Hoffmann, and K. Ruhland, *Chem. Eur. J.*, 2008, **14**, 4479–4483.

[373] E. N. Esenturk, J. Fettinger, and B. Eichhorn, *Chem. Commun.*, 2005, 247–249.

[374] J. M. Goicoechea and S. C. Sevov, *J. Am. Chem. Soc.*, 2005, **127**, 7676–7677.

[375] Z.-M. Sun, H. Xiao, J. Li, and L.-S. Wang, *J. Am. Chem. Soc.*, 2007, **127**, 9560–9561.

[376] F. S. Kocak, P. Zavalij, Y.-F. Lam, and B. W. Eichhorn, *Inorg. Chem.*, 2008, **47**, 3515–3520.

[377] E. N. Esenturk, J. C. Fettinger, and B. W. Eichhorn, *J. Am. Chem. Soc.*, 2006, **128**, 12–13.

[378] B. Kesanli, J. E. Halsig, P. Zavalij, J. C. Fettinger, Y.-F. Lam, and B. W. Eichhorn, *J. Am. Chem. Soc.*, 2007, **129**, 4567–4574.

[379] L.-F. Cui, X. Huang, L.-M. Wang, J. Li, and L.-S. Wang, *Angew. Chem. Int. Ed.*, 2007, **46**, 742–745.

[380] R. B. King, *Dalton Trans.*, 2004, 3420–3424.

[381] J.-Q. Wang, S. Stegmaier, and T. F. Fässler, *Angew. Chem. Int. Ed.*, 2009, **48**, 1998–2002.

[382] B. Zhou, M. S. Denning, T. A. D. Chapman, J. E. McGrady, and J. M. Goicoechea, *Chem. Commun.*, 2009, 7221–7223.

[383] L. R. MacGillivray, in *Encyclopedia of Supramolecular Chemistry*, ed. J. L. Atwood and J. W. Steed, Dekker, New York, 2004, 1100–1105.

[384] M. Ruck, V. Dubenskyy, and T. Söhnel, *Angew. Chem.*, 2003, **115**, 3086–3090.

[385] L. R. Sita and I. Kinoshita, *J. Am. Chem. Soc.*, 1991, **113**, 1856–1857.

[386] H. Hiura, T. Miyazaki, and T. Kanayama, *Phys. Rev. Lett.*, 2001, **86**, 1733–1736.

[387] J. Lu and S. Nagase, *Phys. Rev. Lett.*, 2003, **90**, 115506.

[388] F. Hagelberg, C. Xiao, and W. A. Lester Jr., *Phys. Rev. B*, 2003, **67**, 35426.

[389] P. Sen and L. Mitas, *Phys. Rev. B*, 2003, **68**, 155404.

[390] Q. Sun, Q. Wang, T. M. Briere, V. Kumar, P. Jena, and Y. Kawazoe, *Phys. Rev. B*, 2002, **65**, 235417.

[391] V. Kumar and Y. Kawazoe, *Appl. Phys. Lett.*, 2003, **83**, 2677–2679.

[392] V. Kumar, A. K. Singh, and Y. Kawazoe, *Nano Lett.*, 2004, **4**, 677–681.

[393] R. B. King, I. Silaghi-Dumitrescu, and M.-M. Uţă, *Chem. Eur. J.*, 2008, **14**, 4542–4550.

[394] R. B. King, I. Silaghi-Dumitrescu, and M. M. Uţă, *J. Phys. Chem. A*, 2009, **113**, 527–533.

[395] V. Kumar and Y. Kawazoe, *Appl. Phys. Lett.*, 2002, **80**, 859–861.

[396] J. Lu and S. Nagase, *Chem. Phys. Lett.*, 2003, **372**, 394–398.

[397] S. Neukermans, E. Janssens, Z. F. Chen, R. E. Silverans, P. von Ragué Schleyer, and P. Lievens, *Phys. Rev. Lett.*, 2004, **92**, 163401.

[398] D.-L. Chen, W. Q. Tian, W.-C. Lu, and C.-C. Sun, *J. Chem. Phys.*, 2006, **124**, 154313.

[399] C. Rajesh and C. Majumder, *Chem. Phys. Lett.*, 2006, **430**, 101–107.

[400] C. Rajesh and C. Majumder, *J. Chem. Phys.*, 2008, **128**, 24308.

[401] J.-P. Dognon, C. Clavaguéra, and P. Pyykkö, *Angew. Chem. Int. Ed.*, 2007, **46**, 1427–1430.

[402] X. Chen, K. Deng, Y. Liu, C. Tang, Y. Yuan, F. Hu, H. Wu, D. Huang, W. Tan, and X. Wang, *Chem. Phys. Lett.*, 2008, **462**, 275–279.

[403] Z. Chen, C. S. Wannere, C. Corminboeuf, R. Puchta, and P. von Ragué Schleyer, *Chem. Rev.*, 2005, **105**, 3842–3888.

[404] J. Wang, M. P. Schopfer, A. A. N. Sarjeant, and K. D. Karlin, *J. Am. Chem. Soc.*, 2009, **131**, 450–451.

[405] Z. Chen, S. Neukermans, X. Wang, E. Janssens, Z. Zhou, R. E. Silverans, R. B. King, P. von Ragué Schleyer, and P. Lievens, *J. Am. Chem. Soc.*, 2006, **128**, 12829–12834.

[406] R. B. King, I. Silaghi-Dumitrescu, and M. M. Uţă, *Inorg. Chem.*, 2006, **45**, 4974–4981.

[407] A. D. Zdetsis, *J. Chem. Phys.*, 2007, **127**, 14314.

[408] D.-L. Chen, W. Q. Tian, and C.-C. Sun, *Phys. Rev. A*, 2007, **75**, 132011–132018.

[409] R. B. King, I. Silaghi-Dumitrescu, and M. M. Uţă, *J. Chem. Theory Comput.* , 2008, **4**, 209–215.

[410] X. Zhang, G. Li, X. Xing, X. Zhao, Z. Tang, and Z. Gao, *Rapid Commun. Mass Spectrom.*, 2001, **15**, 2399–2403.

[411] C. Schrodt, F. Weigend, and R. Ahlrichs, *Z. Anorg. Allg. Chem.*, 2002, **628**, 2478–2482.

[412] R. B. King, I. Silaghi-Dumitrescu, and M. M. Uţă, *J. Phys. Chem. A*, 2011, **115**, 2847–2852.

[413] X. Zhang, G. Li, and Z. Gao, *Rapid Commun. Mass Spectrom.*, 2001, **15**, 1573–1576.

[414] G. Li, X. Zhang, Z. Tang, and Z. Gao, *Chem. Phys. Lett.*, 2002, **359**, 203–212.

[415] E. van Lenthe, E. J. Baerends, and J. G. Snijders, *J. Chem. Phys.*, 1993, **99**, 4597–4610.

[416] E. van Lenthe, E. J. Baerends, and J. G. Snijders, *J. Chem. Phys.*, 1994, **101**, 9783–9792.

[417] E. van Lenthe, A. Ehlers, and E.-J. Baerends, *J. Chem. Phys.*, 1999, **110**, 8943–8953.

[418] L. Versluis and T. Ziegler, *J. Chem. Phys.*, 1988, **88**, 322–326.

[419] R. B. King, *Inorg. Chem.*, 1988, **27**, 1941–1947.

[420] R. B. King, *J. Comp. Chem.*, 1987, **8**, 341–349.

[421] P. Pelikán and M. Breza, *J. Mol. Struct.: THEOCHEM*, 1985, **124**, 231–237.

[422] A. Sekiguchi, C. Kabuto, and H. Sakurai, *Angew. Chem. Int. Ed.*, 1989, **28**, 55–56.

[423] H. Matsumoto, K. Higuchi, Y. Hoshino, H. Koike, Y. Naoi, and Y. Nagai, *J. Chem. Soc., Chem. Commun.*, 1988, 1083–1084.

[424] L. R. Sita and I. Kinoshita, *Organometallics*, 1990, **9**, 2865–2867.

[425] A. Sekiguchi, T. Yatabe, C. Kabuto, and H. Sakurai, *J. Am. Chem. Soc.*, 1993, **115**, 5853–5854.

[426] N. Wiberg, H.-W. Lerner, H. Nöth, and W. Ponikwar, *Angew. Chem. Int. Ed.*, 1999, **38**, 1103–1105.

[427] A. Sekiguchi, T. Yatabe, H. Kamatani, C. Kabuto, and H. Sakurai, *J. Am. Chem. Soc.*, 1992, **114**, 6260–6262.

[428] H. Matsumoto, K. Higuchi, and M. G. Soichiro Kyushin, *Angew. Chem. Int. Ed.*, 1992, **31**, 1354–1356.

[429] N. Korber, *Angew. Chem. Int. Ed.*, 2009, **48**, 3216–3217.

[430] B. Zhou, T. Krämer, A. L. Thompson, J. E. McGrady, and J. M. Goicoechea, *Inorg. Chem.*, 2011, **50**, 8028–8037.

[431] F. A. Cotton, C. A. Murillo, and R. A. Walton (ed.), *Multiple Bonds Between Metal Atoms*, Springer, New York, 2005.

[432] J. S. Miller and M. Drillon, *Magnetism: From Molecules to Materials*, Wiley VCH, Weinheim, 2001.

[433] J. E. McGrady, T. Lovell, and R. Stranger, *Inorg. Chem.*, 1997, **36**, 3242–3247.

[434] R. Stranger, P. W. Smith, and I. E. Grey, *Inorg. Chem.*, 1989, **28**, 1271–1278.

[435] J. E. McGrady, *Angew. Chem. Int. Ed.*, 2000, **39**, 3077–3079.

[436] U. Kölle, J. Kossakowski, N. Klaff, L. Wesemann, U. Englert, and G. E. Heberich, *Angew. Chem. Int. Ed.*, 1991, **30**, 690–691.

[437] L. H. Gade, *Angew. Chem. Int. Ed.*, 1996, **35**, 2089–2090.

[438] B. R. Whittlesey, *Coord. Chem. Rev.*, 2000, **206**, 395–418.

[439] G. N. Harakas and B. R. Whittlesey, *J. Am. Chem. Soc.*, 1996, **118**, 4210–4211.

[440] G. Fachinetti, G. Fochi, T. Funaioli, and P. F. Zanazzi, *J. Chem. Soc., Chem. Commun.*, 1987, 89–90.

[441] G. Kong, G. N. Harakas, and B. R. Whittlesey, *J. Am. Chem. Soc.*, 1995, **117**, 3502–3509.

[442] Z. Xu and Z. Lin, *Chem. Eur. J.*, 1998, **4**, 28–32.

[443] K. Uehara, S. Hikichi, A. Inagaki, and M. Akita, *Chem. Eur. J.*, 2005, **11**, 2788–2809.

[444] W. Beck, *Angew. Chem. Int. Ed.*, 1991, **30**, 168–169.

[445] R. G. Teller, R. G. Finke, J. P. Collman, H. Chin, and R. Bau, *J. Am. Chem. Soc.*, 1977, **99**, 1104–1111.

[446] G. H. Golub and C. Reinsch, *Numer. Math.*, 1970, **14**, 403–420.

[447] P. Kiehl, M.-M. Rohmer, and M. Bénard, *Inorg. Chem.*, 2004, **43**, 3151–3158.

[448] T. Mochizuki, T. Nogami, and T. Ishida, *Inorg. Chem.*, 2009, **48**, 2254–2259.

[449] N. Fukita, M. Ohba, H. Ōkawa, K. Matsuda, and H. Iwamura, *Inorg. Chem.*, 1998, **37**, 842–848.

[450] O. Kahn, *Molecular Magnetism*, VCH Publishers, New York, 1993.

[451] T. Krämer, Z. Lin, and J. E. McGrady, *Dalton Trans.*, 2011, **40**, 927–932.

[452] W. Kaim and B. Schwederski, *Bioinorganic Chemistry: Inorganic Elements in the Chemistry of Life*, John Wiley & Sons, Chichester, 1994.

[453] W. B. Tolman (ed.), *Activation of Small Molecules*, Wiley-VCH, Weinheim, 2006.

[454] C. Moreno-Vivián and S. J. Ferguson, *Mol. Microbiol.*, 1998, **29**, 661–669.

[455] S. Suzuki, K. Kataoka, and K. Yamaguchi, *Acc. Chem. Res.*, 2000, **33**, 728–735.

[456] P. Tavares, A. Pereira, J. J. G. Moura, and I. Moura, *J. Inorg. Biochem.*, 2006, **100**, 2087–2100.

[457] B. A. Averill, *Chem. Rev.*, 1996, **96**, 2951–2964.

[458] I. S. MacPherson and M. E. P. Murphy, *Cell. Mol. Life Sci.*, 2007, **64**, 2887–2899.

[459] L. B. Maia and J. J. G. Moura, *J. Biol. Inorg. Chem.*, 2011, **16**, 443–460.

[460] D. Nurizzo, F. Cutruzzola, M. Arese, D. Bourgeois, M. Brunori, C. Cambillau, and M. Tegoni, *Biochemistry*, 1998, **37**, 13987–13996.

[461] F. E. Dodd, J. Van Beeumen, R. R. Eady, and S. S. Hasnain, *J. Mol. Biol.*, 1998, **282**, 369–382.

[462] M. E. P. Murphy, S. Turley, M. Kukimoto, M. Nishiyama, S. Horinouchi, H. Sasaki, M. Tanokura, and E. T. Adman, *Biochemistry*, 1995, **34**, 12107–12117.

[463] J. W. Godden, S. Turley, D. C. Teller, E. T. Adman, M. Y. Liu, W. J. Payne, and J. LeGall, *Science*, 1991, **253**, 438–442.

[464] E. T. Adman, J. W. Godden, and S. Turley, *J. Biol. Chem.*, 1995, **270**, 27458–27474.

[465] A. Kaufman Katz, L. Shimoni-Livny, O. Navon, N. Navon, C. W. Bock, and J. P. Glusker, *Helv. Chim. Acta*, 2003, **86**, 1320–1338.

[466] M. Kukimoto, M. Nishiyama, M. E. P. Murphy, S. Turley, S. H. Elinor T. Adman, and T. Beppu, *Biochemistry*, 1994, **33**, 5246–5252.

[467] E. Libby and B. A. Averill, *Biochem. Biophys. Res. Commun.*, 1992, **187**, 1529–1535.

[468] F. E. Dodd, S. S. Hasnain, Z. H. L. Abraham, R. R. Eady, and B. E. Smith, *Acta. Cryst. D*, 1997, **53**, 406–418.

[469] T. Inoue, M. Gotowda, Deligeer, K. Kataoka, K. Yamaguchi, S. Suzuki, H. Watanabe, M. Gohow, and Y. Kai, *J. Biochem.*, 1998, **124**, 876–879.

[470] M. J. Boulanger, M. Kukimoto, M. Nishiyama, S. Horinouchi, and M. E. P. Murphy, *J. Biol. Chem.*, 2000, **275**, 23957–23964.

[471] K. Kataoka, H. Furusawa, K. Takagi, K. Yamaguchi, and S. Suzuki, *J. Biochem.*, 2000, **127**, 345–350.

[472] M. J. Boulanger and M. E. P. Murphy, *Protein Sci.*, 2003, **12**, 248–256.

[473] Y. Zhao, D. A. Lukoyanov, Y. V. Toropov, K. Wu, J. P. Shapleigh, and C. P. Scholes, *Biochemistry*, 2002, **41**, 7464–7474.

[474] E. I. Tocheva, L. D. Eltis, and M. E. P. Murphy, *Biochemistry*, 2008, **47**, 4452–4460.

[475] A. C. Merkle and N. Lehnert, *Inorg. Chem.*, 2009, **48**, 11504–11506.

[476] P. A. Williams, V. Fülöp, E. F. Garman, N. F. W. Saunders, S. J. Ferguson, and J. Hajdu, *Nature*, 1997, **389**, 406–412.

[477] R. W. Ye, I. Toro-Suarez, J. M. Tiedje, and B. A. Averill, *J. Biol. Chem.*, 1991, **266**, 12848–12851.

[478] E. Weeg-Aerssens, J. M. Tiedje, and B. A. Averill, *J. Am. Chem. Soc.*, 1987, **109**, 7214–7215.

[479] M. A. Jackson, J. M. Tiedje, and B. A. Averill, *FEBS Lett.*, 1991, **291**, 41–44.

[480] E. I. Tocheva, F. I. Rosell, A. G. Mauk, and M. E. P. Murphy, *Science*, 2004, **304**, 867–870.

[481] S. V. Antonyuk, R. W. Strange, G. Sawers, R. R. Eady, and S. S. Hasnain, *Proc. Natl. Acad. Sci. USA*, 2005, **102**, 12041–12046.

[482] M. E. P. Murphy, S. Turley, and E. T. Adman, *J. Biol. Chem.*, 1997, **272**, 28455–28460.

[483] A. Veselov, K. Olesen, A. Sienkiewicz, J. P. Shapleigh, and C. P. Scholes, *Biochemistry*, 1998, **37**, 6095–6105.

[484] J. A. McCleverty, *Chem. Rev.*, 2004, **104**, 403–418.

[485] K. Fujisawa, M. Tanaka, Y. Moro-oka, and N. Kitajima, *J. Am. Chem. Soc.*, 1994, **116**, 12079–12080.

[486] N. W. Aboelella, E. A. Lewis, A. M. Reynolds, W. W. Brennessel, C. J. Cramer, and W. B. Tolman, *J. Am. Chem. Soc.*, 2002, **124**, 10660–10661.

[487] P. Chen, D. E. Root, C. Campochiaro, K. Fujisawa, and E. I. Solomon, *J. Am. Chem. Soc.*, 2003, **125**, 466–474.

[488] A. Weichsel, J. F. Andersen, S. A. Roberts, and W. R. Montfort, *Nat. Struct. Biol.*, 2000, **7**, 551–554.

[489] P. Coppens, I. Novozhilova, and A. Kovalevsky, *Chem. Rev.*, 2002, **102**, 861–883.

[490] A. Ghosh and T. Wondimagegn, *J. Am. Chem. Soc.*, 2000, **122**, 8101–8102.

[491] T. Wondimagegn and A. Ghosh, *J. Am. Chem. Soc.*, 2001, **123**, 5680–5683.

[492] C. L. Hulse, J. M. Tiedje, and B. A. Averill, *J. Am. Chem. Soc.*, 1989, **111**, 2322–2323.

[493] J. A. Halfen and W. B. Tolman, *J. Am. Chem. Soc.*, 1994, **116**, 5475–5476.

[494] E. I. Tocheva, F. I. Rosell, A. G. Mauk, and M. E. P. Murphy, *Biochemistry*, 2007, **46**, 12366–12374.

[495] S. Ghosh, A. Dey, O. M. Usov, Y. Sun, V. M. Grigoryants, C. P. Scholes, and E. I. Solomon, *J. Am. Chem. Soc.*, 2007, **129**, 10310–10311.

[496] O. M. Usov, Y. Sun, V. M. Grigoryants, J. P. Shapleigh, and C. P. Scholes, *J. Am. Chem. Soc.*, 2006, **128**, 13102–13111.

[497] K. Fujisawa, A. Tateda, Y. Miyashita, K. Okamoto, F. Paulat, V. K. K. Praneeth, A. Merkle, and N. Lehnert, *J. Am. Chem. Soc.*, 2008, **130**, 1205–1213.

[498] I. H. Wasbotten and A. Ghosh, *J. Am. Chem. Soc.*, 2005, **127**, 15384–15385.

[499] M. Kujime and H. Fujii, *Angew. Chem. Int. Ed.*, 2006, **45**, 1089–1092.

[500] S. A. de Marothy, M. R. A. Blomberg, and P. E. M. Siegbahn, *J. Comput. Chem.*, 2007, **28**, 528–539.

[501] M. Sundararajan, I. H. Hillier, and N. A. Burton, *J. Phys. Chem. B*, 2007, **111**, 5511–5517.

[502] S. Ghosh, A. Dey, Y. Sun, C. P. Scholes, and E. I. Solomon, *J. Am. Chem. Soc.*, 2009, **131**, 277–288.

[503] N. Lehnert, U. Cornelissen, F. Neese, T. Ono, Y. Noguchi, K. Okamoto, and K. Fujisawa, *Inorg. Chem.*, 2007, **46**, 3916–3933.

[504] H. Yokoyama, K. Yamaguchi, M. Sugimoto, and S. Suzuki, *Eur. J. Inorg. Chem.*, 2005, 1435–1441.

[505] M. Scarpellini, A. Neves, E. E. Castellano, E. F. de Almeida Neves, and D. W. Franco, *Polyhedron*, 2004, **23**, 511–518.

[506] M. Beretta, E. Bouwman, L. Casella, B. Douziech, W. L. Driessen, L. Gutierrez-Soto, E. Monzani, and J. Reedijk, *Inorg. Chim. Acta*, 2000, **310**, 41–50.

[507] E. Monzani, G. J. A. A. Koolhaas, A. Spandre, E. Leggieri, L. Casella, M. Gullotti, G. Nardin, L. Randaccio, M. Fontani, P. Zanello, and J. Reedijk, *J. Biol. Inorg. Chem.*, 2000, **5**, 251–261.

[508] L. Casella, O. Carugo, M. Gullotti, S. Doldi, and M. Frassoni, *Inorg. Chem.*, 1996, **35**, 1101–1113.

[509] R. T. Stibrany, J. A. Potenza, and H. J. Schugar, *Inorg. Chim. Acta*, 1996, **243**, 33–37.

[510] C. E. Ruggiero, S. M. Carrier, and W. B. Tolman, *Angew. Chem. Int. Ed.*, 1994, **33**, 895–897.

[511] N. Komeda, H. Nagao, Y. Kushi, G. Adachi, M. Suzuki, A. Uehara, and K. Tanaka, *Bull. Chem. Soc. Jpn.*, 1995, **68**, 581–589.

[512] F. Jiang, R. R. Conry, L. Bubacco, Z. Tyeklár, R. R. Jacobson, K. D. Karlin, and J. Peisach, *J. Am. Chem. Soc.*, 1993, **115**, 2093–2102.

[513] N. Komeda, H. Nagao, G. Adachi, M. Suzuki, A. Uehara, and K. Tanaka, *Chem. Lett.*, 1993, **22**, 1521–1524.

[514] W. B. Tolman, *Inorg. Chem.*, 1991, **30**, 4877–4880.

[515] C.-S. Chen and W.-Y. Yeh, *Chem. Commun.*, 2010, **46**, 3098–3100.

[516] W.-J. Chuang, I.-J. Lin, H.-Y. Chen, Y.-L. Chang, and S. C. N. Hsu, *Inorg. Chem.*, 2010, **49**, 5377–5384.

[517] M. Kujime, C. Izumi, M. Tomura, M. Hada, and H. Fujii, *J. Am. Chem. Soc.*, 2008, **130**, 6088–6098.

[518] A. K. Nairn, S. J. Archibald, R. Bhalla, C. J. Boxwell, A. C. Whitwood, and P. H. Walton, *Dalton Trans.*, 2006, 1790–1795.

[519] A. Burg, E. Lozinsky, H. Cohen, and D. Meyerstein, *Eur. J. Inorg. Chem.*, 2004, 3675–3680.

[520] J. A. Halfen and W. B. Tolman, *Acta Cryst. C*, 1995, **51**, 215–217.

[521] C. E. Ruggiero, S. M. Carrier, W. E. Antholine, J. W. Whittaker, C. J. Cramer, and W. B. Tolman, *J. Am. Chem. Soc.*, 1993, **115**, 11285–11298.

[522] M. Sundararajan, R. Surendran, and I. H. Hillier, *Chem. Phys. Lett.*, 2006, **418**, 96–99.

[523] R. Silaghi-Dumitrescu, *J. Inorg. Biochem.*, 2006, **100**, 396–402.

[524] G. Periyasamy, M. Sundararajan, I. H. Hillier, N. A. Burton, and J. J. W. McDouall, *Phys. Chem. Chem. Phys.*, 2007, **9**, 2498–2506.

[525] A. C. Merkle and N. Lehnert, *Dalton Trans.*, 2011, DOI: 10.1039/c1dt11049g.

[526] I. M. Wasser, S. de Vries, P. Moënne-Loccoz, I. Schröder, and K. D. Karlin, *Chem. Rev.*, 2002, **102**, 1201–1234.

[527] R. L. Richards and M. C. Durrant, *J. Chem. Research (S)*, 2002, 95–98.

[528] R. R. Eady and S. S. Hasnain, in *Comprehensive Coordination Chemistry II, Vol. 8*, ed. J. A. McCleverty and T. J. Meyer, Elsevier Ltd., Oxford, 2004, 759–786.

[529] M. J. Begley, P. Hubberstey, and J. Stroud, *J. Chem. Soc., Dalton Trans.*, 1996, 4295–4301.

[530] J. L. Schneider, S. M. Carrier, C. E. Ruggiero, V. G. Young Jr., and W. B. Tolman, *J. Am. Chem. Soc.*, 1998, **120**, 11408–11418.

[531] S. M. Carrier, C. E. Ruggiero, and W. B. Tolman, *J. Am. Chem. Soc.*, 1992, **114**, 4407–4408.

[532] A. M. Wright, G. Wu, and T. W. Hayton, *J. Am. Chem. Soc.*, 2010, **132**, 14336–14337.

[533] P. P. Paul and K. D. Karlin, *J. Am. Chem. Soc.*, 1991, **113**, 6331–6332.

[534] W. Lee and W. B. Tolman, *Inorg. Chem.*, 2002, **41**, 5656–5658.

[535] B. Greener and P. H. Walton, *J. Chem. Soc., Dalton Trans.*, 1997, 3733–3740.

[536] B. Greener, L. Cronin, G. D. Wilson, and P. H. Walton, *J. Chem. Soc., Dalton Trans.*, 1996, 401–403.

[537] E. Zueva, P. H. Walton, and J. E. McGrady, *Dalton Trans.*, 2006, 159–167.

[538] S. Niu and M. B. Hall, *Chem. Rev.*, 2000, **100**, 353–405.

[539] P. E. M. Siegbahn, *J. Biol. Inorg. Chem.*, 2006, **11**, 695–701.

[540] B. Mennucci and J. Tomasi, *J. Chem. Phys.*, 1997, **106**, 5151–5158.

[541] E. Cancès, B. Mennucci, and J. Tomasi, *J. Chem. Phys.*, 1997, **107**, 3032–3041.

[542] M. Cossi, V. Barone, B. Mennucci, and J. Tomasi, *Chem. Phys. Lett.*, 1998, **286**, 253–260.

[543] M. Cossi, G. Scalmani, N. Rega, and V. Barone, *J. Chem. Phys.*, 2002, **117**, 43–54.

[544] D. A. McQuarrie, *Statistical Mechanics*, University Science Books, Sausalito, 2000.

[545] G. J. Tawa, I. A. Topol, S. K. Burt, R. A. Caldwell, and A. A. Rashin, *J. Chem. Phys.*, 1998, **109**, 4852–4863.

[546] S. Hwang and D. S. Chung, *Bull. Korean Chem. Soc.*, 2005, **26**, 589–593.

[547] A. W. Addison, N. Rao, J. Reedijk, J. van Rijn, and G. C. Verschoor, *J. Chem. Soc., Dalton Trans.*, 1984, 1349–1356.

[548] K. M. Ervin, J. Ho, and W. C. Lineberger, *J. Phys. Chem.*, 1988, **92**, 5405–5412.

[549] D. Maiti, D.-H. Lee, A. A. Narducci Sarjeant, M. Y. M. Pau, E. I. Solomon, K. Gaoutchenova, J. Sundermeyer, and K. D. Karlin, *J. Am. Chem. Soc.*, 2008, **130**, 6700–6701.

[550] J. A. Halfen, S. Mahapatra, M. M. Olmstead, and W. B. Tolman, *J. Am. Chem. Soc.*, 1994, **116**, 2173–2174.

[551] M. J. Boulanger and M. E. P. Murphy, *Biochemistry*, 2001, **40**, 9132–9141.

[552] L. L. Perissinotti, M. A. Marti, F. Doctorovich, F. J. Luque, and D. A. Estrin, *Biochemistry*, 2008, **47**, 9793–9802.

[553] J. A. Halfen, S. Mahapatra, E. C. Wilkinson, A. J. Gengenbach, V. G. Young Jr., L. Que Jr., and W. B. Tolman, *J. Am. Chem. Soc.*, 1996, **118**, 763–776.

[554] S. Suzuki, T. Yoshimura, T. Kohzuma, S. Shidara, M. Masuko, T. Sakurai, and H. Iwasaki, *Biochem. Biophys. Res. Commun.*, 1989, **164**, 1366–1372.